This electronic thesis or dissertation has been downloaded from Explore Bristol Research, http://research-information.bristol.ac.uk

Author:
Rev, Tamas

Title:
Exploiting thin-ply materials to establish controlled failure in carbon composites

General rights
Access to the thesis is subject to the Creative Commons Attribution - NonCommercial-No Derivatives 4.0 International Public License. A copy of this may be found at https://creativecommons.org/licenses/by-nc-nd/4.0/legalcode This license sets out your rights and the restrictions that apply to your access to the thesis so it is important you read this before proceeding.

Take down policy
Some pages of this thesis may have been removed for copyright restrictions prior to having it been deposited in Explore Bristol Research. However, if you have discovered material within the thesis that you consider to be unlawful e.g. breaches of copyright (either yours or that of a third party) or any other law, including but not limited to those relating to patent, trademark, confidentiality, data protection, obscenity, defamation, libel, then please contact collections-metadata@bristol.ac.uk and include the following information in your message:

- Your contact details
- Bibliographic details for the item, including a URL
- An outline nature of the complaint

Your claim will be investigated and, where appropriate, the item in question will be removed from public view as soon as possible.

Exploiting thin-ply materials to establish controlled failure in carbon composites

By

Tamas Rev

Department of Aerospace Engineering

UNIVERSITY OF BRISTOL

A dissertation submitted to the University of Bristol in accordance with the requirements of the degree of DOCTOR OF PHILOSOPHY in the Faculty of Engineering.

April 2020

Word count: 59732

ABSTRACT

The failure prediction of composite materials is hindered by the lack of accurate theories and difficulties in generating reliable experimental data. To complement the latter, this thesis aims to investigate the behaviour of carbon/epoxy materials under multi-axial loadings using thin-plies. By controlling the failure mechanism of composite laminates, the effect of different stress components can be looked at with regard to the failure strain/strength of the material. An expedient to that is utilizing a very thin-ply carbon/epoxy material (with a ply thickness of only 0.03 mm) that allows unwanted damage mechanisms to be suppressed. Multi-axial stress states are created in the unidirectional (UD) material under uniaxial tensile loading by specially designing the laminates. The thesis also incorporates the basic material characterisation of the thin-ply carbon/epoxy that provides the foundation for these novel tests.

A combined loading of longitudinal tension and transverse compression was applied to the UD thin-ply composite through the scissoring deformation of angle-ply blocks of the same material in which the UD plies were embedded. Three different angle-ply thin-ply laminates were designed using classical laminate analysis (CLA) with varying amounts of transverse compression. It was found that the transverse stresses have very little effect on the failure strain of the thin-ply material. Additionally, one of the key limitations of tensile tests – stress concentrations arising due to gripping effects – was also addressed using a recently developed novel hybrid composite test approach.

A biaxial stress state of longitudinal tension and transverse tension was induced in the UD ply block where transverse tension was due to the indirectly generated residual thermal stresses in the cross-ply laminates. The effect of ply thickness on the fibre failure strain was investigated by designing four different cross-ply configurations with varying thickness 90° blocks adjacent to the central 0° plies. Advanced instrumentation including in-situ and quasi-in-situ X-Ray Computed Tomography (X-CT) and acoustic emission (AE) were utilized to detect and monitor damage accumulation in the specimens. It was found that thin-ply materials are indeed capable of suppressing transverse micro-cracking. The initiation of edge cracks and their progression into the bulk of the material were considered with respect to their effect on failure. A small degradation of the fibre failure strain was found as the 90°-layer thickness increased in the laminates mainly due to the development of edge/transverse cracks. Overall, ply thickness was found to have a small effect on the longitudinal failure strain whereas there was no evidence to suggest an effect for the transverse tensile stresses.

Furthermore, a recently published novel tensile test method is investigated further and used to determine the longitudinal compressive strength under a combined longitudinal compression and transverse tension state of stress. An advanced failure criterion called ONERA progressive failure model (OPFM) and the design of experiments (DOE) were used to design the laminates and optimize the stacking sequence. Material behaviour was investigated with respect to non-linearity of the carbon fibre as well as the effect of ply thickness. The compressive loading was indirectly applied to the 90° layers through the scissoring deformation from the high Poisson ratio of angle plies in which they were embedded. Measurements were carried out using AE, digital image correlation (DIC), video and virtual strain gauge measurements. Post failure, optical microscopy and Scanning Electron Microscopy (SEM) imaging were carried out to highlight the damage state of the coupons. Stress concentrations were addressed by manufacturing shoulder ended specimens. Gauge section compressive failure (fibre kinking) was found in the specimens. The effect of ply thickness on the fibre failure strain was investigated and it was shown that this resulted in higher failure strain/strength values for thinner 90°-layer thickness laminates.

Additionally, the development and fundamental characterization of thin-ply glass/carbon hybrid composite overload sensors which show a striped pattern if triggered are presented along with the proof of concept on a demonstrator application. By doing so, a visual indication of damage can be observed that can be further utilized as a novel structural health monitoring concept for composite and metallic components or structures.

DEDICATION AND ACKNOWLEDGEMENTS

Firstly, I would like to thank my supervisors, Professor Michael R. Wisnom and Dr. Gergely Czél for putting their trust in me and the never-ending support they provided throughout the years. Their professional guidance and knowledge were essential, and I am really thankful for all the stimulating conversations and meetings that we had together. They provided a platform for me to grow, develop critical, scientific thinking and introduced me to the ever-growing, complex but exciting field of composites failure analysis.

Besides, I would like to thank Ian Chorley, Guy Pearn, Peter Whereat for their help and support providing me with training, advice and equipment to carry out my experimental work as well as Dr Xiaodong Xu for his daily based help. I would also like to thank Dr Yusuf Mahadik, Dr. Steve Rae, Dr. Oliver Nixon-Pearson, Dr Marco Longana, Dr Meisam Jalalvand and Dr Mohamad Fotouhi for their guidance and help when needed.

I would like to say a special thank you to some of my colleagues and friends Vincent Maes, Dr. Andres Rivero Bracho, Dr. Rob Worboys, Dr Putu Suwarta, Dr Xun Wu, Dr Aakash Paul and Gabor Soter for all the technical and non-technical conversations and their continued support during my PhD. A big thank you goes to all of my friends, all over the world, who were there for me in need and cheered me through these years.

I wish to thank Professor Paul Weaver for offering me the opportunity to be part of the CDT programme and Sarah Hallworth for her continued support during the first years. I am very grateful to have had the opportunity to spend two international placements over the course of my PhD at word-class institutions, carrying out cutting edge research.

I wish to thank Dr Frédéric Laurin and Dr François-Xavier Irisarri for their help, guidance and supervision during and after my placement at ONERA (The French Aerospace Lab) in Paris, France. I would also like to acknowledge all the technicians, researchers and engineers who contributed and helped me with testing my specimens and acquiring the optical microscopy and SEM images.

I wish to thank Dr. Frank A. Leone and Dr Andrew E. Lovejoy, Dr. Carlos G. Dávila and Dr, Cheryl A. Rose for providing me with the opportunity to spend my research placement at NASA Langley Research Center in Hampton, Virginia. They hosted me and guided me throughout an incredible experience. I would like to also thank Wade Jackson and William Johnston experimental engineers who helped me to test my coupons as well as to carry out X-CT tests throughout my placement.

This work was supported by the Engineering and Physical Sciences Research Council through the EPSRC Centre for Doctoral Training in Advanced Composites for Innovation and Science [grant number EP/L016028/1] and by the EPSRC Programme Grant EP/102946X/1 on High Performance Ductile Composite Technology in collaboration with Imperial College, London.

The PhD Thesis is dedicated first and foremost to my loving grandfather who has always been an unwavering pillar in my life, supporting me in every way possible. This PhD could not have come true without him and his emotional and financial support. I have faced some of the biggest challenges and obstacles in my life during these years, and I would like to say a big thank you to my parents, my grandmother, my sister and my brother, my extended family and all my friends and colleagues who have been there for me throughout this journey, helped me stand up when I fall, and enjoyed the happy moments together.

“Failure is not an option.” (Unless the PhD Thesis subject is about failure)

“To recognize that the greatest error is not to have tried and failed, but that in trying, we did not give it our best effort “

(Gene Kranz, NASA Flight Director Gemini and Apollo Missions)

Bristol, 12 April 2020

AUTHOR'S DECLARATION

I declare that the work in this dissertation was carried out in accordance with the requirements of the University's *Regulations and Code of Practice for Research Degree Programmes* and that it has not been submitted for any other academic award. Except where indicated by specific reference in the text, the work is the candidate's own work. Work done in collaboration with, or with the assistance of, others is indicated as such. Any views expressed in the dissertation are those of the author.

SIGNED: .... Bristol, April 12, 2020

PUBLICATIONS

The work presented in this PhD Thesis was disseminated through various posters, presentations, conference papers and journal publications. A list of the key papers is disclosed here alongside with other publications that the author of this thesis was involved with throughout the course of the PhD program.

Journal Papers

P.1.

T. Rev, M. Jalalvand, J. Fuller, M. R. Wisnom, G. Czél. A simple and robust approach for visual overload indication - UD thin-ply hybrid composite sensors, **Composites Part A: Applied Science and Manufacturing**, Volume 121, June 2019, Pages 376-385. (https://doi.org/10.1016/j.compositesa.2019.03.005)

Conference paper

C.1.

T. Rev, G. Czél, and M. R. Wisnom, “A novel test method to induce bi-axial stress states in thin-ply carbon composites under combined longitudinal tension and transverse compression,” in *ASC 33rd Annual Technical Conference on Composite Materials*, 2018.

C.2.

T. Rev, G. Czél, M. Jalalvand, and M. R. Wisnom, “Unidirectional hybrid composite overload sensors – robust tools for visual overload indication,” in *ICCM21'*, volume 1, August 2017.

Other

X. Xu, M.R. Wisnom, X. Sun, **T. Rev**, S.R. Hallett, Experimental determination of Through-Thickness Compression (TTC) enhancement factor for Mode II fracture energy, **Composites Science and Technology**, Volume 165, September 2018, Pages 66-73. (https://doi.org/10.1016/j.compscitech.2018.06.012)

G. Czél, **T. Rev**, M. Jalalvand, M. Fotouhi, M.L. Longana, O.J. Nixon-Pearson, M.R. Wisnom, Pseudo-ductility and reduced notch sensitivity in multi-directional all-carbon/epoxy thin-ply hybrid composites, **Composites Part A: Applied Science and Manufacturing**, Volume 104, January 2018, Pages 151-164. (https://doi.org/10.1016/j.compositesa.2017.10.028)

M. R. Wisnom, G. Czél, M. Fotouhi, J. Fuller, M. Jalalvand, **T. Rev**, and X. Wu, Reduced tensile notch-sensitivity in pseudo-ductile thin ply composites, In: *18 European Conference on Composite Materials -ECCM 18, 2018.*

X. Xu, **T. Rev**, X. Sun, M. R. Wisnom and S. R. Hallett, Experimental investigation into through thickness compression enhancement effect on mode II fracture energy using bi-axial tests, In: *18th European Conference on Composite Materials -ECCM 18, 2018.*

G. Czél, **T. Rev**, M. Jalalvand M. Fotouhi, M. R. Wisnom, Demonstration of pseudo-ductility in quasi-isotropic laminates comprising thin-ply UD carbon/epoxy hybrid sub-laminates, In: *17th European Conference on Composite Materials -ECCM 17, 2017.*

TABLE OF CONTENTS

CHAPTER 6 LONGITUDINAL COMPRESSION – TRANSVERSE TENSION: A NOVEL TEST METHOD TO INDUCE BI-AXIAL STRESS STATES IN THIN-PLY COMPOSITES 144

CHAPTER 7 OVERLOAD SENSORS – A SIMPLE AND ROBUST APPROACH FOR VISUAL DAMAGE INDICATION 187

LIST OF FIGURES

LIST OF TABLES

LIST OF NOTATIONS AND ABBREVIATIONS

It has to be noted that the latin and greek letters shown below do not reflect specific expressions but general notations. For specific meaning of different notations, the reader is referred to the text of the thesis.

Latin letters

Notation	Description	Unit
A	Crack area	m^2
A	A matrix	N/m
d_f	Filament diameter	µ
E	Youngs modulus	N/m^2 ,Pa
G	Energy release rate	N/mm
G_c	Critical energy release rate	N/mm
G	Shear modulus	N/m^2 ,Pa
h	Thickness	m
L	Length	m
m	Weight fraction	%
M	Weight/mass	kg
N	Load/unit width	N/m
Q	Compliance matrix	N/m^2
$\bar{Q}$	Transformed stiffness matrix	N/m^2
T	Temperature	°C
t	Thickness	m
U	Internal strain energy	J
V	Volume	m^3
V	Volume fraction	-
V	Lamination parameter	-
W	Work of external forces	J
w	Width	m

Greek letters

Notation	Description	Unit
α	Coefficient of Thermal Expansion	1/K
ε	Strain (elongation)	-
ν	Poisson's ratio	-
σ	Stress/strength	N/m^2 ,Pa
ρ	Density	kg/m^3
τ	Shear strength	N/m^2 ,Pa
γ	Shear strain	-

θ	Theta angle	°

Abbreviations

Abbreviation	Description
2D	Two-dimensional
3PB	Three-point bend
4PB	Four-point bend
AE	Acoustic Emission
AP	Angle-Ply
ASTM	American Society of Testing and Materials
CDM	Continuum Damage Mechanics
CFRP	Carbon Fibre Reinforced Plastic
CLA	Classical Laminate Analysis
CLT	Classical Laminate Theory
CNC	Computer Numerical Control
CPT	Cured Ply Thickness
CTE	Coefficient of Thermal expansion
CoV	Coefficient of Variation
DIC	Digital Image Correlation
DOE	Design of Experiments
EMI	Electromagnetic Interference
ESPI	Electronic Speckle Pattern Interferometry
FAW	Fibre Aerial Weight
FBG	Fibre Bragg Grating
FC	Fibre Content
FEA	Finite Element Analysis
FEM	Finite Element Model
FF	Fibre Failure
FOS	Fibre Optic Sensors
FRC	Fibre-reinforced composite
FRP	Fibre-reinforced Polymer
HiPerDuCT	High Performance Ductile Composite Technology
HS	High strength
ICSTM	Imperial College of Science, Technology and Medicine
IFF	Interfibre Failure
IITRI	Illinois Institute of Technology Research Institute

IM	Intermediate Modulus
IRT	Infrared Thermography
LEFM	Linear Elastic Fracture Mechanics
LVDT	Linear Variable Differential Transducer
MTB	Mountain Bike
NASA	National Aeronautics and Space Administration
NDT	Non-Destructive Testing
NTPT	North Thin Ply Technology
ONERA	Office National d'Etudes et de Recherches Aérospatiales
OPFM	ONERA Progressive Failure Model
PAN	Polyacrylonitrile
QI	Quasi-Isotropic
ROI	Region of Interest
ROM	Rule of Mixtures
RPM	Revolutions per minute [1/min]
SEM	Scanning Electron Microscope
SERR	Strain Energy Release Rate
SHM	Structural Health Monitoring
UD	Unidirectional
UHM	Ultra-high modulus
UV	Ultraviolet
WWFE	World Wide Failure Exercises
X-CT	X-ray Computed Tomography

Chapter 1

Introduction

1.1. Background

Fibre reinforced polymers (FRPs) are at the forefront of a generation of materials that are used to advance both the evolutionary and revolutionary development of today's engineering structures. The former one means incremental improvements to the property of existing materials or structures, the latter one means the development of new materials [1]. Their superior properties such as high specific strength and stiffness, enhanced chemical and corrosion resistance and good fatigue properties enable them to satisfy the increasing demands of the aerospace [2] and automotive industries [3], civil engineering [4] and sporting goods [5].

Besides the improvement of mechanical performance, one of the key driving factors for using composite materials is weight savings [6]. Since the invention of carbon fibre in 1958 and the development of its commercial production in the 1960s [7], [8], an exponential increase can be observed in the use of composite materials, especially in the aerospace industry [1]. As an example, Figure 1.1 illustrates how the use of composites by weight percent continuously increases over the years in different civilian and military aircraft as a function of the year of their introduction.

With regard to aerospace, composites nowadays are utilised in both primary and secondary structures: bolted structures, joints [9], guide vanes, fan blades, wing spars, in the fuselage and window/door frames, to name but a few [1], [10]. Since 1982, when the first primary composite structure (horizontal stabiliser for the Boeing 737) was certified, the use of composite structures continued to increase. A great example of that is the Airbus A380 airliner with its 280 tonnes of mass, out of which 25% is made of fibre reinforced composites [1]. An illustration of the composite applications on the A380 aircraft is shown in Figure 1.2 [11].

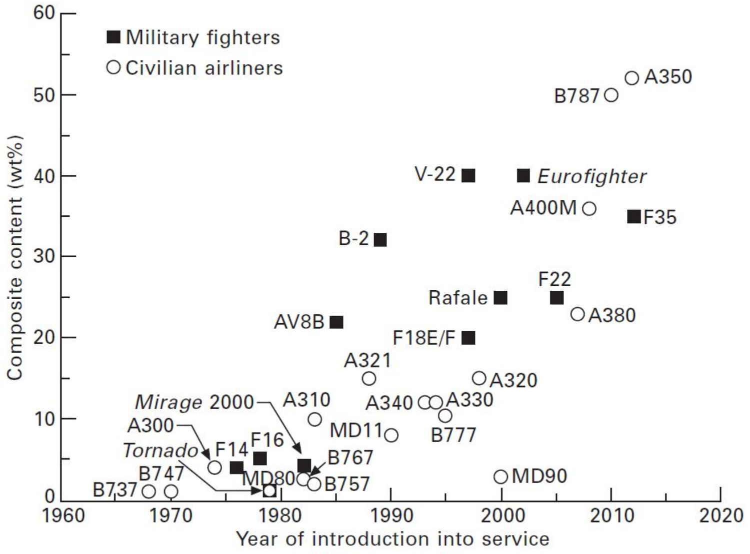

Figure 1.1. Weight percent (wt%) of composite materials used in different types of aircraft obtained from [1].

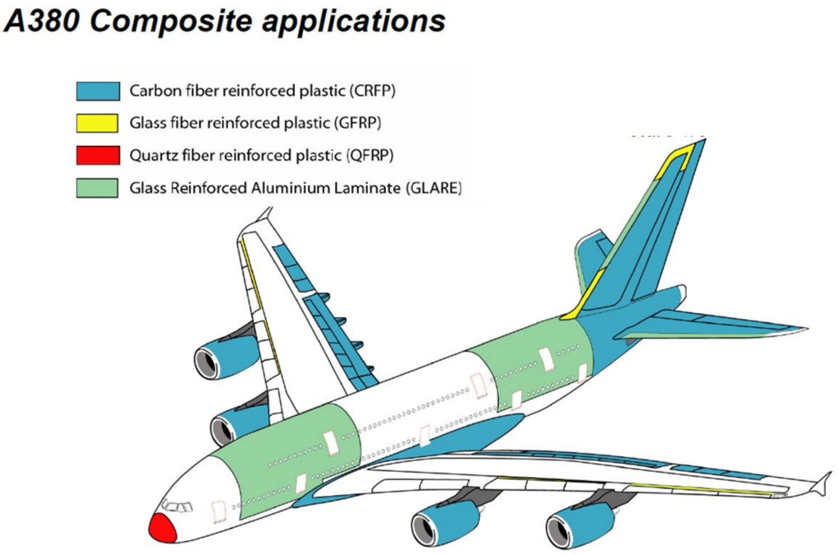

Figure 1.2. Illustration of fibre reinforced composite applications obtained with the Airbus A380 type aircraft, courtesy of Airbus [11]

One of the greatest advantages of fibre reinforced polymers is their versatility: they can be tailor-designed for the application by *e.g.* meeting specific design requirements (strength/stiffness) through different lay-ups, and constituent materials which are crucial as they are used in components with more and more complex geometries and loading conditions.

However, FRPs are anisotropic and heterogeneous, making their application challenging in an industrial setting due to the complexity of structural design while ensuring that the component meets the desired specifications, properties as well as safety requirements. Furthermore, they are limited by their inherent brittleness leading to sudden and catastrophic failure with no significant damage or detectable warning in advance, so structures that pass visual inspection can fail at lower loads than expected [12].

1.2. Problem statement and objectives

One of the greatest challenges – that has been widely investigated today and in past decades - is to predict and accurately model the failure of composite materials. Their failure mechanisms are very complex and different from metals: there are numerous failure modes which can not only influence material behaviour individually but also interact with each other in distinct ways. These failure modes are highly dependent on the stress state in the material, the geometry of the specimens, the stacking sequence, the material properties, and any manufacturing or service induced defects to name but a few [13]. Especially under multi-axial loadings resembling real-life conditions – external loads acting in a combined fashion – it is immensely important to predict and determine the real behaviour of composite materials.

Failure and strength prediction get more and more complex when trying to determine the exact definition of failure or to validate predictions with reliable experimental data. This is underpinned by the findings of the world’s most extensive research program on failure of composites namely ‘The World-Wide Failure Exercises’ (WWFE) [14]–[17], which concluded that there is currently no existing failure criterion that can be universally accepted to predict failure in such fibrous materials. Furthermore, there is a paucity of accurate experimental data in the literature [18], [19]. Even for unidirectional (UD) laminates, accurately determining their fundamental mechanical properties such as failure strain or strength is still a scientific challenge [18].

Consequently, the main research question of the PhD Thesis arises: How can we determine material strength under multi-axial loadings more accurately? This question is tackled throughout the Thesis from two different perspectives.

On one hand, as composite structural design and failure analysis is most often defined on the scale of the elementary UD ply, it is crucial to determine the UD ply strength in the most accurate way possible. This PhD thesis introduces novel testing concepts that can help improve existing methods in determining design allowables such as longitudinal tensile and compressive strength. The ultimate strength of UD carbon/epoxy laminates is often underestimated due to the experimental strength measurements being affected by stress concentrations at the end-tab regions of the coupons [20]. Usually, a significant knock-down in their measured strength can be observed accompanied by either premature failure of the specimens or notably lower measured strains than the expected ultimate failure strain of the utilised fibres. Consequently, for more complex cases such as testing under biaxial loading conditions, the difficulty of acquiring acceptable data magnifies due to issues that include but are not limited to edge effects, gripping related issues, quality of the materials and the consistency of coupon fabrication and testing [18].

Alternatively, establishing composite material behaviour in realistic operation conditions (under multi-axial loadings) can aid the validation of well-established and used failure criteria as well as predictive models. In the PhD Thesis, empirical data are generated for different multi-axial loading cases by the use of novel laminate designs.

Ultimately the main objectives identified are:

1. To determine the real effect of different stress components on the fibre direction strain to failure of the utilized UD thin-ply, carbon/epoxy material,
2. To design laminates and novel testing concepts that allow for the creation of multi-axial stress states in a simple tensile test configuration, and
3. To provide a visual indication of damage by purpose designing for a specific failure mechanism.

It has to be noted that the objectives identified above were modified as the work progressed throughout the PhD. In Chapter 5 and 6, the objective of determining the effect of transverse tensile stresses on tensile and compressive failure respectively was modified to look at the effect of transverse cracking on the failure stress as well as to investigate the effect of changing ply block thickness on transverse cracking.

The means to achieve such objectives was through controlling the damage behaviour of composite laminates so that controlled failure can be obtained. The key methodologies to do that were:

- Using novel, thin-ply carbon fibre/epoxy materials to isolate failure mechanisms;
- Purpose designing composite laminates to achieve/promote the desired failure mode; and

The utilisation of thin-ply materials allows for suppressing undesired damage mechanisms that usually precipitate the sudden failure of composites: transverse micro-cracking and edge delamination. Additionally, thin-ply materials can also be used to promote a specific failure mechanism hence allowing for controlling the damage process up to the final failure of the composite. A side benefit of controlling failure this way is the visual indication of overload and the corresponding damage in composite structures/components (exhibiting a striped pattern when reaching a certain strain level) that can be used for structural health monitoring purposes.

Besides, further understanding the failure mechanisms of such thin- plies can add great value to the conventional ways of designing composite structures. If the basic mechanical properties of unidirectional laminae can be predicted and determined more accurately, the true potential of the composite material can be exploited by using less conservative design envelopes, smaller safety margins and ultimately it would result in a reduction of cost and product lead time as well as a safer operation in service due to increased confidence in structural design and analysis.

1.3. Thesis outline

The work carried out to fulfil the main objectives of the PhD is divided into the following chapters:

Chapter 1 gives a brief introduction to composite materials including their main areas of use and some examples of structural applications in the aerospace industry. It highlights the main issues when designing composite structures and the challenges associated with the failure prediction of such materials. It defines the objectives of the PhD thesis and the structure of the research by outlining the chapters.

Chapter 2 introduces a general overview of failure prediction and damage modelling methods as well as damage mechanisms of composite materials based on the available literature.

Chapter 3 describes the material of choice for this thesis including an investigation into the characteristics and mechanical properties of the material.

Chapter 4 presents a novel test method for generating a multi-axial load case of longitudinal fibre tension and transverse compression that is indirectly put on the UD thin-ply composite laminate through the scissoring deformation of the embedding angle-ply blocks of the same material. The amount of transverse compression is varied through classical laminate design and the effect of transverse compressive stresses is determined.

Chapter 5 presents a multi-axial load case of longitudinal tension and transverse tension that is indirectly applied to the UD thin-ply composite laminate through the residual thermal stresses that are induced in the examined cross-ply laminates. The effect of 90° ply thickness on the 0° fibre failure strain was also investigated.

Chapter 6 presents a novel test method that is used to determine the longitudinal compressive strength of the material under a combined longitudinal fibre compression and transverse tension state of stress. A progressive failure criterion called ONERA progressive failure model (OPFM) and the design of experiments (DOE) was used to design the laminates. The effect of ply thickness on the fibre direction failure strain was also investigated.

Chapter 7 investigates the concept of providing a visual indication of damage through purpose designing hybrid composites that exhibit a specific failure mechanism. A new UD hybrid composite sensor concept is presented and investigated which can be used for structural health monitoring of both composite and metallic structures.

Chapter 8 describes the applicability of the fundamental research work carried out in this thesis and talks about the potential impact of the findings in industry. Furthermore, it concludes the work carried out in the PhD thesis and indicates potential future work that could complement the research presented.

Chapter 2

Literature review

The issues relating to the failure prediction of composites can generally be divided into two different categories: the development of accurate theories and generating good experimental data. According to Christensen [18] out of the two, reliable data acquisition - conceiving and performing quality testing - tends to be the more severe issue. Reliable data in this context means reproducible, i.e. that would provide the same experimental result if repeated or acquired in a different environment using the same circumstances, conditions and assumptions. The lack of reliable measurements [21] makes it very difficult to choose the appropriate criteria over one another, to effectively validate the existing theories or to compare them with each other. To highlight this, some of the vast diversity of theories available in failure prediction and modelling is briefly presented in this chapter. A review of the most often used biaxial testing methods for composite materials is discussed. This way the research presented in the following chapters can be put into context, where novel laminate designs and testing methods are presented to induce biaxial stress states in the investigated thin-ply carbon epoxy material. Furthermore, some of the key failure /damage modes in composite materials are also presented to shed light on the complex interactions that may occur. The literature presented is non-exhaustive due to the vast amount of work done in the different areas. Each chapter in the thesis also includes separate references that are relevant to the specific loading case or topic being discussed.

2.1. Damage mechanisms in fibre reinforced composite laminates

There are several failure modes that can occur in a composite lamina under longitudinal tensile loading. The failure mechanisms are shown in Figure 2.1 as reproduced from [22].

These mechanisms are strongly dependent on the characteristics of the fibre and matrix materials and because they interact with each other, they do not have a consistent sequence of damage onset. Damage could occur during manufacturing, assembly or due to the mechanical and/or environmental loads hence the mechanisms can be categorized as process-induced or service-induced damage [23].

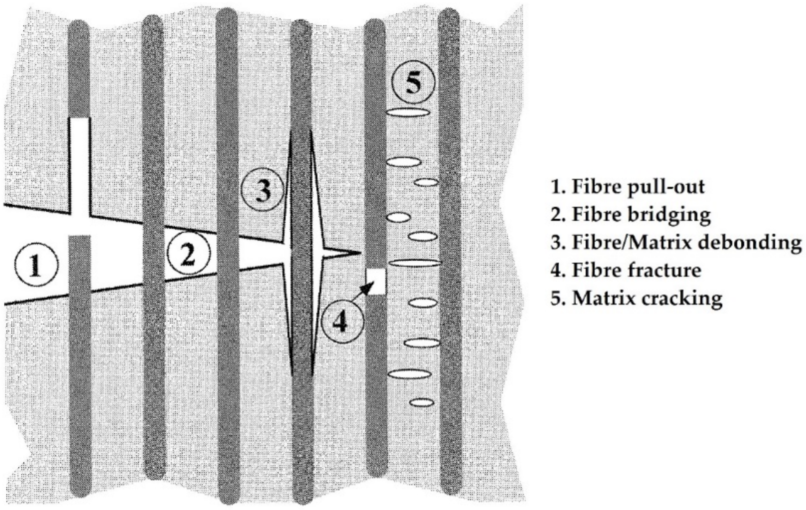

Figure 2.1. Typical damage modes of unidirectional (UD) lamina under tensile loading reproduced from [22].

A short explanation of key mechanisms is presented in the following. However, certain damage mechanisms are discussed in further detail when they are directly relevant to a specific loading case: *e.g.* matrix cracking in cross-ply laminates in Chapter 5 and compressive fibre failure in Chapter 6.

2.1.1. Matrix cracking

Matrix cracking is usually the first damage that occurs in fibre-reinforced composites comprised of standard thickness plies (t ≥ 125 μm) and often takes place when the strength of the matrix is exceeded, at interfaces or due to stress concentrations [24]. It is strongly influenced by the ply orientations within the laminate, the stacking sequence and ply thicknesses [25]. The first cracks appearing under load will grow and propagate through and along the structure leading to other damage initiating and the degradation of the structure up to a critical point where it is rendered unsafe for operation. This is one of the reasons why it is important for researchers to focus on predicting and modelling crack initiation and propagation [23].

On a macroscopic scale there are two types of matrix cracks: intra-ply and inter-ply cracks. Intra-ply cracks initiate and run across the thickness of the ply and they propagate parallel to the fibres.

Inter-ply (interlaminar) cracks, also known as 'delamination' initiate and propagate parallel to ply interfaces. On a microscopic level usually fibre-matrix interfaces and randomly existent matrix flaws are the origins of cracks [25]. Their propagation can most probably be arrested or blunted at ply or at fibre-matrix interfaces [23].

2.1.2. Delamination

On a macroscopic level, the most common failure mechanism is delamination, that has a particularly important role [13], [21], [26]. There have been a large number of criteria proposed to predict and understand the initiation and propagation of delamination. The failure criteria utilized usually incorporate combinations of transverse tension, shear [27], [28] and sometimes longitudinal tension [29] to describe this highly complex damage mechanism but generally fracture mechanics approaches are more common. Delamination is usually caused by high interlaminar stresses and results in a significant loss of stiffness and integrity of the composite structure. Different types of delamination can be distinguished based on where the separation of the layers initiates. Accordingly, delamination can initiate at the free edges of the laminate (*e.g.* at the boundary of a hole or at the end of a tubular shaft), or at particular geometrical features such as ply drops or under impact loads to name but a few. Besides, buckling driven delamination can be distinguished from the types mentioned above when compressive loads are applied [22]. Due to stress singularities such as free edges and ply drops, it is difficult to apply stress-based failure criteria hence the wide use of fracture mechanics approaches to model and predict delamination initiation and propagation. A thorough and critical review of the state of the art of material constitutive models and composite failure theories regarding delamination is presented by Orifici *et al.* [30].

On a micro-scale, but related to delamination, the mechanism of fibre bridging (illustrated on Figure 2.1) can take place usually between two distinct crack surfaces in composites with a low strength matrix. It reduces the stress at the crack tips as it still transfers some stress and allows further interfacial debonding at the fibre-matrix interface [23].

2.1.3. Fibre failure/fracture

Fibre fracture as shown on Figure 2.1 is the most catastrophic of the failure mechanisms as the fibres play a primary load carrying role in the composite. Failure could be the result of tensile or compressive stresses. Under tensile loading conditions fibres fracture when the maximum allowable axial tensile stress (or strain) of the fibre is exceeded. The fibre strengths are highly variable and dependent on defects within the material as well as on the formation of critical clusters [24]. This thesis investigates the influence of additional transverse stresses on tensile fibre failure.

Following fibre fracture that is accompanied by interfacial debonding [24], in a distinct plane to the cracking another micro-mechanism called fibre pull-out can take place (see point 1 on Figure 2.1). It happens during crack advancement when this major energy-absorbing mechanism of the composite tries to pull the fibres out of their sockets;

this mechanism is resisted by friction forces at the fibre-matrix interface [23]. Essentially this mechanism enhances the toughness of the composite. This mechanism also plays a key role in short fibre composites and may increase their fracture energy.

Also, during crack propagation, the stress field evolving ahead of the crack tip can induce shear stress at the fibre-matrix interface leading to another micro-mechanism called fibre-matrix interfacial debonding (see point 3 on Figure 2.1). This failure mechanism is basically a toughening mechanism for fibre reinforced composites.

Too low an interfacial shear strength (τ) causes extensive debonding between fibres and the matrix phase leading to decoupling of the composite constituents. Consequently, the composite structure will lose the advantage of being reinforced due to poor stress transfer between fibres and matrix. If τ is too high, it will cause a negligible amount of interfacial debonding during the failure of the composite leading to low toughness and catastrophic failure [23].

2.2. Failure prediction and damage modelling methods

A wide range of approaches have been developed and utilized on different structural levels (micro, meso and macro-scale) to tackle the complex issue of predicting and modelling the failure of composite materials. The micro-mechanical level represents the constituents of the polymer composite lamina: reinforcement, matrix and interface/interphase. The failure mechanisms at this level are highly dependent on the material properties of the constituents and the loading conditions the lamina is subjected to.

At the meso-mechanical level - between micro scale (constituent level) and macro-scale (laminate level) -, it is a lot more difficult to understand failure as additional damage mechanisms such as delamination, interlaminar shear failure or combinations of inter- and intralaminar damage can also come into effect. Macro- mechanical approaches are often preferred in failure analysis when predicting the overall strength of a composite laminate [31]. A generalised classification for failure prediction methods can be divided into three major categories: failure criteria, progressive damage models and fracture mechanics approaches which will be discussed briefly in the following sections.

2.2.1. Failure criteria

Failure theories generally look at the initial and final parts of the failure locus: damage initiation and the ultimate failure of composite materials [13]. The most extensive research programs conducted in the past 50 years regarding the failure of composites were the World-Wide Failure Exercises (WWFE) Part I.-III. [14]–[17]. The initial exercise from 1996 to 2004 was mainly carried out to provide a comprehensive review of the 19 failure theories available at that time for FRP laminates under two-dimensional (2D) stresses, in-plane, biaxial loading cases in the absence of stress concentrations and to compare their predictive capabilities directly with each other and against experimental measurements [15]. It was concluded that there is no existing failure criterion that can be universally accepted to predict the failure of composite structures [13], [32]. In fact, for 75% of the proposed test cases in the exercise, only a few theories proved successful at giving 'acceptable' correlation with the provided test data [15]. To illustrate the lack of reliability in failure prediction, Figure 2.2 shows the confidence levels displayed by the WWFE theories for different parameters and failure mechanisms [33].

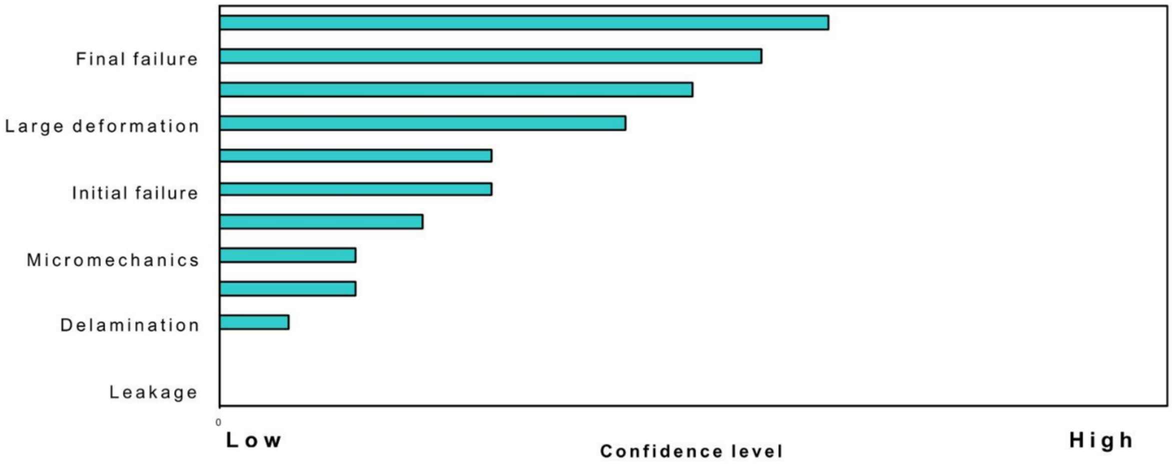

Figure 2.2. Confidence levels predicted by WWFE theories for different failure mechanisms and parameters reproduced from [33]

Generally, failure criteria and the failure analysis of composite laminates can be categorized as (i) Lamina failure criteria or (ii) Laminate failure criteria where the latter one is often comprised of laminate stress analysis with lamina stiffness reduction [34].

Lamina failure criteria are usually based on linear elastic analysis and involve the determination of unidirectional (UD) lamina strength and failure modes under a state of combined stress in orthotropic materials [34]. The in-plane strength of a UD lamina can be characterised by five different material parameters: longitudinal tensile and compressive strength (X_t and X_c), transverse tensile and compressive strength (Y_t and Y_c) and in-plane shear strength (S) respectively. An extensive review on such failure criteria and other existing theories has been conducted by Nahas [35]. More recent ones conducted by De Luca and Caputo [36], Daniel [37] as well as Orifici *et al.* [30] summarize the state of the art in material constitutive modelling, composite failure theories and analytical failure criteria. Usually these criteria do not describe detailed failure processes, hence are considered as 'phenomenological' approaches.

Lamina failure criteria can also be classified depending on whether they are associated with the mode of failure or not. If they are not associated, they may utilize stress or strain polynomial and/or tensorial expressions to predict failure as a function of the UD material strengths. These mathematical expressions often originate from extensive empirical testing where a function has been fitted to the experimentally measured data [13]. Typical examples of such failure criteria are Tsai-Hill [38], [39] Tsai-Wu [40] and Hoffman [41]. The implication is that in order to understand the accuracy of such theories and conclude their reliability, first the fundamental and physical behaviour of the failure mechanisms need to be understood.

As mentioned before, possible modes of lamina failure are fibre rupture, transverse matrix cracking and shear matrix cracking respectively. It has to be noted that both transverse and shear matrix cracking are matrix dominated failures. However, they are separated because some criteria - eg. Maximum Stress [30] - assume that these modes are caused by different independent stress components - σ_{22} and τ_{12} respectively - [34].

Failure criteria that are associated with particular modes of failure (for different loading conditions) often consider the material to be heterogeneous and assume that distinct phases can fail independently of each other. They can be sub-categorized into two groups: interactive and non-interactive (limit) criteria. Interactive failure criteria take the interactions between the different stress and strain components acting on the lamina into consideration.

They use for example quadratic or higher order polynomial equations which indicate failure when the equation is satisfied. The failure mode is determined by comparing stress/strength ratios [13].

However, non-interactive/limit criteria do not consider these interactions; they compare the individual stress or strain components with the corresponding material strengths respectively. For more complex problems - that are subjected to multi-axial loadings - limit criteria often result in significant errors in strength prediction. The most commonly used failure criteria in this group are the Maximum Stress and Maximum Strain criteria [13], [34]. As reported by Sun *et al.* [34] 80% of the participants of an AIAA Failure Criteria Survey claimed to have used these two limit criteria alongside Tsai-Hill [38], [39] and Tsai-Wu [40] from the interactive group.

Other interactive or partially interactive failure criteria include the approaches of Hashin [42] Puck [43] and Hart-Smith [44] along with many others [13], [45]–[50].

It has to be noted that each of these criteria have their own specific assumptions hence it is very difficult to make direct comparisons between them. For instance, in 1973 Hashin and Rotem proposed two distinct quadratic failure criteria based on fibre and matrix failure [51]. Later in 1980, Hashin [42] proposed an extension to three-dimensional problems (stress-states) of the originally proposed linear criterion. Hashin’s later criterion is able to distinguish between fibre failure and matrix failure in both tension and compression as well as interlaminar tensile and compressive failure. However, as indicated by Davila *et al.* [52] in 2005, the quadratic interactions used by Hashin – for example to obtain the plane of fracture for the matrix compression mode – often do not fit the experimental data in the literature.

To address this issue, Davila *et al.* [52] developed and proposed a new set of 6 phenomenological criteria (LaRC03) for predicting the failure of fibre reinforced polymers (FRP) especially to predict matrix cracking under in-plane shear and transverse tension/compression. The failure envelopes predicted by LaRC03 showed good correlation with experimental data. The criterion developed by Puck and Schürmann [43], [53] includes an additional parameter when compared to Hashin's. It takes the angle of matrix fracture into consideration, hence making it able to assess inter-fibre fracture in three different modes as specified in [53].

Laminate failure is generally more complex than lamina failure. In laminates, additionally to the lamina failure mechanisms (eg. fibre failure, matrix tension, matrix shear and compressive failure due to shear instability) three-dimensional (3D) mechanisms can contribute to or cause failure eg. delamination or failure induced by stress singularities such as free edges or notches. As one of the key assumptions of Classical Laminate Theory (CLT) is a two-dimensional (2D) state of stress in the laminate, strength analysis is usually restricted to laminates which are not dominated by such 3D failure mechanisms or it is assumed that they are free from free edge stresses or local stress concentrations due to matrix cracks. Simply put, laminate failure comprises progressive failure processes (sequence of damage progression) taking place eg. lamina failure and interlaminar interactions. Some laminate failure analysis methods assume that after individual plies fail, the laminate itself still has load bearing capacity. Hence, they "discount the ply" and reduce the overall stiffness of the laminate [34]. Sun *et al.* described two distinct methods for stiffness reduction: the parallel spring model and the incremental stiffness reduction model [34].

Laminate failure analysis often uses ply failure criteria especially when delamination and failure due to out-of-plane stresses can be neglected.

One of the most common laminate failure analysis methods is the ply-by-ply discounting method. The laminate is treated as a homogeneous material and CLA is used to determine the ply stresses and strains throughout the laminate. Lamina failure criteria are applied to predict first-ply failure (including its mode). Then, a stiffness degradation approach is used to reduce the overall laminate stiffness due to the failed ply. After, the reduced stiffness laminate is analysed again, and this is repeated over and over until ultimate laminate failure is reached (last-ply failure). However, ultimate failure is often defined by first-ply failure (FPF) by fibre failure or matrix failure (yielding).

An extensive summary of different laminate failure criteria is described in a review by Orifici *et al.* [30]. One of the most used laminate criteria, especially in industry is the maximum strain criteria (which applies to the laminate as a whole).

Laminate failure criteria can be also distinguished based on whether they consider interactions: in some criteria, individual ply failure modes (matrix or fibre failure) are not considered and failure is predicted based on ply failure, for example by Yamada [48], Christensen [54], and Sandhu [55] to name but a few. In other "interactive" criteria such as Tsai-Hill [38], [39] Tsai-Wu [40], Hoffman [41] and others [56]–[58] a failure surface is created using the acquired ply strength data.

2.2.2. Progressive or continuum damage mechanics (CDM)

Progressive failure analysis not only accounts for the initial and final failure locus of composite laminates but takes the stiffness degradation phenomenon (degradation of laminate elastic modulus) into consideration [59]. CDM uses internal variables (damage indices) integrated into material constitutive laws to represent damage in the composite and to describe the initiation and progression of these mechanisms. They usually have an inverse relationship to the material properties [30]. The damage variables and constitutive equations in CDM models usually take the effect of damage induced softening and anisotropy into account.

Typically, CDM models reduce the stiffness of the laminate when a criterion is satisfied. The analysis carries on until the load carrying capacity of the laminate (in a particular direction) is reduced so much that the final failure condition is fulfilled [30].

Some CDM models [60]–[64] use second or fourth order damage tensors to describe stiffness degradation and damage evolution. Damage tensors represent the dissipation energy and damage mechanisms that further the progression of damage. Other models study progressive failure through thermodynamic analysis [65]–[68] but only limited to two-dimensional stress states. A 3D failure model was proposed by Donadon *et al*. [69] to predict damage in composite structures under multi-axial loadings. They incorporated strain rate effects, higher order damage evolution laws, failure criteria and thermodynamic analysis.

An overview on the damage mechanics of composite materials is discussed in [70]. More recently, Liu and Zheng [59] have conducted a very extensive review on the recent developments in progressive failure analysis of composite laminates and constitutive damage modelling by continuum damage mechanics. They have discussed various failure criteria, the damage evolution laws and finite element methods for predicting the variable stiffness failure analysis of composite materials.

Continuum damage mechanics (CDM) is an efficient way to model laminate failure. It is computationally unaffordable to model the overall failure behaviour on the microscale (lamina level) hence the widespread use of continuum damage methods for orthotropic materials [71]. In this thesis a progressive multi-scale approach called ONERA progressive failure model (OPFM) is used to predict the failure behaviour of the designed laminates in Chapter 6, as described in detail in section 6.2.2.1. This approach is one of the many continuum damage models in the literature [65], [67], [72]–[78] provided with different levels of complexity with regard to the utilized failure criteria and degradation laws. Tay *et al.* [79] presented an overview of advances in the modelling and analysis of progressive damage in composite materials. They have also reported that many of the material property/stiffness degradation methods using CDM are done at the ply level, but some use combined micro-macromechanical approaches. Another approach was presented by Llorca *et al.* [80] who have shown a bottom-up multiscale model to carry out high fidelity virtual tests for composite materials. Their numerical simulations take into account the deformation and failure mechanisms at different length scales. An extensive review on multiscale methods for composite materials is presented by Kanoute *et al.* [81].

2.2.3. Fracture mechanics

Fracture mechanics studies the initiation and progression (growth) of cracks within the structure and understanding the different failure modes to ultimately estimate the residual strength of materials. Assuming homogeneous structures it is often feasible to characterise the fracture behaviour of heterogenous composites using linear elastic fracture mechanics (LEFM) [22]. Classical fracture mechanics is most often used to study interlaminar damage such as delamination and debonding. A. A. Griffith's work provided the fundamentals of fracture mechanics, explaining the failure of brittle materials in 1921 [82].

The basic principle states that crack advancement is controlled by the rate of strain energy released by the material. During fracture, when a new surface is created, the energy release rate (G) gives information about the energy available to cause a crack to grow [23]. It is defined in eq. (2.1) as:

$$G = \frac{\partial(W-U)}{\partial A} \quad [J/m^2] \qquad (2.1)$$

where W is the work of external forces, U is the internal strain energy of the structure and A is the area of the crack (length for two dimensional problems). If the available energy release rate in the system (G) is greater than or equal to the critical value (G_C): $G \geq G_C$ then crack propagation will take place. G_C is also called the fracture toughness.

The evolved stress field regardless of the loading conditions can be divided into three major fracture modes that explain the three ways fracture can occur as illustrated in Figure 2.3, reproduced from [22].

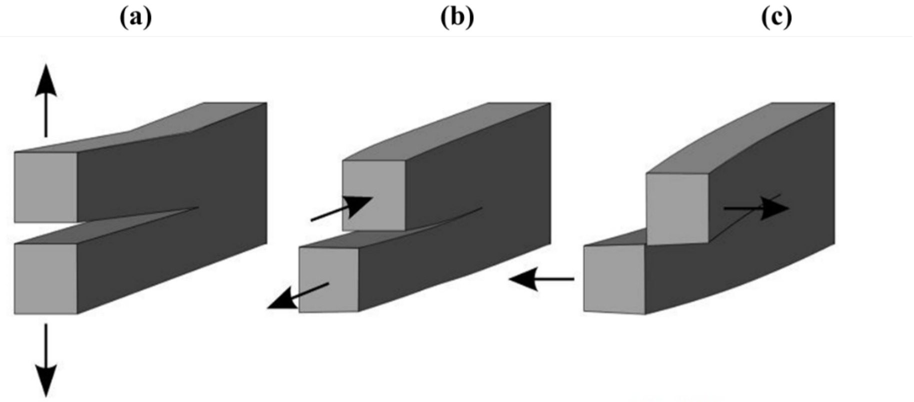

Figure 2.3. The three types of crack growth mechanisms: (a) Mode I – Opening, (b) Mode II – In-plane shear and (c) Mode III – Out-of-plane shear respectively [22]

The pure modes of fracture (Mode I., II. And III.), each have their values of G_c. The mixed mode critical strain energy release rate is dependent on many parameters, for instance loading rate, direction of crack growth and most importantly the ratio of the three crack opening modes mentioned above.

An extensive review on approaches looking at determining the proportion of different components of strain energy release rate (SERR) is conducted by Banks-Sills [83]. In another review Awerbuch and Madhukar [84] describe the most commonly used models and methods in fracture mechanics. Some of the drawbacks and applicability of LEFM methods for fibre reinforced composites are reviewed by Kanninen *et al.* [85]. Furthermore, some of the challenges and state of the art in computational fracture mechanics especially regarding delamination are presented by Krueger [86].

2.3. Biaxial in-plane testing methods for composite materials

Generally, biaxial testing methods may be categorised by the number of loading systems used: (i) single loading system or (ii) two or more independent loading systems [87], [88]. For single loading systems, the biaxial stress/strain ratio is dependent on the configuration of the loading fixture or geometry of the specimens.

These types of tests include but are not limited to anticlastic bending tests of rhomboidal/rectangular plates, bulge tests, cruciform specimens with spatial pantograph, butterfly shaped specimens in Arcan type apparatus, V-notched specimens in a biaxial Iosipescu fixture, equibiaxial loading of disc-shaped specimens and off-axis tension of UD composites [89], [90]. For two or more loading systems, the multi-axial stress/strain ratio is determined by the magnitude of the applied loads. These tests include cruciform specimens under in-plane biaxial loading, thin-wall tubes subjected to a combination of axial loading and torsion or internal/external pressure and round bars under bending-torsion to name but a few [87], [88]. Different studies put emphasis on different loadings [91] or testing methods [87]. For example, a review by Chen and Matthews [92] highlighted the issues in biaxial testing mainly on tubular and cruciform specimens as well as flat plate bending. This review was carried out on specific loading cases and it should be noted that there has been a considerable amount of research done since it was published. Thom [93] also compiled a review where several strength criteria are presented and compared numerically as well as different biaxial testing methods with their characteristic problems are discussed with an emphasis on thin-walled tubes. In a more recent study, Olsson [94] presented a survey on test methods to determine the strength of composite laminates with regard to both in-plane and out-of-plane loadings. Some of the more prevalent methods/specimen types such as tubular specimens (eg. thin walled tubes), cruciform specimens, off-axis tests and Arcan tests will be briefly presented hereinafter.

Tubular specimens are widely used and impose multi-axial loadings to the material structure. Their main applications include pressure vessels, bike frames, cylindrical and other flat structures that are subjected to complex loadings. The main advantage of such tubular tests lies in avoiding free-edge effects as well as allowing to obtain an arbitrary range of controlled, in-plane biaxial load ratios, hence being quite popular [94], [95]. On the other hand, it is complex to manufacture tubes and difficult to control the quality of the specimens [76]. Also, they have a curved surface and the stress induced on the specimens is not uniform over the thickness of the tube.

It is commonly assumed that plane stress assumptions are sufficient to predict and analyse the behaviour of cylindrical tubes under biaxial loadings. However, care has to be taken, as this assumption is only reasonable for thin-walled structures where the radial (out-of-plane) stress is negligible when compared to the average in-plane stress generated. Detailed considerations for the design of tubular specimens can be found in [88]. Tubular specimens and multi-axial tests have been extensively studied by Swanson *et al.* [96], [97] and others [98].

Cruciform specimens were originally developed for metallic materials. A historical review of biaxial tests using cruciforms is presented in [88]. Using this testing method, arbitrary in-plane biaxial loads can be applied to cruciform composite specimens. The manufacturing process is less complex than for tubular specimens, however at the same time, coupons can be much larger and often require additional machining eg. reducing the thickness in the gauge section and fabricating a corner fillet in order to avoid premature failure outside the gauge section [94]. The biaxial loading zone (gauge length) of cruciform specimens is often stronger than the uniaxial loading arms, hence it is difficult to obtain gauge section failures. For that reason, gauge sections with stress concentrations (reduced thickness, holes, notches and cracks) are often investigated to achieve failure in the desired biaxially loaded gauge section.

Cruciform specimens can be more representative of real-life structures that are usually flat or mildly curved, especially in the sense that in-plane biaxial loads can be applied without the presence of out-of-plane stresses (eg. radial stresses in tubular specimens) which can significantly affect the material behaviour [88], [94]. Various authors have been studying the biaxial loading of cruciform composite specimens. Welsh and Adams investigated the biaxial strength of IM6/3501-5 carbon epoxy and IM7-977-2 carbon epoxy materials using various tapered and non-tapered specimen types, with different lay-up configurations [99], [100]. They also reviewed previous work in the area as well as discussed cruciform specimen design considerations. In another study, Smits *et al.* [101] studied the design of composite cruciform specimens to investigate laminates under static and cyclic in-plane complex stress states.

In the following, biaxial Arcan tests are briefly reviewed. The original Arcan fixture was presented in [102]. Since then, modified versions of the experimental fixture [103] have been utilized when testing the shear response of materials coupled with transverse direction tension [104], [105] or compression [106]–[108]. By having multiple loading holes, arbitrary biaxial loadings can be induced on the investigated samples, however, the supporting fixture itself is generally complex. For instance, Laux *et al.* [109] used a modified Arcan fixture (MAF) with an additional anti-buckling rail which stabilises the rig against out-of-plane displacements during compression loadings. This allows for a testing window and loading in tension, compression, shear and their combinations. An illustration of the MAF fixture is shown in Figure 2.4, reproduced from [109].

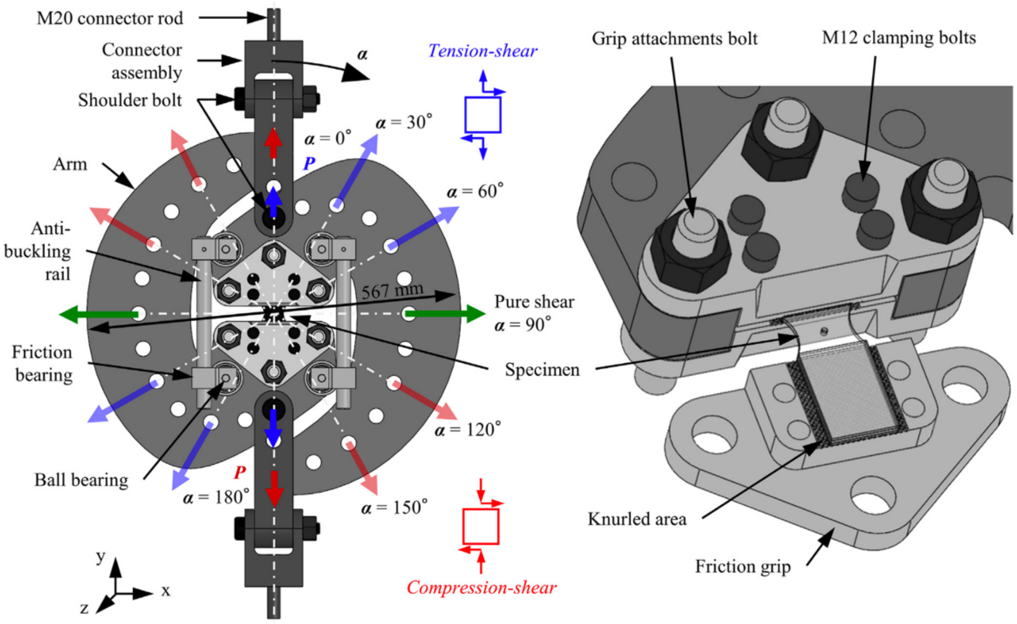

Figure 2.4. An illustration of the modified arcan fixture (MAF) used by Laux *et al.* and reproduced from [109]

2.4. Summary

In general, it can be said that the validity of the failure criteria found in the literature is dependent on their application eg. what type of damage prediction they are utilized for. It is very hard to determine if the acquired material properties such as strength is providing a sufficiently accurate input for the failure mode under investigation. Usually the measured strength values are influenced by stress concentrations arising from testing resulting in premature failures or notably lower measured strains. Furthermore, in experimental testing, multiple failure modes can occur at the same time or in rapid succession hence strength cannot be properly predicted because the structure might be already weakened by other damage mechanisms. In order to have better input for the theories available, ‘cleaner’ experimental data are required with properly isolated failure modes that can be correlated to the respective strength values.

Some of the problems and challenges with regard to the failure of composite materials were also identified in Chapter 1, Section 1.2 where the objectives of the PhD thesis were introduced. This thesis is centred around generating more reliable experimental data where the UD composite material is exposed to a multi-axial stress state in a controlled manner. By isolating different failure mechanisms from each other, their interaction as well as their individual effects on the fibre direction strain to failure/strength can be determined. Additionally, such investigations can extend the scope of data available for very thin-ply composites aiding the development and extension of existing failure criteria that can account for ply thickness and size effects. The literature survey presented in this chapter covered key areas of research. However, relevant literature is also presented in the individual chapters to support the load-case presented or study under investigation.

Chapter 3

Characterisation of spread tow, thin ply carbon/epoxy material

3.1. Introduction

Developing reduced fibre areal weight composite materials and utilizing thin-ply technology have been developing areas of research in the past 20 years especially due to the benefits these materials offer: greater versatility for optimisation, better fatigue properties, higher tensile and compressive strength as well as delaying the onset of micro-damage and delamination to name but a few [110]. In order to fully exploit their properties and to predict their behaviour using Classical Laminate Analysis (CLA) the four basic material constants of the lamina must be identified. Since composite materials are considered to be orthotropic (have three mutually perpendicular planes of symmetry) and specially orthotropic on a ply level (normal stresses are applied in the principal material directions), they require only four material elastic constants to describe their in-plane mechanical behaviour. The properties include the longitudinal (E_{11}) and transverse (E_{22}) Young's modulus, the in-plane shear modulus (G_{12}) and the major Poisson's ratio (ν_{12}). Accurately determining such properties is crucial to the design and optimization of both unidirectional and multi-directional laminates as well as for investigating other trade-offs by using different materials and cost and weight optimisation [111].

For the material chosen, - as an estimation - the rule of mixtures (ROM) [6] can be used to determine the above mentioned four constants using the fibre and matrix properties provided by the manufacturer. On the other hand, experimentally measuring the material properties can provide more accurate inputs for further analytical and experimental work especially since measurements are more representative of a given batch of material.

Since the full range of properties was not available from the manufacturer's data sheets and the research requires the determination of material properties as accurately as possible for the prediction of damage and failure analysis, an experimental characterisation campaign was carried out for the considered thin carbon fibre/epoxy composite prepreg.

3.2. Material choice

The thin ply carbon fibre reinforced polymer (CFRP) chosen for this research is a spread tow, high strength carbon/epoxy prepreg manufactured by SK Chemicals, South Korea under the commercial trade name 'Skyflex USN020' [112]. 'U', 'S', 'N' and '020' denote unidirectional (UD) prepreg type, high strength (HS) fibre type, no scrim and the fibre areal weight (FAW) in [g/m^2] respectively. The fibre constituting the prepreg is Tairyfil TC33 high strength, standard modulus carbon fibre, manufactured by Formosa Plastics. The resin system in the composite is a standard grade epoxy called K51, produced by SK Chemicals [112]. The data supplied by the manufacturer for the prepreg material and its constituents are summarised in Table 3.1.

Table 3.1. Material data supplied by the manufacturer for TC33/K51 carbon/epoxy prepreg

Fibre tensile modulus (E_f)	230	*GPa*
Fibre tensile strength (σ_f*)	3.45	*GPa*
Fibre failure strain (ε*)	1.5	*%*
Fibre density (ρ_f)	1.8	g/cm^3
Filament diameter (d_f)	7	μ
Fibre Areal Weight	20	g/m^2
Resin density (ρ_m)	1.2	g/cm^3
Resin weight fraction (m_m)	43	*%*

The nominal fibre weight content of the prepreg was not specified by the manufacturer, hence it was measured experimentally. The weight [g] of 8 different, 150 mm x 150 mm sized pieces of the uncured prepreg material was measured on a METLER TOLEDO XS105 type precision scale and converted into g/m^2. The result of the prepreg areal weight measurements yielded an average of 43 g/m^2 (C.o.V - 1.8%) for the TC33/K51 prepreg.

3.3. Fibre volume fraction and cured ply thickness

The fibre volume fraction (v_f) highly influences strength and stiffness properties [113] and is dependent on the resin content and the porosity (void content) of the composite material. In practice, these parameters can vary with the material batch, even within one composite laminate, hence the volume fraction has to be adjusted so the empirical measurements can be compared using a common value for the given set of materials [113]. To acquire the most accurate results for the utilized batch, the fibre volume fraction of the TC33/K51 roll was measured experimentally based on the ASTM-D3529M –standard [114] (Procedure B – Matrix burn off) which followed the procedure below:

- The mass of each uncured composite specimen was measured and recorded as M_i; then the samples were put into a ceramic crucible which was weighed and recorded as M_c. The requirement for the tested specimens were a minimum surface area of 0.0064 m^2 and mass of 1 g.
- The crucibles including the composite samples were put into a preheated high-temperature furnace and then kept at 500°C for 5 hours until the resin was burnt off. It has to be noted that burn time was kept at 5 hours in order not to degrade the fibres leading to false measurements.
- After cooling the crucibles to room temperature, the weight of the crucible and composite remains were measured and recorded as M_f.
- The fibre content can be calculated then: $\mathrm{FC} = \frac{(M_f - M_c)}{M_i} \cdot 100 \quad (3.1)$

The fibre mass fraction (FC) was measured to be an average of 49.1% (C.o.V – 4.3 %). From the FC, the fibre volume and fibre volume fraction were determined which yielded 39.1% (C.o.V - 5.16%) for the utilized batch of TC33/K51 prepreg based on an average of 6 tested samples. The fibre volume fraction is significantly lower than the usual values of standard thickness plies ($v_f \sim 60\%$).

The fibre volume fraction can also be estimated using the data supplied by the manufacturer, as seen below:

$$v_f = \frac{V_f}{V_f + V_m} = \frac{\frac{M_f}{\rho_f}}{\frac{M_f}{\rho_f} + \frac{M_m}{\rho_m}} = \frac{\frac{m_f M}{\rho_f}}{\frac{m_f M}{\rho_f} + (1 - m_f)\frac{M}{\rho_m}} = \frac{m_f}{m_f + (1 - m_f)\frac{\rho_f}{\rho_m}} \tag{3.2}$$

where m_f and m_m represent the fibre and matrix weight fraction, ρ_f and ρ_m the fibre and matrix densities, V_f and V_m the fibre and matrix volume and M_f and M_m the fibre and matrix weight respectively. M denotes the overall mass of the composite.

When substituting the data supplied by the manufacturer from Table 3.1 into equation 3.2, it yields an estimated fibre volume fraction of 47 %. The discrepancy between the measured (39.1%) and the calculated values using the manufacturers datasheet (47%) shows that the data provided by the manufacturer was not accurate enough.

3.4. Characterisation design

In order to determine the four basic material constants (E_{11}, E_{22}, G_{12}, and ν_{12}), tensile tests were carried out on 0°, 90° and ±45° laminates according to the appropriate ASTM standards: ASTM D3039/D3039M [115] and ASTM D3518/ D3518M [116] were utilised to design the tensile and shear specimen geometries and tests respectively, however there were some changes made to the originally proposed standards.

These conventional test standards generally assume standard thickness materials – t = 0.125 mm per ply –, hence they need to be adjusted appropriately to the use of thin-plies. Previously, Fuller *et al.* [117] carried out a characterisation campaign on a similar thin-ply material type from SK Chemicals using the same resin system but a different fibre. The sizing guidelines presented in their characterisation campaign proved representative of the material behaviour, hence was built upon for the TC33/K51 material as well. Table 3.2 summarises the nominal specimen geometries for the different characterisation tests. Furthermore, additional tensile tests were carried out with a novel hybrid configuration [20] to determine the failure strain of the material without it being affected by stress concentrations caused by gripping which are discussed in Chapter 4, section 4.4.1 and are not part of this chapter.

Table 3.2. Nominal specimen geometries for the characterisation tests of TC33/K51 thin-ply carbon/epoxy material

Property	Lay-up	Gauge length [mm]	Width [mm]	Thickness [mm]	End-tab length [mm]
Longitudinal tension	$[0]_{16}$	120	20	0.48	40
Transverse tension	$[90]_{16}$	120	20	0.48	40
Shear	$[\pm45_5]_s$	160	25	0.6	40

3.5. Specimen fabrication

All composite laminates were manufactured using a conventional hand lay-up process for prepreg composites followed by autoclave curing of the material. The roll of TC33/K51 prepreg material was taken out of the freezer where it was kept at -20 °C in order to preserve its integrity and prevent it from cross-linking. After defrosting for 12 hours, the material was cut into the desired sizes by a CNC-controlled ply cutting machine (GENESIS 2100) to proceed with hand lay-up.

Each layer was placed on top of the previous one using a wooden alignment board that was created to aid the fabrication process and to keep the ply edges perpendicular.

Care had to be taken especially when laying up angle-ply laminates to ensure the appropriate sequence was created (balanced and symmetrical laminate). Occasionally, a heat-gun was used to aid the lay-up process due to the lack of tackiness between the uncured prepreg layers. Then, vacuum consolidation was carried out after every second ply due to the low thickness of the prepreg material. Each debulking cycle lasted for 10 minutes to ensure that there were no air bubbles trapped in between the layers. In order to get the composite panels ready for autoclave curing, they were placed onto a flat aluminium tool plate and a standard vacuum bagging process was applied. Figure 3.1 illustrates a schematic construction of a composite laminate under a vacuum bag prepared for the autoclave curing.

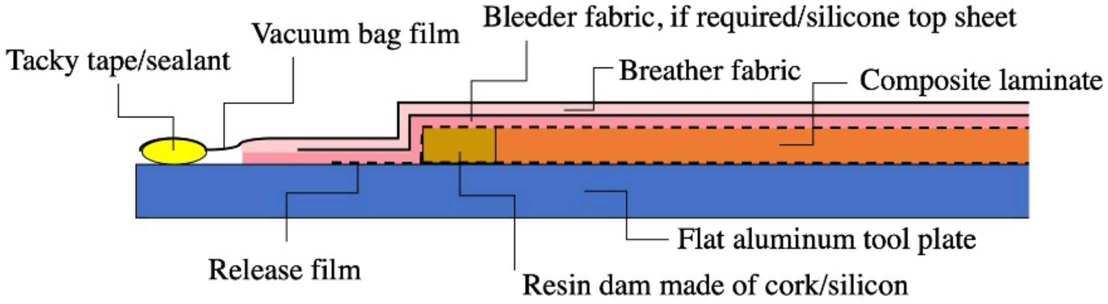

Figure 3.1. Structure of the vacuum bags prepared for curing prepreg laminates in the autoclave

Additionally, there were silicone sheets placed on top of the laminates to promote an even pressure distribution during consolidation and to provide a smooth top surface for the composites. Resin bleed-out had to be prevented with cork dam/silicone strips around the laminates to keep the designed fibre volume fraction of the prepreg. The recommended temperature and pressure cycle provided by the manufacturer can be seen in Figure 3.2. This cycle was slightly modified to a higher applied pressure to ensure better consolidation, and all laminates were cured for 30 mins at 80°C and 90 mins at

125 °C with 0.7 MPa (100 psi) pressure and a heat up and cool down rate of 2°C/min. For consolidation, a 24kW, two vacuum channelled autoclave (made by LBBC Technologies) was used.

After curing, the composite plates were cut into the desired geometry by a CNC controlled diamond wheel cutter. The end-tab region of the specimens was roughened (with a Grit P120 abrasive paper) for better adhesion between the end-tabs and the coupons themselves. Then, commercially available, untapered, 1.7 mm thick composites made of glass fibre fabric/epoxy were used as end-tab materials for all configurations. The end-tabs were roughened as well and bonded to the specimens using an Araldite 2014/1 type epoxy adhesive system. The samples with end tabs were then put into an atmospheric oven to cure the adhesive for 120 mins at 80 °C. Spring clamps were used to apply pressure on bonded surfaces.

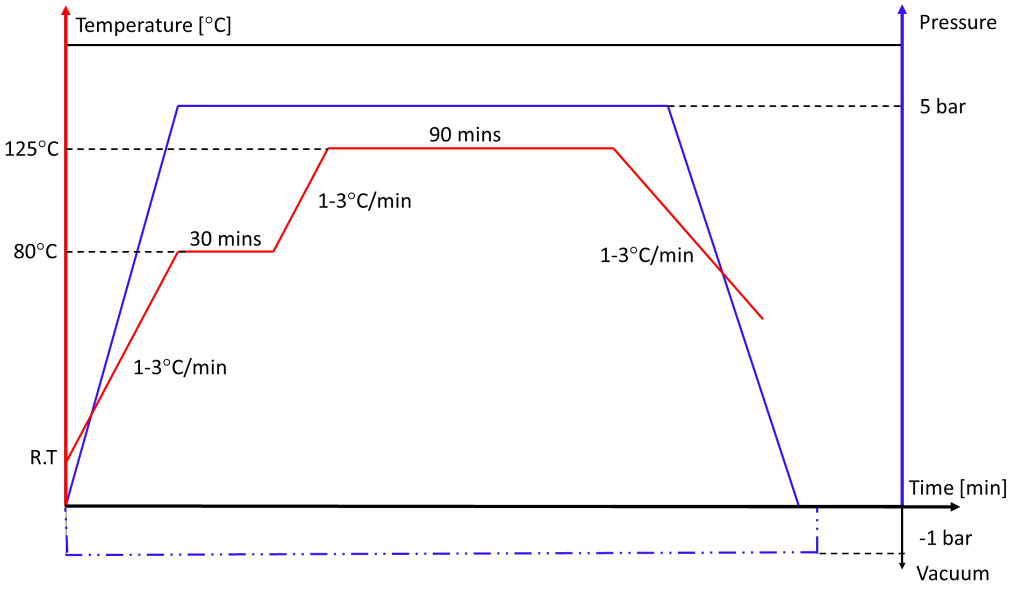

Figure 3.2. Pressure and temperature cycle recommended by the manufacturer for the Skyflex TC33/K51 carbon/epoxy prepreg material, adapted from [77]

After fabrication, all the specimen dimensions (free length/width/thickness) were measured by a standard digital caliper and micrometer at three different positions of each specimen. Once the manufacturing process was completed, all coupons were kept in a desiccator to ensure there was no additional moisture exposure to the specimens before testing.

3.6. Testing procedure and strain measurement

Mechanical testing of all specimens was executed under uniaxial tensile loading and displacement control on computer controlled, universal servo-hydraulic test machines with wedge type hydraulic grips.

- The tensile tests for the longitudinal properties were carried out on an Instron 8801 servohydraulic machine using Instron 2743-401 type hydraulic wedge grips and a 100 kN load cell. The grips had 50 mm wide Instron 2704-521 type serrated steel jaw faces. The uniaxial tensile loading was introduced at a crosshead speed of 2 mm/min, as per ASTM D3039 standard. The clamping pressure was kept as low as possible in order to reduce the unnecessary compressive stress, while still preventing slippage of the specimens at the grips.
- The tensile tests for the transverse properties were carried out on an Instron 8872 servohydraulic machine with 25 mm wide hydraulic wedge grips and a 1 kN load cell. This type of transverse tensile test is very sensitive: the smallest defects/voids within the laminate can initiate fracture and it is highly influenced by the loading rate of the specimens. Hence, the tensile load was introduced at a crosshead speed of 0.2 mm/min. The clamping pressure similarly to the longitudinal tests was kept low, just enough to avoid slippage of the specimens.
- Shear tests were carried out on a similar Instron 8872 machine equipped with a 25 kN load cell. The loading rate of the tests were kept at 2 mm/min as per the ASTM standard.

Both longitudinal and transverse strains were recorded during the testing campaign using an Imetrum video gauge system. This system uses pattern recognition and sub-pixel interpolation to measure strain, rotation, or displacement. Multiple targets are tracked in real time while the software outputs these measurements frame by frame [118]. The targets can be speckled patterns made by spray paint or as used in this study, markers as illustrated on Figure 3.3.

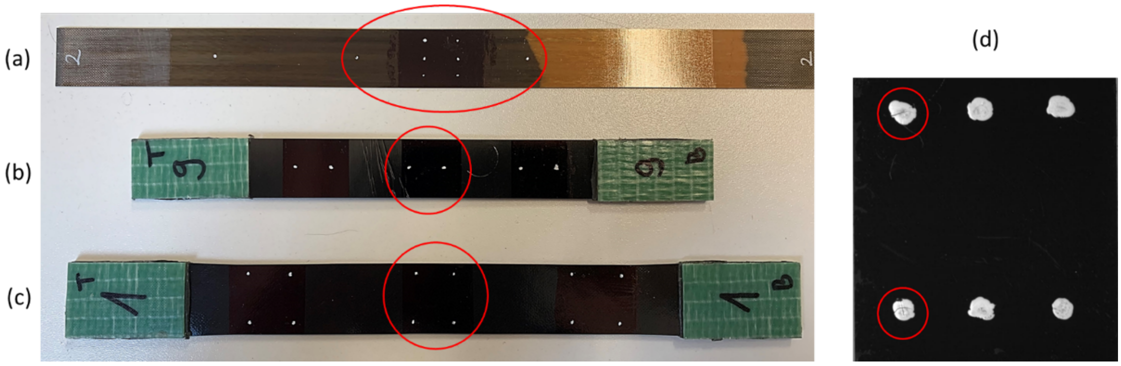

Figure 3.3. Paint markers applied to different specimens used for (a) the hybrid baseline longitudinal tensile tests (b) for transverse tension tests (c) for shear tests. Figure 3.3 (d) illustrates marker dots that exhibited micro-cracking during testing resulting in false strain measurements.

The position of the markers varied depending on the desired strains to be measured for a specific test. Generally, their sizes were kept as small and as far away from each other as possible for each measured strain value.

The marker dots were put on using a white paint marker. Before marking the specimens, all areas were painted with a permanent black marker to increase the contrast between the white marker dots and the surface of the specimens. This was especially important since the tracking algorithms of the video gauge system are based on contrasting backgrounds (black on white or white on black). In some cases, it was found that placing too thick of a paint layer resulted in micro-cracking of the marker dots - see Figure 3.3 (d)) - hence losing the tracking in the system. It has to be noted that the permanent black marker did not reduce adhesion between the marker dots and the specimens. The strain tracking was very accurate without much noise on the data signals for lower strain regimes, however for larger deformations tracking got noisy and the markers disintegrated. Furthermore, it has to be noted that for shorter spanned markers (especially for transverse direction strains at the width of the specimens), accurate tracking was very difficult to achieve.

Consequently, to provide the most accurate results eg. for the major Poisson's ratio measurements, the longitudinal tensile test specimens were equipped with additional T-rosette strain gauges to aid the measurements. The strain gauges utilised for tensile tests were 1-XY36-6/350 type T-rosettes with a nominal resistance of 350 Ohms and a measuring grid length of 6 mm manufactured by HBM.

3.7. Results and discussion

In this section, the empirical measurements will be presented for the different characterisation tests as specified in Table 3.2.

3.7.1. Longitudinal tension

Figure 3.4 – 3.6 illustrate the results of the unidirectional tensile tests for the $[0]_{16}$ laminate. Figure 3.4 and 3.5 show the longitudinal and transverse direction stress-strain responses of the material while Figure 3.6 represents the major in-plane Poisson's ratio as a function of the applied load. The strain was calculated from the displacements recorded by the video gauge and the Poisson's ratio was calculated according to equation (3.3):

$$\nu_{12} = -\frac{\varepsilon_y}{\varepsilon_x} \qquad (3.3)$$

,where ε_x and ε_y represents the longitudinal and transverse direction strains respectively.

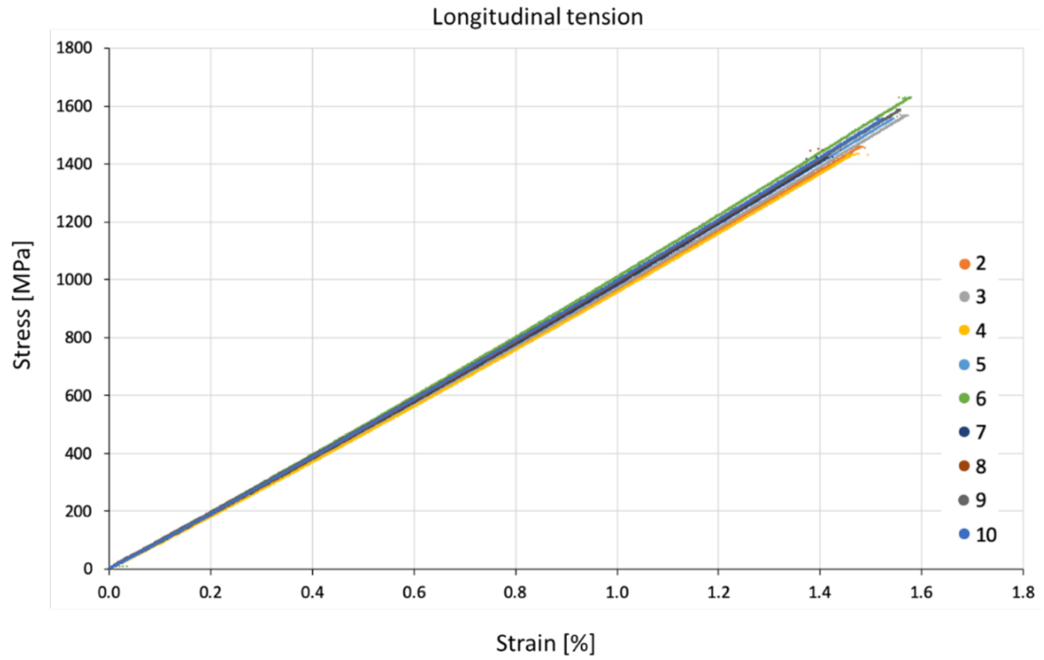

Figure 3.4. The longitudinal direction stress-strain response of the $[0]_{16}$ laminate under uniaxial tensile loading

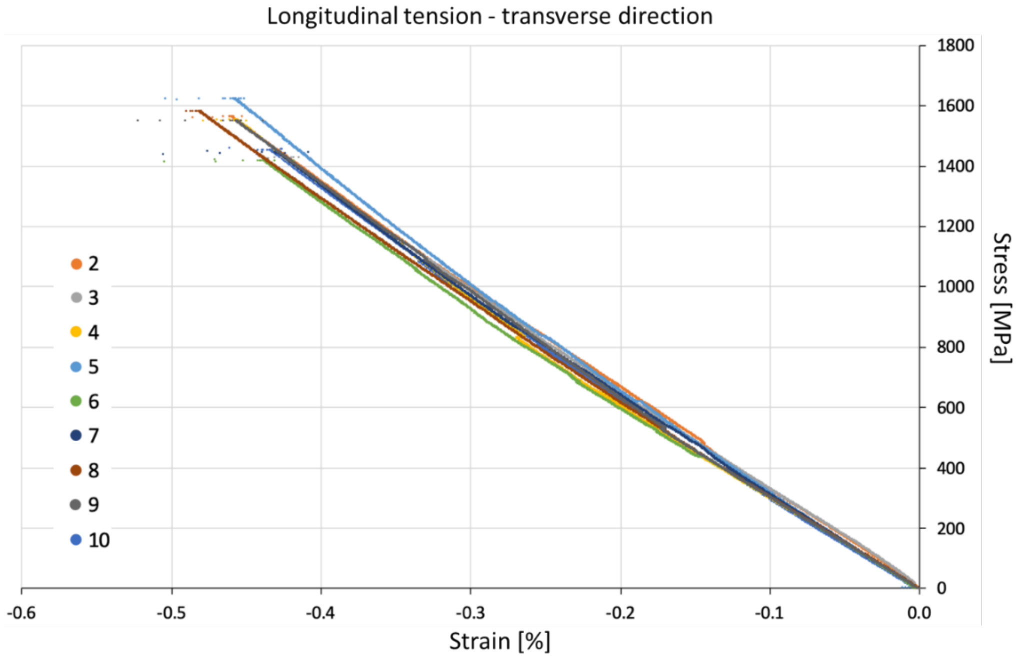

Figure 3.5. The transverse direction stress-strain response of the $[0]_{16}$ laminate under uniaxial tensile loading

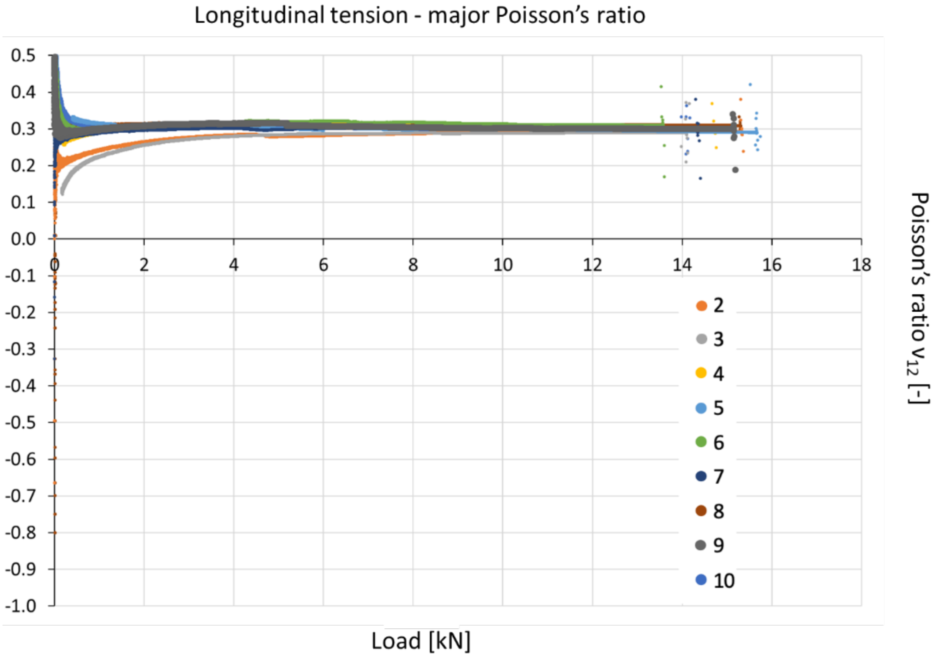

Figure 3.6. The major Poisson’s ratio as a function of the applied load during the uniaxial tensile loading of the specimens

As can be seen from Figure 3.4, the longitudinal direction stress-strain curves of the carbon/epoxy material exhibit some hardening (slightly increased stiffness) in tension. The chord modulus (E_{11}) was calculated in the strain range between 0.1 % to 0.3 % as per the ASTM standard. A summary table for this type of specimen is shown in Table 3.3. The nominal thickness of the coupons was 0.48 mm. Both the modulus (E_{11}) and the calculated macroscopic stress at failure (σ_x) are based on the measured geometrical values rather than the nominal ones. ε_x represents the failure strain of the material.

Table 3.3. Summary of measurements for the $[0]_{16}$ laminate under uniaxial tensile loading

	Thickness [mm]	Width [mm]	Free length [mm]	ν_{12} [-]	ε_x [%]	σ_x [MPa]	E_{11} [GPa]
Average	0.48	20.03	121.33	0.301	1.50	1507	95.3
C.o.V [%]	1.24	0.58	0.41	3.50	4.79	5.09	1.80

After determining the Young's modulus of the material (E_{11} = 95.3 GPa), an estimation can also be carried out with regard to the fibre volume fraction of the batch. The estimation is based on the simple rule of mixtures approach as shown below:

$$E_{11} = E_f v_f + E_m v_m \qquad (3.4)$$

,where E_f and E_m are the fibre and matrix moduli respectively.

Based on the measurements of Fuller *et al.* [117] for the K50 resin system, it is reasonable to assume an elastic modulus of 3 GPa for the matrix (E_m). A volume fraction of $v_f = 41\%$ was found based on equation 3.4 assuming zero void content for the material. However, for further calculations throughout this PhD, the measured 39.1 % volume fraction was used to aid the design and analysis of composite laminates.

3.7.2. Transverse tension

Figure 3.7 illustrates the stress-strain response of the $[90]_{16}$ laminate under uniaxial tensile loading. There were only 6 specimens considered to determine the transverse modulus (E_{22}) of the material. The characterisation tests were very sensitive to the defects within the laminate (both voids and manufacturing induced) leading to premature failure for some of the coupons. The material failure in these types of tests is matrix dominated, hence a higher variability was expected when determining the transverse strength σ_y. The extracted strength – 35 MPa – is lower than the typical transverse strength of a standard ply composite possibly due to the combination of low fibre volume fraction, and possible defects such as voids in the material. The transverse modulus of the material was extracted between 0.05 % - 0.3 % as recommended by the ASTM standard. A summary table including the results of the measurements is shown in Table 3.4

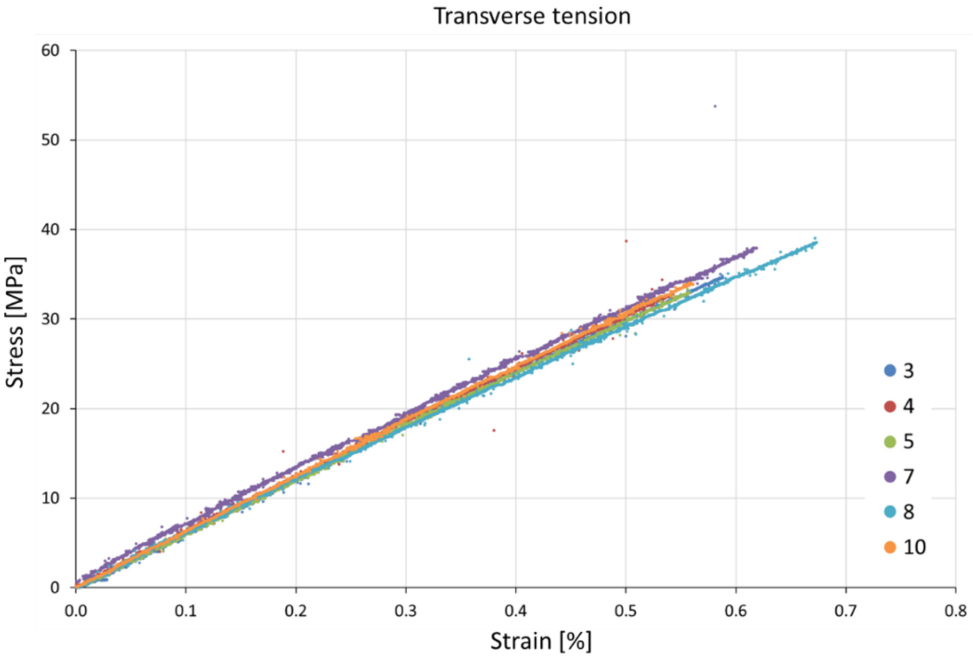

Figure 3.7. Stress-strain response of the $[90]_{16}$ coupons carried out in order to determine the transverse modulus E_{22}

Table 3.4. Summary of measurements for the $[90]_{16}$ laminate under uniaxial tensile loading

	Thickness [mm]	Width [mm]	Free length [mm]	ε_y [%]	σ_y [MPa]	E_{22} [GPa]
Average	0.49	19.97	120.25	0.59	35.2	6.1
C.o.V [%]	1.71	0.08	0.23	8.27	6.95	1.93

3.7.3. Shear

The tensile tests to determine the shear properties, especially the shear modulus (G_{12}) of the TC33/K51 prepreg was carried out in accordance with the ASTM D3518/D 3518M [116] standard. Figure 3.8 and Table 3.5 illustrates the shear stress – strain response of the [±45$_5$]$_s$ laminate and the summary of the measurements respectively. The shear chord modulus was extracted in the strain range 0.1% -1.1% as recommended by the ASTM standard. During testing, very large deformations were exhibited by the specimens resulting in the video gauge marker dots peeling off as well as the necking of the specimens.

The shear stresses (τ_{12}) and strains (γ_{12}) shown in Figure 3.8 were calculated from the measured longitudinal (ε_x) and transverse strains (ε_y) by the video gauge as recommended by the ASTM standard:

$$\tau_{12} = \frac{\sigma_x}{2} \qquad (3.5)$$

$$\gamma_{12} = \varepsilon_x - \varepsilon_y \qquad (3.6)$$

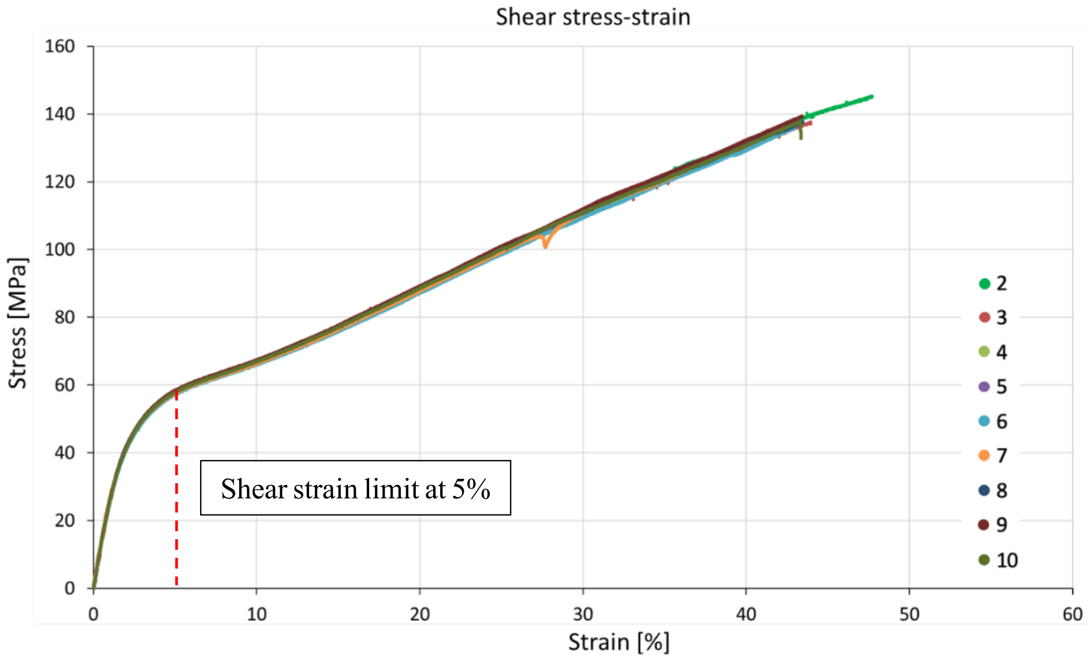

Figure 3.8. The shear stress – strain response of the [±45$_5$]$_s$ laminate under uniaxial tension

The measured macroscopic stresses σ_x were calculated using the measured thickness of the specimens. According to ASTM D3518, the shear strength is determined based on the shear stress at failure or at 5 % strain. In this case, due to the high elongation of the specimens, the shear strength (τ_{12}^*) was determined at the 5 % shear strain margin. The nominal thickness for the shear coupons was 0.60 mm.

Table 3.5. Summary of measurements for the $[\pm45_5]_s$ laminate under uniaxial tensile loading

	Thickness [mm]	Width [mm]	Free length [mm]	γ_{max} [%]	τ_{12}^* [MPa]	G_{12} [GPa]
Average	0.61	25.11	160.88	42.51	57.9	2.47
C.o.V [%]	0.64	0.35	0.29	7.88	0.63	1.63

3.8. Conclusions

A summary of the acquired material properties with their respective coefficients of variation (C.o.V [%]) is shown in Table 3.6 below. All parameters are for tension. The coefficients of thermal expansion (CTE) α_{11} and α_{22} are estimated values for the longitudinal and transverse direction expansion of the prepreg lamina.

α_{11} is based on the reported value of a similar grade T300/5208 carbon/epoxy [119] prepreg whilst α_{22} is an estimated value based on general data for the same grade epoxy from literature [120].

Table 3.6. Summary table of the properties acquired during the characterisation campaign of TC33/K51 thin-ply carbon epoxy material

$\boldsymbol{E_{11}}$	95.3 [GPa]	(1.80%)	ε_{11}^{*}	1.50 [%]	(4.79%)
$\boldsymbol{E_{22}}$	6.11 [GPa]	(1.93%)	ε_{22}^{*}	0.59 [%]	(8.27%)
$\boldsymbol{G_{12}}$	2.47 [GPa]	(1.63%)	γ_{12}^{*}	42.5 [%]	(7.88%)
σ_{11}^{*}	1507 [MPa]	(5.09%)	$\boldsymbol{\nu_{12}}$	0.30 [-]	(3.50%)
σ_{22}^{*}	35.2 [MPa]	(6.95%)	ν_{21}	0.019 [-]	n/a
τ_{12}^{*}	57.9 [MPa]	(0.63%)	CPT	0.030 [mm]	(1.24%)
α_{11}	$-1 \cdot 10^{-6}$ [1/K]	n/a	α_{22}	$4 \cdot 10^{-5}$ [1/K]	n/a

It has to be noted that this characterisation campaign was carried out primarily to determine the four basic material properties (E_{11}, E_{22}, G_{12}, and ν_{12}) in order to use as input for further design and analysis of composite laminates throughout this PhD thesis. The minor Poisson's ratio is a calculated value from the following formula:

$$\nu_{21} = \frac{E_{22}}{E_{11}} * \nu_{12} \qquad (3.7)$$

The strain to failure (ε_{11}^{*}) of the carbon/epoxy is also determined using hybrid tensile specimens as mentioned in section 3.4. This method gives an accurate representation of the material strength as it eliminates the effect of stress concentrations at the gripping areas.

Also, to determine the transverse compressive response of the material, coupons were fabricated to be tested in the rig designed by Haberle and Matthews [121], however due to difficulties (the weight of the rig led to the premature failure of the specimens when placing them in the fixture) the characterisation campaign could not be completed.

Chapter 4

Longitudinal tension – transverse compression: the effect of transverse compressive stresses on tensile failure

The chapter is based on first authored publication C.1. as referenced in the Publication section of the thesis.

Chapter 4 discusses a novel tensile specimen configuration that has been developed to induce a combined stress state of in-plane longitudinal tension and transverse compression in the utilized thin-ply, UD carbon/epoxy layers. Three different multi-directional laminates have been designed incorporating 0° UD carbon/epoxy plies embedded in angle-ply blocks of the same material. The scissoring deformation of the angle-ply blocks induces transverse compression in the central 0° layers when the composite is strained in the 0° fibre direction. The amount of transverse compressive stress was determined from the measured surface strains of the laminates. There were significant in-plane transverse compressive strains generated in the laminates that are much higher than those typically attained in multi-directional laminates, exceeding the 90° fibre direction compressive strain to failure. The results of this study suggest that in practice fibre direction tensile failure is unlikely to be significantly affected by transverse compressive stresses.

4.1. Introduction

With regard to multi-axial and combined loadings, it is even harder to validate predictions mainly due to the lack of accurate loading specific experimental data [18],

[19]. A review of multiaxial and biaxial loading tests for composite materials can be found in Chapter 2, section 2.3.

Even for UD laminates, accurately determining their basic mechanical properties such as failure strain or failure stress is still a scientific challenge [18]. The ultimate strength of UD carbon/epoxy laminates is often underestimated due to the experimental strength measurements being affected by stress concentrations at the end-tab regions of the coupons [20]. Usually, a significant knock-down in their measured strength can be observed, accompanied by premature failure of the specimens and notably lower strains measured than the expected ultimate failure strain of the fibre. Consequently, for more complex cases such as testing under biaxial loading conditions, the difficulty in acquiring acceptable data is magnified due to issues that include but are not limited to edge effects, gripping related issues, quality of the materials and the consistency of coupon fabrication and testing [18].

A debatable part of the failure envelope for carbon composites is the tension – compression quadrant especially when looking at the effect of transverse compressive stresses on the longitudinal (fibre) direction tensile strength. A two-dimensional, strain based maximum shear stress failure criterion was proposed by Hart-Smith [122] who truncated the failure envelope by a 45° cut off between longitudinal tensile strain and transverse compressive strain. A study carried out by Wisnom [123] suggested a controversy between the findings of Hart-Smith and some of the supporting experimental results available in literature for instance by Swanson *et al.* [96], [124].

A more recent study carried out by Catalanotti *et al.* [125] presents a novel three-dimensional failure criterion for UD polymer composites. The criterion considers both longitudinal and transverse failure mechanisms as well as taking the effect of ply thickness on the material strength into account.

It suggests no coupling between fibre tension failure and matrix compression failure in a biaxial stress state as illustrated on Figure 4.1 reproduced from [125].

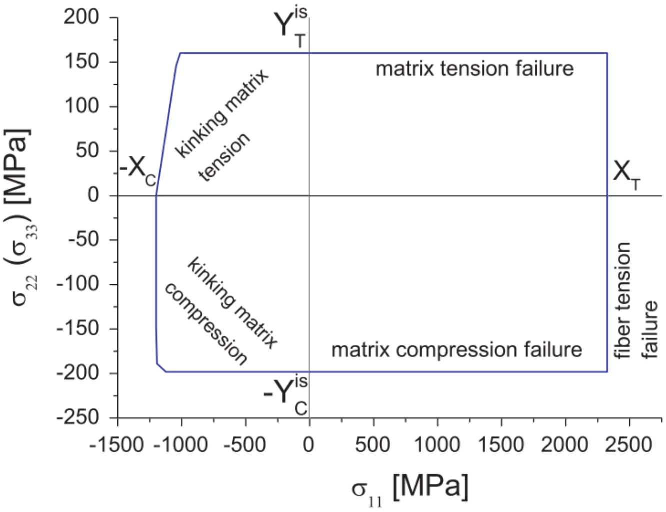

Figure 4.1. $\sigma_{11} - \sigma_{22}$ 2D failure envelope for IM7/8552 carbon/epoxy material reproduced from [125]

To further investigate the problem, this study aims to explore experimentally the effect of transverse compressive stresses on the fibre failure strain of UD thin-ply carbon/epoxy composites. A novel laminate design based on thin-ply laminates of unidirectional (UD) and angle-plies is presented. The bi-axial stress state in the 0° plies is indirectly applied in a tensile test set-up where the contraction of the angle-plies induces compression in the central UD layers when the composite is strained in the longitudinal direction. The test method proposed here offers a reliable solution for acquiring accurate experimental data on this particular biaxial loading scenario due to its repeatability and ease of use.

4.2. Design

4.2.1. Materials

The materials considered in this study were a TC33 carbon fibre by Formosa Plastics as discussed in Chapter 3 and a S-Glass glass fibre supplied by Hexcel. Both epoxy resin systems incorporated were 125 °C cure polymers. The matrix for the glass fibre was a 913-epoxy resin system supplied by Hexcel and a K511 epoxy resin system by Skyflex for the carbon respectively. Basic properties of the applied fibre and prepreg systems are summarised in Table 4.1 and Table 4.2 respectively.

Table 4.1. Fibre properties of the applied unidirectional prepregs based on manufacturers data

Fibre type	Elastic modulus [GPa]	Density [g/cm^3]	Strain to failure [%]	Tensile strength [GPa]
Tairyfil TC33 carbon	230	1.8	1.5	3.45
FliteStrand S ZT S-Glass [20]	88	2.45	5.5	4.8 – 5.1

Table 4.2. Cured ply properties of the applied unidirectional prepregs

Prepreg type	Areal density [g/m^2]	Cured ply thickness [µm]	Fibre volume fraction [%]	Initial elastic modulus [GPa]	Tensile strain to failure [%]	CTE α_L [1/K]	CTE α_T [1/K]
TC33/K51 carbon/epoxy	21[a]	30[a]	39[a]	95.3[a]	1.61[a]	$-1 \cdot 10^{-6}$[b]	$4 \cdot 10^{-5}$[c]
S-Glass/913 glass/epoxy [20]	190	155	51	45.7	3.98	$2 \cdot 10^{-6}$[b]	$3 \cdot 10^{-5}$[c]

[a]Based on measurements as discussed in Chapter 3
[b]Based on reported values for T300/5208 in [119] for the carbon and for the glass [20]
[c]Based on estimated values in general literature for same grade epoxy

4.2.2. Test design

The main objective of this study is to investigate the interaction between longitudinal tension and transverse compression in thin-ply carbon epoxy laminates through a tensile test based method. To be able to determine this interaction in the most accurate way possible, it is important to (i) minimise other stress components (*e.g.* shear) present in the UD laminate and (ii) to account for a challenging issue of tensile testing: the arising stress concentrations near the grips [20].

To address the exclusion of other stress components, the multi-axial stress state is indirectly applied to the UD layers and the laminate as a whole is designed to be balanced and symmetric. This way the in-plane shear coupling terms (A_{16}, A_{26}) and the extension-bending coupling (B matrix) are zero in the ABD matrices of the laminates. In this configuration, the central thin-ply UD carbon/epoxy laminate is embedded in thin-ply, angle-ply blocks of the same material where the scissoring deformation of the angle plies induces the transverse compressive loading on the central UD layers. A schematic of a typical specimen configuration is illustrated in Figure 4.2.

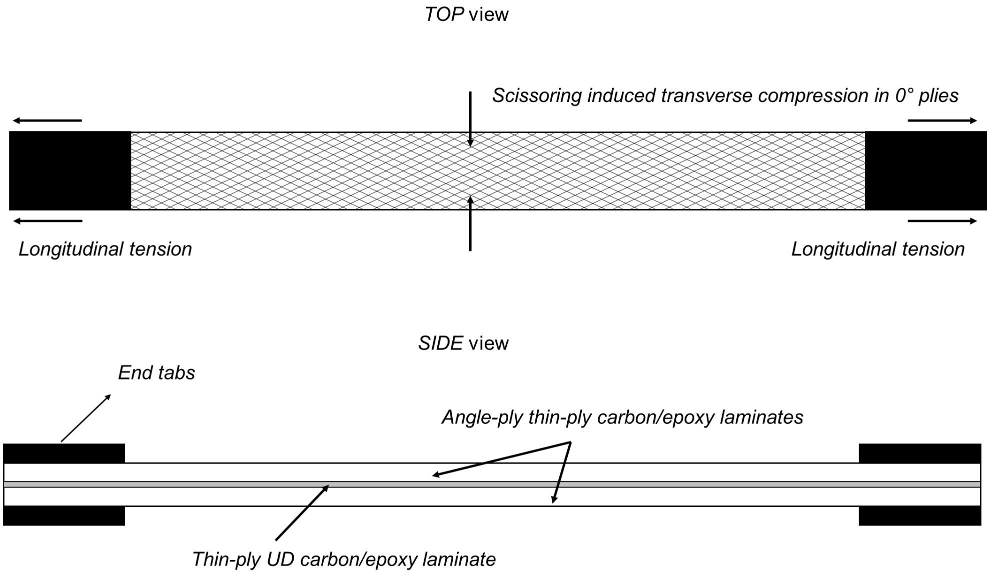

Figure 4.2. Top and side view schematic of the thin-ply UD laminate embedded in thin-ply, angle-ply blocks

The issue of stress concentrations during tensile testing is mitigated by using a novel method developed by Czél *et al.* [20]. They have proposed an interlayer hybrid specimen type consisting of UD glass/carbon hybrid composites for eliminating the end-tab stress concentrations during tensile testing.

Their specimens were deliberately designed for delamination after tensile failure of the central carbon layer. This induces a large load drop during testing which enables simple detection of the tensile failure strain of the carbon layer. The measured values were significantly higher than in conventional non-hybrid baseline carbon/epoxy specimens as the stress concentrations at the grips were eliminated. The coupons were also purpose designed to exclude any hybrid effects that might arise by setting a minimum thickness for the carbon layers. The glass layers in this case also protected the carbon plies from the rough grip faces.

Figure 4.3 (a) reproduced from [20] illustrates the x-direction strain distribution predicted by Finite Element Analysis (FEA) in the glass and carbon layers of a similar UD TR30/epoxy – S-Glass/epoxy specimen. The strain in the carbon layers varies smoothly between zero at the end tab area to the maximum applied strain in the gauge area as shown in Figure 4.3 (b). The stress is kept uniform in the carbon layers as the glass layers shield the carbon from the stress concentrations. This FEA study carried out by Czél *et al.* [20] underpins the advantage of suppressing the stress concentrations and being able to achieve consistent, gauge section failure in the carbon layers.

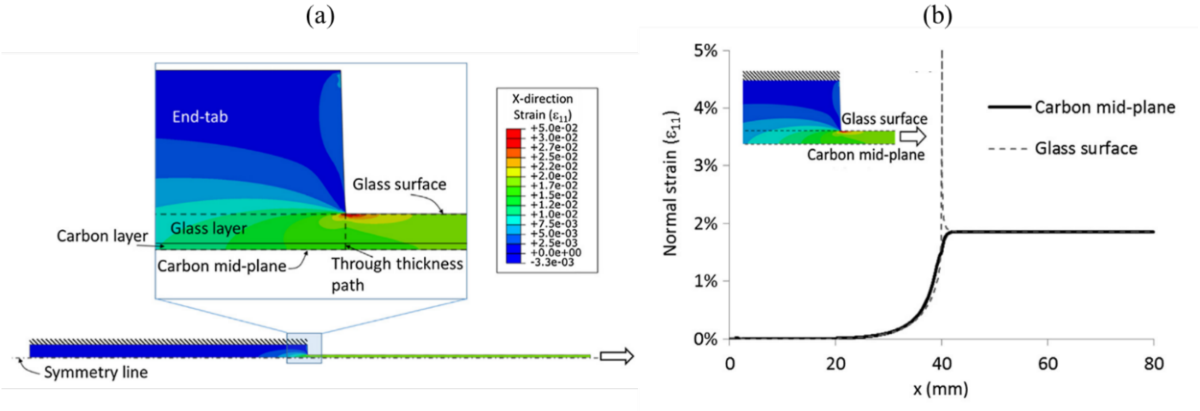

Figure 4.3. (a) loading direction strain distribution predicted by FEA over a tabbed glass/carbon hybrid specimen, reproduced from [20] (b) normal strain along the glass surface and carbon mid-plane, reproduced from [20].

With regard to the current study, the outer angle-plies in Figure 4.2 replace the UD glass layers to suppress tab stress concentrations. However, for shallower angles (close to 0°) embedding the central UD block, their behaviour is stiffer hence they do not provide sufficient ‘protection’ against stress concentrations at the grips. Consequently, the above-mentioned design incorporates additional layers of glass/epoxy in a similar manner to that described in [20].

Another objective is to make sure that the designed composite laminates will fail in the desired manner. In order to do that, it has to be ensured that damage mechanisms such as free-edge delamination and matrix (transverse) cracking – predominant failure mechanisms for angle ply laminates - do not precede nor influence the desired overall longitudinal fibre failure mode in the central UD plies.

Thin-ply materials are shown to be able to delay and suppress the above mentioned damage mechanisms (transverse micro-cracking [126] and free-edge delamination [127], [128]) in different loadings - static, fatigue and impact, as reviewed by Cugnoni *et al.* [129]. Exhaustive reviews of thin-ply polymer composites including their manufacture, microstructure, mechanical performance, and the implications for structural design and application prospects are presented by Galos [130] and Arteiro *et al.* [131].

It is reported that the advantages of using thin-plies - achieving a higher onset of damage such as microcracking or delamination in the composites - comes with a change in the failure mode of the laminates: shifting from a more complex, multi-mode failure with significant delamination to a quasi-brittle failure governed by fibre fracture in the 0° plies. These materials represent a new generation of advanced composites that provide a promising approach to exploit the true potential for carbon fibre composite structures especially by delaying the onset of damage up until a fibre dominated failure is achieved. Hence this study incorporates such materials making it possible to determine the real effect of transverse compression on the longitudinal fibre failure strain of thin-ply carbon/epoxy composites.

The configurations were designed in order to induce various levels of transverse compression in the central UD layers: by varying the angle of the embedding plies different amounts of transverse stress are generated while the composite specimens are strained in the longitudinal direction of the fibres. The key influencing parameters for the amount of transverse compression generated are the angle and the relative thickness of the outer angle-ply blocks. The transverse compression arises from the Poisson's ratio mismatch between the angle-ply blocks and the UD laminate.

By maximizing this mismatch and choosing an optimum angle, the transverse compression can also be maximized in the central UD layers. Furthermore, increasing the number of angle-ply pairs in the blocks increases the magnitude of the transverse stresses put on the central UD layers. The optimization of the stacking sequence was carried out in MATLAB software using Classical Laminate Theory (CLT) assuming a plane stress state for the composite laminates [132]. An illustration of varying transverse to longitudinal stress ratios arising in the central 0° layers as a function of the angle of the angle-ply blocks is shown in Figure 4.4. The chosen angles (see section 4.2.3) are marked with dashed lines on the graph as well. The applied strain for the generated curves was 1.62 % (measured failure strain of the carbon) and the analysis initially was carried out using estimated linear material properties.

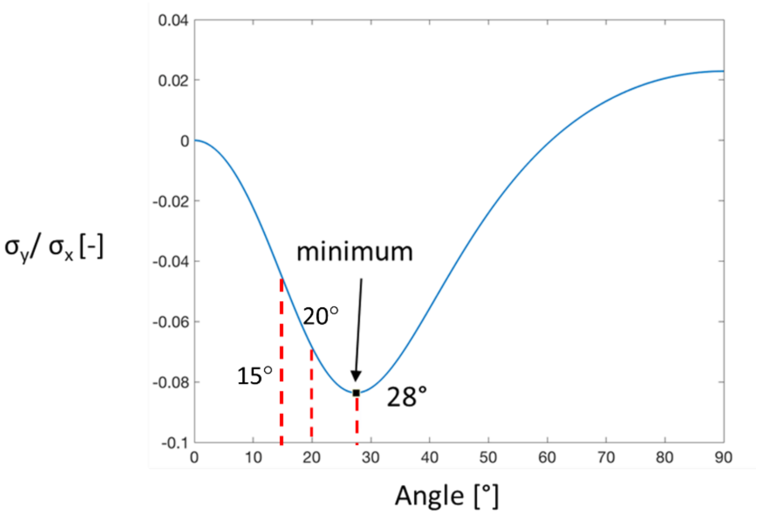

Figure 4.4. Transverse compressive stress to longitudinal stress ratios as a function of the angle of the embedding angle-ply blocks: the chosen angles are marked with red dashed lines on the curve.

Besides, the absolute thickness of the central UD layers plays an important role in ensuring that the hybrid effect is avoided. The hybrid effect in this case is an apparent failure strain enhancement: in a thin-ply interlaminar hybrid configuration which consists of eg. standard thickness glass and thin carbon composite layers, the failure strain of the carbon layers would be higher than the failure strain of the carbon in a non-hybrid configuration due to constraint from the glass layers on forming a critical cluster of broken carbon fibres.

This hybrid effect can result in an increased failure strain for very thin plies and is different from the expected strain enhancement due to the size effect. The magnitude of the size effect is relatively small and it is in addition to the failure strain enhancement due to the hybrid effect as demonstrated previously by Wisnom *et al.* [133].

An illustration of the carbon layer failure strain plotted against the carbon layer thickness for thin-ply materials is shown in Figure 4.5, adapted from [133].

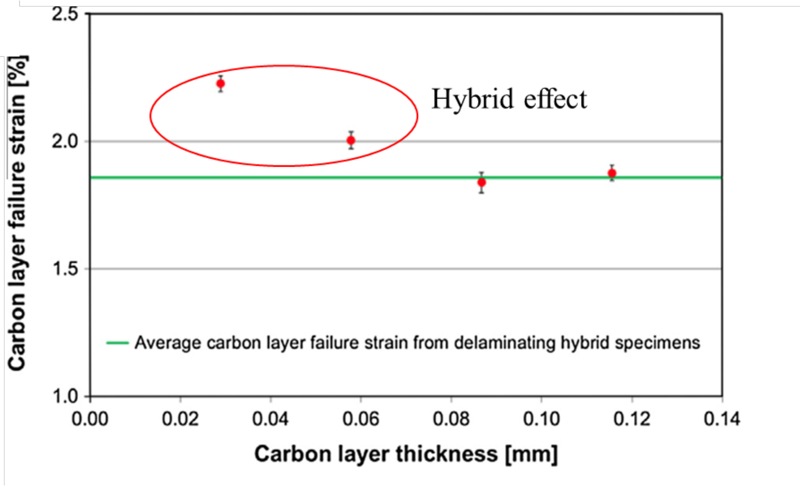

Figure 4.5. Arising hybrid effect (increased carbon layer strain to failure) when the carbon layer thickness is reduced, adapted from [133]

Based on these findings - to avoid any hybrid effects - a central UD layer thickness of 0.12 mm was chosen that is an equivalent to four plies of the utilized high-strength carbon/epoxy material.

4.2.3. Specimen configuration and geometry

Overall, four different configurations were designed which included the baseline specimens that helped to determine the accurate failure strain of the utilised carbon fibre/epoxy material. The baseline configuration as well as the 15° angled specimens were used the hybrid method developed by Czél *et al.* [20], where additional glass layers were used to ensure stress concentrations at the grips were eliminated. In this manner, consistent gauge section failures were expected.

The 15° angle-ply specimens did not incorporate end-tabs as the glass and angle-ply layers together provided sufficient shielding against gripping effects. For the specimens with 20°and 28° angle-ply blocks, the additional glass layers were omitted and carbon only specimens were fabricated with end-tabs as illustrated in Figure 4.2.

A summary of all the configurations is shown in Table 4.3, where SG denotes the S-Glass layers in the laminates.

Table 4.3. Specimen configurations

Configuration	No. of specimens tested [-]	Measured thickness [mm]
$[\mathrm{SG}_2/0_2]_s$-UD hybrid baseline	8	0.768
$[\mathrm{SG}_2/\pm15_6/0_2]_s$	7	1.494
$[\pm20_6/0_2]_s$	7	0.798
$[\pm28_6/0_2]_s$	6	0.806

All carbon coupons tested in the experimental campaign were parallel edge tensile specimens as illustrated in Figure 4.2 with the nominal dimensions of 270/190/20/0.84 mm overall length/gauge length/width/thickness respectively.

4.3. Experimental procedure

4.3.1. Specimen fabrication

All laminates were manufactured by a prepreg lay-up process as described in Chapter 3. After hand-lay-up of the specific plies, a vacuum bagging method was utilised on a flat aluminium tool plate. There were additional silicone sheets placed on top of the laminates in order to ensure a smooth top surface and an even pressure distribution in the autoclave.

The composite plates then were cured at the recommended temperature and pressure cycle provided by the manufacturer. Since both resin systems in the hybrid configurations were similar, only the heat-up, cool-down rate and any dwells occurring were adjusted by using the longest curing time required to obtain the desired mechanical performance. The curing cycle used for the hybrid configuration was 60 mins at 80°C and 100 mins at 125°C with 0.7 MPa applied pressure and a heating rate of 2°C/min.

The cycle used for carbon only laminates was 30 mins at 80°C and 90 mins at 125°C with a similar pressure cycle and heating rate.

After curing, the composite plates were cut into the desired geometry by a Computer Numerical Control (CNC) diamond wheel cutter. Un-tapered, 1.7 mm thick glass fibre fabric/epoxy was used as the end-tab material for two of the configurations. The end-tabs were bonded to the specimens using an Araldite 2014/1 epoxy adhesive system. The samples with end tabs were then put into an atmospheric oven to cure the adhesive for 120 mins at 80°C.

4.3.2. Testing method

Mechanical testing of the specimens was carried out similarly to the tensile tests in Chapter 3 on a universal, servo hydraulic Instron 8801 machine with a 100 kN load cell. The grips were Instron 2743-401 type hydraulic wedge grips with 50 mm wide Instron 2704-521 type serrated steel jaw faces. The uniaxial loading was introduced under displacement control at a crosshead speed of 2 mm/min as per ASTM D3039 standard. Clamping pressure was kept low enough to minimise end tab failures yet avoiding any slippage at the grips.

Longitudinal and transverse strains were measured using an Imetrum video gauge system, with the test machine outputting the corresponding force signals. The high-definition extensometer videos recorded during the tests were kept for further post-mortem analysis.

4.4. Results and analysis

4.4.1. Baseline configuration

When hybrid baseline specimens were loaded, the fracture of the carbon layer resulted in delamination from the embedding glass layers followed by the progression of delamination along the gauge length of the specimens.

Since the objective was to extract the failure strain of the UD material, the coupons were not loaded extensively beyond the first significant load drop that corresponds to the 0° carbon layer failure (point 1 on Figure 4.6). However, if loaded further after the first load drop (point 2 on Figure 4.6), residual load bearing behaviour due to the high elongation glass layers could be observed. A typical response of such hybrid specimens is presented in Figure 4.6 (a) reproduced from [20] and (b) acquired from the measured load-time curves.

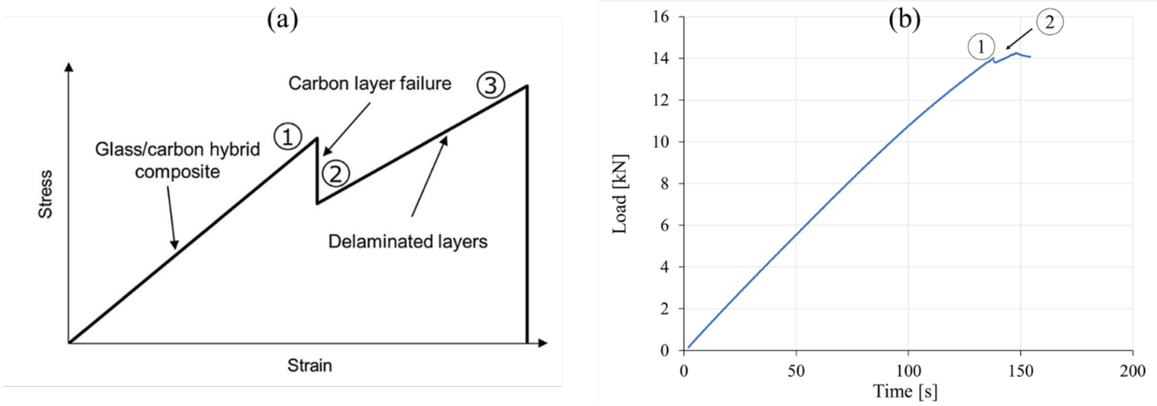

Figure 4.6. Stress-strain response of UD glass/carbon hybrid specimens (a) reproduced from [20] (b) acquired during testing

Figure 4.7 (a) shows the stress-strain curves of the tested hybrid glass/carbon baseline configuration up until the first load drop. The fracture of the carbon layer in the centre of the light (orange) coloured delaminated area and the subsequent delamination – shown as orange colour on the coupons - can be seen in Figure 4.7 (b).

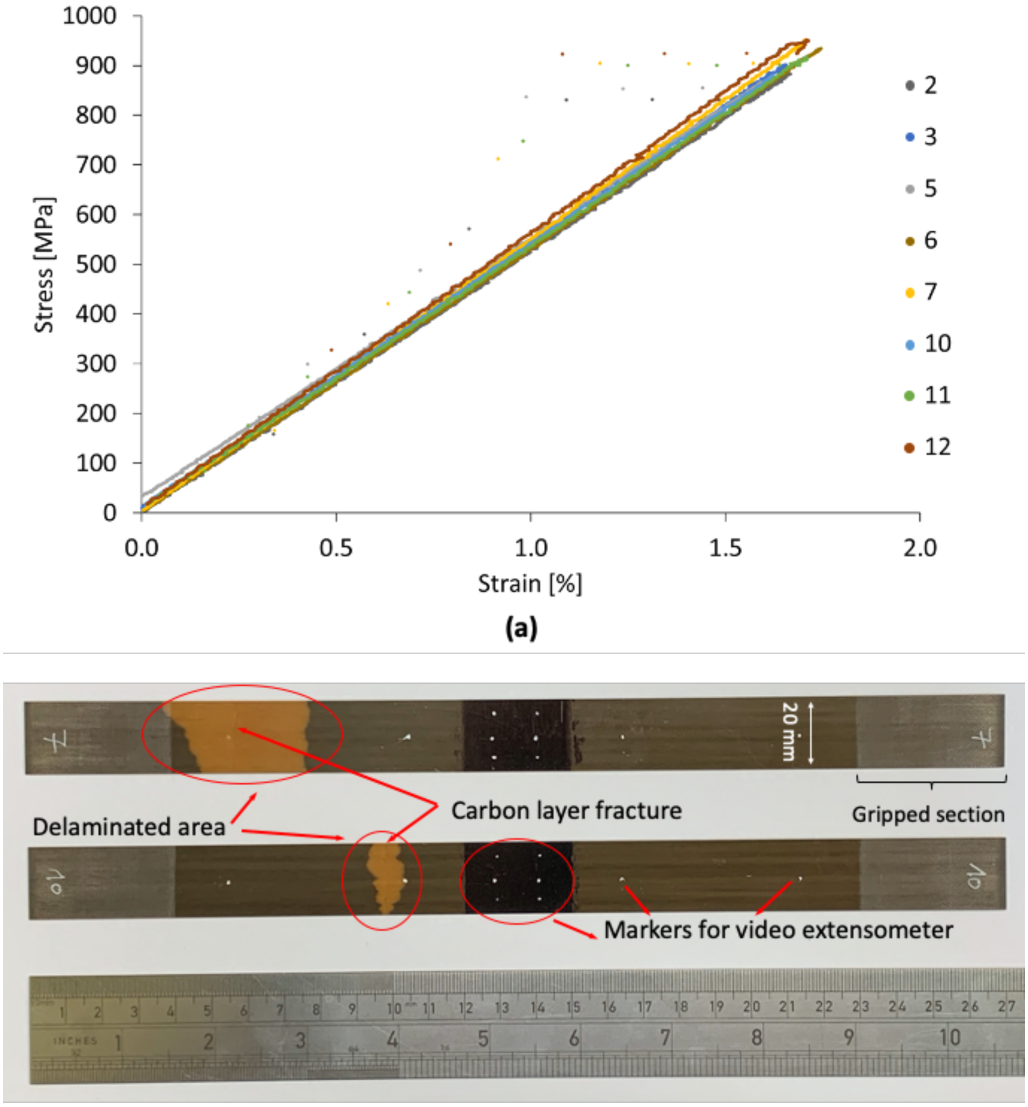

(a)

(b)

Figure 4.7. (a) Mechanical test results of the hybrid glass/carbon baseline configuration with (b) illustration of the behaviour of typical tested coupons: the carbon layer failure followed by sudden delamination from the embedding glass layers. The specimens did not incorporate end-tabs when tested and showed consistent gauge section failures.

It has to be noted that the results were affected by residual thermal strains that originate from the mismatch in the CTE of the different fibres. Residual thermal strains were calculated for force-equilibrium between the carbon/epoxy and glass/epoxy layers assuming constant strain at different places through the thickness and a 100 °C temperature drop from cure temperature to room temperature.

The CTE values for the different prepregs can be found in Table 4.2. For the longitudinal direction, the property of a similar grade carbon fibre [119], and the same type glass fibre [20] and for the transverse direction, general estimates from literature of the same grade epoxy were utilised.

The results of the baseline tests including the correction with the calculated residual thermal strains are illustrated in Table 4.4. This table also includes the test results of a non-hybrid baseline for comparative purposes: 16 layers of the same TC33/K51 carbon/epoxy material. The moderate increase (10%) in the failure strain of the hybrid specimens can be attributed to the elimination of stress concentrations and the associated premature failure scenarios which were more representative of the tensile tests carried out with the non-hybrid configuration. Furthermore, a decrease in the variability of the strain to failure can be seen for the hybrid configuration that underpins that conventional tensile testing methods are less reliable than the hybrid one presented in [20].

Table 4.4. Baseline tensile test results for the TC33/K51 material in a non-hybrid and hybrid all UD configuration

Configuration	No. of specimens tested [-]	Measured carbon layer failure strain [%] (C.o.V.[%])	Corrected carbon layer failure strain – incl. thermal strains [%]
$[0_{16}]$- non-hybrid UD baseline	9	1.50 (4.8%)	-
$[SG_2/0_2]_s$ - hybrid UD baseline	8	1.65 (3.0%)	1.62

4.4.2. Angle-ply/UD configurations

Figure 4.8 (a) – (f) illustrates the typical longitudinal and transverse stress-strain responses of the different angle-ply/UD laminates. It can be seen in Figure 4.8 (a) – (b) that for the shallower angle $[SG_2/\pm15_6/0_2]_s$ configuration, both the longitudinal and transverse responses are linear up to failure.

However, in the case of the larger angle angle-ply/UD configurations - $[\pm20_6/0_2]_s$ and $[\pm28_6/0_2]_s$ respectively – a gradual change in the stiffness of the laminates can be observed.

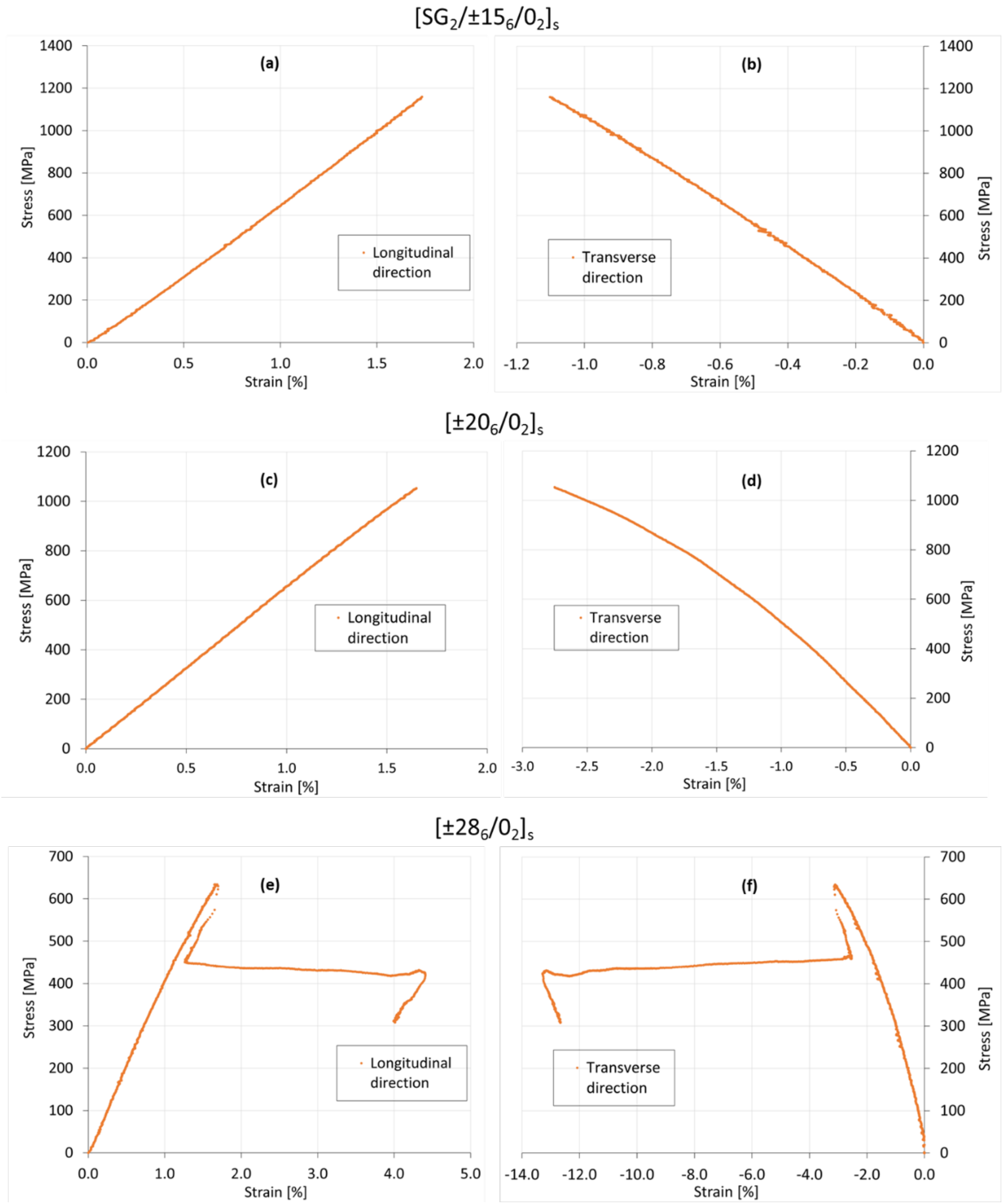

Figure 4.8. Typical longitudinal and transverse stress – strain responses of the different angle-ply/UD configurations: (a) – (b) - $[SG_2/\pm15_6/0_2]_s$, (c) – (d) - $[\pm20_6/0_2]_s$, and (e) – (f) - $[\pm28_6/0_2]_s$ respectively.

Both responses become non-linear in the transverse direction. This non-linearity is mainly associated with the angle-ply blocks surrounding the unidirectional material: there is no in-plane shear arising at the laminate level, however there are very strong presence of in-plane shear at the lamina level in the angle-ply blocks. Besides, the indirectly applied high transverse compressive stress also plays a role in the non-linear character of the transverse stress-strain curves.

In the experimental campaign, primarily surface strains are considered because they can be directly acquired by the video extensometer. Since transverse stresses cannot be measured, they have to be calculated from the measured strains. The fibres in the central 0° UD block experience transverse strain that is not only due to the effect of the surrounding angle-plies but also inherently from the UD material (Poisson's ratio). In other words, if the central UD block did not experience any compression from the neighbouring ply blocks, it would still have transverse strain in the material. Consequently, to determine the amount of transverse compressive stresses, the measured strains are corrected and converted into stresses using linear assumptions.

In the following sections the methodology for the corrections, determining the actual mechanical transverse stress put on the central 0° UD laminate and the estimation of the residual thermal stresses will be presented.

4.4.2.1. Determination of mechanical transverse stresses

Under pure uniaxial loading, there is no laminate level transverse stress arising. However, in the presented configurations, there is transverse stress arising in the 0° plies due to the Poisson's contraction of the angle-ply blocks. These stresses cannot be measured directly hence they need to be determined from the measured surface strains and material properties.

Both longitudinal and transverse strains are directly measured on the surface of the specimens. Assuming that they are constant through the thickness of the laminate, they can be used as the strains of the central 0° UD layers.

Hence, an equality can be written in the form of the measured strains of the whole laminate ($\varepsilon_{meas.}$) and strains of the central 0° block (ε^{0}):

$$[\varepsilon_{meas..}] = [\varepsilon^0];$$

$$[\sigma^0] = [Q^{0^*}][\varepsilon^0] \ ; \ [\sigma_{appl.}] = [Q^*_{lam.}][\varepsilon_{meas..}];$$

$$\rightarrow \ [\varepsilon_{meas.}] = [S^{0^*}][\sigma^0] , \qquad (4.1)$$

where $Q^{0^*}$and $Q^*_{lam.}$ represent the reduced stiffness matrix of the UD carbon block and the laminate respectively, S^{0^*} represents the reduced compliance matrix of the UD carbon block and σ^0 and $\sigma_{appl.}$ represent the stresses in the UD carbon block and the stresses applied to the laminate respectively. Reduced refers to the fact that the in-plane shear-coupling terms are zero.

Inverting equation (4.1) yields as follows:

$$[\sigma^0] = [Q^{0^*}][\varepsilon_{meas.}]$$

$$\begin{bmatrix} \sigma^0_{11} \\ \sigma^0_{22} \end{bmatrix} = \begin{bmatrix} \frac{E_{11}}{1-\nu_{12}\nu_{21}} & \frac{\nu_{12}E_{22}}{1-\nu_{12}\nu_{21}} \\ \frac{\nu_{12}E_{22}}{1-\nu_{12}\nu_{21}} & \frac{E_{22}}{1-\nu_{12}\nu_{21}} \end{bmatrix} \begin{bmatrix} \varepsilon_{xx} \\ \varepsilon_{yy} \end{bmatrix} \qquad (4.2)$$

where E_{11} and E_{22} represent the longitudinal and transverse direction moduli, ε_{xx} and ε_{yy} the measured longitudinal and transverse surface strain and ν_{12} and ν_{21} the major and minor Poisson's ratios respectively.

When equation (4.2) is expanded for each component, the stresses in the central 0° block are calculated as per the following:

$$\sigma^0_{11} = \frac{E_{11}}{1-\nu_{12}\nu_{21}}\varepsilon_{xx} + \frac{\nu_{12}E_{22}}{1-\nu_{12}\nu_{21}}\varepsilon_{yy} \quad (4.3)$$

$$\sigma^0_{22} = \frac{\nu_{12}E_{22}}{1-\nu_{12}\nu_{21}}\varepsilon_{xx} + \frac{E_{22}}{1-\nu_{12}\nu_{21}}\varepsilon_{yy} \quad (4.4)$$

where equation (4.4) represents the mechanical transverse compressive stresses generated in the central UD layers (σ_{22}^{0}). The first term in equation (4.4) represents the stress that is required to overcome the Poisson strain in the central 0° block.

Table 4.5 shows a summary of the material properties used for the UD carbon/epoxy lamina as discussed in Chapter 3. All properties are based on measurements except the minor Poisson's ratio which is calculated as follows:

$$\nu_{21} = \frac{E_2}{E_1} * \nu_{12} \qquad (4.5)$$

Table 4.5. Measured basic material properties of the TC33/K51 lamina

	E_1 [GPa]	E_2 [GPa]	ν_{12} [-]	ν_{21}* [-]	G_{12} [GPa]	CPT [mm]
TC33/K51 carbon/epoxy	95.3	6.11	0.301	0.019	2.47	0.030

*Calculated from ν_{12}

A summary of the measured strains (ε_{xx}, ε_{yy}) and the calculated macroscopic stresses (σ_{xx}) and mechanical stresses (σ_{11}^{0} and σ_{22}^{0}) can be found in Table 4.6. All values are averages for each set of the tested specimens with the variability included in the table and they represent the strain/stress at failure or at the first significant load drop of the specimens.

Table 4.6. Summary table of the measured strains and the calculated macroscopic stresses, as well as the estimated mechanical stresses in both the longitudinal and transverse direction.

Configuration	ε_{xx} [%] (C.o.V. [%])	ε_{yy} [%] (C.o.V. [%])	σ_{xx} [MPa] (C.o.V. [%])	σ_{11}^{0} [MPa] (C.o.V. [%])	σ_{22}^{0} [MPa] (C.o.V. [%])
Baseline $[SG_2/0_2]_s$	1.65 (3.0)	-0.50 (5.0)	900 (3.7)	1572 (0.03)	-0.5 (3.24)
$[SG_2/\pm15_6/0_2]_s$	1.60 (5.09)	-1.04 (6.45)	1092 (4.42)	1516 (5.55)	-33 (7.31)
$[\pm20_6/0_2]_s$	1.62 (3.16)	-2.84 (7.70)	1053 (3.48)	1502 (3.22)	-145 (9.17)
$[\pm28_6/0_2]_s$	1.62 (1.89)	-2.91 (4.52)	625 (2.72)	1504 (1.84)	-149 (5.17)

To further investigate the accuracy of the estimation of the transverse normal stress induced on the laminates, a non-linear analysis was also carried out based on the transverse compression response of the utilized TC33/K51 material.

Since characterising the TC33/K51 material in transverse compression could not be successfully completed as mentioned in Chapter 3, data on the material response was taken from the characterisation campaign of Fuller *et al.* [117]. The transverse compression curves were acquired on a similar material using the same resin system (K51 by Skyflex) but a similar fibre from a different manufacturer (TR30 by Mitsubishi Rayon) and exhibited a highly non-linear behaviour. The TR30/K51 prepreg exhibited a similarly low fibre volume fraction of 42.5% as well as both the tensile and compressive transverse modulus of the material was found to be 6 GPa, which agrees well with the utilized thin-ply prepreg in this thesis. Figure 4.9 shows the transverse compression stress – strain curve from [117].

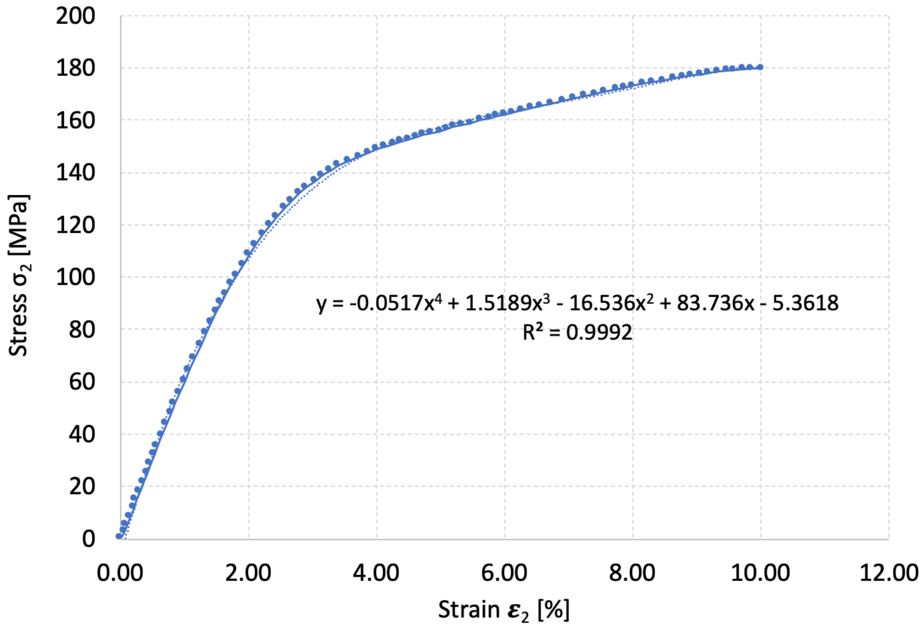

Figure 4.9. Transverse stress-strain curve adapted from [117].

A regression analysis was carried out where the response in Figure 4.9 was fitted by a fourth order polynomial curve. The equation and the R value are displayed in Figure 4.9.

This way, the mechanical strains (after the deduction of the Poisson strain) (ε_{yy}^{Mech}) can be used to estimate the amount of transverse compressive stresses using the non-linear material curve. The calculated mechanical strains (see Table 4.7) were substituted into the polynomial equation presented in Figure 4.9. Based on that, the estimated non-linear transverse compressive stresses ${\sigma_{22}^{0}}^{NL}$ for the different configurations are calculated as shown in Table 4.7. In the non-linear study, only the non-linearity in compression is taken into account. The effect of non-linearity due to shearing of the angle plies does not need to be accounted for (even though it affects the overall response of the specimens, there is no shear present in the central UD block).

Table 4.7. Summary table for the predicted transverse compressive stresses using linear (σ_{22}^{0}) and non-linear analysis (${\sigma_{22}^{0}}^{NL}$)

Configuration	ε_{yy} [%] (C.o.V. [%])	ε_{yy}^{Mech} [%] (C.o.V. [%])	σ_{22}^{0} [MPa] (C.o.V. [%])	${\sigma_{22}^{0}}^{NL}$[MPa]
$[SG_2/\pm15_6/0_2]_s$	-1.04 (6.45)	-0.56 (6.45)	-33 (7.31)	-36
$[\pm20_6/0_2]_s$	-2.84 (7.70)	-2.36 (7.70)	-145 (9.17)	-118
$[\pm28_6/0_2]_s$	-2.91 (4.52)	-2.42 (4.52)	-149 (5.17)	-120

As can be seen in Table 4.7, the predicted transverse compressive stresses using the non-linear approach (${\sigma_{22}^{0}}^{NL}$) exhibit about a maximum of 20% difference when compared to the stresses (σ_{22}^{0}) using linear assumptions. A direct comparison of stresses for the different configurations using the linear and non-linear approaches can be found after section 4.4.2.2.

4.4.2.2. Thermal residual stresses

The calculated longitudinal (σ_{11}^{0}) and transverse stresses (σ_{22}^{0}) of the central UD block need to be corrected for thermal residual stresses arising in the laminate. These residual thermal stresses can be significant and are a result of the mismatch in CTE between the angle-ply and UD blocks.

Figure 4.10 shows a schematic of the thermal behaviour of an angle-ply/UD multi-directional laminate upon cooldown from the initially unconstrained, stress - free cure temperature (T_0) as seen in Figure 4.10 (a) to the final ambient temperature (T_f) shown in Figure 4.10 (c).

Figure 4.10 (b) exhibits an unconstrained state for the laminate where the central carbon plies and the angle-ply (AP) blocks are free to contract thermally independently of each other to the final temperature.

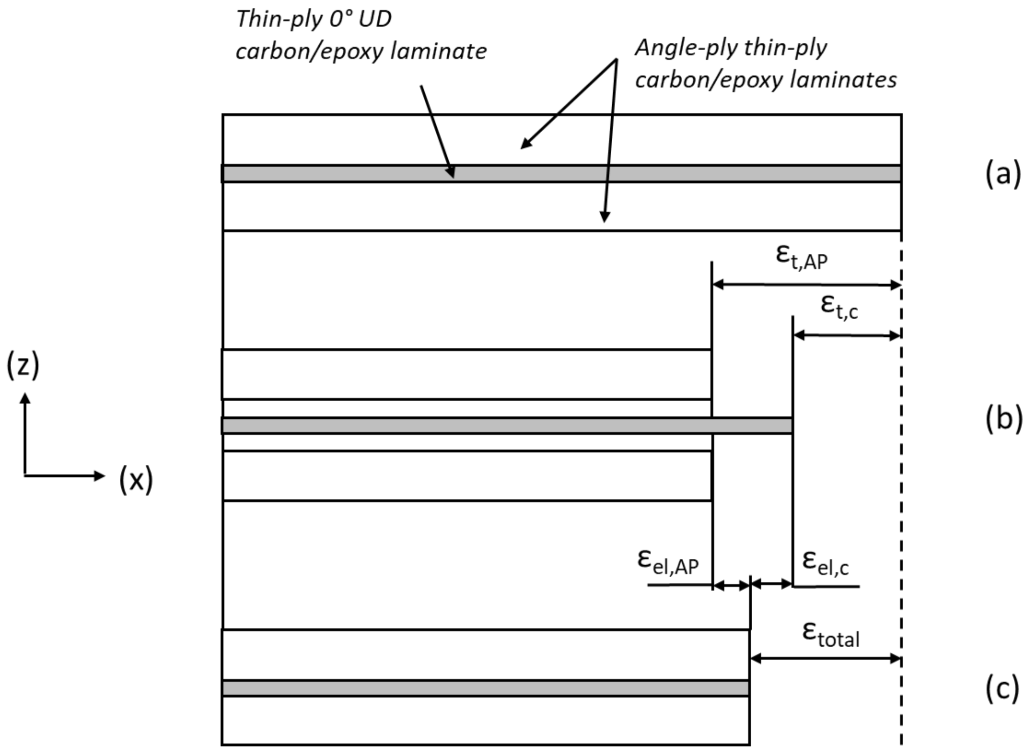

Figure 4.10. A schematic illustration of the thermal behaviour of an angle-ply/UD laminate upon cooldown from the cure temperature: (a) initially unconstrained, stress-free state (b) unconstrained state – free thermal contraction on cooldown to ambient

temperature (c) final constrained state. The illustrated strains are in the direction of the central 0° fibre (x).

The notations for free thermal strains such as $\varepsilon_{t,c}$ and $\varepsilon_{t,AP}$ in Figure 4.10 illustrate the central 0° UD block and the angle-ply blocks (AP) respectively. They are the strains that the central or AP blocks would undergo if they cool down in an unconstrained state. They can be calculated in the following way:

$$\varepsilon_{t,c} = \alpha_c \cdot (\Delta T) \; and \; \varepsilon_{t,AP} = \alpha_{AP} \cdot (\Delta T) \qquad (4.6)$$

where $\alpha_c \; and \; \alpha_{AP}$ are the effective CTE of the UD and AP blocks, and $\Delta T = T_0 - T_f$ the temperature difference between cure and ambient temperature.

ε^{total} is the total (midplane) strain which is the sum of mechanical/elastic strain ($\varepsilon_{el,c}$) due to applied loads and thermal strains (ε^T). ε_{total} can be calculated using Classical Laminate Analysis (CLA) for force-equilibrium between the UD block and the angle-ply blocks assuming a plane stress state for the laminate (constant strain through the thickness) and a temperature change ΔT of 100°C. Firstly, the thermal loading is calculated as

$$[N^T] = \begin{bmatrix} N_x^T \\ N_y^T \\ N_{xy}^T \end{bmatrix} = \sum_{k=1}^{n} \begin{bmatrix} \overline{Q_{11}} & \overline{Q_{12}} & \overline{Q_{16}} \\ \overline{Q_{12}} & \overline{Q_{22}} & \overline{Q_{26}} \\ \overline{Q_{16}} & \overline{Q_{26}} & \overline{Q_{66}} \end{bmatrix}_k \begin{bmatrix} \varepsilon_x^T \\ \varepsilon_y^T \\ \gamma_{xy}^T \end{bmatrix}_k (h_k - h_{k-1}) \qquad (4.7)$$

,where $\varepsilon_x^T = \alpha_x \Delta T, \varepsilon_y^T = \alpha_y \Delta T \; and \; \varepsilon_{xy}^T = \frac{\gamma_{xy}^T}{2} = \alpha_{xy} \Delta T$, as well as $\bar{Q}$ represents the transformed stiffness matrix and h represents the position of each ply in the laminate relative to a reference height respectively.

Then, the calculated thermal forces $[N^T]$ are substituted into equation (4.8) from which the midplane strains of the laminate are calculated. It has to be noted that in this case there are no external loads applied $[N^{ext}]$, only thermal loads which constitute the applied loading.

$$[\varepsilon^{total}] = [A]^{-1}[N^T] \quad (4.8)$$

,where $[A]^{-1}$ represents the inverse A matrix of the laminate.

The difference between the total strain (ε^{total}) and the free thermal strain is the elastic strain $\varepsilon_{el,c}$ and $\varepsilon_{el,AP}$ for the central UD and angle-ply blocks respectively. The elastic strain is associated with the residual stresses that are caused by the constraint from other plies. In the case of the central UD carbon layers it is determined as follows:

$$[\varepsilon_{el,c}] = [\varepsilon^{total}] - [\varepsilon_{t,c}] \qquad (4.9)$$

Once the elastic strain of the central block is determined, the residual stresses can be calculated using Classical Laminate Theory (CLT) in the following way:

$$[\sigma_{res}] = [Q^*][\varepsilon_{el,c}] \qquad (4.10)$$

where Q^* represents the reduced stiffness matrix of the UD carbon block.

The calculated residual thermal stresses for the central UD carbon block (σ_{res}) and the estimated longitudinal ($\sigma_{11}^{0^*}$) and transverse stresses ($\sigma_{22}^{0^*}$) using both linear and non-linear approaches including thermal corrections for each configuration can be found in Table 4.8. The free thermal strains were determined to be 0.010 % for the longitudinal direction and -0.40 % for the transverse direction in the central UD carbon layers respectively. It has to be noted that the Poisson effect is also accounted for in the thermal calculations. All the corrected stresses presented are based on the measured strain to failure values found in Table 4.6.

Table 4.8. Summary of the residual thermal corrections in the central UD layers

Configuration	Longitudinal σ_{res} [MPa]	Transverse σ_{res} [MPa]	Corrected $\sigma_{11}^{0^*}$ [MPa]	Corrected $\sigma_{22}^{0^*}$ [MPa]	Corrected $\sigma_{22}^{0^{NL*}}$ [MPa]
Baseline $[SG_2/0_2]_s$	-19.0	5	1553	4.5	4.5
$[SG_2/\pm15_6/0_2]_s$	4.6	4.2	1521	-29.3	-31.8
$[\pm20_6/0_2]_s$	32.2	3.5	1534	-141.1	-116.5
$[\pm28_6/0_2]_s$	48.9	8.3	1553	-140.4	-109.7

Furthermore, a short sensitivity study was carried out with regard to the utilized estimated CTE values to look at their effect on the predicted thermal corrections. Since the transverse property of the prepreg is the dominant one, the transverse CTE of the carbon fibre was changed from the original value of $4 \cdot 10^{-5}$ [1/K] to $2 \cdot 10^{-5}$ and $6 \cdot 10^{-5}$ [1/K] respectively. The summary of the predictions is shown in Table 4.9 below.

Table 4.9. Summary table of the predicted residual thermal stresses in the central UD block as part of a sensitivity study on the transverse CTE of the thin-ply carbon fibre

	$\alpha_T = 4 \cdot 10^{-5}$ original		$\alpha_T = 2 \cdot 10^{-5}$		$\alpha_T = 6 \cdot 10^{-5}$	
Configuration	Long. σ_{res} [MPa]	Trans. σ_{res} [MPa]	Long. σ_{res} [MPa]	Trans. σ_{res} [MPa]	Long. σ_{res} [MPa]	Trans. σ_{res} [MPa]
$[SG_2/\pm15_6/0_2]_s$	4.6	4.2	3.7	9.2	5.45	-0.9
$[\pm20_6/0_2]_s$	32.2	3.5	20.2	14.0	44.3	-7.1
$[\pm28_6/0_2]_s$	48.9	8.3	28.7	16.5	69.0	0.1

As can be seen from Table 4.9, a 50% change in either direction of the transverse CTE of the material results in a change of the predicted transverse residual stresses of only a maximum of about 10 MPa, which is not very significant when compared to the high transverse compressive stresses of over 100 MPa predicted with either linear or non-linear approaches.

Figure 4.11 illustrates the estimated transverse stresses as a function of the estimated longitudinal stresses at failure in the central UD block, taking account of the Poisson contraction and the residual thermal stresses in the laminates. Both estimations, using linear assumptions and the non-linear approach is illustrated on Figure 4.11.

Overall, it can be said that using the linear approach to estimate the transverse stresses in the central UD block is a simple method with easy data acquisition as the strains are directly measured and stresses can be quickly calculated. On the other hand, using the non-linear approach gives a more accurate representation of the stress state induced on the material, but it is more complex to calculate especially that it requires an additional characterisation test (nonlinear transverse compression). Even though the non-linear assumptions improved the estimations, the conclusions as described later on are not affected by these changes.

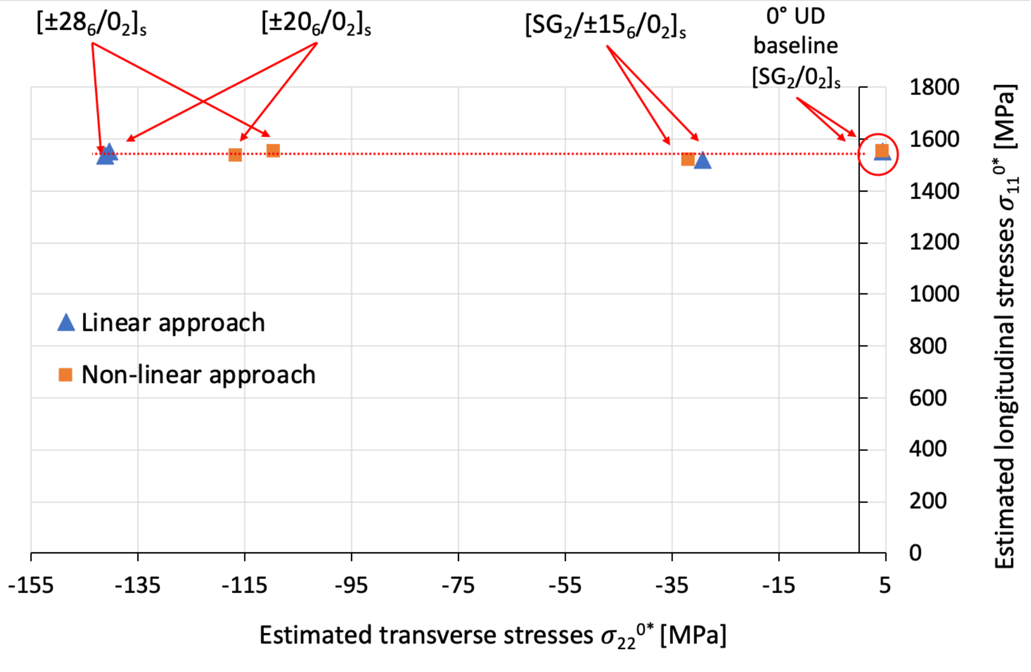

Figure 4.11. The estimated transverse stresses as a function of the longitudinal stresses at failure in the central UD carbon block, including corrections for the Poisson contraction and the residual thermal stresses. Both linear and non-linear approaches are displayed.

4.4.2.3. Failure analysis

Typical failed specimens of each configuration and their respective failure mechanism are illustrated in Figure 4.12.

The coupons with the shallower angle lay-up $[SG_2/\pm15_6/0_2]_s$ were designed and tested in a hybrid configuration to eliminate the stress concentrations arising at the grips during tensile loading. All specimens failed in the gauge section with fibre failure in a similar manner to the baseline specimens as described in Section 4.4.1. Immediately following fibre fracture in the central 0° layers, the laminate as a whole delaminated from the shielding glass layers hence changing the colour visible to the naked eye of the observer - orange colour on Figure 4.12 (a) -. A typical failure pattern of this configuration can be also seen in Figure 4.12 (a).

In contrast, the other two lay-ups of $[\pm20_6/0_2]_s$ and $[\pm28_6/0_2]_s$ were tested in a non-hybrid configuration, with end tabs. The $[\pm20_6/0_2]_s$ type coupons exhibited a sudden fibre failure in the gauge section as it is shown in Figure 4.12 (b). The corresponding stress-strain curve in the mechanical test results (Figure 4.8 (c)) also exhibits a mostly linear behaviour up to failure. However, for the $[\pm28_6/0_2]$ configuration, a large drop can be observed on the stress-strain curves in Figure 4.8 (e) – (f). This large drop corresponds to the fracture of the 0° layers followed by instant delamination. Both the 20- and 28-degree configurations exhibited similar strains to failure (1.62 % from Table 4.6) that corresponds to the fibre fracture of the central 0° plies. An illustration of a failed coupon is shown in Figure 4.12 (c). The central UD block delaminated from the surrounding angle-ply blocks was pulled out in order to observe the fracture surface. The post-mortem examination of the specimens showed that the delamination initiated at the interface between the angle-ply and UD ply blocks at the location where the first fracture of the 0° layers occurred [132].

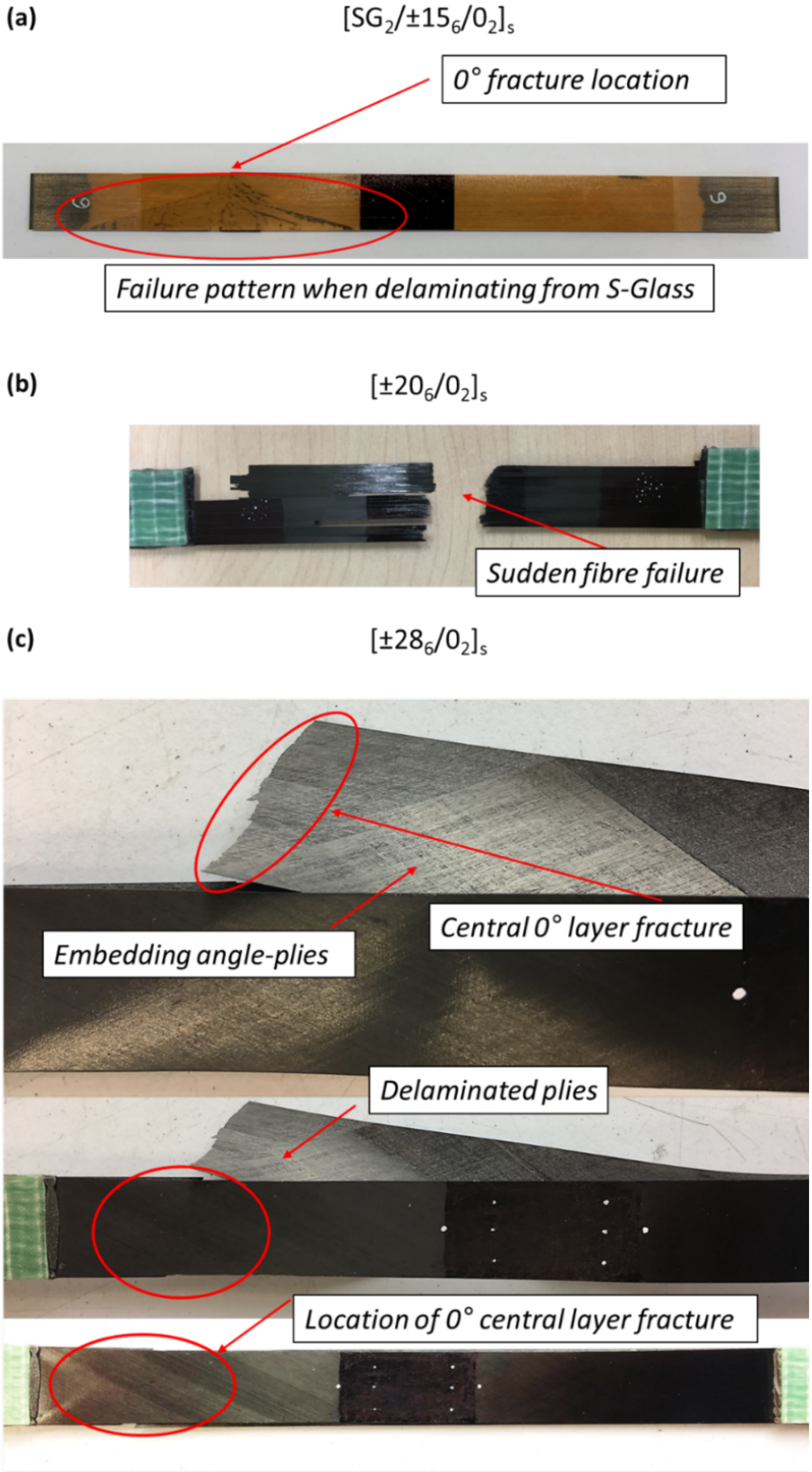

Figure 4.12. Illustration of the three configurations and their failure mechanisms: (a) $[SG_2/\pm15_6/0_2]_s$ hybrid configuration with 0° fibre fracture followed by delamination from the glass layers (b) $[\pm20_6/0_2]_s$ non-hybrid configuration with catastrophic 0° fibre failure and (c) $[\pm28_6/0_2]_s$ configuration with 0° fibre fracture followed by instant delamination from the angle plies.

As can be seen from Table 4.6, there was a very high in-plane transverse compressive strain measured in the central UD block of the larger angle angle-ply configurations: 2.84 % and 2.91 % for the 20° and 28° angles respectively with a transverse to longitudinal strain ratio of 1.46 and 1.49. The corresponding transverse stresses applied to the 0° UD plies including thermal effects are estimated to be around 140 MPa for both cases using linear assumptions and around 115 MPa using a non-linear estimate. The strains and the estimated stresses for these two layups are very similar mainly due to the non-linear behaviour of the material: the original design curve in Figure 4.4 shifted in a way that the two configurations are now located on either side of the minimum.

Furthermore, these overall transverse strains measured for the 20° and 28° configurations respectively (-2.84 % and -2.91 %) are higher than can be typically achieved in a multi-directional laminate because they are more than double the fibre direction compressive strain to failure of the 90° plies [132]. The measured data can be also illustrated using strains. Figure 4.13 shows the measured longitudinal failure strains as a function of the overall measured transverse strains for the different configurations including the baseline tests.

In a typical quasi-isotropic (QI) laminate, the 90° ply would fail in fibre compression before the laminate reaches to -1.5 % transverse compressive strain. When compared with the measured baseline failure strain (1.65%), the trend suggests that high in-plane transverse compressive strains and hence the estimated high in-plane transverse compressive stresses do not influence the longitudinal failure strain of the material.

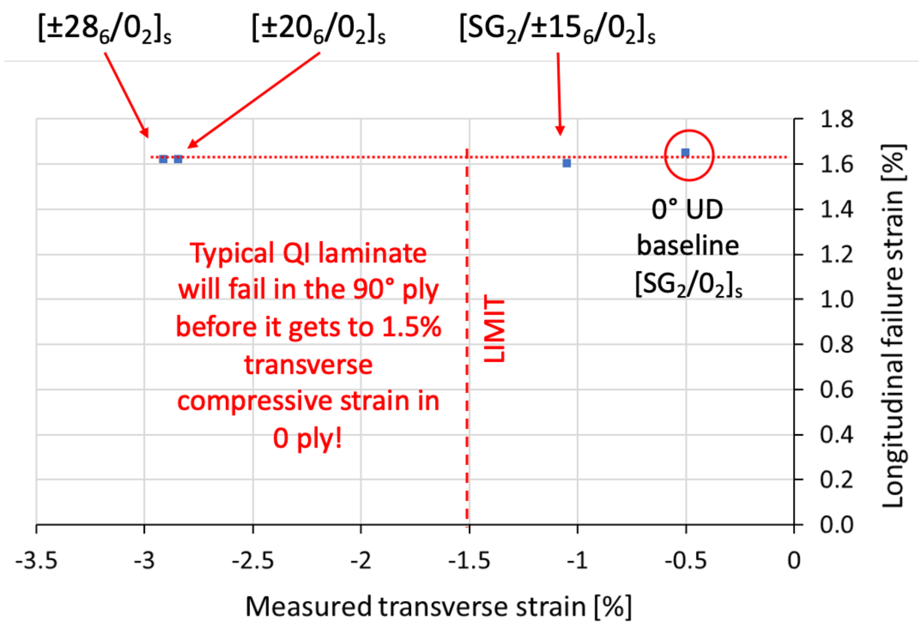

Figure 4.13. The longitudinal strain to failure as a function of the overall measured transverse strains for all configurations including the baseline tests (not corrected for thermal stresses).

4.5. Conclusion

A novel design of composite tensile specimen was presented incorporating thin-ply, angle-ply/UD composites, where a multi-axial stress state of longitudinal tension and transverse compression is induced in the central 0° layers by the scissoring deformation of the embedding angle-ply blocks of the same material. Three configurations were manufactured with variable amounts of transverse stresses generated in the central 0° layers.

The 20° and 28°configurations exhibited an estimated maximum of about 115 MPa of in-plane transverse compressive stress using non-linear predictions. When compared to the measured baseline failure strain of the material, the significant transverse compressive strains applied – with a maximum of 2.91% for the 28°configuration - did not seem to affect the overall strain to failure of the 0 plies.

The baseline measurement was carried out using a novel hybrid composite testing method by Czél *et al.* [20] which proved to be successful in determining the accurate strain to failure of the investigated material.

The specimens incorporating shallower angle angle-ply blocks exhibited sudden fibre failure while the 28° configuration exhibited fibre fracture immediately followed by delamination. Furthermore, the achieved in-plane compressive transverse strains are much higher than could be attained in a typical multi-directional laminate, exceeding the 90° fibre direction strain to failure, suggesting that in practice fibre direction tensile failure is not significantly affected by transverse compressive stresses. This result goes against interactive failure theories such as Tsai-Hill and Tsai-Wu which consider the interaction of longitudinal fibre tension and transverse compression to be important. However, the findings of this thesis are more representative of the material behaviour since they were determined experimentally. The presented novel testing method is capable of generating reliable experimental data for a bi-axial stress state of longitudinal tension and transverse compression.

As an additional remark, it has to be noted, that similarly to the conclusions above, the effect of shear on the tensile failure of TC35/K51 was also determined not to have a significant affect. The study by Jalalvand *et al.* [134] illustrated in Figure 4.14 shows the fibre direction failure strain in function of varying amounts of shear stresses.

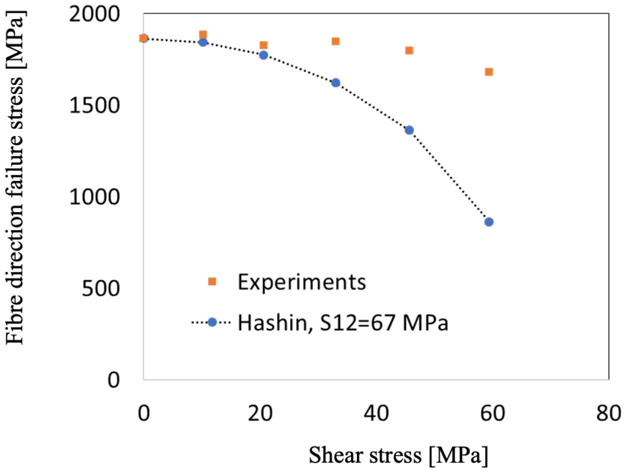

Figure 4.14. Fibre direction failure stress of [±θ]s (θ = 0°, 5°, 10°, 15°, 20°, 25°) laminates as a function of different amounts of shear stresses induced, adapted from [134]

Chapter 5

Longitudinal tension – transverse tension: a study of cross-ply laminated composites

---

The work discussed in this chapter, similarly to the previous one, is aimed at inducing a specific multi-axial stress state in the unidirectional composite material. The bi-axial stress state of longitudinal tension and transverse tension is generated by means of residual thermal stresses that arise in cross-ply laminated composites due to the difference between thermal expansion of the differently oriented layers and the temperature difference between the maximum cure temperature and room temperature [135], [136]. Furthermore, since transverse matrix cracking is one of the most common damage mechanisms associated with cross-ply laminates, its effect is investigated on the failure strain of the material. Additionally, the influence of the 90° ply thickness is also examined for this thin-ply carbon/epoxy material.

In the following section, some of the key topics in the literature associated with this chapter will be presented. The short literature review is not exhaustive but rather aimed at highlighting the main research background.

5.1. Background

One of the most common examples of transverse micro-cracking is observed in cross-ply laminates in the 90° plies when the laminate is loaded in the 0° direction under monotonic or fatigue tensile loading. Transverse cracks start forming in the 90° plies perpendicular to the loading direction after the strain of the laminate exceeds a critical level. These intralayer cracks usually propagate through the width of the 90° layer/block and can result in interfacial cracks when reaching ply interfaces. The interfacial cracks may initiate macroscopic delamination between the 0° and 90° layers [137], [138].

Furthermore, transverse cracking can be followed by other secondary damage mechanisms eg. longitudinal cracking (matrix cracks parallel to the loading direction) or fibre fracture. Usually, cracks can initiate from material defects such as voids or areas with excess resin or high fibre volume fraction.

These secondary damage mechanisms are often caused by high interlaminar stresses and are dependent on various parameters such as laminate geometry, 0° and 90° layer thicknesses, constituent materials, loading history and manufacturing method [139].

For thicker composite laminates, transverse cracking often precedes delamination which was demonstrated experimentally by Wang and Crossman [140], [141]. However, for laminates constituting thin-ply layers the nature of secondary damage is usually different. Jamison *et al.* [142] observed local fibre fracture preceding matrix cracking and ultimately local interior delamination before failure. In a more recent work by Sebaey *et al.* [143], it was concluded that for thicker transverse plies the strength of the laminate is controlled by full width transverse cracks whilst for thinner plies, longitudinal matrix cracking (parallel to the coupons mid-plane) preceded transverse matrix cracking (it has to be noted that presumably, this also depends on the 0° ply thickness). An illustration of the typical damage mechanisms in cross-ply laminates is shown in Figure 5.1, reproduced from [144].

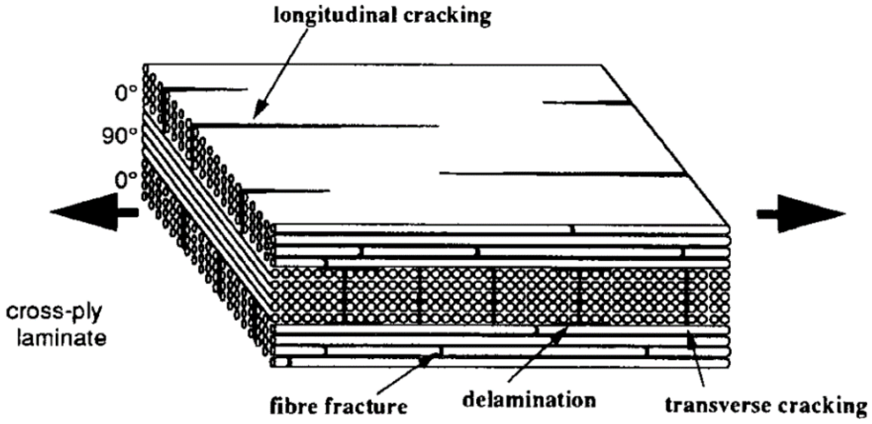

Figure 5.1. Typical damage mechanisms in cross-ply laminates, reproduced from [144]

Transverse cracking prior to final failure directly results in the degradation of certain mechanical and thermal properties such as the effective stiffness, Poisson's ratio or Coefficients of Thermal Expansion (CTE) of the layers and moisture ingression [145], [146].

Furthermore, micro-cracking induces stress concentrations locally at the crack tips, that can result in delamination as mentioned above. Besides, the load is redistributed in the adjacent 0° plies after crack formation.

A comprehensive review of matrix micro-cracking, experimental observations on its initiation and progression and its effects under different loading and environmental conditions as well as analysis methods for modelling the damage process in both glass and carbon composites was conducted by Abrate [147] and more recently by Nairn [145] and Berthelot [144] in 2000 and 2003 respectively. Additionally, stress distributions in cross-ply laminates and literature on the interaction between transverse cracking and delamination were also reviewed.

Generally, models investigating crack initiation and propagation can be divided into two different categories: stress or fracture mechanics-based approaches [144]. The former approach considers damage development that is controlled by the strength of the transverse plies, whereas the latter approach assumes the formation of a crack when the total energy released during the process is equal to the critical strain energy release rate (G_c) of the material. Berthelot [144] emphasized that in either case it is necessary to take account of the inherent defects in the material and consider the statistical distribution of strength or energy release rate. In some cases, the onset and propagation of transverse cracks are investigated using a coupled stress and energy criterion [137], [148], [149].

The formation of the first transverse cracks in cross-ply composite laminates has been extensively studied in the literature both experimentally and theoretically. Bailey, Garrett, and Parvizi *et al.* [150]–[153] carried out various experiments to investigate the initiation of transverse cracks. They varied the inner layer thickness of $[0/90]_s$ laminates whilst keeping the 0° ply thickness constant [150]. When comparing the critical applied strain as a function of the total thickness of the inner 90° plies, a thickness effect was found as illustrated in Figure 5.2, reproduced from Nairn [145].

As the thickness of the 90° plies decreases, the critical strain to induce cracking increases. This effect was found for both carbon and glass fibre reinforced composite laminates. The results also emphasize that the first failure of the transverse layer is not only stress or only strain dependent as defined by most of the existing failure criteria. For instance, García *et al.* [137] used a coupled stress and energy criterion to predict the above mentioned effect which showed good agreement with the experimental results from the literature. Complementing their study, a review of the three major theoretical models explaining thickness effects was included as well.

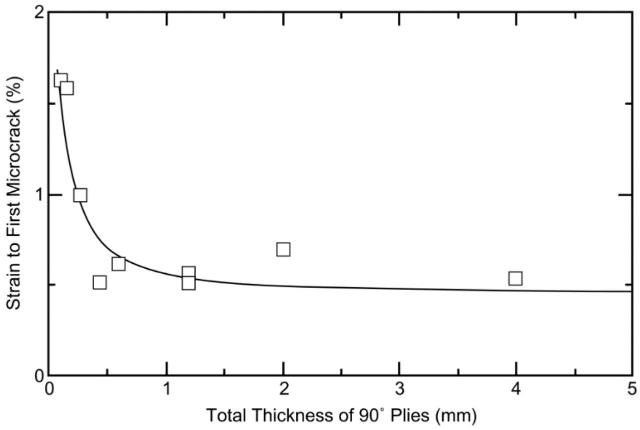

Figure 5.2. Cracking strain in glass fibre $[0/90]_s$ composite laminates as a function of the 90° ply thickness reproduced from [145] replotting the results of [151]

The study carried out by Parvizi *et al.* [150] demonstrated that the thickness of the 90° plies not only affects the initiation but also the formation (propagation) of the cracks. In the utilized glass fibre composites, larger thicknesses (above 0.5 mm) resulted in cracks that went across the whole width of the block instantaneously, whilst for thicknesses between 0.4 and 0.1 mm there were individual free edge cracks that propagated gradually across the laminate as loading increased. Under 0.1 mm it was reported that matrix micro-cracking was completely suppressed before final failure [145]. Parvizi also showed that the cracking constraint observed above can be explained by Aveston and Kelly’s energy approach [154].

There is also evidence on the suppression of micro-cracking using thin-ply carbon fibre laminates. An example of it is a study carried out by Sihn *et al.* [126] who studied thickness effects on laminated composites and demonstrated the suppression of matrix micro-cracking, delamination and splitting damage on thin-ply carbon laminates under static, impact and fatigue loadings. In recent work done by Amacher *et al.* [129] in 2018, they investigated thin-ply carbon composite laminates to study the influence of ply thickness on the ultimate strength and damage initiation as well. A delay in the onset of damage or complete suppression of transverse micro-cracking and delamination was found for the examined thin materials. Furthermore, an improved structural behaviour was exhibited for bolted-joint bearing especially in hot-wet conditions.

Kohler *et al.* [155] in 2019 investigated transverse cracking in the bulk and at the free edge of thin-ply carbon composites. Above a certain ply thickness (for thicker plies), transverse cracking propagated quickly towards the centre of the specimens whereas for thinner plies damage was significantly delayed even up to a point where full width transverse cracks did not develop prior to ultimate failure.

Similarly to the ply thickness effects observed for glass composites, early investigations on the initiation and progression of transverse cracking and thickness effects in carbon fibre cross-ply laminates are also reported widely in the literature [141], [156]–[159].

Generally, for carbon fibre cross-ply laminates, when loading is increased, the transverse cracks start to accumulate, and crack density keeps increasing with the applied stress until the final failure of the specimen. However, it is found for cross-ply laminates made out of glass fibre reinforcements that the evolution of crack density can often saturate prior to ultimate fracture [144].

As loading of the specimen progresses and crack density increases, the degradation of thermomechanical properties occurs as well. One of the representative measures to characterise this effect in the laminate is to determine the stiffness degradation as a function of the developed crack density or the applied load/strain [160]. An example of such stiffness degradation curves is illustrated in Figure 5.3, reproduced from [161].

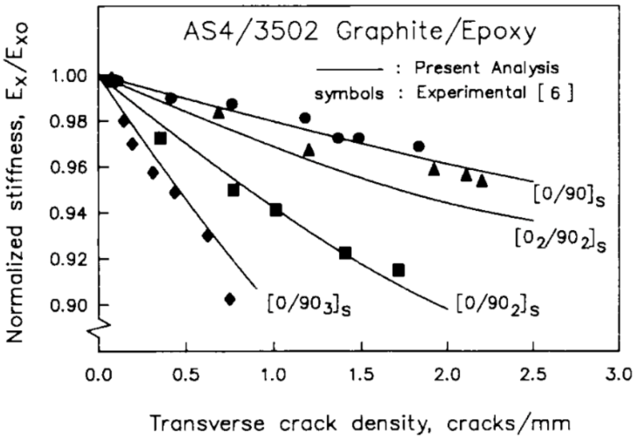

Figure 5.3. Stiffness reduction curves in function of transverse crack density for $[0_n/90_m]_s$ AS4/3502 graphite/epoxy composite laminates [161]

Experimental studies looking at the microcrack density as a function of the applied load are widely reported in the literature in various configurations and material systems [141], [150], [153], [159], [162]–[166].

Alternatively to cross-ply composite laminates, transverse tensile stresses can also be generated in unidirectional plies in tension by using sub-laminates exhibiting a negative Poisson’s ratio in the transverse direction. Laminates exhibiting such negative transverse Poisson’s ratio are referred to as auxetic laminates in literature. This way, a combined stress-state of longitudinal tension and transverse tension may be achieved. A brief review of such materials is presented in the following.

Auxetic materials or auxetics - as described by Evans *et al.* [167] - exhibit a negative Poisson’s ratio: they expand laterally when stretched longitudinally (in the fibre direction) or shrink laterally when compressed in the longitudinal direction [168]. They can exhibit a negative Poisson’s ratio both in and out - of plane of the composite. Research began into auxetics in the late 1980s with the fabrication of synthetic auxetic polyurethane foam [169]–[171], however there are also naturally occurring auxetic materials such as single crystals of arsenic [172], different cubic elemental metals [173], and different forms of skin eg. load bearing cancellous bone from human shins [174] or salamander skin [175] to name but a few.

Auxetic materials can exhibit enhanced properties such as shear modulus (hence shear resistance) as well as indentation and thermal shock resistance and better energy absorbance when compared to conventional (non-auxetic) materials. Other advantages include enhanced fracture toughness and crack growth resistance [168]. An extensive literature survey on auxetic material properties, their structural mechanisms, the latest advances and applications in auxetics especially focused on the aerospace and defence industries was carried out by Liu [176]. Furthermore, an interesting property of such negative ν materials is that they exhibit synclastic or double curvature resulting in a dome shape without the need for machining or forcing the material to take up that shape [177]. This results in good formability and hence useful in applications where complex shapes need to be formed.

To generate transverse tensile stresses in the composite laminates based on the auxetic phenomenon requires specially designing a laminate (angle-ply composites) that exhibits a negative Poisson's ratio. Alternatively, other types of auxetic composites can be manufactured by using auxetic components, auxetic inclusions (discs, spheres, blades..etc) and preforms for instance as described in a review by Wang *et al.* [168].

One of the key requirements of designing such auxetic angle-ply laminates is for the individual lamina (prepreg) to be highly anisotropic. This was suggested by Clarke *et al.* [178] who designed and predicted the properties (Poisson's ratios) of a range of angle-ply carbon/epoxy laminates using CLA. For this reason, stiffer materials such as carbon fibre are the appropriate choice rather than glass fibre or other forms of reinforcement [177]. Also, using prepreg materials with higher fibre volume fraction was suggested as a way of enhancing Poisson's ratios [179].

Generally, analysis or modelling has to be carried out to determine possible stacking sequences that exhibit the desired auxetic properties. Evans *et al.* [180] modelled negative Poisson's ratio effects in network embedded composites (with shaped microstructural networks) for the first time.

In another study by Evans *et al.* [181], specially designed software is introduced which allows for matching the mechanical properties of laminates with predicted negative ν to laminates with similar properties but with a positive ν. Continuous carbon/epoxy prepreg systems were used to achieve in-plane and out-of-plane negative Poisson's ratio for the laminates, provided that the fibre volume fraction and anisotropy of the materials were sufficient. Alderson *et al.* [179] have studied manufacturing techniques that auxetic laminates can be fabricated with as well as studied how the property of the laminates (static indentation and low velocity impact) are affected by achieving through thickness and in-plane negative Poisson's ratio. Carbon/epoxy materials have been widely used to manufacture auxetic laminates and to investigate their mechanical behaviour. Alderson and Coenen [182] used UD carbon/epoxy to fabricate auxetic laminates and investigate their low velocity impact response. Bezazi *et al.* [183] used T300/914 carbon/epoxy to investigate auxetic behaviour for static and cyclic fatigue loadings. Donoghue *et al.* [184] used AS4/3501-6 whereas Coenen and Alderson [185] used IM7/8552 carbon/epoxy respectively to look at the fracture toughness and static indentation resistance of laminates with a negative Poisson's ratio.

When using such auxetic laminate designs, often the lay-up sequence is not balanced hence other stresses such as shear can be present in the laminates. Initially, design optimization using CLA was carried out to find configurations that exhibit the highest possible amount of predicted transverse tensile stresses (most negative Poisson's ratio). One of the possible lay-up configurations found e.g. $[12/65/12/12/65/12/0_2]_s$, exhibited a biaxial stress state with shear as well having in-plane shear coupling terms (A_{16}, A_{26}) which were non-zero. The amount of the additional in-plane stress component (shear) predicted was significant. Consequently, and also due to the complexity of carrying out such tests (use of oblique end-tabs) it was decided to not pursue this design approach.

5.2. Design

The main objective of this study is to design cross-ply composite laminates that exhibit a multi-axial stress state of longitudinal tension and transverse tension in the 0° UD layers. This way, if sufficient transverse stresses were generated, the effect of transverse tension on the strain to failure of the UD material could be investigated.

Furthermore, the effect of varying the 90° layer thickness on the longitudinal failure strain could also be investigated. In the following paragraphs, the distinct design considerations (maximizing the transverse stresses, hybrid effect and thickness effect) are described and the designed laminate configurations are presented.

5.2.1. The effect of 90° ply thickness on the amount of transverse tensile stresses generated

Ideally, the cross-ply configurations should incorporate a ratio of 0° to 90° plies that maximizes the transverse tensile stresses generated in the laminate due to the combination of residual thermal stresses and Poisson ratio restraint. An initial study was carried out investigating $[90_n/0_2]_s$ laminates where n = 2,4,6,8,10, and 12 to determine the effect of increasing the 90° ply thickness on the amount of transverse tensile stress generated in the central UD plies. The analysis was carried out using Classical Laminate Theory (CLT) and plane stress assumptions and it was found that in configurations where n was greater than 8, the tensile stresses did not in fact increase when extra 90° plies were added. A summary of the predicted stresses generated in the central UD plies assuming a fibre direction failure strain of 1.62 % for the laminates is shown in Table 5.1. The estimated longitudinal and transverse stresses include both the mechanical and residual stresses in the different configurations.

Furthermore, since the amount of transverse tensile stresses that could be induced in the inner UD laminate was limited, it was decided to shift the focus of the study to investigate thickness effects as well as it was decided to limit the 90° block thickness to a maximum of 8 plies.

Table 5.1. Summary table of the predicted stress state in the central UD plies of the investigated $[90_n/0_2]_s$ laminates at 1.62% strain

	σ_y/σ_x [-]	σ_x [MPa]	σ_y [MPa]
$[90_2/0_2]_s$	0.032	1529	49
$[90_4/0_2]_s$	0.033	1510	50.2
$[90_6/0_2]_s$	0.034	1492	50.4
$[90_8/0_2]_s$	0.034	1477	50.4
$[90_{10}/0_2]_s$	0.034	1456	50.2
$[90_{12}/0_2]_s$	0.035	1444	50.1

5.2.2. Configuration design

Similarly, to the previous chapter (Chapter 4, section 4.2.2), the absolute thickness of the central UD layers played an important role in the construction of the lay-up and design of such cross-ply laminates. To ensure that hybrid effects were avoided and to be consistent with the previous study, a central UD ply thickness of 0.12 mm (four plies of TC33/K51 material) was chosen as the basic configuration.

To investigate thickness effects, configurations needed to be designed in a way that allows for varying the number of 90° plies while maintaining the overall stress state (stiffness) of the laminates.

A basic structure was proposed – $[Y/X/90_n/0_4/90_n/X/Y]$- where the central UD laminate is surrounded by 90_n blocks where n = 1,2,4, and 8. The outer part of the laminates (marked with X) consisted of only 0° and 90° plies in order to keep the overall stiffness consistent for each configuration. Additionally, glass layers (marked with Y) were incorporated on the surface of the laminates in order to shield the stress concentrations arising at the grips during static tensile testing and to acquire repeatable and consistent results with clear gauge section failures of the specimens. This issue as previously described in Chapter 4 was addressed by using a novel interlayer hybrid composite specimen concept developed by Czél *et al.* [20]. The glass layer thicknesses were calculated according to the design formulas developed by Czél *et al.* in order to ensure that the glass layers can still carry the load after the failure of the carbon composite.

An illustration of a typical specimen comprising the thin-ply carbon/epoxy cross-ply laminate, its structure and the embedding protective glass layers is shown in Figure 5.4.

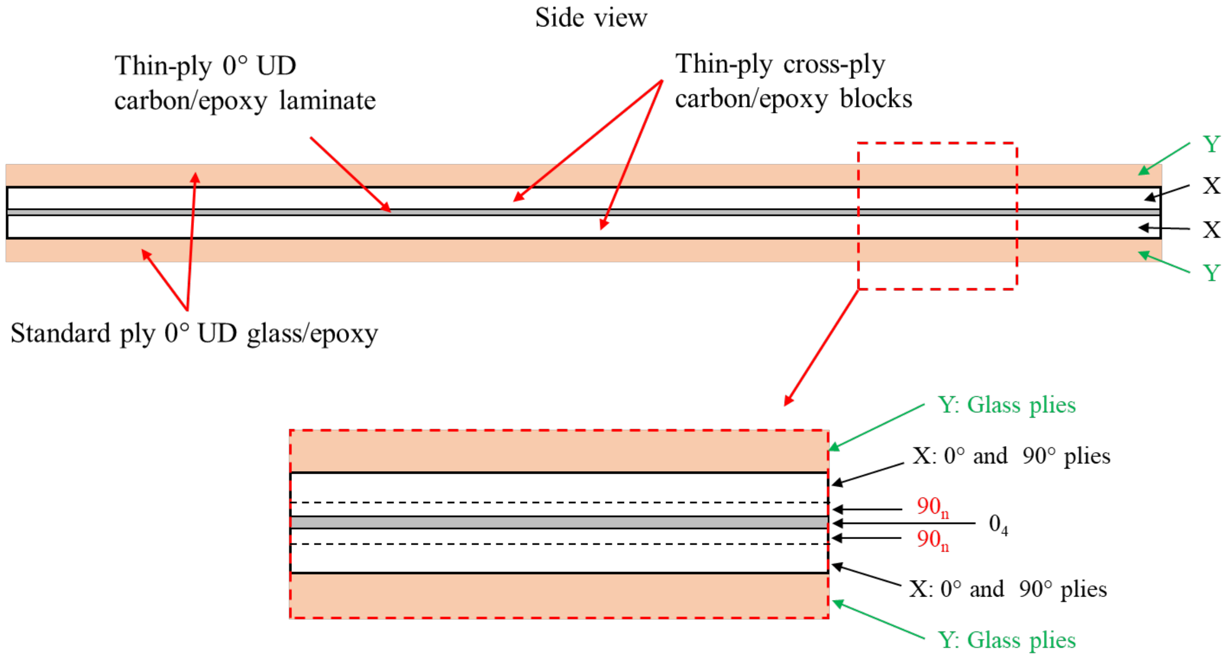

Figure 5.4. Schematic of a typical cross-ply laminate configuration: thin-ply UD carbon/epoxy is surrounded by blocks of thin-ply cross-ply carbon blocks, embedded in standard thickness UD glass/epoxy ply blocks.

For the first three configurations with n = 1,2,4 90_n blocks, the number of adjacent 0° and 90° plies were kept the same. However, for the configuration with 8 blocked 90° plies adjacent to the central UD layers, it was not possible to keep the stiffness ratio constant as there was an excess number of 90° plies within the laminate.

Hence, this configuration had a slightly higher stiffness when compared to the others. It has to be noted that there were no additional 0° layers incorporated in order to minimise the overall number of layers in that configuration keeping close to a total of 28 plies in order to be consistent with the previous study in Chapter 4. Besides, additional 0° layers would have had to be blocked together resulting in the risk of premature failure occurring away from the central block.

A summary of the four different lay-ups designed using CLA can be found in Table 5.2. The table also includes the longitudinal and transverse stresses predicted in the central UD plies at an estimated strain to failure of $\varepsilon = 1.62\%$.

The transverse thermal residual stresses in the UD plies were calculated to be 16 MPa for configuration 1.-3. and 19 MPa for configuration 4. respectively which is already incorporated in the transverse stresses (σ_y) in Table 5.2 below. The green colour represents the embedding glass layers, while the red represents the 90_n blocks with varying number of plies adjacent to the central UD layers. Shear stresses are zero in all configurations.

Table 5.2. A summary table of the designed laminate lay-ups: green colour represents the embedding glass layers, while the red represents the 90_n blocks

	Configuration	Stress in central UD plies		
		σ_y/σ_x [-]	σ_x [MPa]	σ_y [MPa]
1.	$\mathbf{[0_6/(0/90)_5/0/90/0_2]_s}$	0.023	1522	35
2.	$\mathbf{[0_6/0_2/90/(0/90)_3/0/90_2/0_2]_s}$	0.023	1522	35
3.	$\mathbf{[0_6/0_2/90/0_2/90/0_2/90_4/0_2]_s}$	0.023	1522	35
4.	$\mathbf{[0_6/0_2/90/0_2/90/0_2/90_8/0_2]_s}$	0.026	1518	40

To determine the stacking sequence of the outer 0° and 90° blocks (marked with X), first, the 90° and 0° plies were placed as single layers as many times as needed to reach a total of 28 plies for each laminate (consistently with the previous study in Chapter 4). Then, as the 90_n block increased adjacent to the central UD laminate, some of the 90° plies were placed in a different position and the adjacent 0° plies were blocked.

Overall, blocking of more than two plies needed to be avoided where possible in order to prevent any premature failure in the outer 0° and 90° plies so that the 90_n blocks can control the failure of the central UD laminate.

For instance, in a laminate such as: $[0/90_2/0/90_2/0/90_n/0_2]_s$, the single 0° layers are predicted not to fail due to the arrangement of the other plies. There may be transverse cracking in the adjacent 90° blocks, however this is countered by the so-called hybrid effect where a single 0° ply would exhibit a higher strain to failure than in the 4 central plies, hence not failing before the latter.

All cross-ply coupons (Type 1.-3.) were parallel edge specimens with nominal dimensions of 270/190/20/2.70 mm overall length/gauge length/width/thickness respectively. Type 4 specimens had the same nominal dimension except in the thickness direction with a nominal value of $t = 2.94$ mm. Since this study utilizes the same S-glass/epoxy as well as the same thin-ply carbon/epoxy material used in the previous chapter and throughout this thesis, the reader is referred to Chapter 4, section 4.2.1 for detailed material properties.

Overall, it has to be noted that since the predicted amount of transverse stresses did not seem sufficient to investigate the effect of transverse tensile stresses on the longitudinal strain to failure of the central UD block, the emphasis was put on determining the effect of matrix cracks on the fibre failure strain.

5.3. Experimental

In this section, the experimental campaign carried out will be presented with regard to the manufacturing process used, the testing instrumentation and the mechanical test results. To complement the mechanical testing of the laminates, advanced measurement techniques including X-Ray Computed Tomography were used for identification of damage during the loading process, as discussed later.

5.3.1. Manufacturing

The fabrication of the composite laminates followed a similar manufacturing procedure as in previous chapters: hand lay-up of the layers followed by an autoclave consolidation procedure using a vacuum bagging method on a flat aluminium tool plate. The cure cycle utilised was 60 mins at 80°C and 100 mins at 125°C with 0.7 MPa applied pressure and a heat up and cool down rate of 2°C/min. In the finishing stage, the specimens were cut to the desired nominal geometry specified above using a CNC controlled diamond particle coated cutting wheel. After that, each end of the specimens was hand-sanded using Grit P120 polishing paper in order to increase the surface roughness of the composites at the gripped sections (40 mm at each end).

5.3.2. Test method

All uniaxial tensile tests were carried out in accordance with the ASTM D3039 standard [186] on an Instron 8801 universal servo-hydraulic mechanical testing machine. The machine was equipped with a 100 kN rated load cell and hydraulic wedge grips. The grips were similar to the one mentioned in Chapter 4, Section 4.3.2 with 50 mm wide Instron 2704-521 type serrated steel jaw faces. Loading was introduced under displacement control at a crosshead speed of 2 mm/min. Clamping pressure was kept as low as possible, but sufficient to avoid slippage of the coupons. The strain measurement was carried out using an Imetrum video gauge system outputting the corresponding force, time and strain data.

In addition, a PCI-2 acoustic emission (AE) system was used to verify damage events during the loading process. The AE sensors acquiring the data were a PAC WSA type, broadband, piezoelectric transducers with a frequency range of 100-1000 kHz. The maximum sampling rate was 40 MHz and the gain selector of the preamplifier and threshold value were set to 40 dB. 40 dB was selected to filter out all background noises eg. coming from the testing machine. The acoustic sensors were attached to the back face of the tensile specimens by clip gauges. Silicone grease was used to provide coupling between the specimens and the sensor. An illustration of the test instrumentation used for mechanical testing is shown in Figure 5.5.

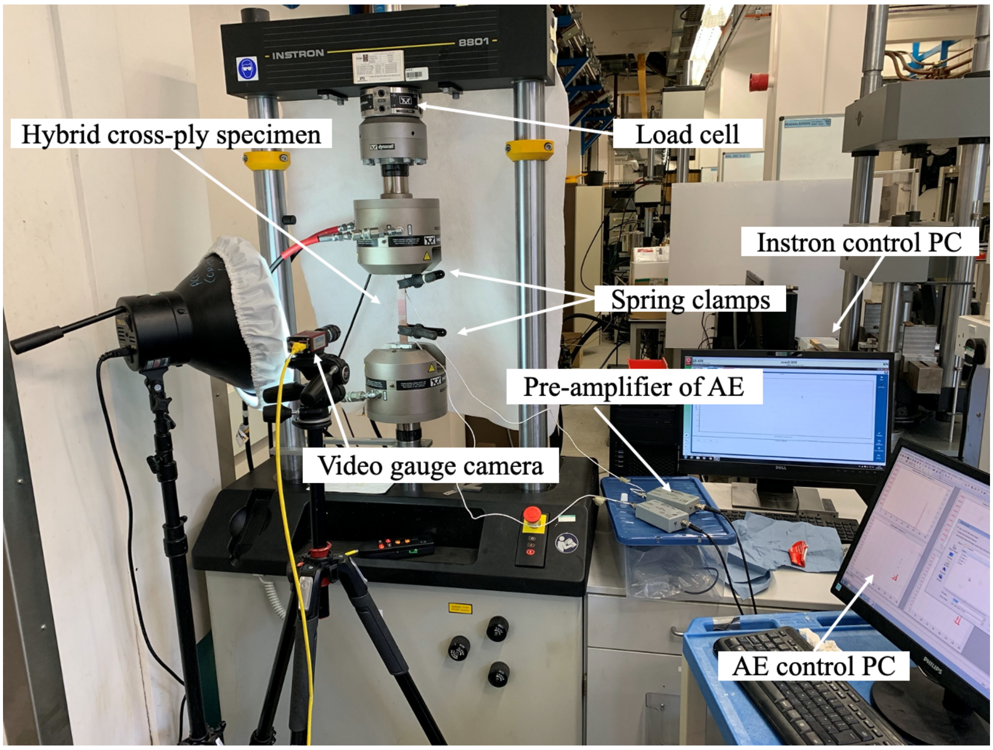

Figure 5.5. Test set-up and data acquisition systems for mechanical testing excluding the video gauge control system PC

5.3.3. – In-situ X-Ray Computed Tomography (X-CT)

There are various methods that can be used for assessing the damage state of composite materials and its growth during the loading process. To investigate matrix micro-cracking, acoustic emission (AE) measurements have been widely used in the literature [187], [188] as well as infrared thermography (IRT) [189], ultrasonic scanning [190], video observations [143], [191], electronic speckle pattern interferometry (ESPI) [192], [193], embedded piezoelectric actuators [194] and X-Ray radiography [195] to name but a few.

In recent years, X-Ray Tomographic techniques have been continuously developing as a non-destructive testing (NDT) technology [196] that has helped in investigating the degradation of mechanical properties and the damage initiation process as well as providing input for progressive damage models. A study by Bayraktar *et al.* [197] describes the new developments in X-CT with regard to composite materials and the fundamental principles of X-CT, its advantages as well as the detection of damage on different levels - macro, meso and micro scale - using a medical scanner. Even more enhanced 3D visualization techniques, such as microfocus CT and synchrotron radiation CT offer the capability to highlight damage such as cracks, delamination, fibre fracture and voids down to a resolution of 1 μm [198], [199] or less.

One of the biggest advantages of utilizing in-situ measurements is that they are not affected by crack closure effects which can mask the damage. If imaged in-situ under load, the damage state can be recorded in its most accurate representation. Consequently, the actual crack length is measurable and the development of damage can be assessed in-situ when examined at various load levels [200]–[202]. For instance, Hufenbach *et al.* [196] discussed a novel test device that integrates a high precision CT with an integrated testing rig. Based on available literature, it is clear that there is no standard method for in-situ CT testing of composite materials and a balance has to be found between the desired degree of information and the experimental effort that is put into testing [196].

In the study presented here, a collaborative project was set up between NASA Langley Research Centre in Hampton, Virginia, USA and the Bristol Composites Institute at the University of Bristol. An in-situ testing rig developed at NASA by Matheson [203] was utilized to carry out interrupted, in-situ X-CT tests of the designed configurations (see Table 5.2. above). The illustration of the testing fixture is shown in Figure 5.6.

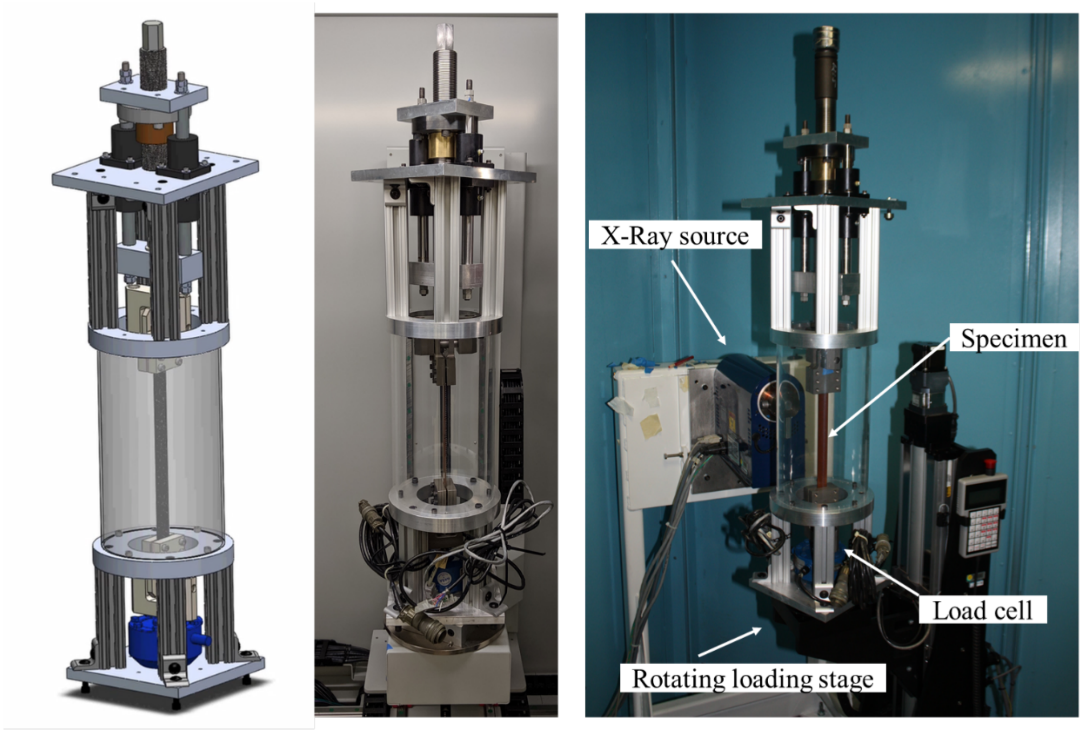

(a) (b) (c)

Figure 5.6. In-situ test fixture (a) design reproduced from Matheson [203] (b) real life testing fixture at the NASA Langley Research Facility (c) testing rig integrated to the loading stage in the X-CT scanner at NASA.

The main objective of the collaboration was to execute interrupted tests in order to detect the existence and record the extent of cracking in the presented laminate configurations at subsequent load levels. Another objective was to determine the effect of 90° layer thickness on the cracking strain of the material. Additionally, there were exploratory tests carried out to get familiar with the equipment, set up the fixture for the appropriate loading as it is designed for both compressive and tensile load applications and to develop an efficient method for loading and scanning the specimens to highlight the desired damage. This way testing parameters can be consistent, and the results are comparable. The data generated throughout this collaboration can provide further experimental input to validate different analytical and modelling approaches as well as in-situ strength predictions. The results and outcome of the collaborative project will be discussed as part of the results, in section 5.4.3.

The X-ray CT system that has been utilized in this investigation was manufactured by HYTEC, Inc. The CT consists of a Varian PaxScan 4030E detector with 2300 x 3200 pixels resolution. The X-Ray source consisted of a Kevex 130kV microfocus end window tube and the X-Ray settings ranged from 100 -115 kV with the current being set in the range of 100-115 mA. The CT system has a rotating loading stage where the in-situ testing rig was purpose designed to fit and rotate while the stationary X-Ray source was in operation. An average of 1700 images per scan were taken (1700 steps in the 360-degree rotation of the specimen). Each image had a capture time of 1 second. For the reconstruction and viewing of the images, a commercially available software VG Studio Max from Volume Graphics was used.

5.4. Results

5.4.1. Mechanical testing

The stress- strain response of the four different configurations tested are presented in Figure 5.7 (a) – (d). The curves correspond to the ultimate failure of the cross-ply carbon laminate within the glass layers. Plotting of the graphs was stopped at the point of the load drop corresponding to carbon fracture, hence it is not visible on the graphs. When compared to the baseline UD measurements discussed in Chapter 4, section 4.4.1, the laminates exhibited a similar response if loaded beyond carbon layer failure: the glass layers exhibited residual load capacity.

A slight tension hardening can also be observed in the response of all configurations. The measured failure (drop) load, longitudinal and transverse direction strains at carbon failure and the calculated stress at the load drop are shown in Table 5.3.

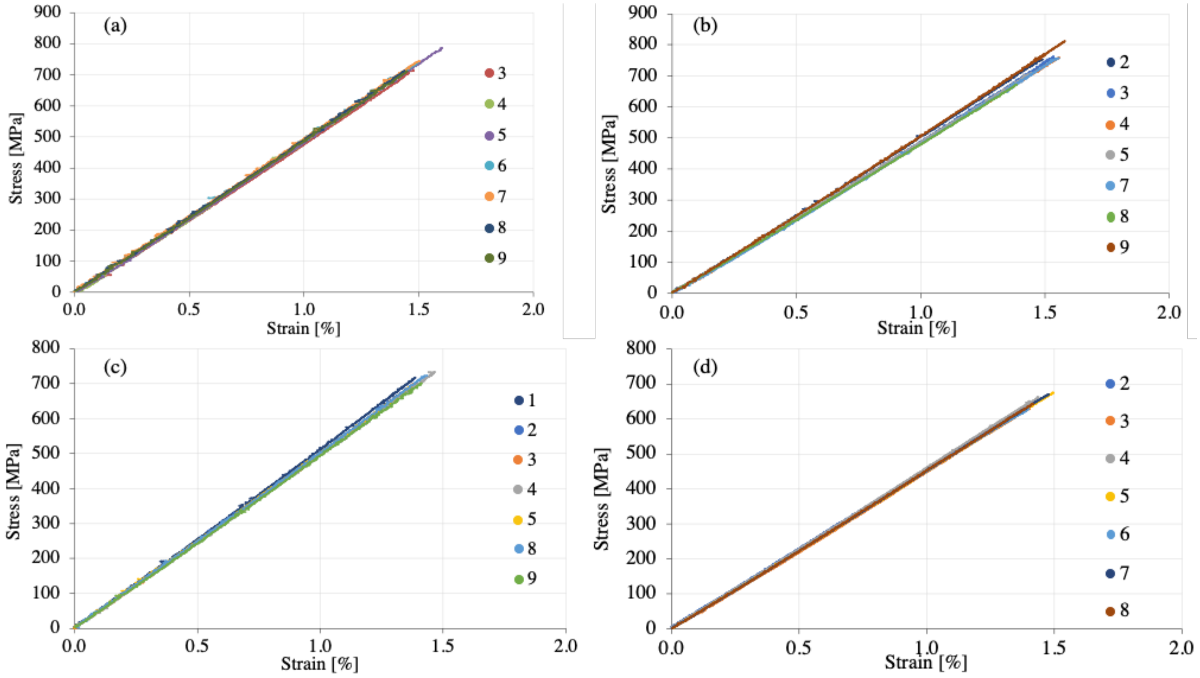

Figure 5.7. Stress – strain responses acquired during mechanical testing of the designed (a) Type 1, (b) Type 2, (c) Type 3 and (d) Type 4 configurations respectively

Table 5.3. Summary table of the mechanical measurements for the cross-ply configurations

Configuration	No. of spec. tested [-]	Drop load P [kN] (CoV%)	Long. strain at load drop ε_{xx} [%] (CoV%)	Trans. strain at load drop ε_{yy} [%] (CoV%)	Stress at load drop σ_{xx} [MPa] (CoV%)
Baseline $[SG_2/0_2]_s$	8	13.8 (3.2)	1.65 (3.0)	-0.50 (5.0)	900 (3.7)
1. $[0_6/(0/90)_5/0/90/0_2]_s$	7	41.1 (5.2)	1.50 (4.5)	-0.20 (10.0)	732.8 (4.7)
2. $[0_6/0_2/90/(0/90)_3/0/90_2/0_2]_s$	7	41.6 (4.7)	1.51 (4.6)	-0.21 (10.1)	746.6 (4.7)
3. $[0_6/0_2/90/0_2/90/0_2/90_4/0_2]_s$	7	39.5 (1.4)	1.41 (3.0)	-0.20 (5.1)	708.9 (2.5)
4. $[0_6/0_2/90/0_2/90/0_2/90_8/0_2]_s$	7	39.0 (2.6)	1.43 (3.3)	-0.15 (8.2)	646.9 (3.4)

All the acquired data in Table 5.3 represent average values with the corresponding number of coupons tested and their respective variability (coefficient of variation [%]).

Table 5.4 summarises the calculated mechanical longitudinal σ_{11}^{0} and transverse direction σ_{22}^{0} stresses in the central UD block at failure accounting for the effect of Poisson's ratio. The predicted stresses in both longitudinal $\left(\sigma_{11}^{0^*}\right)$ and transverse direction including thermal corrections $\left(\sigma_{22}^{0^*}\right)$ are presented as well. The calculations of the mechanical stresses and the predicted stresses including thermal effects are based on the principles explained in Chapter 4, Section 4.4.2. The difference between the estimated transverse stresses in Section 5.2.2 and the ones presented below are due to the latter one being calculated at a lower level of strain (from the measured failure strain values) rather than a fixed strain of 1.62 %.

Table 5.4. Estimated mechanical longitudinal and transverse stresses and the predicted combined mechanical and thermal stresses generated in the cross-ply laminate configurations

	Mechanical		Mechanical + thermal	
Configuration	σ_{11}^{0} [MPa] (C.o.V. [%])	σ_{22}^{0} [MPa] (C.o.V. [%])	$\sigma_{11}^{0^*}$ [MPa]	$\sigma_{22}^{0^*}$ [MPa]
Baseline $[SG_2/0_2]_s$	1572 (0.03)	-0.5 (3.24)	1553	4.5
1. $[0_6/(0/90)_5/0/90/0_2]_s$	1435 (4.5)	15.3 (6.8)	1407	31.7
2. $[0_6/0_2/90/(0/90)_3/0/90_2/0_2]_s$	1433 (5.5)	15.1 (5.7)	1406	31.5
3. $[0_6/0_2/90/0_2/90/0_2/90_4/0_2]_s$	1344 (2.7)	13.7 (9.7)	1316	30.1
4. $[0_6/0_2/90/0_2/90/0_2/90_8/0_2]_s$	1368 (2.8)	17.3 (4.1)	1336	35.8

5.4.2. Acoustic emission measurements

In this section the AE measurements are illustrated with regard to the AE energy released (Figure 5.8), the amplitude of acoustic events (Figure 5.9) as well as the cumulative AE energy (Figure 5.10). All three figures illustrate an example specimen of each configuration: (a) Type 1, (b) Type 2, (c) Type 3 and (d) Type 4 respectively for comparative purposes.

It has to be noted that the time axes on all curves were synchronised using the start of loading as a datum so that they are comparable with each other.

The AE energy curves on Figure 5.8 do not show significant damage events prior to the final failure of the carbon block. However, in all specimen types some higher energy events (marked on Figure 5.8 prior failure) can be found just before the load drops which mark the failure of the carbon cross-ply block. This is also highlighted in Figure 5.9, where for the Type 1.-3. coupons, higher amplitude events occur just before the failure of the carbon block. However, for the Type 4. specimens, there are damage events initiating above the amplitude threshold at around 60% of the peak failure load which differ from the damage events described.

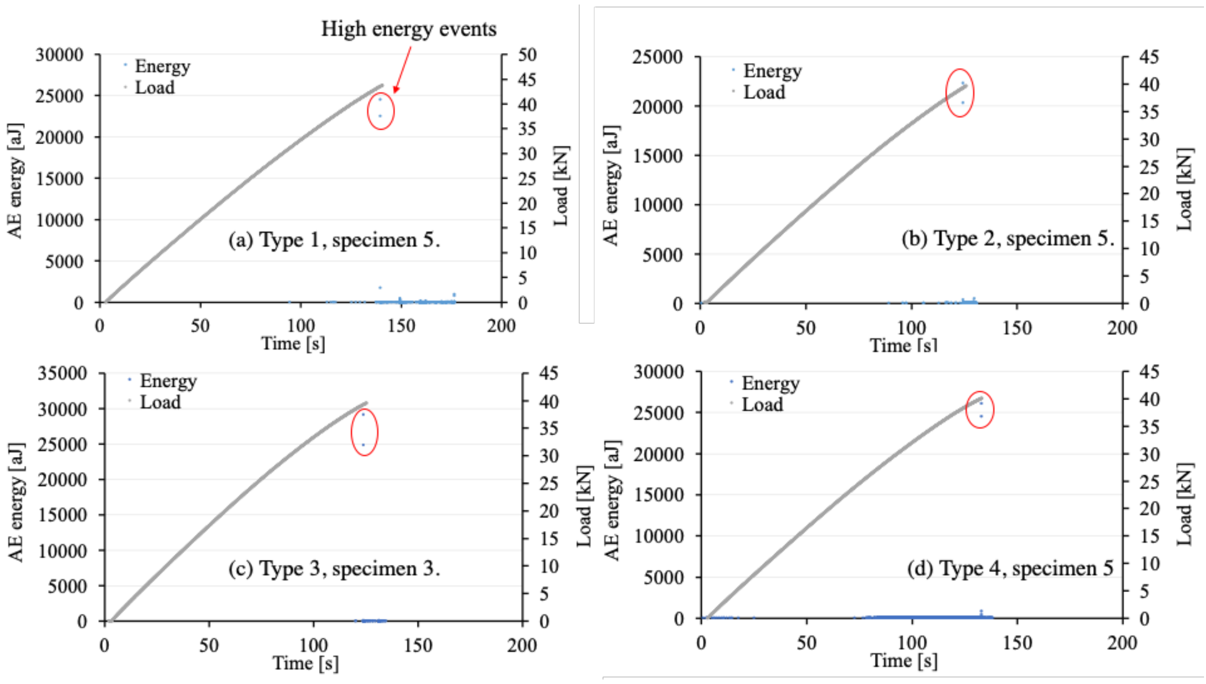

Figure 5.8. AE energy data acquired during testing of the different type configurations: (a) Type 1 (b) Type 2 (c) Type 3 and (d) Type 4 respectively

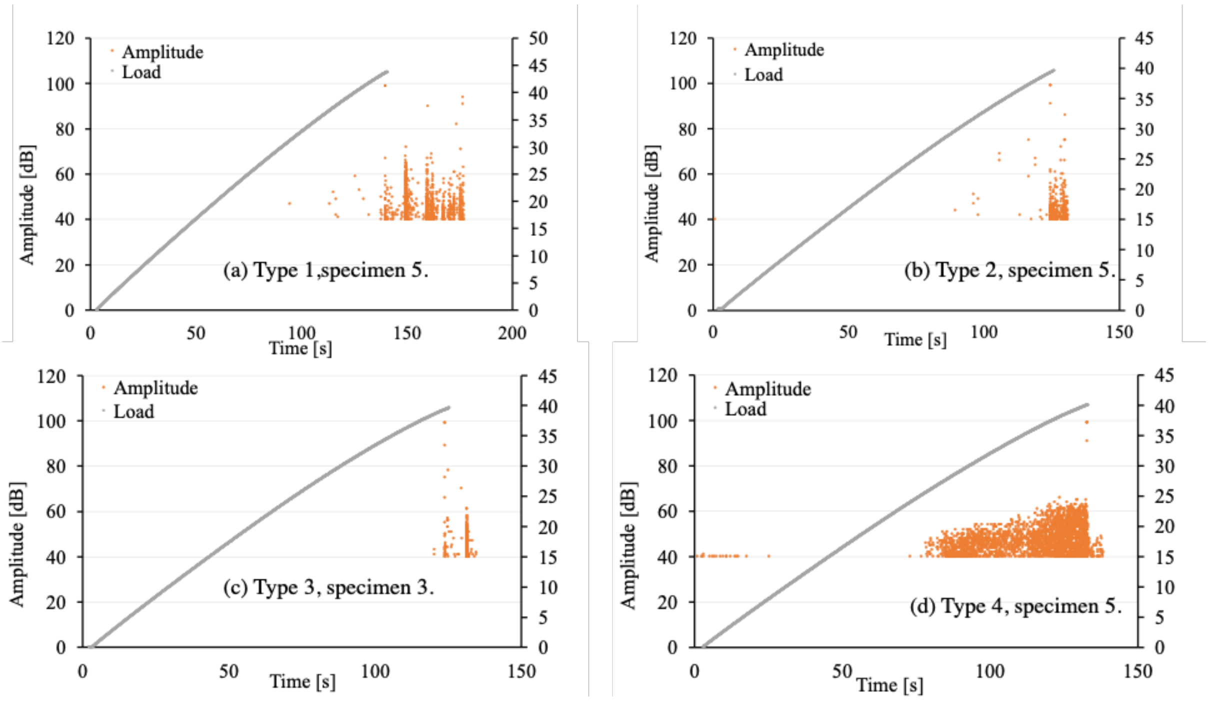

Figure 5.9. The amplitude of the acoustic events measured during testing of the different type configurations: (a) Type 1 (b) Type 2 (c) Type 3 and (d) Type 4 respectively

The cumulative energy curves are presented in Figure 5.10. Type 1.-3. specimens do not show a rise in cumulative energy until the failure of the carbon block. However, for Type 4. specimens, damage events appear earlier during loading which is indicated by the rise in the cumulative energy prior to failure. These observations give an indication of damage, but further investigation is required to determine the true damage state of the specimens.

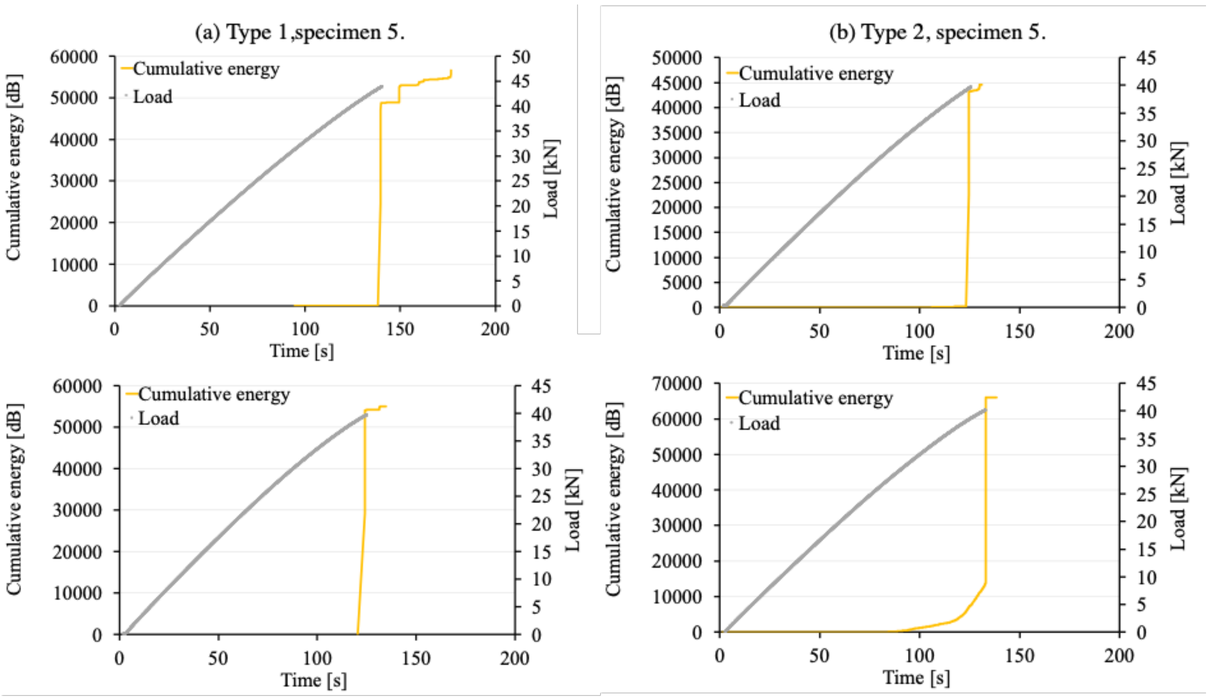

(a) Type 1 ,specimen 5.

(b) Type 2, specimen 5.

(c) Type 3, specimen 3.

(d) Type 4, specimen 5

Figure 5.10. The cumulative energy measured during testing of the different type configurations: (a) Type 1 (b) Type 2 (c) Type 3 and (d) Type 4 respectively

5.4.3. Damage analysis and in-situ X-CT measurements

In this section, damage and failure analyses of the four different configurations are presented based on optical microscopy, in situ and quasi in-situ X-CT tests. Some tests were interrupted in order to assess damage prior to final failure, some specimens were only examined post failure. The key results are presented in order to determine the failure mechanism of the thin-ply cross - ply composite laminates.

Initially, in-situ X-CT tests were carried out to assess the damage state and the presence of cracks in the different configurations. These tests involved taking an intact specimen and loading it to a specific load level in order to open up the cracks within the laminate and then conducting X-Ray CT examination.

For Type 1 and Type 2 specimens with 90_1 and 90_2 layers adjacent to the central UD block, transverse cracking within the 90 layers was not expected due to the low layer thickness. However, for the Type 3 and Type 4 coupons with blocks of 90_4 and 90_8 plies adjacent to the central zeroes, the appearance of transverse cracks was more likely due to the increased layer thickness.

After initial tests it was found that simply using an in-situ X-CT test is not sufficient to highlight cracking occurring in such thin-ply specimens. An example of this is shown in Figure 5.11 where (a) a Type 4 specimen interrupted at 95.9% load level was scanned in-situ (with a nominal load applied to open up the cracks) and (b) the same specimen was scanned in an unloaded (but already damaged state) using dye penetrant. It can be clearly seen that using dye penetrant is necessary to highlight edge damage in the specimens.

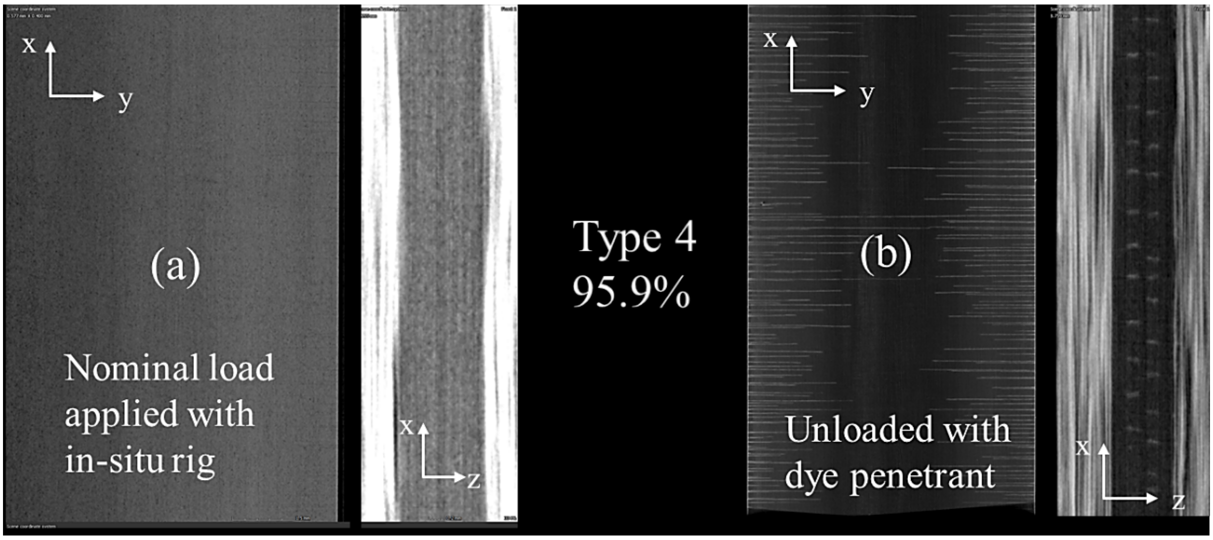

Figure 5.11. Comparison of X-CT images of the same Type 4 specimen taken (a) using an in-situ method with a nominal load applied (b) with no in-situ testing rig, in an unloaded state using dye penetrant.

Consequently, a quasi in-situ or ‘ex-situ’ X-CT procedure was developed that proved successful in showing the desired damage state of the specimens. It consisted of the following steps which are illustrated in Figure 5.12.

1. The specimen was loaded to a set percentage load level to generate damage within the coupon.
2. The specimen was unloaded
3. Dye penetrant was applied with a syringe on the edge of the specimens
4. The specimen was loaded up to a nominal load of ≈ 24.5 kN (60% of average peak failure load) to open up any cracks present
5. Dye penetrant was applied again on the edge of the specimens so that it can infiltrate/penetrate the cracks through the capillary action
6. The specimen was unloaded
7. X-CT scan was performed

It has to be noted that the double application of dye penetrant was carried out only to make sure the dye penetrated all the cracks possible, however it was not necessary. The dye penetrant utilized was a zinc iodide solution that contained ZnI_2 powder, water, isopropyl alcohol, and Kodak Photo Flo type wetting agent.

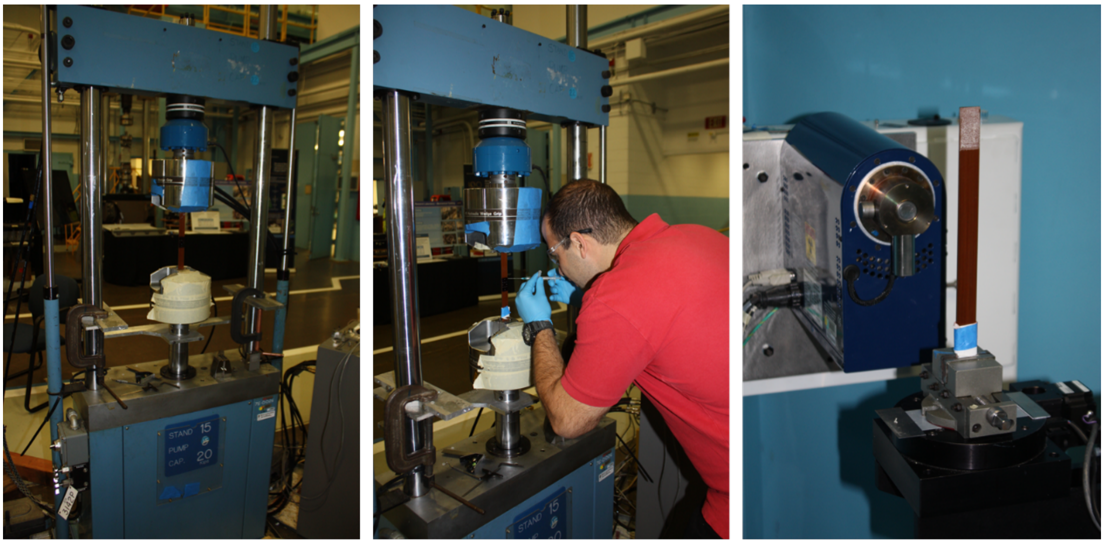

Step 1.–2. Step 3.–6. Step 7.

Figure 5.12. An illustration of the developed quasi in-situ X-CT procedure

The testing matrix with the load levels acquired for the interrupted tests for each configuration is shown in Table 5.5. The load levels are not consistent due to the variation of coupon failure during testing.

The specimens with load levels written in *italic* style were tested and scanned at the NASA Langley Research facility whereas the ones with **bold** style were loaded at the University of Bristol but scanned at NASA.

The percentage of load levels appropriate to the given configuration were determined: for the Type 1 and Type 2 specimens it was desirable to achieve the highest load level possible as cracking was not expected, whilst for Type 3 and Type 4 coupons it was desirable to reduce the load level to be able to determine the onset of first cracking. It has to be noted that in some cases (Type 1 and Type 2 configuration) higher load levels could not be achieved for the interrupted tests due to the premature failure of the specimens.

Table 5.5. Test matrix for the interrupted in-situ X-CT tests

Configuration	Average failure load [kN] (CoV%)	Load levels for interrupted tests [%] (Equivalent load in [kN])				
1. $[0_6/(0/90)_5/0/90/0_2]_s$	41.1 (5.2)	*89.0* *(36.6)*	*86.7* *(35.6)*	*84.5* *(34.7)*	-	-
2. $[0_6/0_2/90/(0/90)_3/0/90_2/0_2]_s$	41.6 (4.7)	**92.7** **(38.6)**	-	*85.0* *(35.4)*		
3. $[0_6/0_2/90/0_2/90/0_2/90_4/0_2]_s$	39.5 (1.4)	**95.9** **(37.9)**	**90.1** **(35.6)**	*85.0* *(33.6)*	*80.0* *(31.6)*	*70.0* *(27.7)*
4. $[0_6/0_2/90/0_2/90/0_2/90_8/0_2]_s$	39.0 (2.6)	**95.9** **(37.4)**	-	**83.9** **(32.7)**	*80.0* *(31.2)*	*70.0* *(27.3)*

In the following, a number of images will be presented for each configuration. All the X-CT scans illustrated here were taken using dye penetrant. The scanned areas of the specimens were 35 x 20 mm with a resolution of 17.6 microns per voxel. The images represent all damage within the carbon layers. An additional image of the X-CT tests carried out can be found in Appendix A.

5.4.3.1. Type 1. configuration - $[0_6/(0/90)_5/0/90/0_2]_s$

X-CT images taken of the configuration with a single 90 ply adjacent to the central UD block can be seen in Figure 5.13 (a) and (b). They were taken at the highest load level achieved prior to failure - 89% of the previous final failure load - for this configuration. Maximum and minimum highlight (the intensity of projection) represent different processing parameters with regard to the grey scale value setting when handling raw data in the software.

Maximum highlight is favourable for showing areas with the presence of dye penetrant especially at the edges, whereas minimum highlight is favourable for areas which are not penetrated. The highest interrupted load level for this configuration does not show evidence of transverse cracking or edge cracking. However, some local damage - delamination – can be observed on Figure 5.13 (b). This interfacial damage is likely to be due to material induced defects. On Figure 5.13 (c) traces of very small edge cracks are visible at very high magnification.

Figure 5.14 exhibits an image taken under an optical microscope where the edge of the specimen was treated with ultraviolet (UV) dye penetrant. This way, under UV light the penetrated dye shows up with high contrast, without the use of a developer. The image of the failed coupon was taken at the location of failure. The 0°-layer fracture can be seen with transverse cracks spread through the thickness of the cross-ply carbon block. Since there were no transverse cracks found away from the failure location in the specimen, the UD block is believed to have fractured first followed by instant transverse cracking through the laminate leading to the failure of the whole carbon block and delamination from the embedding glass layers. The glass block can be seen in one side only as the other side did not fit the image due to magnification.

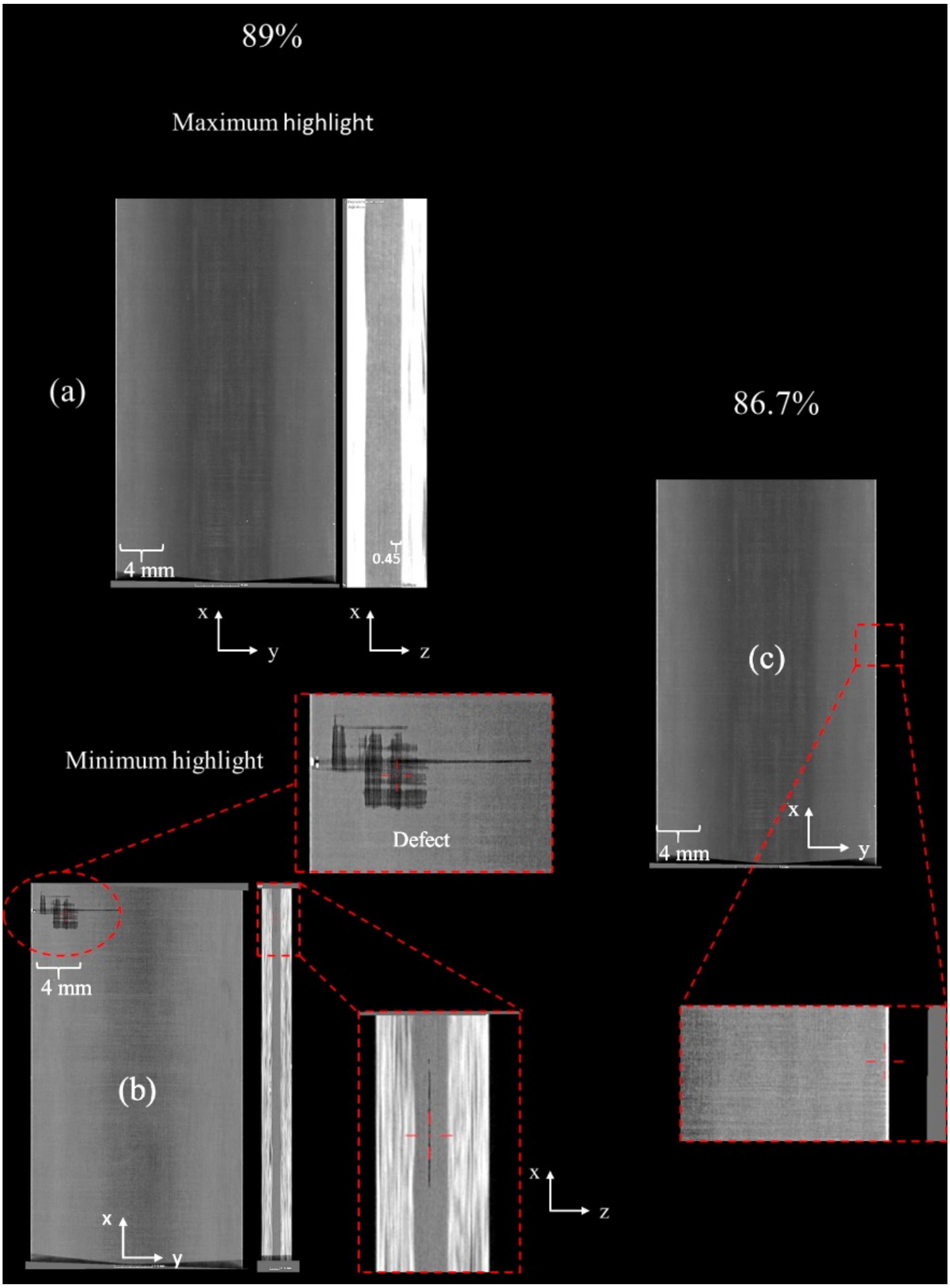

Figure 5.13. X-CT images taken of a Type 1 specimen with (a) maximum highlight (showing dye penetrated areas typically connected to the surface of the specimen) and (b) minimum highlight showing any encapsulated / enclosed internal damage away from the edges. The damage highlighted is a result of material or manufacturing defect. On Figure

5.13 (c) images of specimen loaded to a lower interruption load level is presented showing edge cracks.

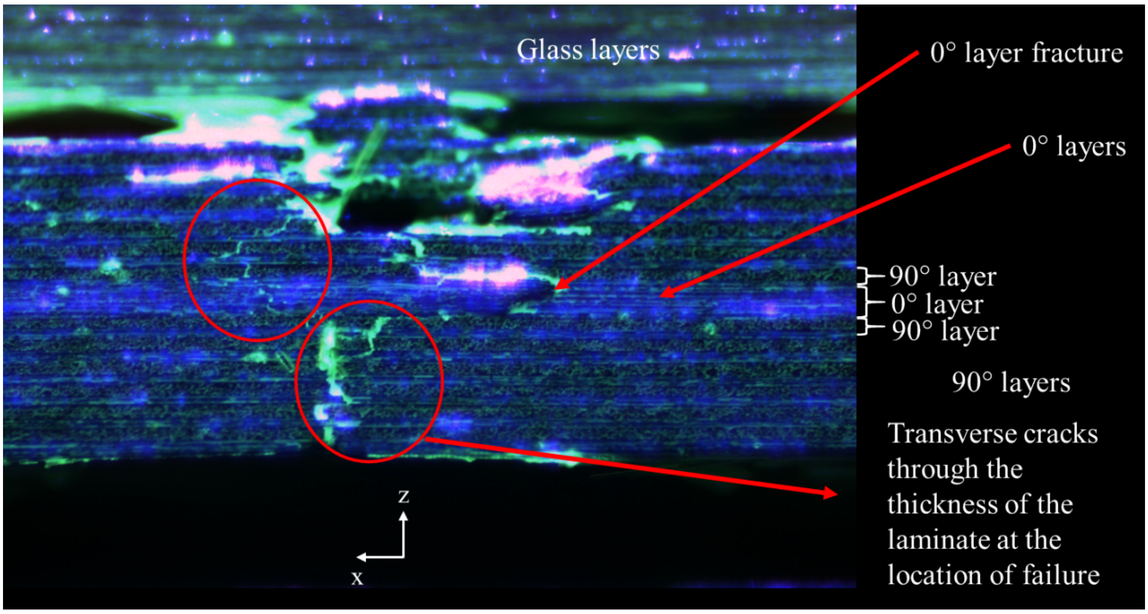

Figure 5.14. An image taken under a Zeiss optical microscope: UV dye paint was applied on the edge of a failed Type 1 specimen to highlight cracking and damage at the location of failure.

5.4.3.2. Type 2. configuration - $[0_6/0_2/90/(0/90)_3/0/90_2/0_2]_s$

The damage highlighted for the configuration with a double 90° block at 92% and 85% of the peak failure load is shown in Figure 5.15 (a) and (b) respectively. As can be seen on Figure 5.15 (a), there is a similar damage pattern present in the carbon layer and some damage in the glass layers possibly due to material defects. Furthermore, small cracks are visible in close proximity (within 1 mm) of the edge of the specimen interrupted at 85% on Figure 5.15 (b). These edge cracks are only present in the 90° blocks adjacent to the central UD laminate and they do not extend fully across the width of the specimen.

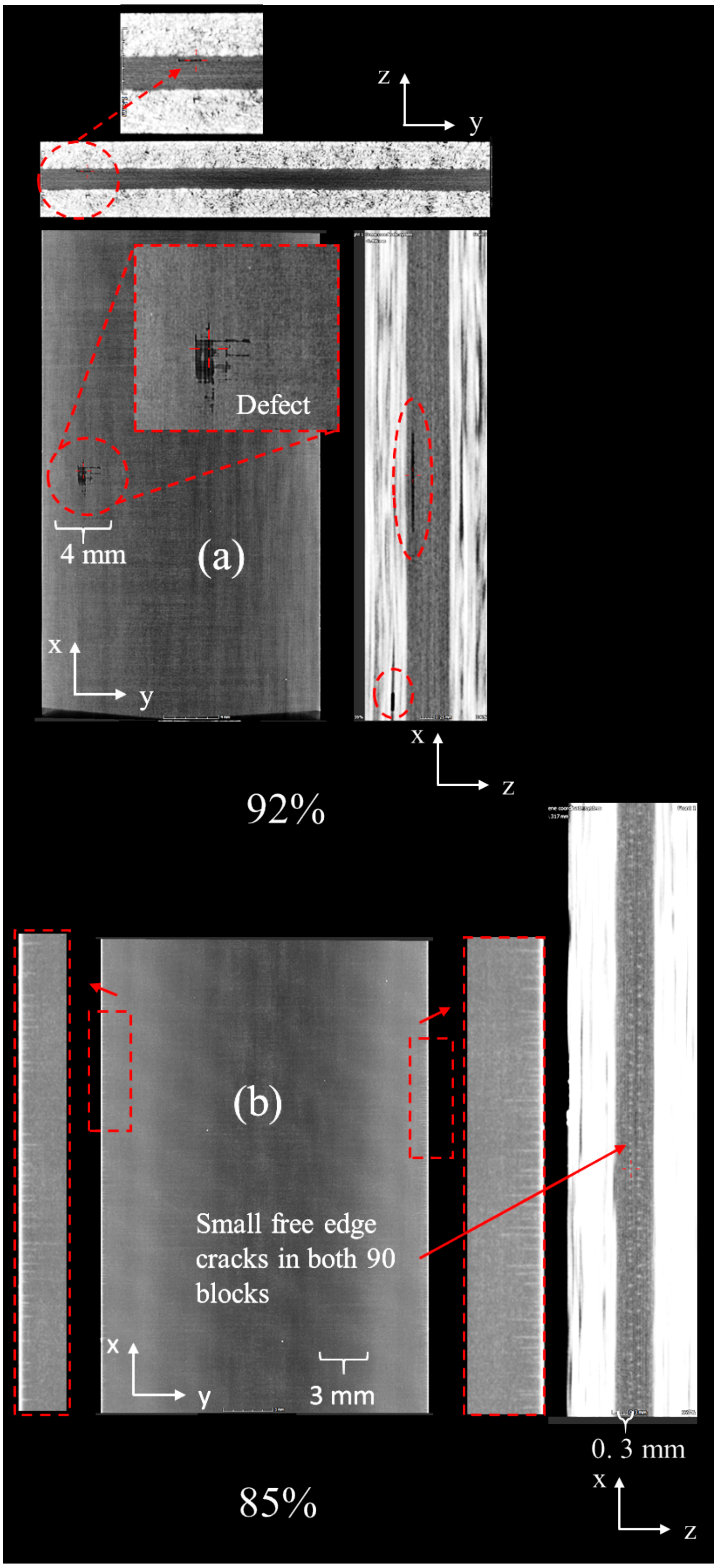

Small free edge cracks in both 90 blocks

Figure 5.15. X-CT images taken of Type 2 specimens interrupted at (a) 92% and (b) 85% of the peak failure load. The images show a similar damage pattern to the Type 1

specimens due to inherent material defects as well as some free edge cracks that do not extend across the width of the specimen.

5.4.3.3. Type 3. configuration - $[0_6/0_2/90/0_2/90/0_2/90_4/0_2]_s$

The processed X-CT image of an interrupted Type 3 specimen at 95.9% of the failure load is shown in Figure 5.16.

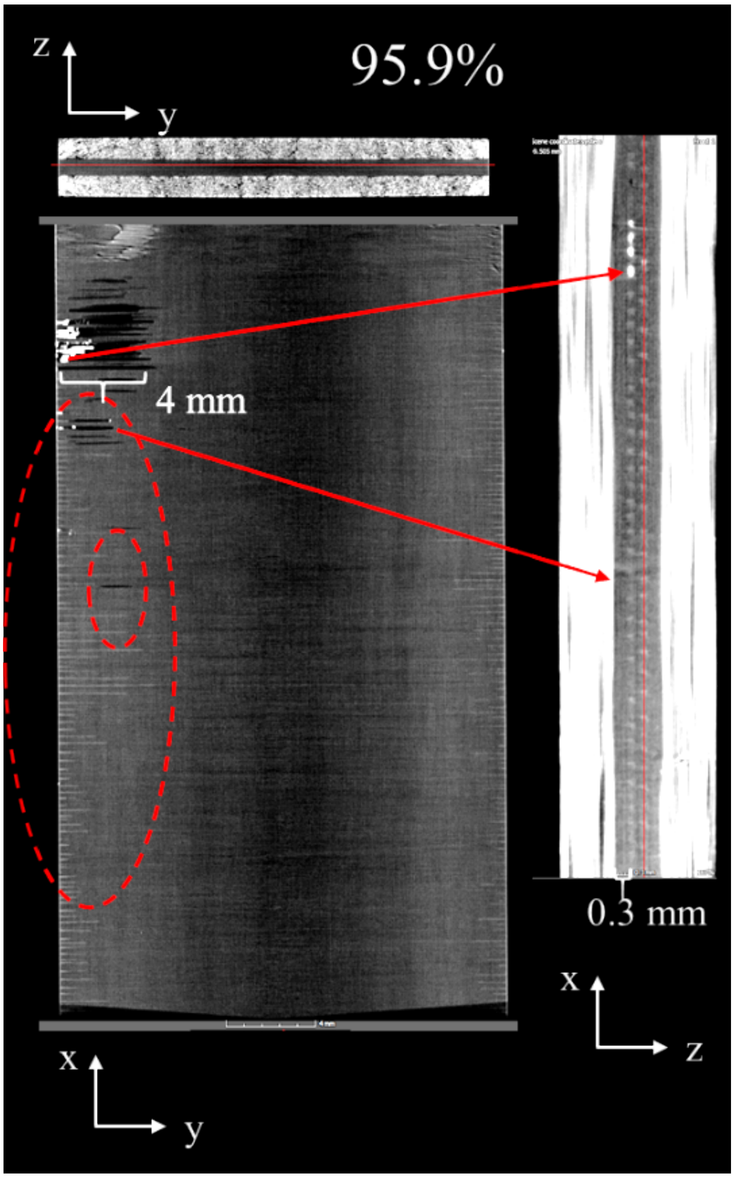

Figure 5.16. X-CT damage representation of an interrupted Type 3 specimen at 95.9% of the peak failure load

On Figure 5.16, free edge cracks can be observed that extended even further than previous configurations but not across the whole width of the specimens. These cracks can only be found within the 90° blocks surrounding the UD plies not in other 90° plies away from the midplane. Another representation for such interrupted Type 3 specimens with decreasing load levels is presented in Figure 5.17 (a) – (c). Three additional load points – 85%, 80% and 70% - are shown respectively with both maximum (left side) and minimum highlight (right side) of each configuration as discussed above.

The edge cracks are visible on the left side of Figure 5.17 (a) – (b) and (c) respectively where a decrease in both density and the length of such cracks can be observed. On the right side, any internal damage away from the edges within the carbon plies is presented. Some small local delamination due to transverse cracks as well as fibre splits in the outer 0° layers can be found.

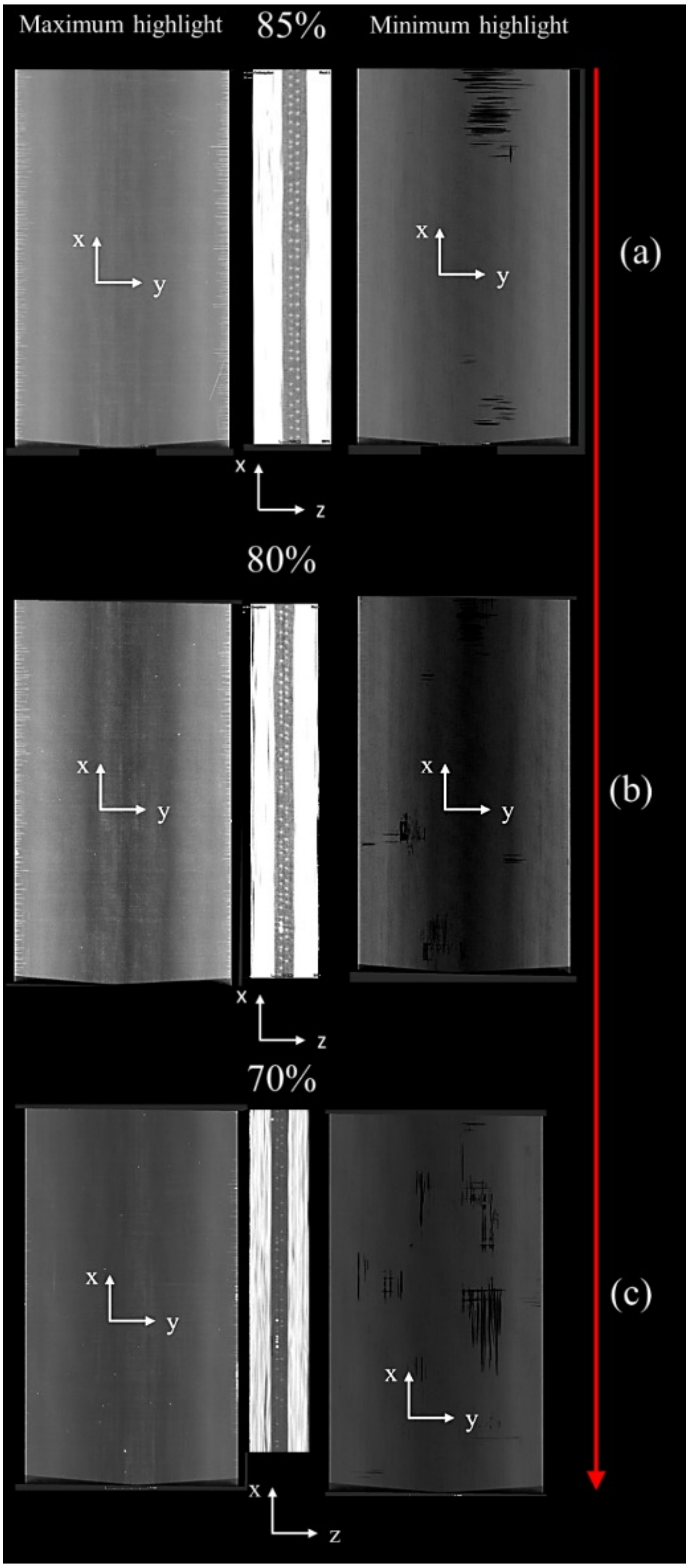

Figure 5.17. X-CT scans of Type 3 specimens interrupted at (a) 85% (b) 80% (c) 70% of the peak failure load respectively. On the left image of each load level the maximum

highlight can be found showing the free edge cracks in the laminate whereas on the right, the internal damage is presented within the carbon layers.

5.4.3.4. Type 4. configuration - $[0_6/0_2/90/0_2/90/0_2/90_8/0_2]_s$

Figure 5.18 exhibits the X-CT scans of the interrupted coupons with four different load levels – 95.9%, 83.9%, 80% and 70% respectively. Transverse cracks can be clearly seen on the images, even extending across the whole width of the laminates. Again, it must be emphasized that these transverse cracks are only present within the thick 90° blocks adjacent to the central UD laminate. The higher the load level and the amount of damage generated in the laminates, the higher the crack density and longer the crack length. The coupon interrupted at 83.9 % of the peak failure load on Figure 5.18 exhibits an increased density of cracks when compared to the coupon with the highest load level achieved (95.9 %). It is due to that particular specimen being exposed to in-situ loading for an extended period of time.

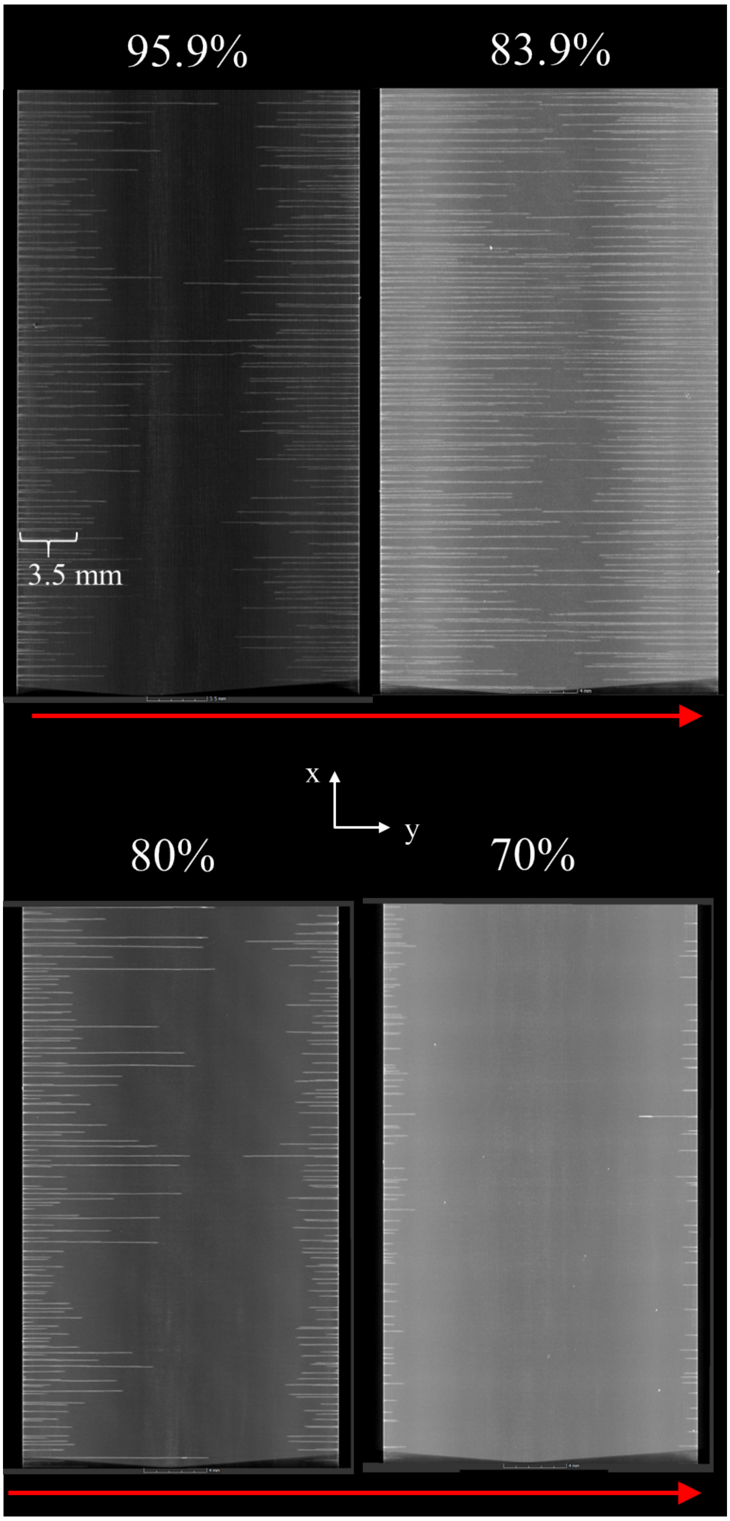

Figure 5.18. X-CT scans of the interrupted Type 4 specimens at four different load levels – 95.9%, 83.9%, 80% and 70% respectively, exhibiting transverse cracking across the width of the laminates within the thick 90° blocks adjacent to the zeroes. The crack length and density increase as the load level increases.

5.4.3.5. General observations

Overall, the X-Ray images taken for all configurations exhibited some form of damage due to material defects. There were no transverse cracks observed in the outer 90° plies (either single or double block) but only in the thicker ones adjacent to the central UD layer. This way the failure of the laminates was indeed only influenced by the 90° block adjacent to the central UD layer. There were no full width transverse cracks found in the Type 1, Type 2 or Type 3 laminates, however with the 90_8 block, for the Type 4 coupons full width transverse cracks appeared as well.

The damage mechanism of thin-ply laminates differ from that of the thicker ones: for thin-ply composites, damage may initiate at low stress levels but that does not necessarily lead to the final failure of the laminate. Crack propagation is mostly energy driven, and so for thin layers, if a crack was to develop within the layer, it would not have enough energy to propagate. Hence, for thin plies there can be some localised damage especially around the interfaces (such as edge cracks), however, there is not enough energy to grow the damaged sites. Crack initiation is dependent on clusters of fibres, weak points, local stress concentrations, defects, voids etc, and once a critical stress level is reached, a crack propagates instantaneously through the thickness and width direction if the ply is thick.

The free-edge cracks and the full width transverse cracks observed can be differentiated as separate mechanisms when defining the onset of damage in thin-ply, cross-ply laminates. This behaviour was also investigated for thin-ply composites with a varying 90° ply thickness from 300 μm down to 30 μm by Kohler *et al.* [155] who observed a similar behaviour where edge cracks and full width transverse cracks were considered as separate mechanisms with different onset stresses. They concluded that the propagation of edge cracks into the bulk was specific to layer thicknesses between 50 μm to 200 μm. When these transverse cracks propagated, the dominant damage mechanism following transverse cracking was delamination for thicker plies, and translaminar fracture of the 0° plies for thinner plies respectively. The supporting AE measurements picked up damage events only when the edge crack propagated into the bulk of the specimens.

This was also illustrated in this study as the Type 4 specimens exhibiting extensive transverse cracking (propagating from the edge into the bulk, across the width) was picked up by the AE measurements (Figure 5.9).

In other cases (Type 1.-3.) there were no damage events exceeding the 40-dB threshold set for the sensors, except the ones very close to failure. For these cases, also there was no evidence of full width transverse cracks within the interrupted specimens.

This study is a good indicator that free-edge cracks alone are not a reliable indicator of damage for thin-ply laminates. The dominant damage mechanism is the propagation of such edge cracks into the bulk of the specimens which can be experimentally determined through AE measurements and X-CT examination.

5.4.4. General discussion of results

An illustration of the estimated longitudinal failure stress as a function of the 90_n block thickness for all configurations including the baseline measurements without any 90 plies is shown in Figure 5.19. All stresses presented include corrections for the Poisson effect as well as thermal residual stresses.

As can be seen from Figure 5.19, there is a 7.6 % reduction in stress from the baseline measurements of the UD material to the configuration with single and double 90_n layers. This reduction in stress is likely to be due to the early free-edge cracks appearing in the 90° plies in the Type 1 and 2 configurations. When specimens are loaded, the UD block experiences additional stress concentrations imposed on it due to the free edge cracks appearing in the 90° plies. If there were no edge cracks appearing, the stress distribution in the 0° plies would be more uniform and at a lower level. Besides, the thermal stresses could have also contributed to the initiation of such free edge cracks.

A study carried out by Xu *et al.* [204] looking at effects of transverse cracking on un-notched and notched strengths of quasi-isotropic (QI) carbon/epoxy laminates showed that in a typical unnotched QI carbon/epoxy laminate with no damage present, the 90 degree ply experiences an increase in stress at the free edges as illustrated in Figure 5.20 reproduced from [204]. This increased stress state (or the extra strain present in the 90°layers) could have led to the initation of small free-edge cracks early on.

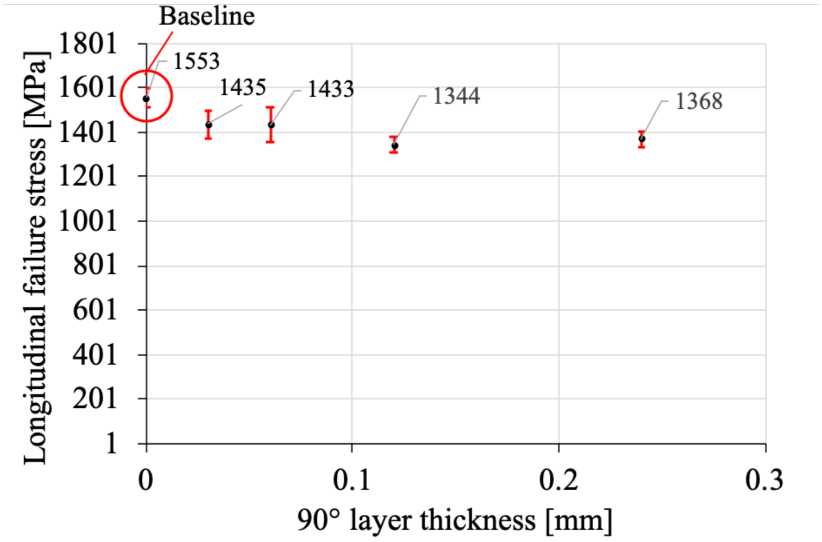

Figure 5.19. 90°-layer thickness in function of the estimated longitudinal failure stress for all Type 1.-4. specimens including the baseline measurements. All stress data shown include corrections for the Poisson effect as well as residual thermal stresses. Error bars are displayed based on strain measurements.

When the 90° block thickness increases for the Type 3 and Type 4 configurations, we can see a further decrease in both the strain to failure and the calculated failure stresses in Table 5.3. This decrease is believed to be due to the free-edge cracks extending into the bulk of the specimens - in the case of Type 4 coupons all the way across the width - affecting a larger volume of the material.

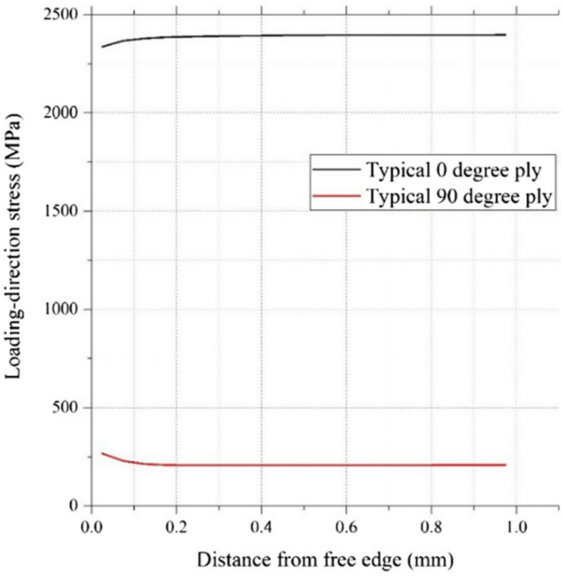

Figure 5.20. Free edge effects predicted in unnotched QI carbon epoxy laminates with no damage present, reproduced from [204]

Generally, as the block thickness increased, there was additional loading put on the 0-degree plies due to the presence of extended edge cracks (Type 1-3 specimens) and/or transverse cracks (Type 4 specimens) which led to the further decrease in the mechanical properties. There are two factors that may contribute to this.

On one hand, there are free edge effects, and the onset of full transverse cracks causes stress concentrations near the edges of the laminate. These stress concentrations can lead to the redistribution of load from 90° plies onto the adjacent 0° plies. This effect is illustrated by the study of Xu *et al.* [204] who carried out FE simulations on a slice of a quasi-isotropic IM7/8552 laminate with a layup of $[45/90/\text{-}45/0]_{4s}$, with full cracks in all the 90° layers and boundary conditions representing a repeating array of cracks. This showed the effect of the special state of stress near the free edge, but since only one element was used per ply, it was insufficient to model the localised stress concentration due to the crack. The analysis showed about 5 % increase in stresses at the edges in the 0° plies when compared to the mid-section stresses as shown on Figure 5.21, reproduced from [204].

On the other hand, stress concentrations are also imposed on the 0° plies locally due to the transverse cracks in the laminate.

In a modelling study by Melnikov *et al.* [205], a drop in the predicted strength was observed when investigating the influence of transverse cracks on the failure of 0° plies (and therefore their strength) in cross-ply laminates.

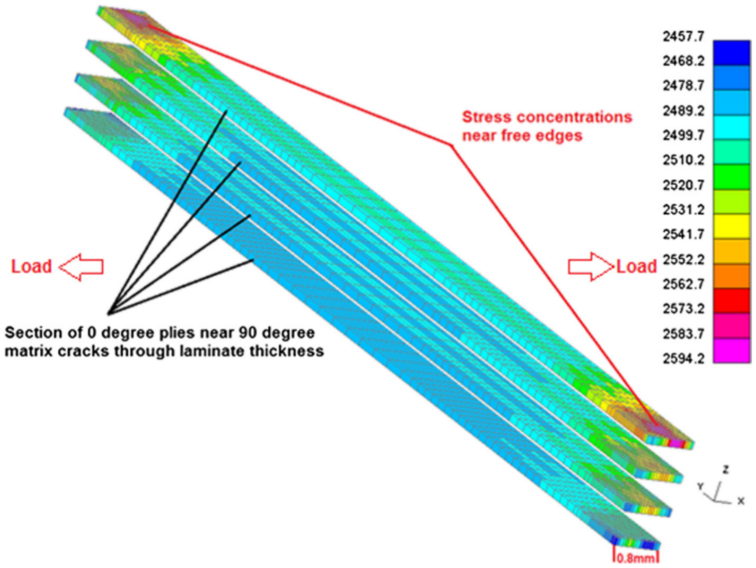

Figure 5.21. Stress distribution in the 0° plies close to ultimate failure with 90° matrix cracks present in the model, reproduced from [204]

Their models found a 3.9 % decrease in strength for thin-ply cross-ply laminates when compared to the UD composite, assuming a single crack in the laminate. For the calculations, a fibre break model was used accounting for strain non-uniformity and stress concentrations induced by the transverse cracks. The stress concentrations generated around the crack tips in the model were distinct for thick and thin plies due to the difference in their opening displacements.

The models are not directly comparable with the experimental results presented here because the materials and layups are different. It is uncertain if Poisson contraction and thermal effects are accounted for in their model. Furthermore, this study does not take account of the non-linear behaviour of the material.

Overall, it can be said that both effects mentioned above – stress concentrations imposed locally on the 0° plies and free edge effects – are present in this study and would be expected to affect the strength of the laminates. The measured strength reductions in the experiments are small and of a similar order compared to the studies presented above.

5.5. Conclusion

A biaxial stress state of longitudinal tension and transverse tension was successfully induced on the UD layers by means of residual thermal stresses. Since the generated transverse stresses did not seem sufficient to investigate its effects on the UD ply block, the emphasis was put on investigating the effect of transverse cracking on the fibre direction strain to failure. Four different cross-ply configurations were designed with varying thicknesses of 90° plies adjacent to the central 0 plies. It was found that thin-ply materials are indeed capable of suppressing transverse micro-cracking away from the edges. Quasi in-situ X-Ray CT tests were successfully carried out to determine the extent of damage (edge cracks and matrix cracks) within the configurations.

Furthermore, AE measurements were carried out which successfully indicated the presence of full width transverse cracks (Type 4 configuration) but not the free-edge cracks. The initiation of edge cracks and their progression into the bulk of the material has to be differentiated.

Even though there is local damage present as free-edge cracks, there is not enough energy for these to grow (Type 1-3 configuration). Type 4 configuration exhibited extended transverse cracks across the full width of the specimens. A small drop can be found in the failure strain of the Type 1 and Type 2 configurations which can be attributed to the small edge cracks present. As these cracks further develop across the width of the specimens, a larger volume of the material is affected, hence the continued degradation of the properties due to the imposed stress concentrations both locally and globally (laminate level) on the zero degree layers. Matrix cracking indeed results in reduced failure strain/strength values, but their overall effect is small.

Chapter 6

Longitudinal compression – transverse tension: a novel test method to induce bi-axial stress states in thin-ply composites

---

A novel testing approach inspired by a study of Laurin *et al.* [206] is introduced incorporating thin-ply, UD/angle-ply composite laminates. The combined loading of longitudinal compression and transverse tension at the ply level is applied indirectly in a tensile test set-up through the Poisson contraction of the laminates. Using the advantages of thin-ply composites to delay or suppress the onset of damage, these materials are good candidates for evaluating the interaction between fibre kinking and transverse stresses. They provide versatile solutions for stacking sequence optimization and higher compressive strengths are reported when utilizing such materials [207]. The selection of the stacking sequence was carried out using a design of experiments (DOE). To achieve the desired multi-axial stress state in the UD layers, an advanced failure criterion developed by Laurin *et al.* [119] is used to ensure that any premature or undesired failure mode is avoided. It is necessary to use such failure criteria especially since in a multi-directional laminate there is a competition between the different damage modes. Three different configurations were experimentally investigated using advanced measurement techniques such as DIC and AE as well as post failure examination using optical microscopy and Scanning Electron Microscope (SEM) imaging. Size effects and their effect on compressive failure were also investigated.

This study was carried out in collaboration with ONERA, the French Aerospace Lab in Châtillon, France. The design and optimization part of the study was conducted at ONERA during a research placement undertaken by the author, whereas the laminates were manufactured at the University of Bristol.

Testing of the coupons and some post failure imaging was also carried out during further research placements at the facilities in ONERA.

6.1. Background

This section similarly to previous chapters, will cover some of the key topics in the literature related to the discussed study. The mentioned references are not exhaustive but highlight the key research areas.

Compressive strength of carbon composites is usually lower than their ultimate tensile strength which makes it both a key design consideration and a limiting factor in structural design [208]. Experimentally determining the in-plane longitudinal compressive strength of UD plies still poses great technical challenges especially since the compressive failure mechanism being sensitive to the alignment and geometry of the specimens, the way that the load is introduced, overall buckling as well as the arising stress concentrations [206]. For these reasons, one of the biggest challenges for many industries is to be able to determine UD ply compressive strengths in the most accurate way and to take material variability into account as recommended by aeronautical standards [113]. If compressive behaviour is better understood and novel, more reliable measurement techniques are developed, the confidence in compressive properties can be enhanced, aiding the safety of structures that are predominantly controlled by compressive failure *e.g.* under hot-wet conditions, impact loading, bearing loading in mechanical joints and at notches [209].

6.1.1. Compressive failure

Compression failure [208]–[231] has been extensively studied in the literature and it was found that for the most commonly used high strength (PAN based) carbon/epoxy composites when the UD material is subjected to uniaxial compressive loading, the failure mechanism is controlled by shear instability.

This instability results in short-wavelength buckling [220]- commonly called micro-buckling– of the fibres followed by plastic deformation in the surrounding matrix allowing further rotation of the fibres. This rotation induces additional shear stresses (both in and out-of-plane) leading to the formation of fibre failure and 'kink-bands'. A schematic illustrating the three phases of compressive failure is shown in Figure 6.1 [232]: (a) initially, localised elastic-plastic shearing and buckling of the fibres occur followed by a transient stage (b) where the localised kinking areas grow and form the so-called kink bands.

Figure 6.1 (c) demonstrates the lateral propagation of such macroscopic kink-bands resulting in an overall failure of the specimen. It has to be noted that for carbon fibre reinforced polymers (CFRP) due to their inherent brittleness and sudden, catastrophic fracture, the three stages of compressive failure are very difficult to observe experimentally [233], [234].

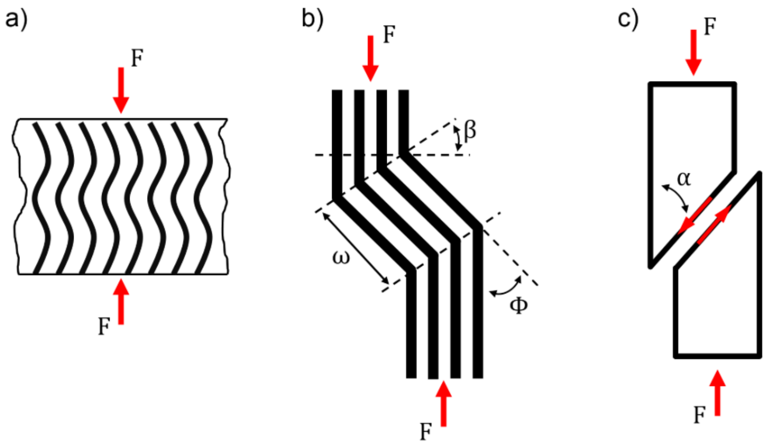

Figure 6.1. Three stages of damage contributing to the compressive failure of CFRP: (a) in-plane fibre micro-buckling (b) formation of kink-bands and their geometrical features (c) final failure, reproduced from [232].

Overall, shear instability is mainly influenced by geometrical imperfections such as fibre waviness and random fibre spacing [212] and highly dependent on the shear characteristics of the matrix material (*e.g.* the yield strength, shear stiffness).

In various studies [208], [209], [211], [218], [230], [235]–[237], it was found that the key factor influencing the UD compressive strength is the arising in-plane shear stresses which reduce the compressive performance significantly. These in-plane shear stresses are mostly induced by initial fibre misalignment or fibre waviness. An example of it is a study carried out by Wisnom [209] who looked at initial fibre misalignment effects on the compressive failure of XAS/914 carbon/epoxy even at very small angles as illustrated in Figure 6.2. It has to be noted that fibre waviness and misalignment are distinct defects in the material. Waviness represents a periodic (*e.g.* sinusoidal) mis-orientation of the fibres when compared to the neutral axis of the fibres in the x direction. On the contrary, misalignment is a mis-orientation of the fibre when compared to the neutral axis of the composite.

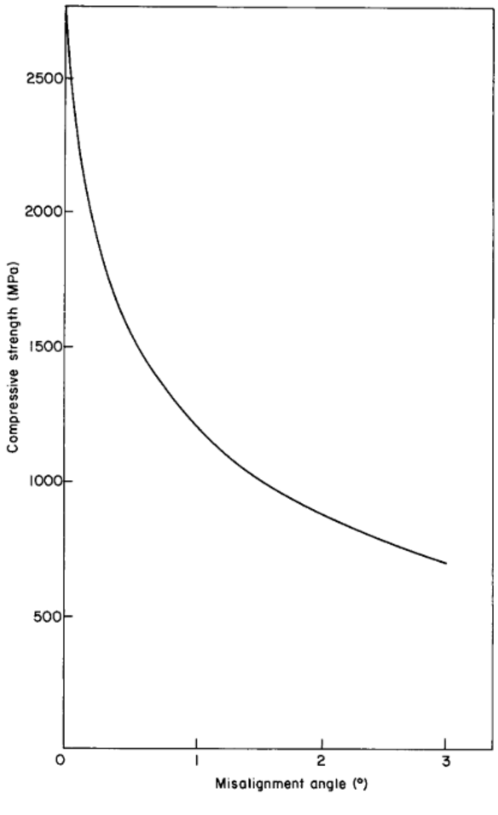

Figure 6.2. Predicted compressive strength as a function of the fibre misalignment angle of XAS/914 carbon/epoxy UD prepreg, reproduced from [209]

Most failure theories that predict the compressive strength usually consider fibre stability as the basis of their predictions. One of the earliest and most well-known models was published by Rosen [238]. Rosen's model is dependent on the fibre volume fraction of the composite where two different modes of micro-buckling were distinguished: an in-plane (shear mode) for higher volume fractions which leads to kink-band formation with increasing loads, and an out-of-plane micro-buckling (extension mode) for lower V_f materials. The shear mode usually predicts lower values for most composites and hence is considered as the critical compressive failure mode [225]. The model presents the compressive strength (σ_c) in the following form as seen in Equation (6.1):

$$\sigma_c = \frac{G_m}{1-V_f} \qquad (6.1)$$

,where G_m is the shear modulus of the matrix and V_f is the fibre volume fraction of the composite.

It is based on strain energy principles where fibres are modelled as perfectly straight beams (2D layered elastic model with rigid fibres) significantly overestimating the compressive strength of the material [209], [211] when compared to experimental measurements.

6.1.2. Compressive testing methods

With regard to determining the compressive strength of the UD material, there are various standards, methods and fixtures available in the literature. Standards usually define the ultimate compressive strength of the material with respect to the initiation of the kinking process. The main differences rely on the load introduction to the specimens and geometrical considerations.

The Illinois Institute of Technology Research Institute (IITRI) compression rig [239] introduces compression to tabbed specimens through shear loading at the trapezoidal wedge grip faces. The relevant standard for the utilization of such fixture can be found in the ASTM D3410/D3410M manual [240]. Alternatively, in other studies, - a rig designed by Haberle *et al.* [121] and also used by Soutis *et al.* [241] - compression is introduced by end loading using a modified (Imperial College of Science, Technology and Medicine) ICSTM fixture or otherwise called the ‘Imperial College Rig’ as illustrated in Figure 6.3. Currently, this is one of the most commonly used compression testing fixture that is supported by the ASTM D695-15 standard [242]. Additionally, a method was also developed for combined (shear and end) loading of compression specimens as defined by the ASTM D6641/D6641M standard [243], however it is less often used in compression testing.

Coupons for compressive testing are usually designed to be with relatively small gauge lengths (low slenderness ratio) to avoid overall buckling and preferably as thin as possible to reduce material costs. It is very difficult to achieve gauge section coupon failure especially because most measurements are hindered by stress concentrations. The premature failure of the specimens (usually still by fibre kinking) can result in a knock-down in their measured strength/strain values and high variability (coefficient of variation - C.O.V) of the results.

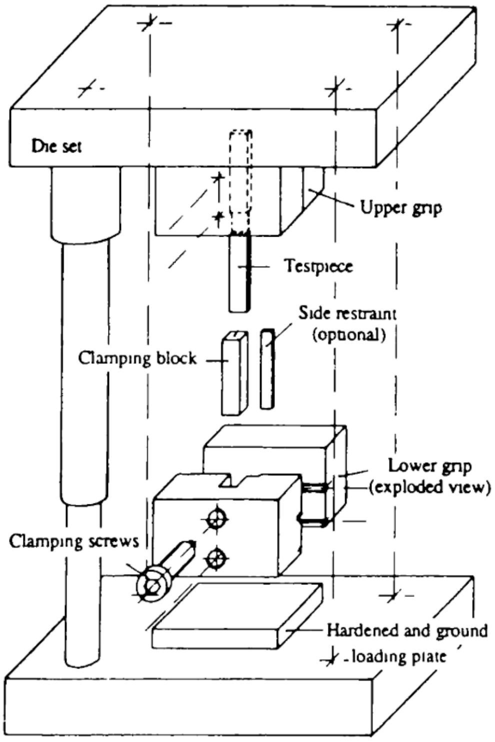

Figure 6.3. A schematic exploded view of the Imperial College compression testing fixture ICSTM, reproduced from [121]

6.1.3. Size effects

A strength reduction can be observed in the studies carried out by Lee and Soutis [241], [244], [245] who experimentally investigated the effects of specimen size on the axial compressive strength of T800/924C, IM7/8552 and T300/924C carbon/epoxy systems. In all cases a significant decrease in compressive strength was observed as the thickness and volume of the specimens increased as shown in Figure 6.4, reproduced from [245]. In Figure 6.4, even though the trend is quite similar for the two distinct materials: T800/924C and IM7/8552 on the left and right respectively, they differ in their scaling as the curve for T800/924C is thickness scaled and for IM7/8552 is volume scaled respectively. Hence, it can be postulated that the decrease in compressive strength is more influenced by the thickness of the specimens. The thicker the specimens, the larger the shear loads required to apply the desired compressive loading, which may lead to earlier failure and the effect shown below.

On the other hand, the reported variability of the measurements improved as a lower scattering can be seen for thicker laminates. In the study, stress concentrations were suggested to be the main cause of reduction in the compressive strength of the laminates. However, it was noted that for compression, the key factors in influencing size effects in UD composites were fibre waviness, void content and the increasing shear stresses with thicker specimens. Furthermore, for a comprehensive review on size (volume) effects and supporting experimental data with regard to the unnotched compressive strength of carbon and glass composite laminates, the reader is referred to a study presented by Wisnom [246].

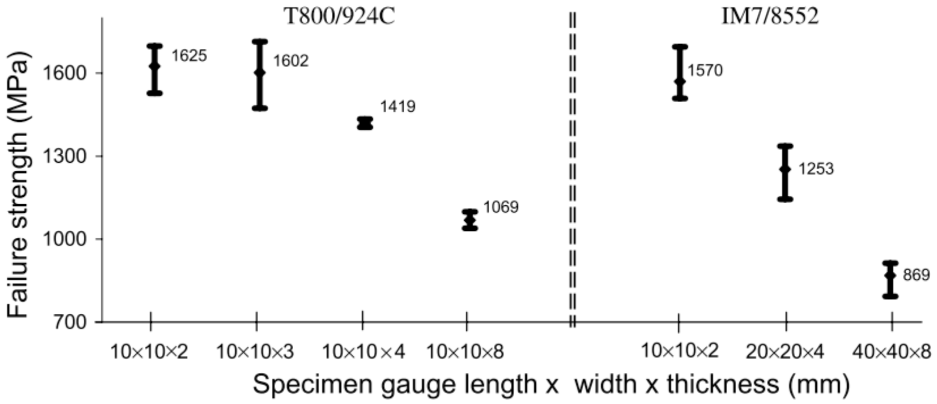

Figure 6.4. Average compressive strength of UD T800/924C and IM7/8552 carbon/epoxy composites with increasing specimen thickness and volume respectively, reproduced from [245].

6.1.4. Bending tests

As an alternative to conventional compression tests, bending tests have also been proposed as a means of measuring the UD compressive strength [247]–[250]. However, when identifying the fibre direction compressive strength using three- (3PB) and four-point bend (4PB) testing methods, premature failure of the specimens can often be observed due to the arising stress concentrations under the rollers.

Besides, for bending tests, the strain gradient effect through the thickness also has to be accounted for as it overestimates the measured compressive strength due to the constraint on instability from the adjacent less highly stressed material.

Also, a compression test fixture with pivots [251]–[253] was investigated as a way to determine the compressive strength of composite materials in bending. Bending loads are generated by the eccentricity of the device offsetting the mid-plane of the specimens. When large eccentricity is applied, it is equivalent to a quasi-pure bending test (4PB). This way, stress concentrations are avoided both at the grips and at the rollers due to the lack of contact. Damage and failure can be directly observed on the surface at the gauge section of the specimens. On the other hand, it requires non-linear finite element analysis (FEA) in order to determine the compressive strength of the material from test data although strain can be directly obtained.

6.1.5. Current study

Laurin *et al.* [206] developed a novel tensile test method which indirectly determines the longitudinal compressive strength of a 90° CFRP ply in an angle-ply laminate. The compression is put on the 90° fibres without any external loading through the Poisson contraction of the laminate when tested under uniaxial tension. However, in such a test, there are also transverse tensile stresses arising in the laminate hence creating a multi-axial stress state of longitudinal compression – transverse tension in the 90° layers. In Laurin’s study, it was assumed that such transverse tensile stresses do not affect the estimation of the longitudinal compressive strength. Considering thin-ply materials can further advance the investigation of the coupling between compressive failure and transverse stresses. Also, potentially due to the amount of transverse stresses generated, transverse cracks may appear in the laminate. To investigate this and possible ply thickness effects, this study aims to explore the design possibilities that can be achieved using such thin materials while determining the compressive strength by using the above mentioned non-conventional tensile test method under a multi-axial stress state of longitudinal compression and transverse tension.

6.2. Design and optimization

A Poisson effect can be observed when an angle-ply/90° laminate is put under uniaxial tension. This effect essentially induces indirect compressive loading on the 90° plies, potentially leading to their compressive failure. However, this compressive failure may be preceded by other damage mechanisms as illustrated in Figure 6.5, reproduced from Laurin *et al.* [206]. The macroscopic behaviour of a $[90/30_2/\text{-}30_2]_s$ laminate [16] predicted by the ONERA Progressive Failure Model (OPFM) [119] shows transverse cracking in both the 90° and ±30° plies prior to compressive failure.

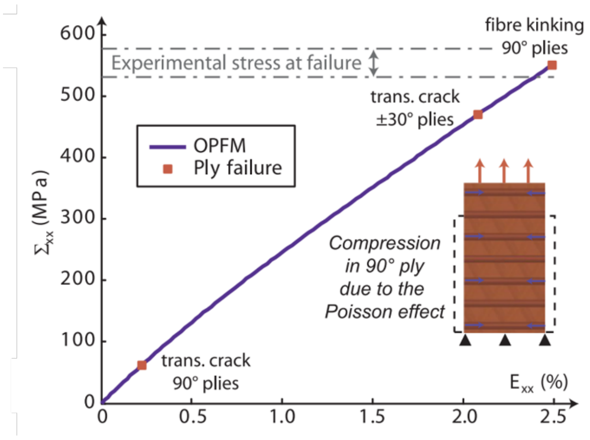

Figure 6.5. Macroscopic behaviour of a E-Glass/LY556 $[90/30_2/\text{-}30_2]_s$ laminate: the damage predicted by the OPFM model [119] under uniaxial tensile loading

Eyer [254] studied the interaction between matrix damage and the compressive strength of composites in the fibre direction. It was shown that matrix damage (transverse cracking) does significantly affect the UD compressive strength. Furthermore, when damage as such appears prior to final failure, the load is redistributed in a complex manner and it is difficult to determine the actual compressive strength of the material.

In the study by Laurin *et al.* [206], the ultimate compressive strength was determined without detecting any damage such as matrix cracks or delamination prior to final failure (fibre kinking in the 90° plies). The damage scenario was validated by using in-situ thermography, post failure X-Ray CT and fractography using SEM imaging.

6.2.1. Lay-up optimization

Initially, the design involved finding laminate solutions that comply with the lay-up structure of $[(\pm\theta_1)/(\pm\theta_2)/(\pm\theta_3)/(\pm\theta_4)\ldots/90_n]_s$ while satisfying the condition of exhibiting longitudinal fibre compressive failure in the 90° plies with no preceding in-plane damage. The lay-up shown above defines the possible design space as the stacking sequence does not influence the membrane properties of the designed laminates. To achieve such failure and the multi-axial stress-state in the UD (90°) layers, an advanced failure criterion (OPFM) developed by Laurin *et al.* [119] is considered (section 6.2.2).

The lay-up optimization to achieve a maximum amount of transverse tensile stress in the 90° plies was carried out using a design of experiments (DOE) in commercially available MATLAB software, as discussed in Section 6.2.3. A schematic illustration of a typical specimen and the proposed design concept is shown in Figure 6.6.

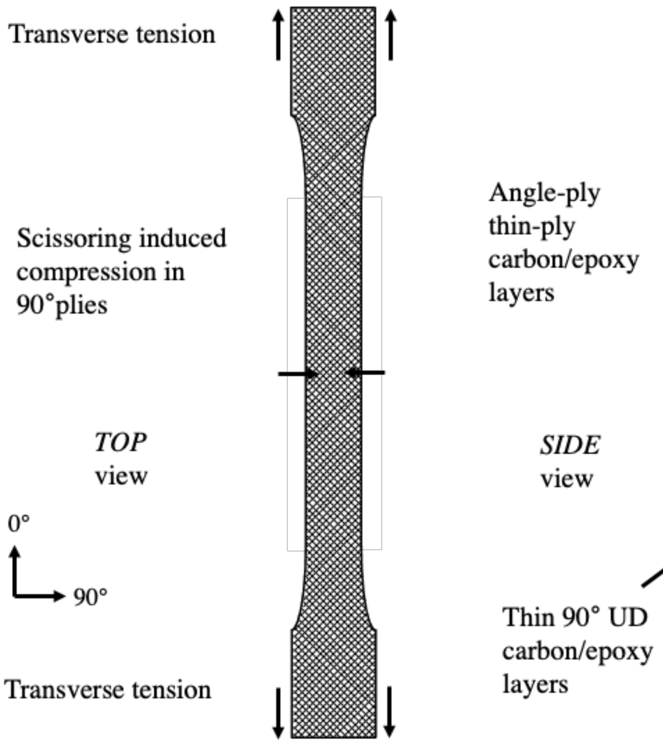

Figure 6.6. A schematic illustration of a typical specimen where the thin-ply central 90° UD block is embedded in thin-ply angle ply blocks of the same material. A combined stress state of longitudinal compression and transverse tension is induced in the central UD plies.

Additionally, there were other constraints applied throughout laminate design including some industrial laminate design guidelines [113] (so it can be more easily re-generated by industry and picked up as a test design) as per the following:

- Symmetry, balance, contiguity and disorientation ($\Delta\theta \leq 45°$ to limit delamination edge effect)
- Using ply orientations for the ±θ plies: $0° < \theta < 90°$ with a minimum increment of 15°: 15°, 30°, 45°, 60° or 75° only
- Only in-plane (membrane) loading is considered
- Lay-up configurations providing sufficient thickness due to the use of thin-ply material (TC33/K51 carbon/epoxy)
- Blocked angle plies have to be avoided due to the dependency of transverse tensile (Y_t) and shear strengths (S_e) on ply thickness

6.2.2. Laminate failure and the ONERA Progressive Failure Model (OPFM)

In multi-directional laminates, it is necessary to use failure multi criteria because often there is a competition between failure and damage modes. In the proposed laminate design, there are four possible modes of failure: (i) damage appearing in the 90° layers that can result in matrix failure by transverse tension or (ii) damage appearing in the $\pm\theta$ layers leading to matrix failure by a more complex stress state mainly due to shear, (iii) tensile fibre failure in $\pm\theta$ layers (for angles close to 0°) generated due to applied macroscopic tensile loading and (iv) 90° fibre failure in longitudinal compression. It has to be noted that the damage modes are highly dependent on the thickness of the laminate and the transverse tensile (Y_t) and shear strength (S_e) of the material. A limitation of the proposed approach consists in neglecting edge delamination which could appear, especially at the interface of $90°/\pm\theta$, depending on the considered stacking sequence. This point will be discussed later in section 6.3.3.

6.2.2.1. ONERA Progressive Failure Model (OPFM)

The failure criterion used in this study is a 2D multiscale progressive failure approach called the OPFM model [119] under plane stress hypotheses, made for describing the failure behaviour of laminates under multiaxial in-plane loadings. The extension of this model to 3D multiscale failure under triaxial loadings was also developed by Laurin *et al.* [255].

The key points include the viscoelastic behaviour of the matrix, the non-linear elasticity in the fibre direction of the utilized carbon prepreg, the influence of ply thickness (90° block thickness) on the transverse tensile (Y_t) and in-plane shear (S_e) strengths, an advanced failure criteria as well as the consideration of thermal residual stresses. In the following, a brief description will be given with regard to each point, however the reader is referred to the original study by Laurin *et al.* [119] for in depth interpretation.

The OPFM model predicts the ply-by-ply failure sequence of the laminate until final failure is reached. Final failure is described by a stress based, mesoscopic failure criterion which distinguishes between a fibre failure mode (FF) and an interfibre failure mode (IFF) in both tension and compression. This criterion is based on Hashin's assumptions, but it is further improved by taking into account the coupling between the shear strength and the transverse stresses (*i.e.* apparent strength enhancement for combined transverse compression and in-plane shear loading and strength decrease for combined transverse tension and in-plane shear loading. Furthermore, a degradation variable (coupling between the longitudinal tensile strength and degradation of the matrix) - d_f - is introduced to describe the degradation of interfibre strengths due to premature fibre failure occurring for high longitudinal stress levels.

Interfibre failure in this case is defined as the onset of transverse cracking. A good agreement was found between the predicted failure envelopes by OPFM and the experimental test data found in the literature as shown in Figure 6.7 reproduced from [119].

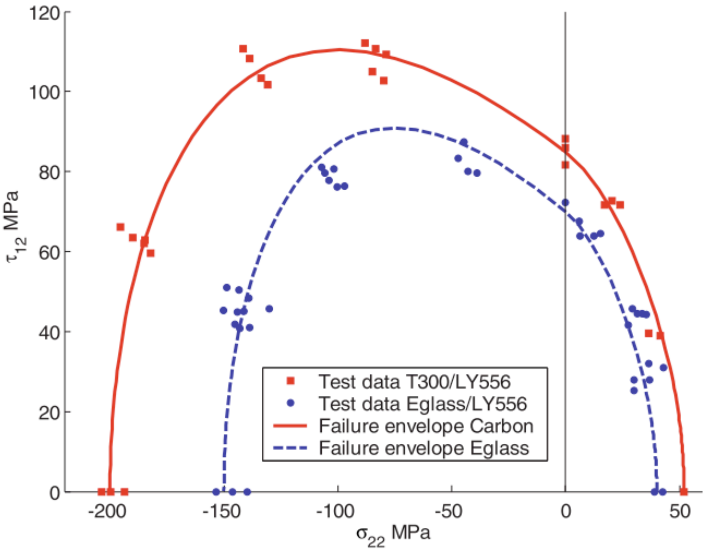

Figure 6.7. Failure envelopes of UD plies under a combined transverse and shear loading predicted by the OPFM criterion [119]

In the model, the ply behaviour is described by thermo-viscoelastic considerations. Thermal residual stresses may have a significant effect on the prediction of first ply failure hence they are accounted for in the model considering in a simple manner the introduction of the thermal strain and simulating the cooling and the end of the curing process. Additionally, the viscoelasticity of the matrix is introduced in order to describe the non-linearity observed on UD ply subjected to in-plane shear loading. It also allows for taking account of the effect of loading rate and to be able to describe creep and relaxation tests. The progressive degradation model is based on continuum damage theory and is thermo-dynamically consistent. Stiffness degradation is differentiated for fibre and interfibre failures. Also, the evolution of damage variables and the effect of failure on mesoscopic behaviour are treated separately.

6.2.2.2. Other considerations

In progressive damage analysis, the in-situ interfibre strength plays a crucial role in determining the onset of damage or predicting the first transverse crack in laminates [143]. The in-situ effect was first discovered by Parvizi *et al.* [150] who studied the failure of cross-ply glass fibre reinforced composites. Higher transverse tensile strengths were reported for the UD ply in a constrained state (surrounded by different fibre orientations) compared to the strength of the ply in an all UD laminate. Therefore, the in-situ strength depends on the layer thickness, the stiffness of the constraining plies, and the position of the ply under investigation in the laminate [143], [256]. The influence of layer thickness was investigated by various authors such as Wang [257] and Camanho *et al.* [258] who found that thinner plies exhibited higher in-situ transverse strength values. This layer thickness effect is demonstrated in Figure 6.8 (a) reproduced from [255]. The figure shows the apparent transverse tensile strength as a function of the ply or layer thickness. It can be stated that the onset of transverse cracking needs to fulfil two different criteria which are both necessary. The stress criterion relates to the initiation of transverse cracks whereas the energy criterion corresponds to the propagation of such micro scale damage through the thickness of the layer. This phenomenon and the in-situ interfibre strength is incorporated in the OPFM. The fitting parameters for the energy criterion (G_{Ic} and G_{IIc}) were adopted from the previous study by Laurin *et al.* [206] who have applied the model on different carbon/epoxy materials eg. IM7/8552 and AS4/3501-6 which the G_{Ic} and G_{IIc} values are known for. It has to be noted that the energy release rates are related to the threshold and evolution of transverse cracks.

Furthermore, the non-linear elastic behaviour of carbon fibre in the fibre direction is also taken into consideration by the model. A hardening in tension and softening in compression can be observed [259] which makes it an important parameter to consider when identifying the compressive strength of the UD material. This non-linear behaviour may be partly affected by the initial waviness of the fibres inside the composite materials. The behaviour is illustrated in Figure 6.8 (b) [260].

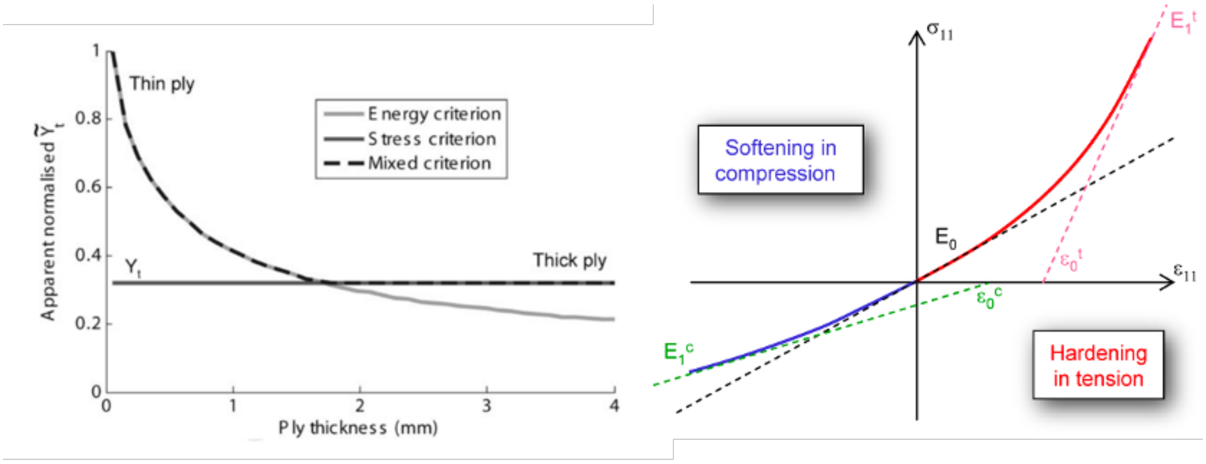

(a) (b)

Figure 6.8. Illustration of (a) the layer thickness effect on the apparent transverse tensile strength (Y_t) reproduced from [255] b) the fibre direction non-linear elastic behaviour of carbon fibre materials reproduced from [260]. Both curves are generated using the multiscale model in [255].

The parameters needed for material identification were determined from the basic material characterisation tests presented in Chapter 3. Parameters associated with non-linear elasticity such as E_{11}, ν_{12}, E_1^t (asymptotic Young modulus in tension) and ε_1^t (corresponding asymptotic strain in tension) were identified using the tensile tests carried out on the 0° laminate. Viscoelasticity parameters, including β_{22} and β_{66} coefficients, represent the viscoelastic material coefficients for transverse tension and in-plane shear tests respectively. If the β_{22} coefficient was zero, a linear elastic response would be obtained for the material in the transverse direction. They were determined, along with $E_{22}, G_{12},$ and γ, using the classical tensile tests carried out on the 90° laminate and the tensile tests on the ±45° laminate respectively.

The results of model identification on the TC33/K51 laminate are illustrated in Figure 6.9 (a) – (c). Non-linear behaviour can be observed in the 0° laminate that is subjected to tension as shown on Figure 6.9 (a). Additionally, the viscoelasticity of the matrix plays a major role on the behaviour of the ±45° laminate under tension as plotted on Figure 6.9 (c). Overall, it can be said that the behaviour of the material was captured well by the OPFM.

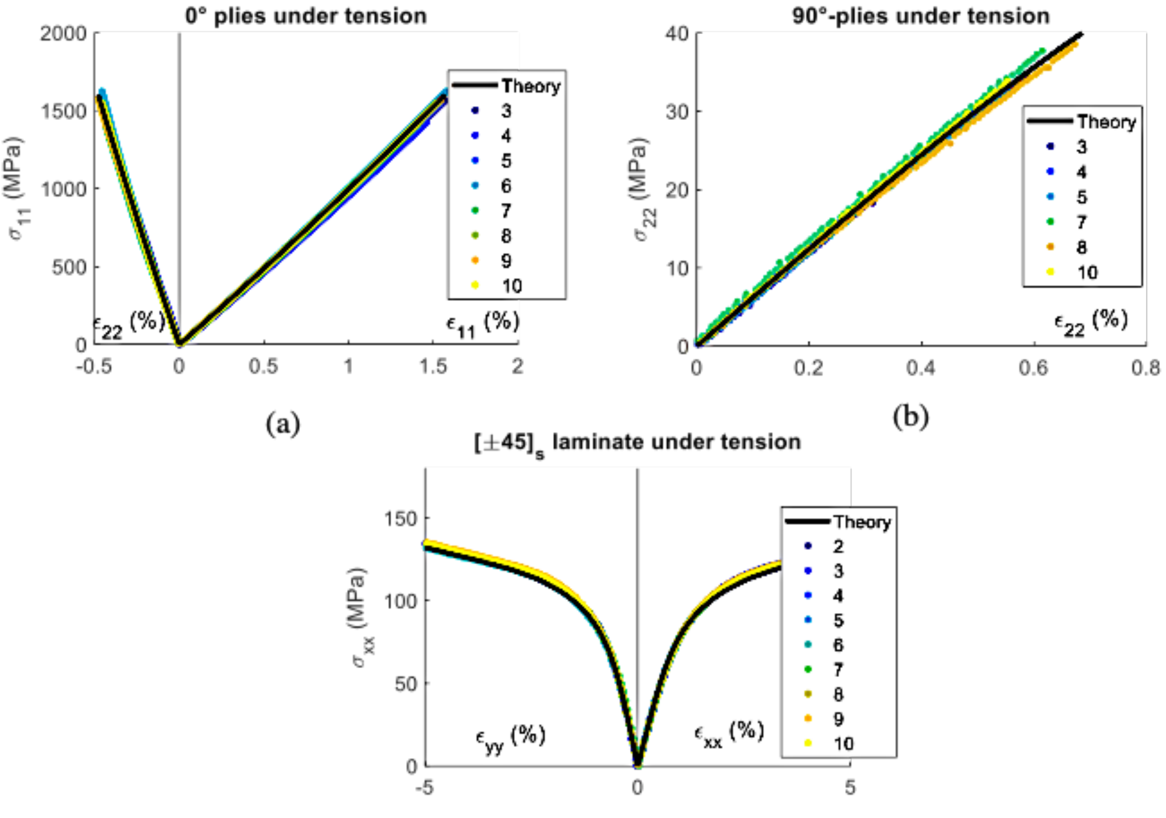

(a)

(b)

(c)

Figure 6.9. Results of model identification on the thin-ply TC33/K51 material: (a) 0° laminate under tension (b) 90° laminate under tension and (c) ±45° laminate under tension

The input parameters used in the MATLAB code for the OPFM model included ply orientations of the examined laminate, their ply thicknesses, the definition of material properties as well as defining the load case, both mechanical and thermal. The output parameters of the model include the incremental value of the generalised loads (N and M) and the midplane deformations and curvatures as well as the damage history for each ply in the order of occurrence. Additionally, the OPFM assumes that the transverse tensile stresses do not affect the longitudinal compressive strength of the material if no matrix cracks are generated prior failure. The assumption is underpinned by a study of Hütter *et al.* [261] who demonstrated experimentally on E-Glass/LY556 tubular specimens that the interaction between transverse stresses and longitudinal compression is not significant.

6.2.3. Design of Experiments (DOE)

In the design of composite structures, on the laminate scale, there are three design variables that can be changed to vary laminate properties: the number of plies, ply orientations and the stacking order. A DOE is used in order to explore the design space and find the configurations that can satisfy the set conditions.

One of the first constraints in such a design of experiments was to set the total number of plies to 28 which is consistent with other experimental studies carried out as part of this PhD. Also, a baseline of four 90° plies $(90_2)_s$ was used as the central block in the laminate similarly to previous test cases which eliminated hybrid effects in tension.

Using this baseline $[(\pm\theta_1)/(\pm\theta_2)/(\pm\theta_3)/(\pm\theta_4)/(\pm\theta_5)/(\pm\theta_6)//90_2]_s$ configuration, an initial optimization was carried out to investigate possible stacking sequences for:

- Achieving different amounts of transverse tensile stresses while,
- Ensuring that the desired failure mode is first ply failure by longitudinal compression in the 90° plies and,
- To investigate the effect on the failure mechanism by varying the thickness of the central 90° block

As a first estimate, linear elastic behaviour was assumed for the thin-ply TC33/K51 prepreg. Before enumerating the possible designs to evaluate their behaviour and first ply failure mode, the DOE was simplified as follows:

1. All laminates:
   for the $[(\pm\theta_1)/(\pm\theta_2)/(\pm\theta_3)/(\pm\theta_4)/(\pm\theta_5)/(\pm\theta_6)//90_2]_s$ configuration there are 12 plies to be defined → 12^{12} possibilities (with θ varying every 15°).
2. Balanced laminates only:
   e.g. $[(\pm\theta_1)/\ldots/(\pm\theta_6)/0/(\pm\theta_1)/\ldots/(\pm\theta_6)/90_2]_s$
   → 6^6 possibilities (0°, 15°, 30°, 45°, 60° or 75°)
3. Membrane only:
   for an in-plane loading and an uncoupled laminate (where B = 0), the OPFM model does not take into account the stacking order of the plies. Thus, it is sufficient to consider one representative laminate only for each group of laminates sharing the same membrane behaviour, *i.e.* same proportions of plies in each allowed orientation. Orthotropic membrane behaviour can be parametrized using only two non-dimensional parameters, the lamination parameters V_1^A and V_3^A, as defined below. Similar proportion membrane property laminates do not show on the design map: only one representative point is considered, reducing the number of possibilities to 381 points

These 381 candidate laminates were evaluated using the OPFM model. Figure 6.10 shows that all the configurations with predicted first ply failure (FPF) mode of longitudinal fibre compression are towards the bottom right hand corner of the design plot, illustrated by a 45° cut off in the figure. In the end, 51 configurations exhibit the desired failure mode.

The two lamination parameters are shown in Equation (6.2) and (6.3) defined by Tsai *et al.* [262]. Since symmetrical and balanced configurations are used, the membranes are orthotropic, and two parameters are enough to describe that.

$$V_1^A = \frac{1}{h}\sum_{k=1}^{n} h_k \cos(2\theta_k) \qquad (6.2)$$

$$V_3^A = \frac{1}{h}\sum_{k=1}^{n} h_k \cos(4\theta_k) \qquad (6.3)$$

where h represents the total thickness of the laminate, h_k and θ_k the thickness and the angle of the ply k respectively. n represents the total number of plies.

A sample output by the DOE analysis for the stacking sequences mentioned above is shown in Figure 6.10. It illustrates a plot of the design space with all the evaluated laminate configurations and their first ply failure mode (FPF) as defined by the DOE. Note that the laminates corresponding to the points in the figure are only defined in terms of number of plies per ply orientation.

The stacking order is constrained so that the laminates are symmetrical; otherwise it can be defined based on the usual strength-related laminate design guidelines and engineering judgement.

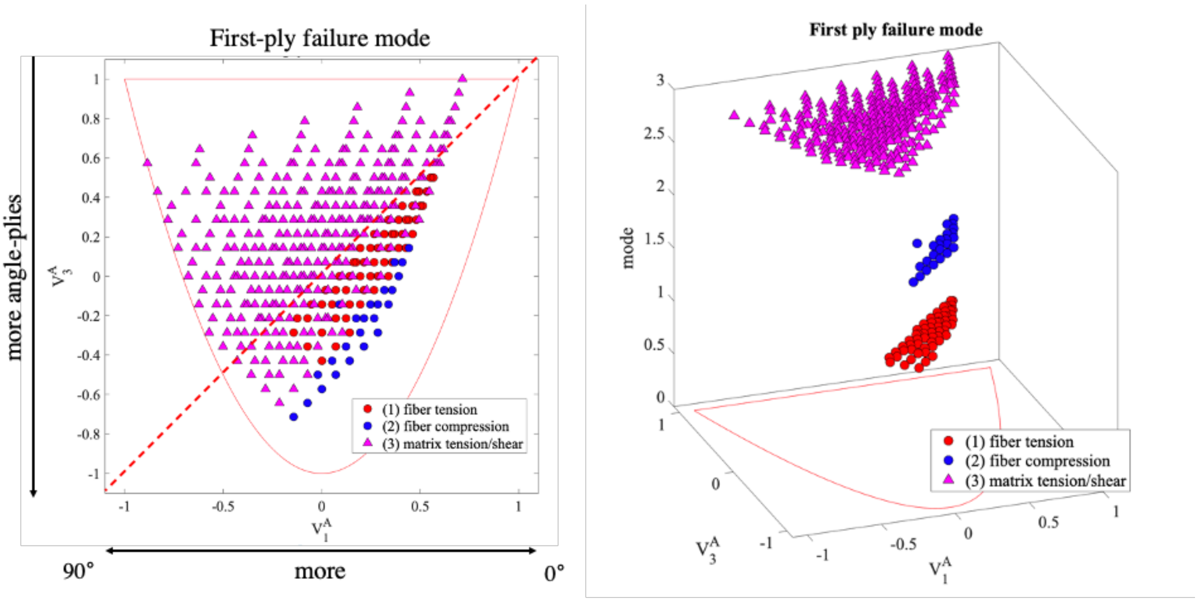

Figure 6.10. Generated laminates defined by the DOE and their respective first ply failure modes: (1) fibre tension, (2) fibre compression and (3) matrix tension/shear failure

The blue markers represent the laminates with a first ply failure mode of longitudinal compression in the central 90° layers which is the region of interest. The x and y axes represent the two lamination parameters respectively. As V_1^A changes from -1 to 1, the ratio of 90° to 0° plies is changing with 1 being fully 0° and -1 being a fully 90° laminate respectively. The same applies to V_3^A where 1 represents a laminate consisting of fully 0° and 90° plies whilst -1 represents a laminate of only angle plies (±45°).

Interestingly, if the optimized laminates are plotted by the orientation of their first failed ply, a point can be observed in the design space which is a laminate with a FPF of fibre compression in the 75° ply. This predicted failure is due to the presence of shear coupling in that particular laminate as seen in Figure 6.11 (a). Figure 6.11 (b) illustrates the predicted transverse stresses generated in the 90° layers at FPF. The transverse stresses range from 85 MPa to 115 MPa.

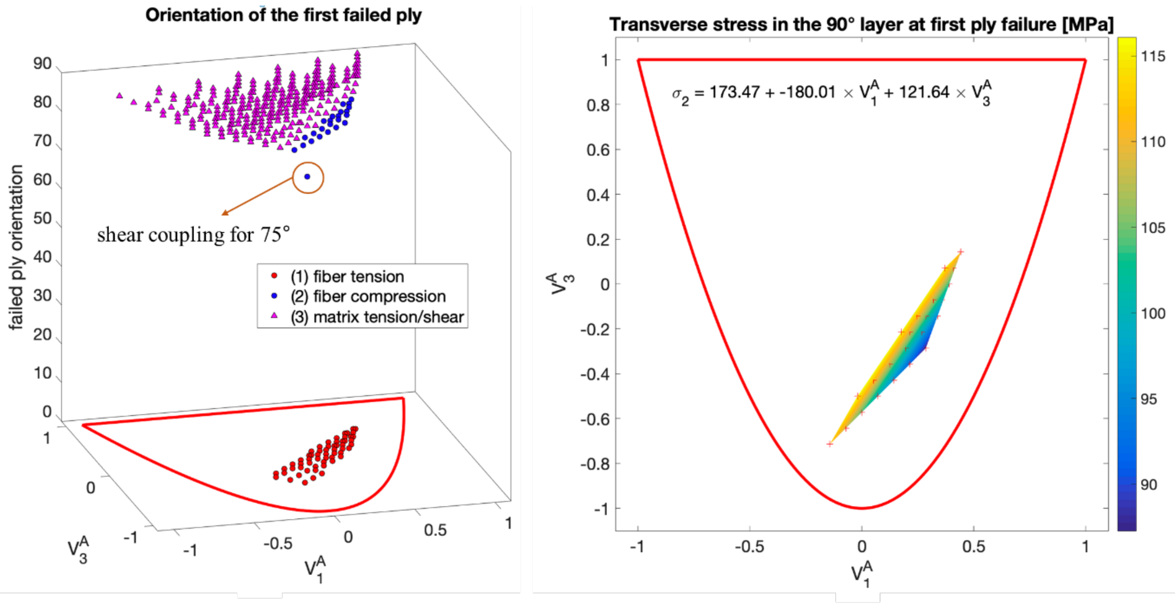

(a)

(b)

Figure 6.11. Generated laminates defined by the DOE and categorised by (a) the orientation of the first failed ply (b) the predicted transverse stress in the 90° layers at FPF.

The colour bar shows the range of predicted transverse stresses based on the equation presented in Figure 6.11 (b) using the V_1^A and V_3^A lamination parameters. Only the points on the two-dimensional (2D) design space plot which relate to laminates that are predicted to fail by longitudinal fibre compression are shown.

Further results and plots generated by the DOE and categorised by the orientation of the first ply, by the predicted longitudinal and transverse stresses in the central 90° block at FPF can be found in Appendix B.

Based on this preliminary analysis, 53 laminate configurations were found that satisfy the design requirements. A stacking sequence of $[(\pm45_6)/(90_2)]_s$ from the yellow region of Figure 6.8 (b) has been chosen mainly due to its ease of manufacturing, the simplicity of the lay-up as well as the high amount of transverse stress predicted in the laminate.

Due to the high amount of transverse stresses (111 MPa) predicted in the chosen laminate, the interaction between transverse stresses and compressive failure can be also investigated. A short study was also carried out using the OPFM to look at the effect of changing the central 90° block thickness on the predicted failure mechanisms of the laminates. The results are shown in Figure 6.12 where the $[(\pm45_6)/(90_n)]_s$ laminate configuration was investigated with a varying number of central 90° plies: n = 1,2,..16. It can be clearly seen that there is a shift in the predicted failure mechanism of the laminates: for very thin 90° UD blocks (n =1-4) the overall failure is longitudinal compression whilst for thicker central blocks (n=5-16) the final failure changed to matrix tension in the 90° plies or shear in the outer angle plies. The change in failure mechanism can be attributed to two effects. Firstly, a size effect where the transverse tensile strength of the 90-degree layer decreases as its thickness increases. It goes from an energy driven critical failure to a stress driven failure. Also, the overall stiffness of the laminate $(A_{(1,1)}/t)$ decreases when the proportion of 90-degree plies increases. Hence, the ratio of $\varepsilon_{22}/\varepsilon_{11}$ decreases (macro strains) resulting in a change in the elastic behaviour.

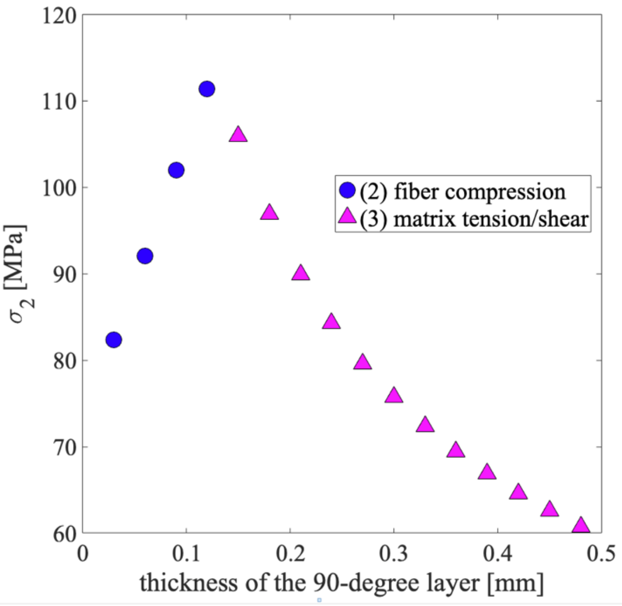

Figure 6.12. The effect of 90°-layer thickness on the first ply failure mechanism predicted by the OPFM and DOE analysis

6.2.4. Configurations

As the range of transverse stresses predicted for the $[(\pm 45_6)/(90_2)]_s$ configuration (see section 6.2.3) was not sufficiently varied to investigate the effect of transverse stresses on the longitudinal compressive failure, the emphasis of the study was shifted to look at the effect of changing the 90° layer thickness on the longitudinal compressive strength of the material.

To look at such thickness effects, the initial stiffness of the original laminate - $[(\pm 45_6)/(90_2)]_s$ -was kept and only the stacking order (dispersion of the 90° plies) was changed. By comparing such laminates with various 90°-layer thicknesses, thickness effects can be evaluated with the same total thickness for all the considered configurations. The stacking sequences defined for each *Type* of configuration can be seen below, as it will be referred to hereinafter:

- 90° layer thickness - 1 ply -: $[(\pm45)_4/\mathbf{90}/(\pm45)/\mathbf{90}/(\pm45)]_s$ – ***Type I.***
- 90° layer thickness - 2 plies -: $[(\pm45)_5/\mathbf{90_2}/(\pm45)]_s$ – ***Type II.***
- 90° layer thickness - 4 plies -: $[(\pm45_6)/(\mathbf{90_2})]_s$ – ***Type IV****.*

6.3. Experimental

This section describes the experimental campaign carried out including the manufacturing and test methods, the tensile test results with regard to the different specimen types, and the description of the failure and damage scenario based on experimental observations. The identification of the longitudinal compressive strength is discussed as well as further analysis of test data.

6.3.1. Specimen manufacturing, configuration and geometry

The manufacturing process utilized is similar to that used in previous studies: hand-lay-up of the thin-ply TC33/K51 material followed by autoclave curing of the laminates in a vacuum bag on a flat aluminium tool plate. The cure cycle utilized was 30 mins at 80°C and 90 mins at 125°C with 0.7 MPa applied pressure and a heat up and cool down rate of 2°C/min.

There were three plates manufactured in total: one laminate for each configuration Type I, II, and Type IV respectively. 8 Type I and Type II coupons were fabricated with only the dog-bone shaped geometry illustrated in Figure 6.6. However, for the Type IV configuration, two distinct geometry specimens were fabricated: 5 dog-bone shaped specimens with no end-tabs applied as seen in Figure 6.13 (a) and 5 conventional, straight sided coupons with woven, balanced glass fibre/epoxy end-tabs applied illustrated in Figure 6.13 (b).

This way, a comparison could be made between the two types of specimens with regard to the effect of stress concentrations during testing on the compressive strength. All dimensions in Figure 6.13 are in *mm*.

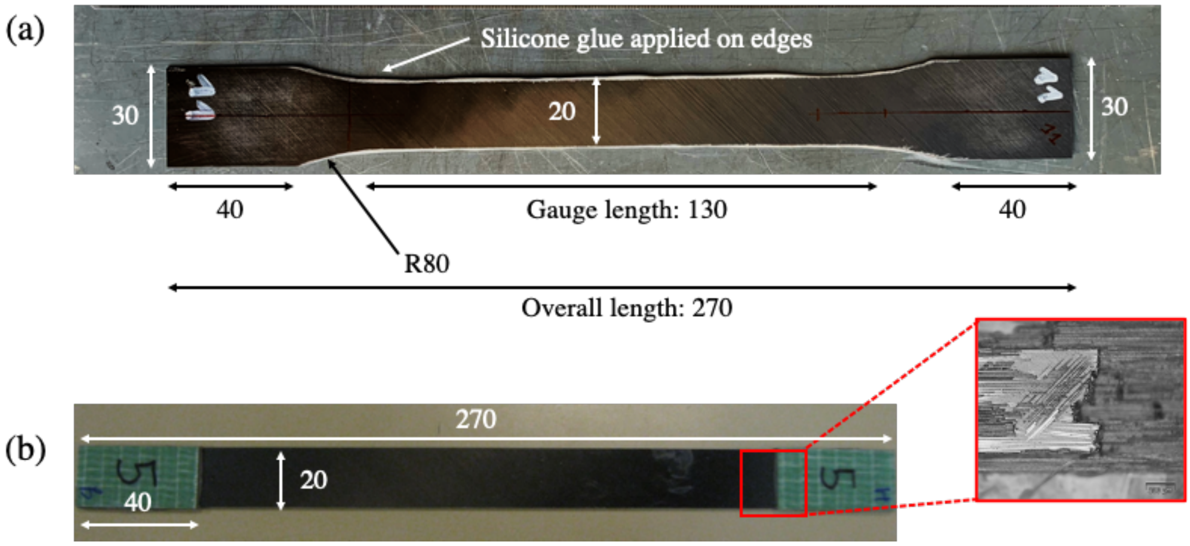

Figure 6.13. Illustration of geometry and dimensions for the fabricated coupons: (a) dog-bone shaped specimens treated with a thin silicon glue layer on the edges against delamination damage occurring during testing, (b) conventional tensile test specimens with glass/epoxy end-tabs applied to their ends showing failure.

Since the first dog-bone type specimen exhibited delamination across the width during testing, these coupons had a thin layer of transparent Araldite 2011 two-part epoxy adhesive system (Araldite 2011/A resin and Araldite 2011/B hardener respectively) applied to their edges similarly to Laurin's study [206] in order to suppress delamination damage occurring as shown in Figure 6.13 (a) and discussed in section 6.3.3. This is crucial in order to be able to determine the longitudinal compressive strength the most accurate way possible.

The straight sided, parallel edge specimens had nominal dimensions of 270/190/20/0.84 mm overall length/free length/width/thickness respectively. Due to the very low overall thickness of the laminates, the specimens were cut using a high-precision CNC controlled milling machine with high revolutions per minute (RPM) milling heads in order to avoid any machine induced damage in the composites. The gripping areas of the specimens were hand sanded in order to enhance surface roughness for either end-tabbing or to aid gripping during tensile testing. The end-tabs were applied to the straight sided coupons by an Araldite 2014 two-part epoxy adhesive system and cured in an atmospheric oven at 80°C for 2 hrs.

Also, since the parallel edge specimens failed prematurely due to the arising stress concentrations from gripping, those measurements and results were discarded from further interpretation. These specimens exhibited two times larger scatter and 8% lower stress at failure due to failure initiating from the tab areas thought to be because of local combined shear and compression as illustrated on the micrograph in Figure 6.13 (b).

6.3.2. Measurement methods

The tensile tests were carried out using an electromechanical Zwick test machine with a maximum load capacity of 10 kN and an Instron servo-hydraulic machine with a maximum load capacity of 100 kN. All tests were carried out under displacement control, and for the specimens tested with the servo-hydraulic machine, a low gripping pressure and a loading rate of 0.2 mm/min.

Additionally, to record displacements Linear Variable Differential Transformer (LVDT) sensors have been used during testing. Two acoustic emission (AE) sensors were placed on the back face of the specimens in order to detect any localised damage events that might occur. The threshold value set for the AE sensors were 40 dB in order to avoid any machine related noises.

For strain measurement, a Digital Image Correlation (DIC) system has been used, with two 12 bit cameras having a resolution of 2000 x 2000 pixels. Using the gathered data, virtual strain gauges determined the in-plane strains on the specimen surfaces. The experimental set-up and the data-acquisition systems and test machines are illustrated in Figure 6.14 (a) and (b). Through a convergence study, it was found that varying the grid size for the virtual gauge had a negligible effect on the average strain values extracted, hence a 10 x 10 mm grid size was used throughout the measurements. The DIC data was processed in the commercially available software Vic3D$^{©}$. All the specimen surfaces were black and white speckled to aid the DIC measurements as shown in Figure 6.14 (a) and (b).

Besides, for damage evaluation as well as for the examination of specimens after interrupted tests, C-scan ultrasonic non-destructive testing (NDT) method has been utilized. C-scan is the image produced when the NDT data plotted on a plan view of the specimens. Scanning Electron Microscope (SEM) images were also taken to assess the final failure mode of the specimens with high resolution.

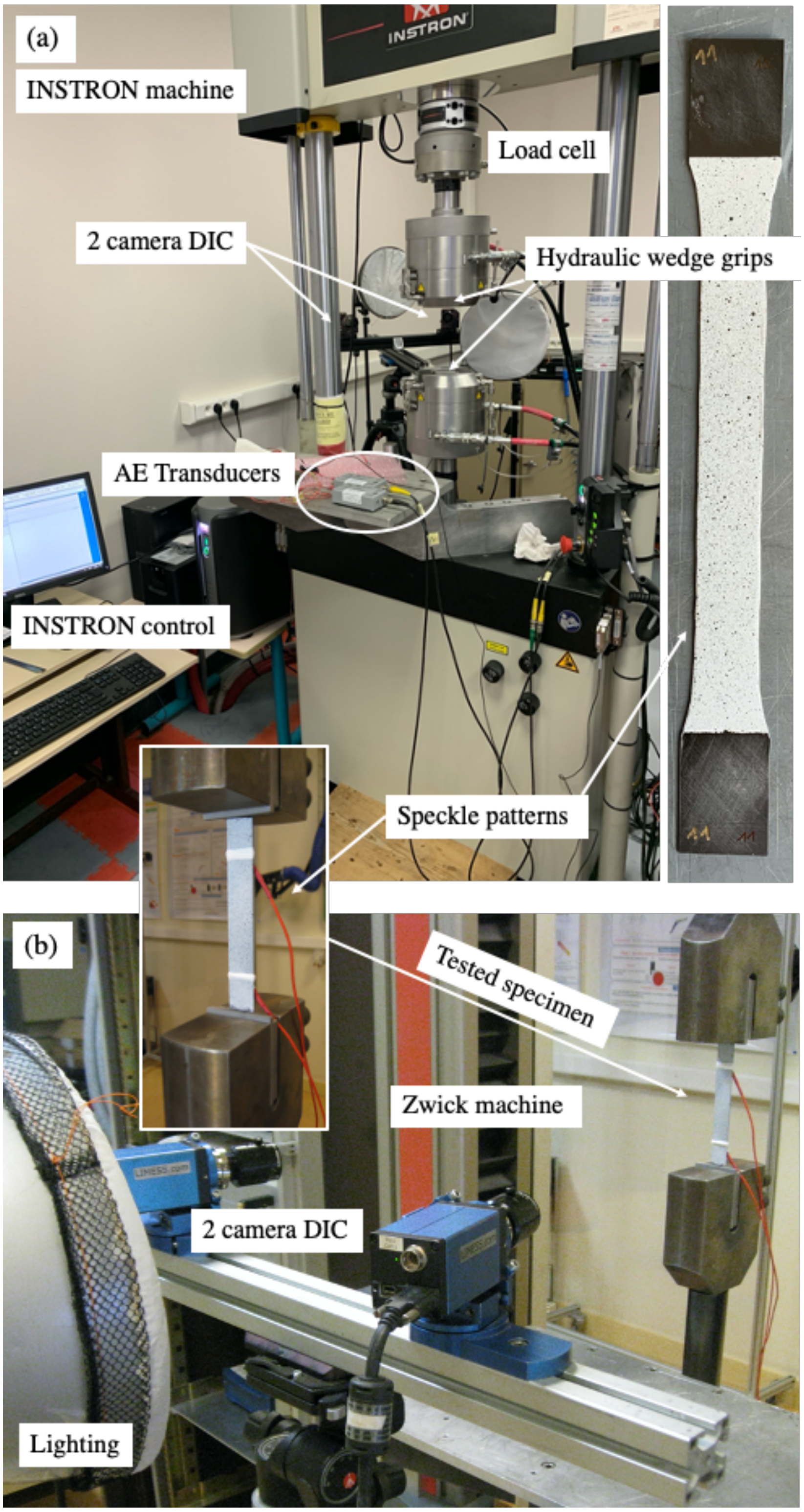

Figure 6.14. Test set-up and data acquisition systems for tensile testing of the specimens: (a) Instron servo-hydraulic mechanical testing machine and (b) Zwick electro-mechanical testing machine (ONERA, Composite Materials and Structures department, Châtillon, France).

6.3.3. Tensile test results

6.3.3.1. Free-edge delamination

As mentioned before in section 6.3.1, it was necessary to apply glue at the edges of the thin-ply specimens. One dog-bone shaped (shoulder ended) coupon (specimen 6, Type IV) was tested without glue and delamination progressed across the whole width, which was also detected by the AE measurements. The load-time response of this particular specimen with the AE data and the damage occurred is shown in Figure 6.15 (a). Figure 6.15 (b) exhibits the stress-strain response of the tested Type IV specimens, where delamination appearing in specimen 6 can be clearly seen from the deviation of the stress/strain curve. Free-edge delamination took place at the 45°/90° interface and is shown by the processed C-scan image in Figure 6.15 (c). There is a 13% drop in the failure stress when compared to the specimens without delamination damage. Furthermore, the measured strain at failure does not accurately represent the compressive failure strain of the 90° plies either. Consequently, glue was applied to the edges of all other specimens tested. It has to be noted, that the glue was only added to avoid edge effects and the mechanical properties of the glue had no influence on the obtained results.

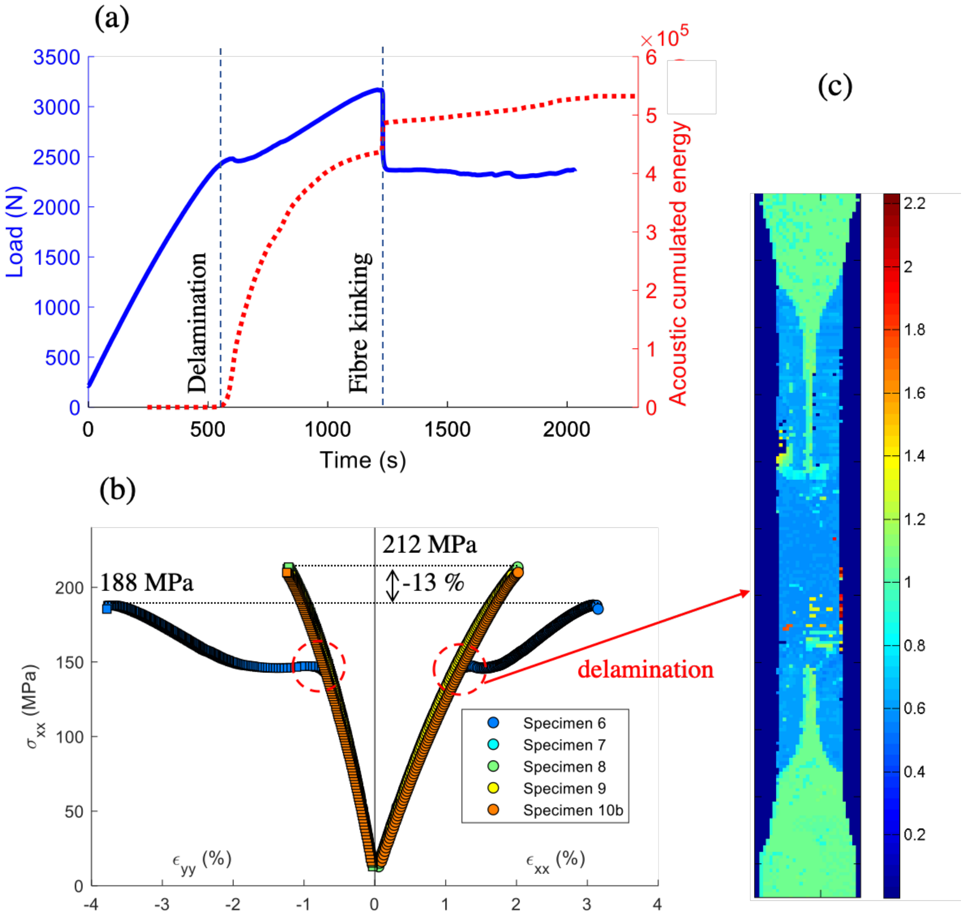

Figure 6.15. The (a) load-time response of the Type IV specimen which did not have glue applied at its edges and delaminated extensively (b) stress-strain curves of the tested Type IV specimens (c) NDT image of the delaminated Type IV specimen.

6.3.3.2. Macroscopic behaviour

The measured macroscopic stress-strain responses of Type I, Type II and Type IV specimens are illustrated in Figure 6.16 (a)-(c) respectively. All figures include an additional black curve which represents the predictions performed by the OPFM. It can be stated that the OPFM predictions captured the macroscopic behaviour of the specimens within 5% accuracy. In all cases, the stress-strain responses in both the longitudinal and transverse direction are slightly non-linear up to failure.

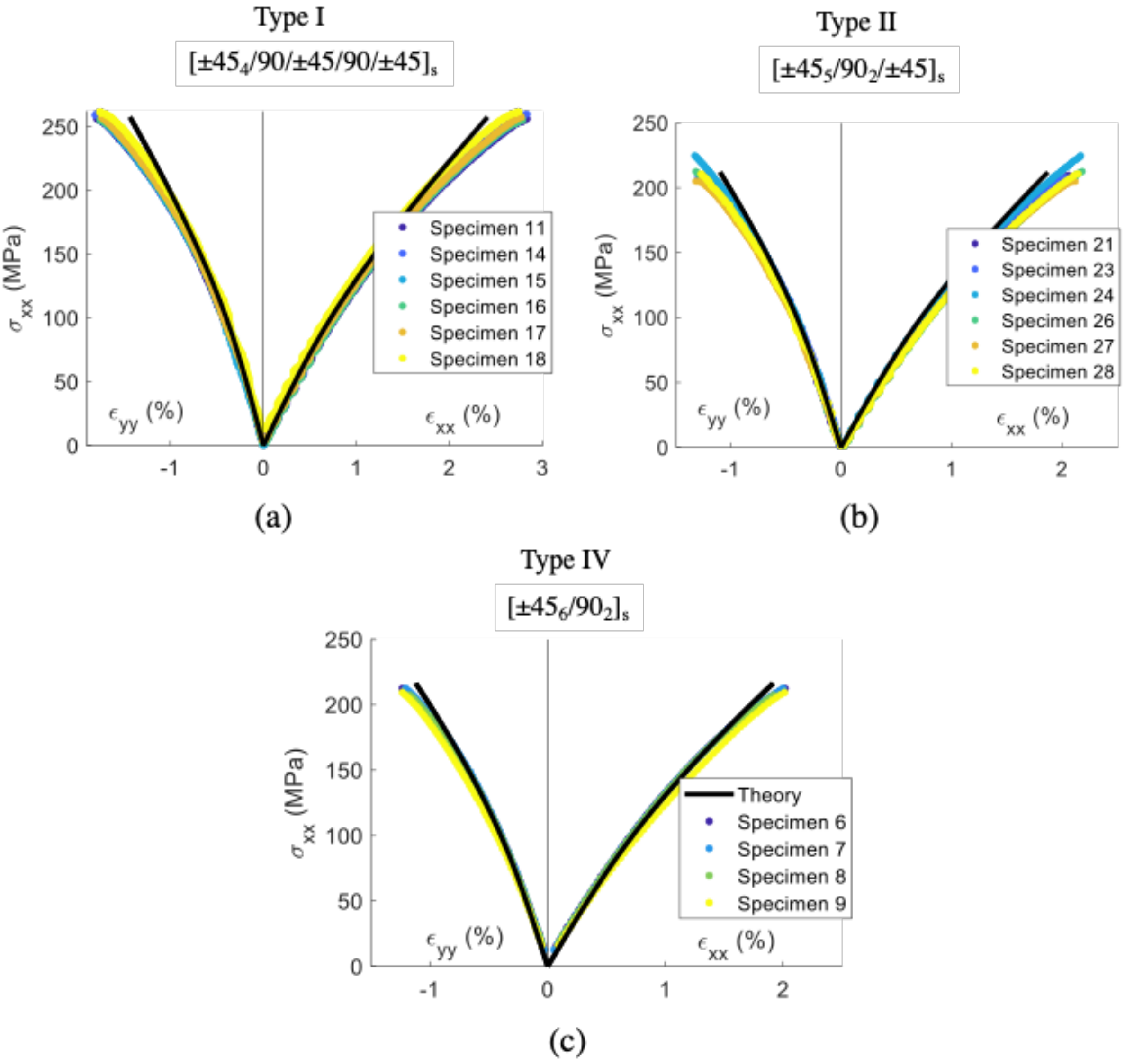

(a) (b) (c)

Figure 6.16. The macroscopic stress-strain response of (a) Type I (b) Type II and (c) Type IV specimens compared with the predictions by the OPFM model (theory curve)

The reason for that is the in-plane shear stresses generated in the ±45° plies resulting in the non-linear behaviour of the matrix, as captured in the OPFM model. A summary table including the measured longitudinal and transverse strains at failure using the virtual strain gauge, the measured average macroscopic stresses and the estimated longitudinal compressive stress in the 90° plies identified with the OPFM model can be seen in Table 6.1. Furthermore, an illustration of the virtual strain gauge grid and the mapped surface strains of a Type IV specimen are illustrated in Figure 6.17.

Table 6.1. Summary table of the experimental results for Type I, Type II and Type IV configurations

Configuration	Measured longitudinal strain at failure ε_{xx} [%] (CoV%)	Measured transverse strain at failure ε_{11}- 90° plies [%] (CoV%)	Macroscopic stress σ_{xx} – laminate at failure [MPa] (CoV%)	Compressive stress σ_{11} – 90° plies at failure [MPa] (CoV%)
Type I	2.79 (1.7)	-1.77 (1.4)	257 (1.1)	-1238 (1.4)
Type II	2.13 (2.2)	-1.31 (2.6)	212 (2.9)	-962 (3.9)
Type IV	2.02 (3.3)	-1.21 (2.2)	212 (1.8)	-964 (2.1)

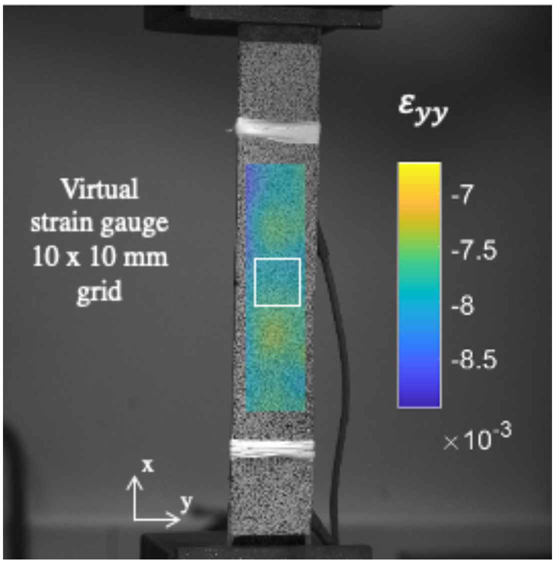

Figure 6.17. Illustration of the virtual strain gauge area and the mapped surface strains of a Type IV specimen at an earlier stage during the loading process

The macroscopic stress of the laminate σ_{xx} is calculated by dividing the load output of the machine by the measured gauge section area (width · thickness) of the specimens. Then, the compressive stress at failure in the 90° plies σ_{11} can be calculated from the OPFM model. The ultimate compressive strength (X_c) is then identified as the longitudinal compressive stress at failure in the 90° plies. Besides, the longitudinal compressive strain at failure is directly extracted from the tests as it is equivalent to the transverse strain measured: $\varepsilon_{yy} = \varepsilon_{11}$.

The introduction of the glue on the edges of the specimens allowed for avoiding free-edge deamination and thus validated the proposed analysis framework. It can be stated that for the experimental measurements there is low scatter on both the failure strains and stresses. A factor that contributes to this is the reduction of stress concentrations at the jaw faces due to the dog-bone shape of the specimens as well as due to the specimens being indirectly loaded through the Poisson's effect of the laminate. Consequently, all specimens exhibited consistent gauge section failures.

6.3.4. Failure, damage scenario and analysis

There were three different kinds of damage analysis tools used in this study. In-situ AE measurements have been carried out mainly in order to monitor any damage occurring during testing, prior to failure. Additionally, interrupted tests have been carried out to investigate any damage (delamination or matrix cracking) at load levels close to failure. Post failure, optical microscopy and SEM imaging were used to highlight the damage state of the specimens and to confirm their failure mode.

6.3.4.1. AE measurements

Figure 6.18 illustrates the load-time curves of different type specimens with the cumulative energy of the detected AE events plotted on the graphs. Type I and Type II specimens show a similar behaviour: there is no sign of significant acoustic activity prior to the first load drop. For the Type II specimen, as it can be seen on Figure 6.18 (b), there is a rise in the cumulative energy just before the maximum load, but it is most probably due to machine related noises. Figure 6.18 (c) shows no AE events prior to final failure despite the Type IV configuration having the thickest 90° block in the laminate which is the most likely to exhibit any micro-cracking damage out of all types. The first load drop on all curves represents the compressive failure (fibre kinking) of the 90° plies.

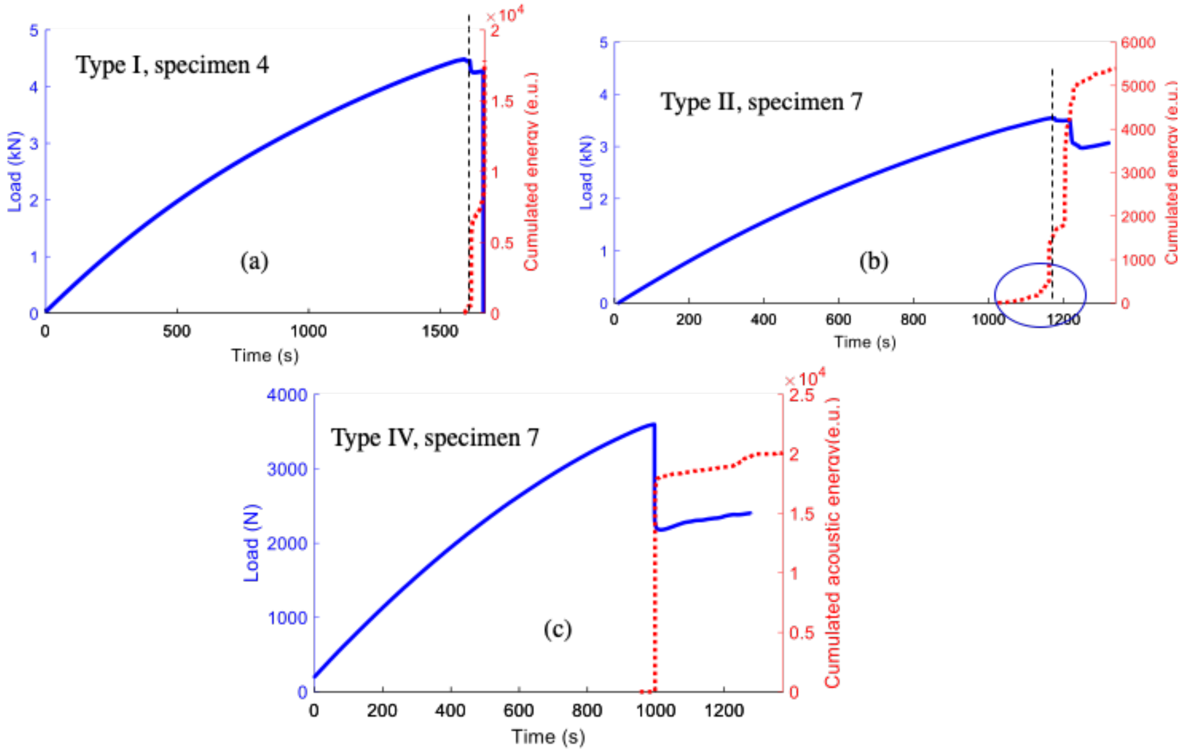

Figure 6.18. Illustration of the AE events detected during testing of (a) Type I (b) Type II (c) Type IV specimen. The cumulative AE energy is plotted on the load-time curves of the coupons.

6.3.4.2 Analysis of the final failure mode

Since the Type IV specimens are the most likely to exhibit matrix cracks out of all configurations, an in-depth failure pattern analysis was carried out. The outer ±45° plies of some coupons were removed (polished off) in order to observe the central 90° plies and the failure pattern. Images taken with optical microscopy observation of the central 90° block are shown in Figure 6.19 (a). A fairly traditional compressive failure with fibre micro-buckling occurring can be seen which is also consistent with the angled fracture surfaces as seen on the close-up images. A gauge section compressive failure can be observed with kink-bands forming in the mid-width and gauge section of the specimen which is normally very hard to achieve. Higher resolution images taken by optical microscopy of the investigated coupon can be found in Appendix B.

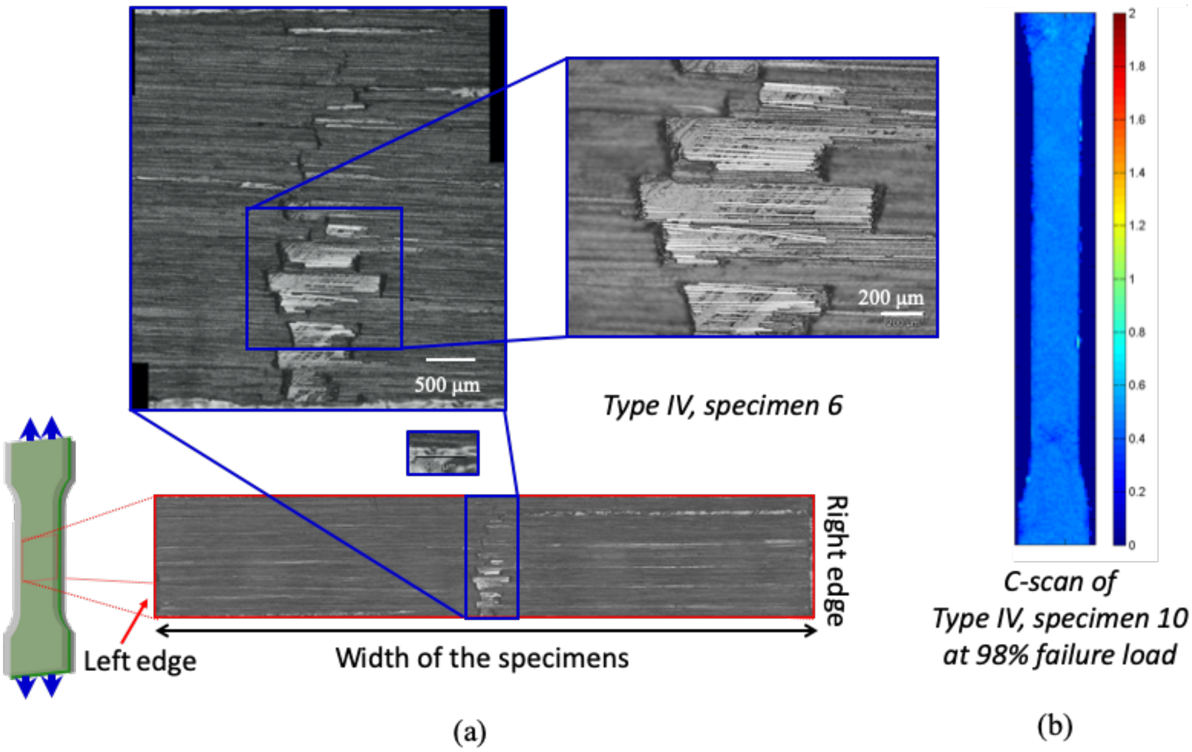

Figure 6.19. Illustration of the failure pattern investigation for the Type IV specimens: (a) optical microscopy observations showing kink-band formation and micro-buckling of the 90° fibres (b) C-scan results of a different specimen showing no signs of delamination and transverse cracking.

Additionally, an interrupted specimen of the same type (Type IV, specimen 10) was stopped at 98% of the failure load in order to examine it with a C-scan analysis. The results of the imaging are seen in Figure 6.19 (b): there is no evidence of any delamination or transverse cracking damage present. The high load level achieved with the interrupted test (close to failure) is a result of the low scatter of the test data (1.8%) for this configuration.

Furthermore, SEM analysis was also carried out in order to further investigate the failure pattern of these specimens. A summary of the high-resolution images can be seen in Figure 6.20. This figure exhibits a mapping of the damage present in the coupon. Certain areas are highlighted on the lowest magnification (25x) image in the top left and investigated further with higher magnifications even up to 450x which corresponds to the fibre microscale.

Higher resolution image examples of this coupon with 25x and 450x magnification can be found in Appendix B.

There is a clear pattern of transverse cracks throughout the specimen with a spacing of about 200 μm as shown with the red marker circles. However, within these cracked regions, there is clear evidence of fibre micro-buckling (as shown on the magnified images) which raises the question as to what occurred first: transverse matrix cracking or fibre micro-buckling in the 90° plies. Unfortunately, due to the difficulty of determining this experimentally a clear conclusion cannot be drawn.

It can be postulated that, based on the measured longitudinal failure strains for the Type IV specimens (2.02 %) compared to the measurements of the cross-ply study presented in the previous Chapter, transverse matrix cracking would be expected in the central 90° layers.

In Chapter 5, the Type 4 configuration with a block of 8 90° plies adjacent to the central 0° UD layers exhibited full width transverse cracks at an average longitudinal strain of 0.95% (initiation point of high energy AE signals). Using simple fracture mechanics scaling ($\sqrt{2}$ multiplication), the longitudinal strain at first crack for the Type 3 configuration (with 4 90° plies adjacent to the central UD) can be estimated. It yields an approximate longitudinal strain of 1.34% which is far less than the measured 2.02 % for the Type IV specimens in this study. Following the same argument suggests that Type II specimens may have had transverse cracks (estimated longitudinal strain of 1.90% at first crack, compared with measured maximum strain of 2.13 %) but not Type I specimens (estimated at 2.69 % compared with 2.79 %) which is consistent with the strength results shown in Figure 6.21 (b).

Overall, based on the arguments above, it may be stated that transverse cracks probably preceded fibre micro-buckling in the 90° plies in Type II and Type IV specimens but probably not in Type I specimens.

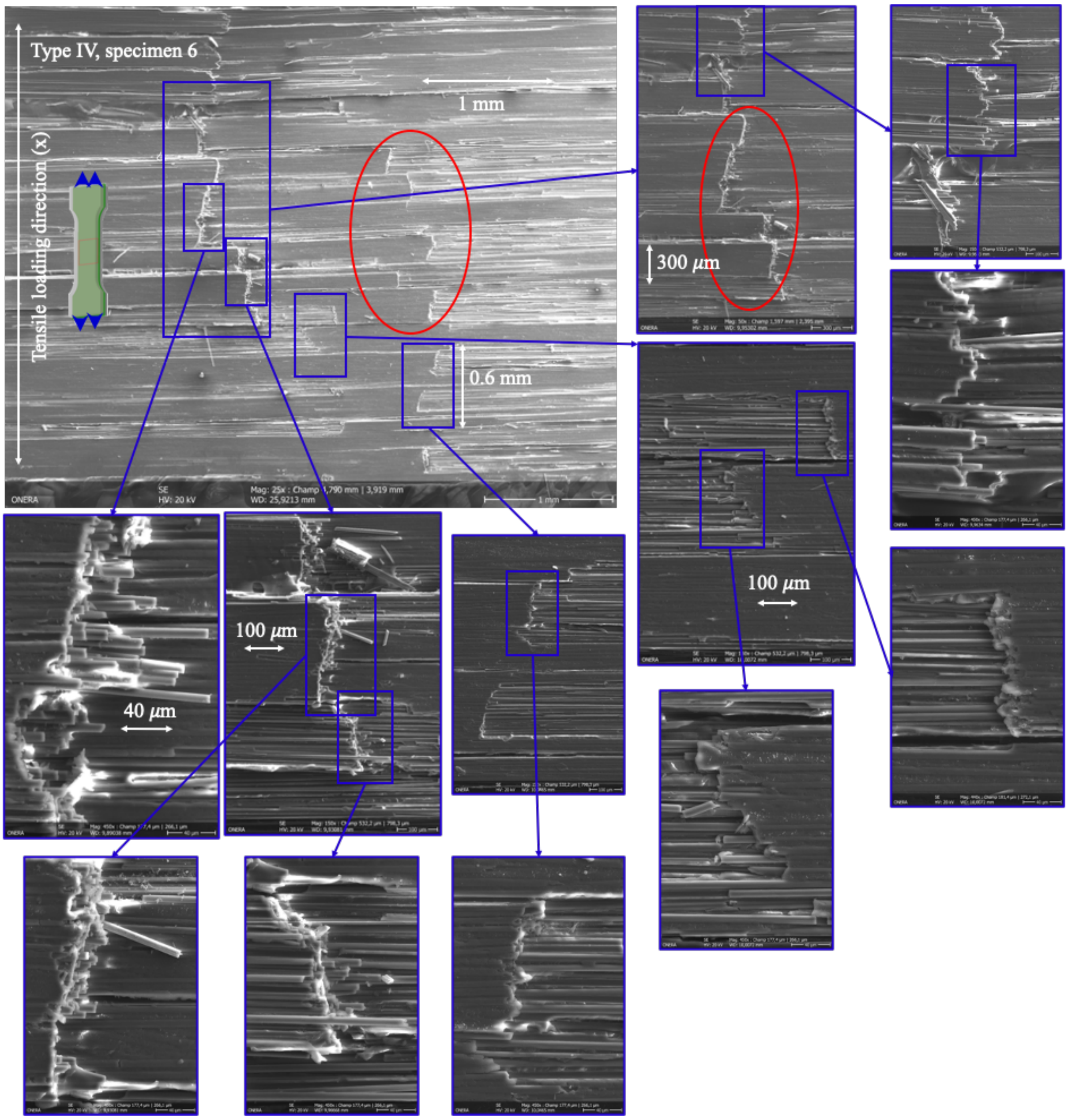

Figure 6.20. SEM damage map of a Type IV specimen highlighting the damage present in the central 90° plies. The largest image is taken with the lowest resolution of 25x magnification, whereas the smaller images are at a magnification of 450x.

6.3.5. Discussion

Figure 6.21 (a) summarizes the experimental results of all three types of specimens, where the measured longitudinal and transverse strains are plotted as a function of the macroscopic stress in the longitudinal direction. All configurations exhibited a similar, slightly non-linear behaviour up to final failure. Figure 6.21 (b) illustrates the dependence of 90°-layer thickness (number of 90° plies) on the determined compressive strength of the material.

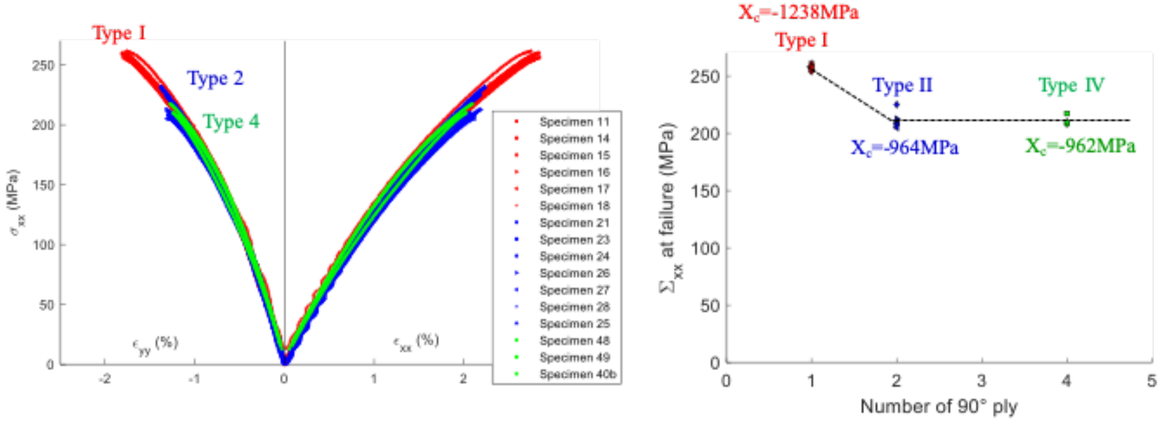

(a) (b)

Figure 6.21. (a) Summary stress-strain results of the experimental measurements for all three specimen configurations (b) Illustration of the 90°-layer thickness dependence of the determined compressive strength.

As can be seen in Figure 6.21 (b), there is a decrease in the compressive strength as the number of 90° plies increases. Type II and Type IV specimens exhibit a similar compressive strength of about -963 MPa whilst for the Type I specimens it is 23% higher (-1238 MPa). As an approximate comparison due to the lack of data in literature, a generic baseline compressive strength value of -1250 MPa is taken from a review by Galos [130] on thin-ply composite materials [130]. This indicative baseline strength is similar to the compressive strength values exhibited by the Type I specimens, presuming no transverse cracks in the coupons. The type of the designated fibre is unknown, but it is manufactured by North Thin Ply Technology (NTPT) who works with similarly high-modulus fibre composites such as TC33/K51.

Furthermore, a compressive failure strain of 1.36 % was found by Xun Wu in limited tests at Bristol University [263] using the same TC33/K51 carbon /epoxy material in the compression side of a sandwich beam configuration with a 40 mm wood core and 0.5 mm compression skin. Only two specimens were tested, and the beams exhibited roller failure, so not too much weight can be placed on the result. Further tests were planned but could not be carried out.

Using a linear approximation, the estimated compressive stress at failure can be calculated from the value mentioned above by multiplying the acquired strain with the elastic modulus of the composite: -0.0136 [-] · 95300 [MPa] = -1296 MPa. This -1296 MPa estimate is consistent with the obtained data in this Chapter.

The reason for the difference in compressive strengths and the compressive strains to failure (as seen in Table 6.1) of different Type of specimens could be attributed to two distinct effects.

One of them is a constraint or ply thickness effect as the support changes around the 90° fibres. This is important because the compressive failure mechanism is instability controlled, and as the 90° plies get more dispersed within the laminate, their support from the ±45° plies changes. An explanation to that could be that as the 90° fibres microbuckle, the parameter affecting their support is the distance between the 90° plies and the ±45° plies.

This thickness effect is also shown by modelling carried out by Drapier *et al.* [224], [264] who studied the influence of structural parameters on the compressive failure strain and strength of UD carbon composites. Their models took the influence of matrix plasticity and initial fibre waviness into account and ply meso-structural considerations such as ply thickness, boundary conditions and loading type were also considered. One or both surfaces of the specimen were assumed clamped.

A figure illustrating the predictions by their model is shown in Figure 6.22, reproduced from [224]. The maximum strain to failure is plotted as a function of the UD ply thickness which shows similar trends to the curve that has been experimentally achieved in this study (Figure 6.21 (b)). In their simulation, a plateau can be observed for higher ply thicknesses whereas for thin-plies an increase in the longitudinal strain to failure is shown. It is due to fibre kinking and compressive failure being mainly a buckling problem at the fibre scale.

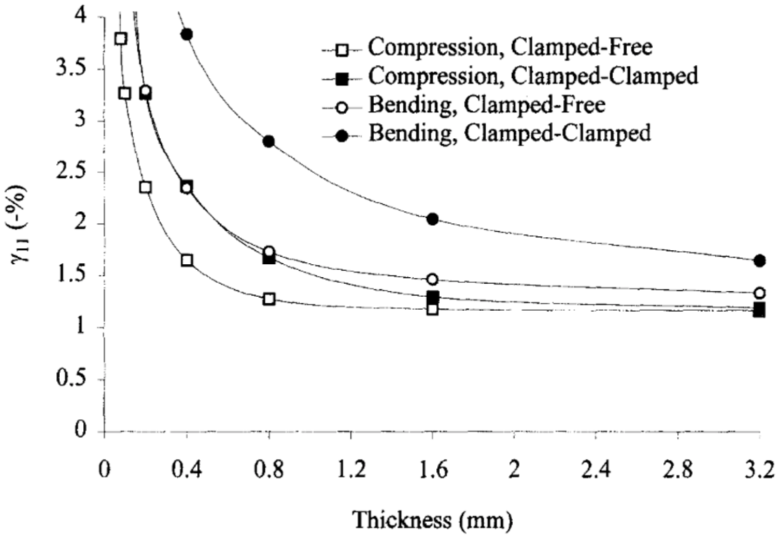

Figure 6.22. Thickness dependence of the longitudinal compressive failure strain, as predicted by Drapier *et al.*, reproduced from [224]

The other effect is that the support also changes around the 90° fibres as transverse cracks start to appear within the 90° block, hence affecting the compressive strength of the ply. Transverse cracks appearing in the Type IV and Type II specimens might therefore explain the reduction of strength for those laminates. However, it has to be noted that the cracks are only confirmed experimentally for the Type IV specimens. Further investigation is underway to determine the damage present in the Type I and II specimens in order to draw definite conclusions.

In order to investigate the influence of transverse stresses on the longitudinal compressive failure of the plies, the evolution of the transverse tensile stress in the 90° plies from OPFM is plotted as a function of the longitudinal compressive stress as illustrated in Figure 6.23 (a).

The beginning of the curve starts from a non-zero stress value due to the presence of thermal residual stresses. Figure 6.23 (b) shows the evolution of the longitudinal compressive stress in the 90° plies as a function of the applied macroscopic stress.

The evolution of both σ_{11} and σ_{22} is non-linear: an increase in the applied macroscopic stress induces a slightly higher increase in the estimated longitudinal compressive stress in the 90° ply. This can be attributed to the non-linear behaviour in the 45° plies, due to the viscosity of the matrix, especially under in-plane shear loading, reducing their apparent stiffness and therefore the proportion of load that they carry. This behaviour shows the important effect of non-linearity on the longitudinal compressive strength identification.

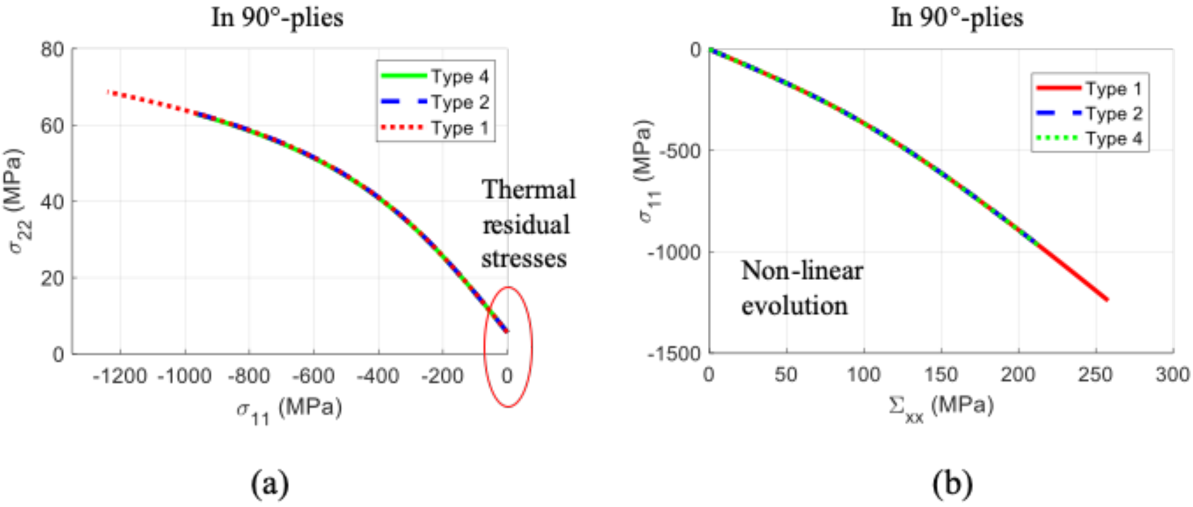

(a) (b)

Figure 6.23. Schematic of the evolution of (a) transverse tensile stress in the 90° plies as a function of the longitudinal compressive stress and (b) compressive stress in the 90° plies as a function of the applied macroscopic stress.

6.4. Conclusion

A novel specimen design has been successfully utilized to determine the longitudinal compressive strength of a thin-ply carbon/epoxy material. The compressive loading was indirectly applied to the 90° layers through the Poisson contraction of the laminate. Under uniaxial loading, a multi-axial stress state was induced in the UD 90° layers: longitudinal compression combined with transverse tension. Design optimization was carried out using the design of experiments with an advanced failure criterion called OPFM. Once a configuration was selected, the lay-up sequence was modified in a way that ply thickness effects could be investigated.

A decrease was found in the compressive strength/strain to failure of the material for thicker 90°-layer laminates (Type II and Type IV). It was concluded, that there are two mechanisms that may contribute to this decrease in longitudinal compressive strength, transverse cracking or the constraint/ply thickness effect, however it is very difficult to differentiate between them and determine the dominant one. Further investigation (microscopy or interrupted tests) is necessary to establish whether transverse cracks occurred in other specimen types.

The obtained longitudinal compressive strengths for the Type I, determined with OPFM, is consistent with values found in literature or in other work performed currently at Bristol. Moreover, it can be noted that the associated scatter is very low for this configuration (CoV around 1.4%), allowing to determine high B-basis values for the design of composite structures. B-basis values correspond to the lower 90% confidence limit defined in [113] as: “at least 90% of population equals or exceeds value with 95% confidence”.

Furthermore, it can be said that the non-linear behaviour of such thin-ply laminates was well captured by the OPFM model. Based on the micrographs and SEM images, a gauge section compressive failure (fibre micro-buckling/kinking) was found in the mid-width of the Type IV specimens. A pattern of transverse cracks was also found 200 μm apart and it was argued that matrix cracking might have preceded the fibre microbuckling. This is consistent with the cracking found in the cross-ply study in Chapter 5 and suggests that cracking might be the dominant effect for thicker 90° layers.

Chapter 7

Overload sensors – a simple and robust approach for visual damage indication

The chapter is based on P.1. and C.2. first authored publications as referenced in the Publication section of the thesis. The work discussed here - including design, analysis, experimental work and data processing - was carried out by the author of this PhD with the work in section 7.6 carried out together with Dr Jonathan Fuller.

The concept presented emerged from some of the research done as part of the HiPerDuCT (High Performance Ductile Composite Technologies) programme. This programme grant was a collaborative research project between the University of Bristol and Imperial College London. The aim of the programme was to improve and overcome the key limitation of conventional composites: their inherent lack of ductility by designing, manufacturing and evaluating composite systems that could fail gradually and undergo large deformations whilst still carrying load. These structures then could ensure a more reliable, safer and longer service life as well as reduced design and maintenance requirements [265].

7.1. Introduction

As was previously shown, utilizing thin ply materials can create multi-axial stress-states and consistent material failure behaviour by effectively suppressing secondary failure mechanisms such as transverse/matrix micro-cracking and delamination. The same methodology using thin-ply composites to target or promote a specific failure mode allows the design and development of unidirectional hybrid composite overload sensors. Additionally, controlling the damage mechanism of composite laminates could lead to preventing structures from sudden failure [266]. The novel UD hybrid sensor concept presented and investigated here can be used for structural health monitoring of both composite and metallic structures.

The term ‘pseudo-ductility’ is used when talking about achieving controlled and gradual failure and for the composite structure having the ability to deform non-linearly without fracture [266]. Many different strategies were developed to achieve ‘pseudo-ductility’ in composites and make them more damage resistant. Reinforcing materials such as nano-materials or elastomers can be incorporated into the matrix to improve the toughness of the resin itself or more ductile constituents can be utilised as reinforcing fibres eg. metals. The architecture of the composite laminates can be re-designed as well *e.g.* through the hybridisation of primary reinforcements [20], [267]–[275] or fibre reorientation concepts [128], [276], [277] as demonstrated in the HiPerDuCT programme.

Czél *et al.* [268], [278] combined the advantages of thin-ply materials with the gradual failure of hybrid composites in order to achieve pseudo-ductile stress – strain responses. Their approach to combine UD glass/epoxy and thin-ply carbon/epoxy plies into interlayer hybrid composites resulted in a design that allows the fragmentation of the lower strain constituent, avoiding catastrophic failure and unstable delamination. This is mainly due to the low energy release rate that primarily depends on the thickness of the lower strain component layer in the hybrid composite as discussed in this chapter. During the experiments, it was observed that the carbon ply cracks (fragmentation) and local delamination are clearly visible to the naked eye due to the translucency of the glass plies. Inspired by this observation, the development and characterisation of the UD hybrid composite overload sensor concept is presented in this chapter. The proof of concept for the bonded-on sensors was also demonstrated on a real-life structural application.

7.2. Background

Fibre reinforced composite materials are increasingly used in advanced lightweight applications especially in the aerospace and space sector [279] as well as automotive, civil engineering [280] and high-end sporting goods [110], [281].

In high volume applications, it is of immense importance to ensure an appropriate safety margin as a sudden failure or collapse could lead to the loss of human life as well as significant financial costs. In these areas, the scope of composite applications is hindered as sudden failure and poor residual load bearing capacity cannot be tolerated. Instead, higher safety margins and conservative design envelopes have become the standard practice in composites design and manufacture. Another issue is that failure may occur without preceding detectable damage or warning of any kind especially for composite materials [268], [282].

Structures that pass visual inspection can fail at much lower loads than expected [267] hence it is crucial to monitor their integrity as well as detect damage (if there is any) before final failure occurs. As a result, damage detected in time can not only prevent sudden, catastrophic failure but it can also indicate the need for further, more thorough non-destructive testing (NDT) so appropriate repair or maintenance can be carried out when necessary, leading to no unexpected down-time and enhanced service lives. The process of monitoring damage during service life is often referred to as Structural Health Monitoring (SHM). It is very common, especially in civil engineering and transportation applications where sensors based on different principles - such as fibre optics, piezoelectrics, magnetostricity, and self-sensing - are used in order to assess the integrity or certain physical or chemical properties of a structure or component. An extensive review on SHM techniques as applied to composite structures can be found in the study by Amafabia *et al.* [283]. In general, a structural health monitoring system comprises three different constituents: the sensor itself that is coupled with the monitored structure, as well as a data acquisition and a data evaluation system [284], [285].

For the health monitoring of civil structures, fibre optic sensors (FOS), particularly Fibre Bragg Grating (FBG) sensors have been often used to mitigate the risk of unexpected failure. Especially for composite materials that are prone to failure due to an overload or an impact event, these lightweight sensors can be utilised at various locations without significantly affecting the performance of the structure [284], [286]. A drawback of such sensors is that they require equipment to detect the signals and process data. Fibre optic sensors are insensitive to electromagnetic interference (EMI) and sense various parameters such as strain or displacement.

Even though they are brittle, and need to be encapsulated in a protective material, they are extensively used in civil applications such as bridges, tunnels, pipelines and in a currently expanding field: wind turbine blades [285] as discussed in a comprehensive review on optical fibre sensing technologies by Ye *et al.* [287].

Another emerging technology for SHM is the field of self-sensing composites. These multi-functional materials are able to indicate their own physical conditions such as stress, strain or temperature as well as deformation and damage [284]. *E.g.* a change in electrical conductivity is used for monitoring damage as it can be directly related to fibre breakage [288]. In a similar way, various other damage mechanisms e. g. delamination [289] and matrix cracking [290], under different loading conditions [291]–[293], have been investigated.

These measurements are based on a piezoresistive principle: incorporating a conducting element e. g. carbon particles, nanomaterials (carbon nanofibres and carbon nanotubes [294]) or short or continuous carbon fibres [284], [295], [296] that form a 'sensing' network in the composite. When the composite is subjected to an overload or deformation, this network is disturbed, hence changing the electrical resistivity of the overall structure.

As mentioned above, when demonstrating pseudo-ductile behaviour in thin-ply interlayer glass/carbon-epoxy hybrid composites, the pattern observed by Czél and Wisnom [267] during the gradual failure of the specimens inspired the idea of sensing damage on the surface of a structure due to the translucent nature of the constituent glass-epoxy layers that made delamination detection possible to the naked eye. Various other authors have tried to combine the advantageous pseudo-ductile behaviour achieved by fibre hybridisation with the functionality of self-sensing. Bakis *et al.* [297] demonstrated pseudo-ductile tensile behaviour with the capability of monitoring strain and damage by the hybridization of low-strain piezoresistive carbon fibres and high-strain non-conductive fibres. Nanni *et al.* [298] have designed a system consisting of a carbon-glass hybrid structure that offers good structural properties while acting as a warning signal when reaching certain loading conditions. In both studies, the sensors are based on a piezoresistive principle while being low-cost, versatile and easy to fabricate.

The sensors proposed here indicate an overload by simply exhibiting a change in appearance in contrast with other strain sensors that are based for example on the change of electrical properties induced by deformation. They are robust and lightweight, completely wireless, and do not require any data acquisition or evaluation system hence offering a low-cost and simple visual solution for strain overload indication. This novel concept can be simultaneously used for SHM and structural load-carrying purposes. The hybrid composite sensors can either be a sensing layer as part of the structure or can be bonded on to the surface of composite or metallic structures. They can provide information about the magnitude of the overload by combining various sensing materials indicating different strains. They can also provide information on the direction of overload by applying an array of sensors integrated in different directions.

7.3. Sensing mechanism

This section gives a summary on the principle behind the unidirectional hybrid composite sensor concept as well as the underlying failure mechanism that enables visual overload indication. The reader is referred to a pending UK Patent [299] for further information on the concept.

As has been reported above, well-designed thin ply-hybrids can develop fragmentation of the higher modulus/lower strain material constituent followed by gradual and dispersed delamination avoiding catastrophic failure. The carbon ply cracks appear along the gauge length of tensile specimens in a well-dispersed, striped pattern [268], [278] as illustrated in Figure 7.1 (a) [268].

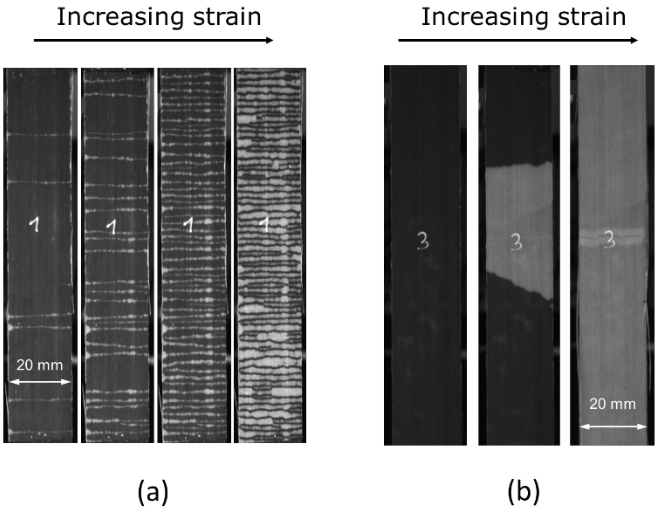

Figure 7.1. Visual patterns based on different failure mechanisms of thin-ply glass/carbon hybrids: (a) carbon layer fragmentation followed by stable, dispersed delamination [268] (b) carbon layer fracture followed by sudden delamination [20].

Figure 7. 1 (b) represents another pattern type and failure mechanism for thicker carbon layers: a single fracture of the low strain material followed by sudden, unstable delamination [20], where the fracture of the stiffer layer translates to a significant stress drop at the corresponding strain to failure of the low strain material on the stress-strain curves. While the latter one gives a clearer indication of an overload event as it is easier to observe the delamination through the translucent glass layer, the former mechanism with multiple fragmentation and decreasing spacing between cracks allows for a quantitative indication on the severity of the overload event.

The principle behind the UD hybrid sensor concept is based on a unique feature of the purpose-designed thin interlayer glass/carbon hybrid composites: the change in their appearance when loaded beyond a predefined strain. The sensor is on the surface of the component, and experiences similar strains as the material beneath. It consists of a 'sensing' layer and an outermost layer, which in this case are a carbon sensing layer and glass outermost layer respectively. The schematic of a typical sensor setup and its attachment to a substrate material is illustrated in Figure 7.2.

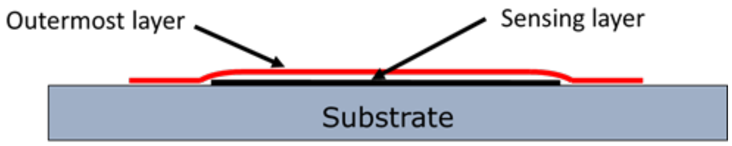

Figure 7.2. Schematic of a hybrid composite strain overload sensor attached to a substrate material

The originally intact carbon layer absorbs the incident light through the translucent glass layer showing a dark appearance as shown in Figure 7. 3 (a). After the strain exceeds the failure strain of the carbon layer, it develops multiple fractures and the incident light is reflected back from the locally damaged glass/carbon interface around the carbon layer fractures, exhibiting light stripes as illustrated in Figure 7. 3 (b). Hence, the visible interfacial damage is directly related to the unique failure mechanism of such hybrid composites.

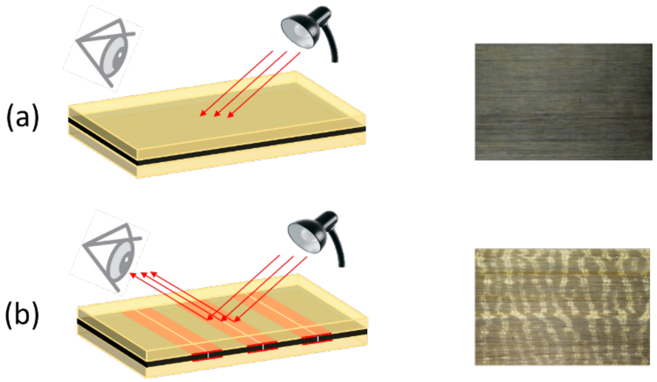

Figure 7.3. The sensing mechanism behind the hybrid composite strain overload sensors: (a) intact carbon layer absorbing light at glass/carbon interface (b) striped pattern visible due to light being reflected from locally damaged glass/carbon interface around the sensing layer cracks.

7.4. Materials and configuration design

7.4.1. Choices in design, manufacture and sensor integration

There are various parameters influencing the design of the proposed hybrid composite sensors. Their geometry (length and width) can be varied as well as the stiffness ratio of the sensor to the substrate by either changing the thickness of the layers or by utilising different composite prepreg materials. The most important parameter is the sensors' trigger strain that is controlled by the failure strain of the carbon fibre sensing layer. The integration of the sensors can be achieved by either co-curing or retrofitting by bonding onto finished parts. By co-curing on the surface, the sensor can act as a structural sensing layer while by retrofitting it will likely act as a discrete sensor on the structure. Furthermore, the sensors can indicate both the magnitude of the overload strain (pre-defined by the sensing layer material) and the direction of a given overload strain if multiple sensors are utilised in various directions. The material system proposed in this study is suitable for the fabrication of sensors designed for tensile load dominated applications, although fragmentation in thin ply hybrids has also been reported in compression [20].

7.4.2. Materials

There is a wide range of materials that can be used for demonstrating the concept explained above, however two criteria must be considered: (i) in order to apply such composite sensors, the strain to failure of the 'sensing' carbon fibre has to be considered according to the surface strain of the material underneath and (ii) the thickness of the sensing material has to be thin enough to exhibit failure with fragmentation and dispersed delamination. The applicable strain range currently for carbon fibre materials satisfying these conditions is from 0.3% - 2%, however it can be extended by using a wider range of materials or innovative methods such as pre-weakening the sensing layers as outlined in the report by Varkonyi [300].

The material considered as an outermost, translucent layer was a standard thickness UD S-glass/epoxy prepreg supplied by Hexcel. The sensing layer was thin UD XN80 carbon/epoxy prepreg produced by North Thin Ply Technology (NTPT).

For the demonstration of the sensors, a substrate material of IM6 carbon fibre reinforced epoxy prepreg supplied by Cytec has been used. The resin systems used for the sensor and substrate have a similar cure temperature, hence they are suitable to be cured together in the autoclave. The basic material data of the applied fibres and prepreg systems can be found in Table 7.1 and Table 7.2.

Table 7.1. Fibre properties of the applied unidirectional prepregs based on manufacturers data (carbon fibre types: IM – intermediate modulus, UHM – ultra high modulus)

Fibre type	Manufacturer	Elastic modulus [GPa]	Density [g/cm³]	Strain to failure [%]	Tensile strength [GPa]
Granoc XN80	Nippon GFC	780 (UHM)	2.17	0.5	3.43
Hextow IM6	Hexcel	279 (IM)	1.76	1.9	5.72
FliteStrand S ZT S-glass	Owens corning	88	2.45	5.5	4.8-5.1

Table 7.2. Cured ply properties of the applied unidirectional prepregs

Prepreg type	Areal density[1] [g/m²]	Cured ply thickness[2] [μm]	Fibre volume fraction[2] [%]	Initial elastic modulus[2] [GPa]	Tensile strain to failure [%]
XN80/ TP 402 carbon/epoxy	63	63	46.5	364.4	0.5[3]
IM6/950 carbon/epoxy	135	153	50	141.2	1.8[2]
S-glass/913 glass/epoxy	190	155	51	45.6	3.9[3]

[1] Based on manufacturer's data
[2] Calculated using manufacturer's data
[3] Based on measurements

Additional adhesives were utilised for the fabrication of specimens with retrofitted sensors: including an Araldite 2014/1 type two-part epoxy adhesive (Huntsman), 913 resin film (Hexcel), a commercially available Permabond cyanoacrylate adhesive, and an M-Bond AE-15 two-part high-elongation adhesive system (Vishay) developed for the application of strain gauges.

7.5. Experimental

7.5.1. Sensor response and accuracy

One of the key design parameters influencing the sensing performance of such hybrid composites is the critical or ineffective length of the sensing layer. Sensing layers shorter than the ineffective length are not capable of reaching the fibre fracture strain, hence rendering them unable to function properly. The assumed strain distribution along the length of the sensing layer is illustrated in Figure 7.4.

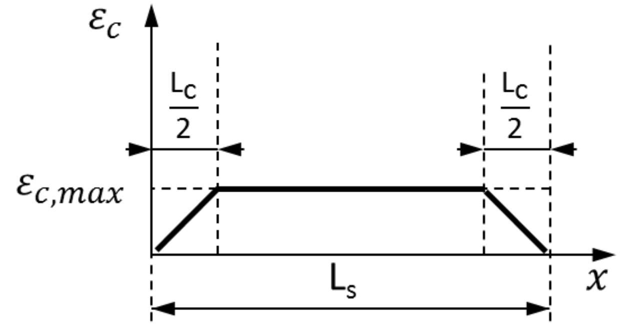

Figure 7.4. Strain distribution in the sensing layer along its length (L_s) at trigger strain (if $\varepsilon_c = \varepsilon_{c,max}$)

Calculations have been carried out to estimate the critical length L_c of different thickness carbon/epoxy sensing layers. The principle is similar to the Kelly-Tyson equation applied at the ply rather than the fibre/matrix level as given in equation (7.1) [12]:

$$L_c = \frac{E_c \ \varepsilon_{c_{max}} \ t_c}{\tau_{max}} \quad (7.1)$$

where E_c is the Young modulus of the sensing carbon layer, ε_{cmax} is the strain to failure of the carbon layer, t_c is the thickness of the sensing layer and τ_{max} is the interfacial shear strength at the glass/carbon layer interface. τ_{max} is assumed to be 100 MPa based on test results of the same resin system used in [301].

The critical length L_c is required to assess the transfer of tensile stresses (from the substrate) through shear to the sensing layer. This ineffective length is strongly dependent on the stiffness of the constituent sensor layers. The calculated values for the constituent layers are illustrated in Table 7.3.

Table 7.3. Calculated critical length values for the carbon constituent layer(s) with different number of incorporated sensing plies

	$XN80_2$	XN80
Critical length [mm]	4.87	2.44

Another key parameter to consider when designing such sensors is the sensor to substrate stiffness ratio. It is important to determine how much the stiffness of the substrate is affected by the sensor. Simple calculations can be carried out with respect to the axial stiffness of the sensor and substrate to check the stiffness increment caused by the sensors. Building on that, a simple elastic analytical model was developed that allows for an assessment of whether a calibration is necessary to account for this effect.

The input parameters of the model include the moduli of the prepreg materials, cured ply thicknesses (CPTs), lay-up (number of plies), the length and width of the coupons as well as the applied uniaxial load. In this manner, the sensor behaviour can be tailored to fit different substrate materials/components and trigger strains.

The equivalent stiffness model determines average strains based on calculating an effective stiffness for a certain section of the specimen using simple series and parallel rules that account for the connection between the distinct materials. This model is dependent on the area of interest (along the free length of the specimen) and does not take through thickness strain variation into consideration as it is a pure tensile model not accounting for asymmetry induced bending. The model assumes a tensile specimen fitted with a long type hybrid composite sensor (see section 7.4.3) which is illustrated along with a schematic of the stiffness model in Figure 7.5.

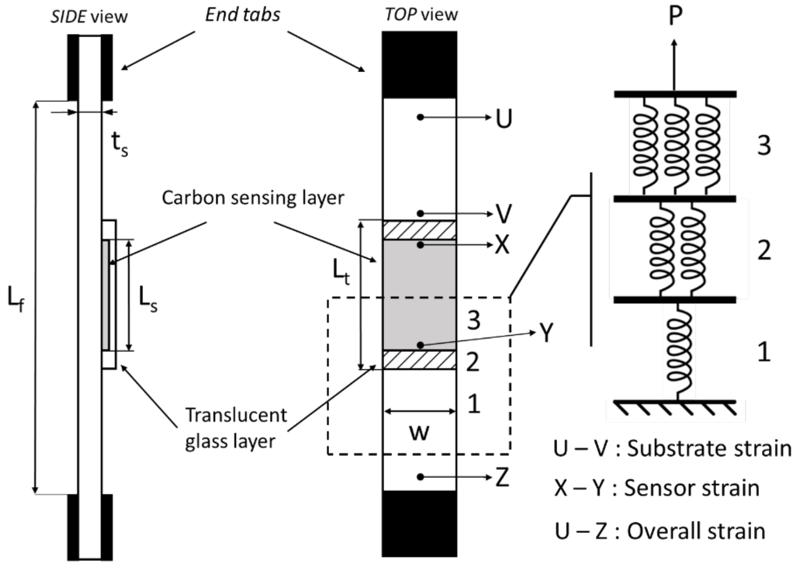

Figure 7.5. Schematic of the (a) side and (b) top view of an unidirectional tensile specimen equipped with a hybrid composite overload sensor, (c) schematic of the elastic stiffness model representing the behaviour of the UD laminate.

In general, the lowest stiffness sensors on high stiffness substrates provide the most accurate results by not increasing the substrate stiffness significantly. It has to be noted that accuracy in this case represents the percentage error between the substrate strain and the sensor strain. Figure 7.6 illustrates the percentage error calculated by the model as a function of the substrate thickness for different grade carbon fibres. UD substrates with 60% fibre volume fraction was considered with the optimal hybrid sensor configuration (one layer of S-Glass/913 and one layer of XN80 carbon/epoxy.

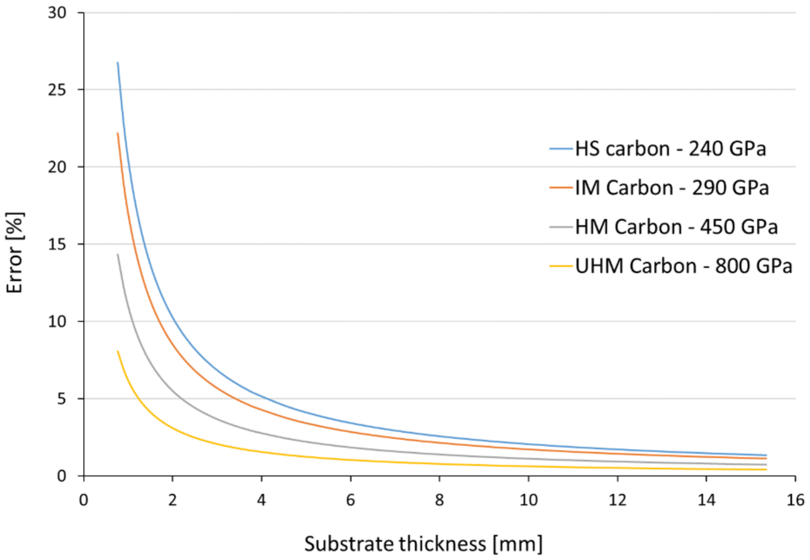

Figure 7.6. Accuracy of sensor strain measurement predicted by the analytical model

In practice, the sensors have to be made the thinnest and narrowest possible if the substrate has a relatively low stiffness. The graph above is a useful tool for deciding whether the sensors need to be calibrated or not as a first estimate when applying them to various stiffness structures. In order to achieve an error less than 10% with the carbon fibres utilized in this study, a minimum substrate thickness of 2.15 mm is required. The error calculated by the model represents the difference in average strain of the UD hybrid sensors (sensor strain between points X and Y on Figure 7.5) and the substrate (strain between points U and V on Figure 7.5) discarding the effect of bending. As the strain has a relatively small variation through the thickness, this simple model can give a reasonable indication of the extra stiffness added by the sensor and it is suitable for running parametric studies.

Furthermore, to compare with the analytical predictions and the experimental measurements, a finite element model (FEM) was also set up in a commercial software package (Abaqus). The finite element analysis (FEA) incorporated a 2D shell model of the laminate along the gauge length of the specimen up until the end-tab regions. The analysis was carried out using conventional linear 4 noded S4R shell elements with the definition of linear elastic properties assuming transverse isotropy for the distinct materials as summarised in Table 7.4.

An offset was applied to certain shell elements to account for the asymmetry and different thicknesses of the different regions on the specimen. A static load case was run where the specimen was encastre along one edge and loaded at the other one constraining all degrees of freedom except translation in the loading direction. Due to the length of the specimen the boundary conditions do not affect the stress/strain state of the sensor area.

Table 7.4. Linear elastic material properties utilized in the finite element model

Material	E_1 [GPa]	E_2 [GPa]	G_{12} [GPa]	ν_{12} [-]	G_{13} [GPa]	G_{23} [GPa]	ν_{23} [-]
UHM carbon/epoxy	364.57	10.9	3.7	0.31	3.7	3.7	0.45
IM6/950 carbon/epoxy	141.5	13	4.6	0.31	4.6	4.5	0.45
S-glass/epoxy	46.55	10.5	3.8	0.26	3.8	3.6	0.45

7.5.2. Manufacturing

All composite laminates have been fabricated similarly to the processes detailed in Chapters 3–6. Following hand lay-up, a standard vacuum bagging method was applied on a flat aluminium tool plate with additional silicone sheets placed on top of the laminates.

They were then cured in an autoclave at the recommended temperature and pressure cycle. As different material combinations were used, the highest cure temperature and longest curing time of all the constituent prepregs' individual cure cycles have been used to ensure full cure for all the prepreg systems and to obtain the desired mechanical performance. The curing cycle used for the co-cured plates - consisting of the substrate laminate and the hybrid sensor layers - as well as for the substrate plates cured on their own was 155 mins at 137 °C, with 0.7 MPa applied pressure and a heating rate of 2°C/min. In this material combination, the 137 °C peak temperature is due to the IM6/950 material's curing cycle being 135 °C with an additional 2 °C overrun. The cycle used for the sensor laminates to be retrofitted was 165 mins at 127 °C, with 0.7 MPa applied pressure and a heating rate of 2°C/min.

The 127 °C peak temperature in this case reflects the highest 125 °C cure temperature for the S-Glass/913 material, also with an additional 2 °C overrun.

All the tensile test coupons were fabricated by using a diamond cutting wheel. Un-tapered, 1.7 mm thick end-tabs made of a balanced woven glass fibre fabric reinforced composite laminate were bonded to the specimens using an Araldite 2014/1 type epoxy adhesive system. The samples were then put into an atmospheric oven to cure the adhesive for 120 mins at 80 °C. Regarding the separately manufactured sensor laminates to be retrofitted, sensor strips were cut to the desired width and their surfaces were roughened with coarse sandpaper before attachment to the substrate/component.

Various adhesives and methods have been utilised for bonding the sensors to the substrates. The two fabrication techniques included simple mechanical clamping and vacuum-assisted envelope bagging to ensure an adequate and uniform pressure while curing the adhesives. Both fabrication methods have been applied using the three previously mentioned adhesives, giving a total of 6 differently bonded retrofitted specimen types.

7.5.3. Specimen configuration and geometry

All sensors consist of one or two plies of XN80/epoxy and one ply of S-glass/epoxy prepreg material. The schematic of the specimens both co-cured and separately manufactured sensor strips are illustrated in Figure 7.7 (a) and (b) respectively.

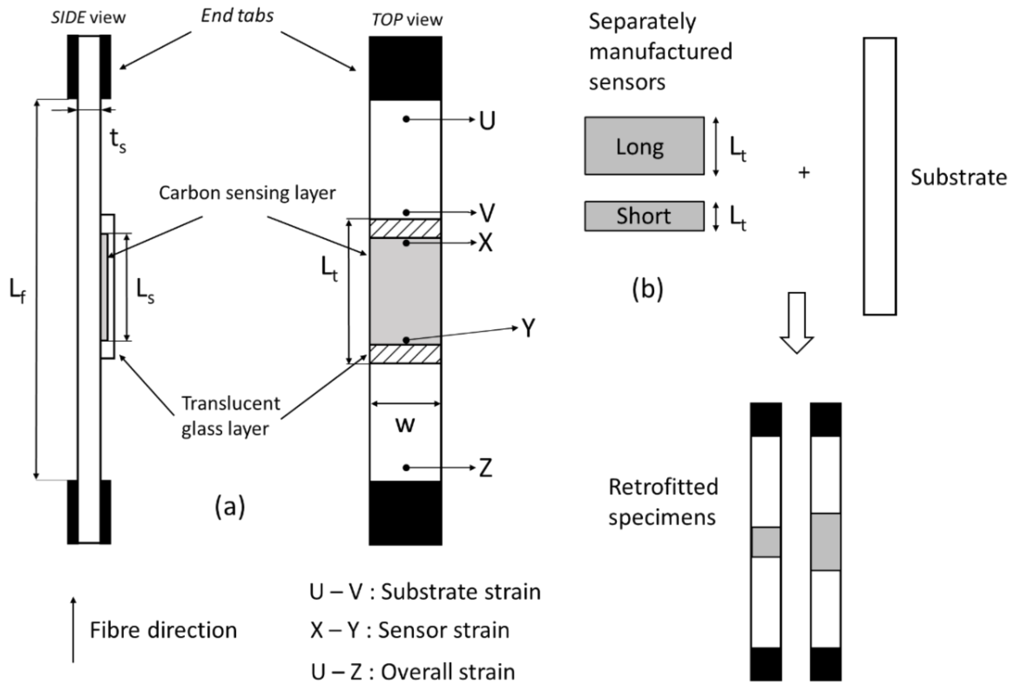

Figure 7.7. An illustration of (a) a unidirectional tensile specimen equipped with hybrid composite strain sensor (b) separately manufactured sensor strips for retrofitting purposes.

The nominal specimen dimensions were 260/160/20/2.4 mm overall length/free length (L_f) /width (w)/thickness (t_s) respectively while nominal sensor dimensions were 50/30 mm (long sensor) and 20/10 mm (short sensor) total length (L_t)/sensing layer length (L_s) respectively. The substrate laminates comprised 15 plies of unidirectional IM6/950 carbon/epoxy prepreg.

The co-cured specimens were fabricated with long, single and double ply XN80/epoxy sensor laminates in the central section on one side to investigate the effect of different stiffnesses added to the structure. The effect of the different integration methods was investigated by fabricating specimens with both co-cured and retrofitted sensors.

After initial testing it was found that the single ply XN80/epoxy sensors worked satisfactorily and visually indicated the overload of the substrate. The retrofitted specimens were fabricated with only single XN80/epoxy sensing plies.

The retrofitted specimens were also equipped with both long and shorter length sensors to investigate the effect of sensing layer length on the sensor trigger strain. The curved sensors (see section 7.6) for the demonstrator application were fabricated using both longer and shorter sensor geometries as well as various widths depending on the geometry of the component they are designed for. A summary illustrating the various configurations can be found in Table 7.5.

Table 7.5. Summary of the fabricated configurations

	Double layer sensor	Single layer sensor	Long sensor	Short sensor
Co-cured specimens	✕	✕	✕	
Retrofitted specimens		✕	✕	✕
Demonstrator application		✕	✕	✕

7.5.4. Test methods

Mechanical testing of both co-cured and retrofitted specimen types was carried out on an Instron 8801 100 kN test machine with wedge type hydraulic grips under uniaxial tensile loading and displacement control at a crosshead speed of 1 mm/min. The clamping pressure was kept high enough to avoid slippage of the specimens in the grips. Various local (sensor) and global strains (see Figure 7.5 or 7.7) were measured using an Imetrum videogauge system, with the test machine outputting the corresponding force signals. The high-definition extensometer videos recorded during the tests were kept mainly for determining the first fracture of the carbon sensing layer by visual inspection.

Another optical analysis method, Digital Image Correlation (DIC) was also used in order to determine the strain distribution of the co-cured specimens fitted with single layer XN80/epoxy sensors. The specifications and parameters for the DaVis DIC measurement system are summarised in Table 7.6.

Table 7.6. DIC measurement specifications

Technique	Stereo DIC
Software	LaVision DaVis 8.3.1
Subset Size [pixels]	29
Step Size [pixels]	10
Camera	VC-Imager 16MPixel
Lens	Tokina ATX AF 100/2.8
Resolution [pixels]	3404 x 4800
Field of view [mm]	101.4 x 66.8
Spatial resolution [μm]	216
Strain resolution [με]	135

Additionally, a PCI-2 acoustic emission (AE) system was used to verify the onset of fragmentation in the hybrid sensors. The AE sensor acquiring the data and its settings were similar to the one discussed in Chapter 5 under section 5.3.2. The acoustic sensors were attached to the back face of the tensile specimens (bottom side of the substrate) by using a hot melt adhesive gun. Firstly, the sensors were positioned on the back face of the specimens with silicone grease underneath, then the hot melt adhesive gun was used to go around the circumference of the sensors and the glue was applied to hold them at their boundaries to the specimen. Silicone grease was used to provide sufficient acoustic coupling between the specimens and the sensors. Furthermore, each specimen was tapped by a stiff object at the start of the tests in order to provide a time reference point to the various data acquisition systems.

7.5.5. Results and discussion

7.5.5.1. Sensor trigger strain identification

Figure 7.8 (a) shows the load-strain response of a typical tensile specimen fitted with a long unidirectional hybrid sensor comprising a single ply of XN80 carbon/epoxy and S-glass/epoxy prepreg. Figure 7.8. (b) illustrates the response of such a coupon visually when triggered.

The substrate strain (defined between points of U and V in Figure 7.7) represents the surface strain of the substrate only, the overall strain (defined between points U and Z in Figure 7.7) represents the overall extension measured along the free length of the specimen, while the sensor strain (defined between points X and Y in Figure 7.7) shows the surface strain of the sensor. The red dashed and continuous lines illustrate the strain and load respectively at which the first sensing layer fracture occurred. Stresses and strains were determined from the logged data based on visually inspecting the videos recorded during testing and extracting the time for the first visible fracture of the sensing layer. The load-strain curves of Figure 7.8 show how the stiffness of this specimen has been increased locally due to the integration of the sensor (difference between green and blue curves). This stiffening effect demonstrates that the trigger strain of the sensors has to be corrected for the added stiffness by the sensor to represent the strain in the free-standing substrate.

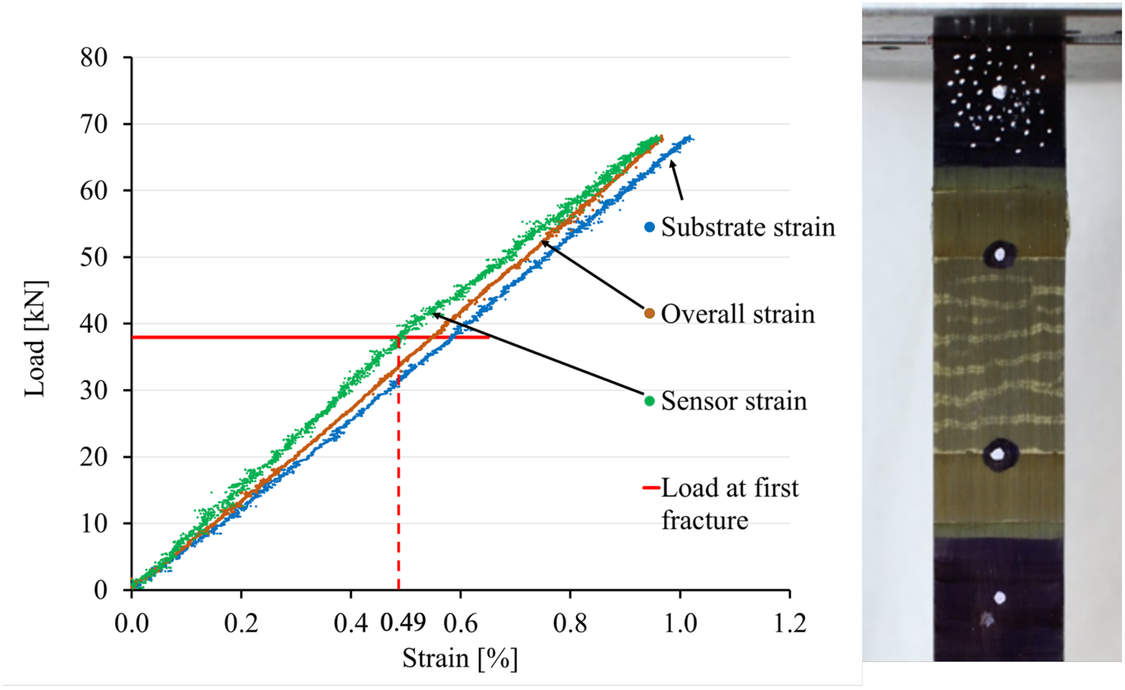

(a) (b)

Figure 7.8. (a) typical load-strain response of a tensile specimen fitted with a co-cured, single layer XN80/epoxy UD hybrid sensor (b) illustrates the visual response of a typical coupon when triggered.

7.5.5.2. Experimental validation for baseline configuration

As mentioned earlier, preliminary tests have been carried out in order to investigate a range of stiffnesses (different number of carbon sesning layers) added to the structure. The minimum stiffness (one carbon sensing layer) satisfactorily indicated the overload of the substrate material.

Then, a comprehensive set of specimens were tested with the optimal configuration: co-curing a long, single XN80 ply carbon/epoxy sensor to the substrate laminate. Co-curing was chosen as the attachment method as this proved to have the highest integrity of the sensor to the substrate and provided the most accurate sensor response. The summary of the test results is given in Table 7.7.

Table 7.7. Summary of test results for the optimal sensor configuration

Integration method/sensor type	No. of specimens tested [-]	Overall strain (at first crack in sensor layer) [%] (C.o.V%)	Sensor strain at first crack in sensor layer [GPa] (C.o.V%)	Substrate strain at first crack in sensor layer [%] (C.o.V%)	Substrate stress at first crack in sensor layer [MPa] (C.o.V rel.%)
Co-cured/Long single ply [XN80]/SG	5	0.58 (3.9)	0.52 (3.3)	0.62 (4.6)	820 (5.2)

All the results presented are average surface strain values. For these specimens, the average apparent stiffness (load per unit strain) at the section where the sensor is placed (measured between points X and Y on Figure 7.7) is 75.60 kN / % strain while at the substrate only section it is 66.69 kN /% strain based on the initial slope of the load-strain curves. This resulted in a mismatch between the sensor and substrate strains at trigger which can be corrected [302].

Furthermore, - in addition to the optimal configuration -, co-cured long double XN80 ply sensor specimens and retrofitted (long and short single ply type) specimens have been tested as shown in Table 7.8.

Table 7.8. Summary of test results for the optimal sensor configuration

Integration method/sensor type	No. of specimens tested [-]	Overall strain at first crack in sensor layer [%] (C.o.V%)	Sensor strain at first crack in sensor layer [GPa] (C.o.V%)	Substrate stress at first crack in sensor layer [MPa] (C.o.V rel.%)
Co-cured/Long double ply $[XN80]_2$/SG	3	0.58 (2.4)	0.49 (3.6)	814.0 (5.3)
Retrofitted/Long single ply [XN80]/SG	4	0.57 (4.1)	0.54 (3.6)	748.1 (2.5)
Retrofitted/Short single ply [XN80]/SG	3	0.63 (4.1)	0.56 (5.9)	910 (2.1)

7.5.5.3. Comparison of different sensor configurations

Regarding the co-cured configurations, both the long single (Table 7.7) and double ply (Table 7.8) sensors show consistency in measured overall and sensor strains and the stress state in the substrate at the appearance of the first crack. The sensor strains measured for these specimens at the first crack appearance in the sensor layer (0.52% and 0.49% for single and double plies respectively) are close to the quoted failure strain (0.5%) of the UHM XN80 carbon fibres (see Table 7.2). The single XN80 ply carbon/epoxy sensor specimens exhibited slightly higher trigger strains at the first carbon failure than the ones with two plies. There are various factors that can contribute to this change.

One of them is the hybrid effect [133]. In the case of a single XN80 ply sensor, the development of critical clusters is more restrained as the thickness of the sensing carbon ply (63 μm) is only in the order of a few fibre diameters, hence the formation of the first macroscopic crack may have been delayed. Another possible influence is the volume effect, whereby the smaller volume of material for a single ply sensor reduces the probability of finding defects of a certain size within the sensing layer, therefore increasing the strain at first fracture.

When the sensing layer is thin, there is less added stiffness, and the sensor measures the substrate strain more accurately. However, in this case, the hybrid effect may increase the failure strain of the sensing layer, slightly increasing the strain of the substrate at which the sensor triggers. On the other hand, when the sensing layer is thick, the hybrid effect is negligible, but the substrate strain and the strain of the sensor may differ because of the added stiffness. This potential difference in strains could decrease the accuracy of the sensors, especially in the case of thin substrate components. Regarding the retrofitted specimens, they were only equipped with single XN80 ply sensors (Table 7.8). The specimens with shorter sensors showed higher trigger strains as well as elevated stresses in the substrate at the first fracture of the sensing layer. This general trend, an increase in overall strain in the case of the specimens fitted with shorter sensors – is because the stress from the substrate and the glass layer was transferred to the sensing layer along the ineffective length of the layer (half ineffective length at both ends). The ineffective length is calculated to be 2.44 mm and 4.87 mm (see Table 7.3) for single/double XN80 ply sensing layers respectively (this is one of the reasons why there were no short double ply sensors tested). In the case of the retrofitted short, single ply sensor specimens, it means that approximately a quarter of the volume of the sensing layer is not fully loaded, hence the corresponding extra volume effect may have delayed the appearance of the first crack in the sensor slightly. Despite this, the short sensors may still be suitable for smaller components where it is not possible to fit the longer ones but they have to be designed with special attention to the effects highlighted above and calibrated to the substrate stiffness.

7.5.5.4. Comparison of analytical, FEA prediction and experimental measurements

In order to compare the results of the basic analytical model (neglecting the effect of bending), and the more accurate one by the FEA (accounting for bending), a common load case had to be set.

A single XN80 ply carbon/epoxy long sensor specimen was theoretically loaded with a uniaxial tensile load of 20kN (~0.3-0.4% strain). This preceded the failure strain of the UHM carbon fibres hence keeping the load case in the linear region of the stress-strain curves (as it is seen in Figure 7.8).

The results were validated against strain gauge measurements. There were two specimens where strain gauges were placed on the top surface of the glass layer of a co-cured sensor and on the back surface of the substrate. These gauges were placed in order to determine the strains through the thickness of the specimens at a given cross section within the sensor area. A summary of the results compared with the strain gauge measurements can be seen in Table 7.9.

Table 7.9. Summary of the strain results output by different models for a 20kN load case at the sensor area. The table shows the calculated curvatures and strain variation between the topmost and bottommost surfaces of the specimen.

Model/test method	Sensor top surface strain [%]	Substrate bottom surface strain [%]	Average through thickness strain [%]	κ curvature [1/m]	Difference between top and bottom surface strain [%]
Analytical model	0.282*	0.282*	0.282	n/a	n/a
FE model	0.260	0.303	0.282	-0.171	14
Strain gauge measurements	0.254	0.315	0.285	-0.243	19

*The analytical model outputs a constant average strain across the thickness of the specimen and the sensor

Figure 7.9 shows the contour of strain output by the FEA for (a) the bottommost point of the substrate and for (b) the topmost point of the glass layer. Figure 7.9 (c) illustrates the comparison of through thickness strain distributions predicted by FEA and measured by the strain gauges. The graph shows the difference between the predictions and experimental values. On the vertical axis, zero represents the bottom of the substrate/backface of the specimen.

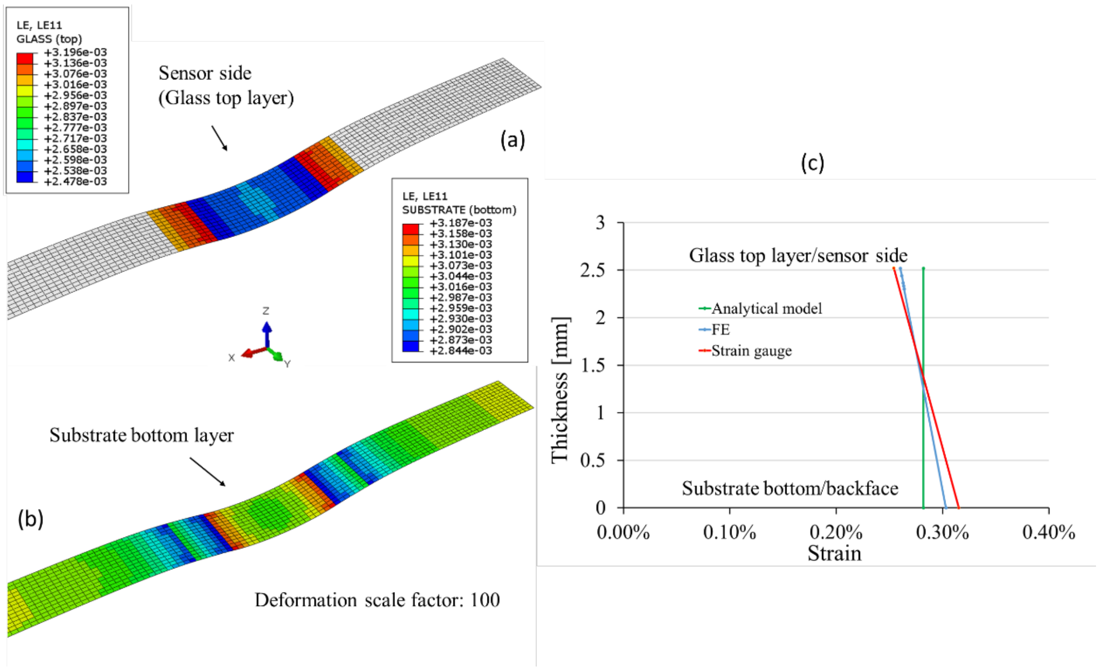

Figure 7.9. Contours of axial strain in the (a) top-most point of the glass layer; (b) bottom-most point of the substrate (c) comparison of through-thickness strain variation from different models and strain gauge measurements.

As shown in Table 7.9, the strain calculated by the analytical model exhibits a large deviation from the strain gauge results. It is due to the nature of the calculation not accounting for bending, which assumes uniform strains through the thickness of the laminate. The FEA model is much more realistic, capturing the actual geometry and boundary conditions of the specimen with the sensor (giving the deflected shape and variation along the length). However, the through thickness average strains are comparable: the value of the stiffness model and the FEA predictions have a deviation of only around 1% when compared to the experimental value. The reason for the small deviation are believed to arise from i) the assumptions made (material properties, boundary conditions) and ii) the accuracy of the measurement system (*e.g.* misalignment of gauges).

7.5.5.5. Damage visualization and trigger strain verification

Digital Image Correlation (DIC) and Acoustic Emission (AE) measurements have been carried out to verify the time and appearance of the first sensing layer fracture.

The strain distribution of a co-cured specimen with the optimal sensor configuration can be seen in Figure 7.10. The original specimen and the area used for the analysis is shown in Figure 7.10 (a), while the other plots show the strain distribution before carbon layer fragmentation in Figure 7.10 (b), at first crack appearance in Figure 7.10 (c), and after well dispersed cracking and local delamination in the hybrid composite sensor in Figure 7.10 (d). The area used for DIC analysis only covered half the width of each specimen, as the other half was used for visual confirmation of the sensor concept as illustrated in Figure 7.10 (a).

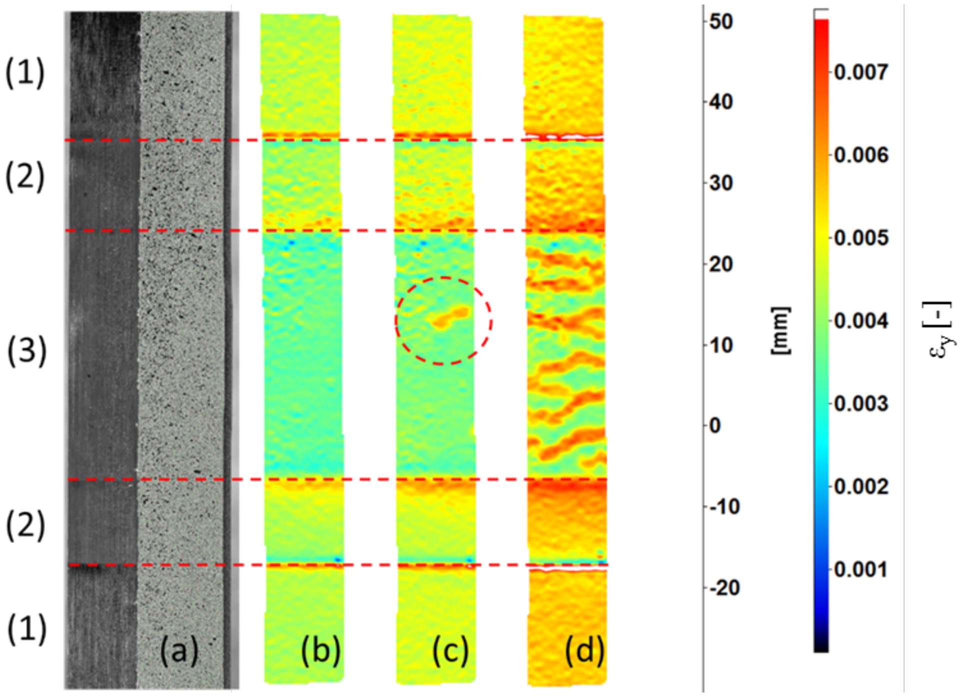

Figure 7.10. Longitudinal strain distribution of a specimen equipped with a co-cured single ply long XN80/epoxy and S-Glass/epoxy sensor. The figure illustrates (a) the original specimen and the area used for DIC analysis, (b) the strain distribution on the surface of the specimen before carbon layer fragmentation (c) at first crack appearance in the carbon sensing layer (d) after well-dispersed cracking and local delamination occurring in the hybrid sensor laminate.

The numbered regions in Figure 7.10 represent distinct areas of the specimens: (1) substrate only (2) substrate + glass layer and (3) substrate + glass + carbon sensing layer.

Local strain concentrations can be observed at the transitions between different material regions. In order to quantitatively assess the strain variation and more adequately resolve the strain field, a high resolution DIC measurement system should be used specifically directed at a smaller area - Region of Interest (ROI) - eg. around the sensors: region (3) on Figure 7.10 (a).

In order to further confirm how accurately the trigger strain of the sensors is determined, the results were also compared with acoustic emission measurements on the specimens. Figure 7.11 illustrates the (a) acoustic emission energy and (b) cumulative acoustic energy as a function of the applied load in the case of a co-cured specimen fitted with a long, single XN80/epoxy ply sensor.

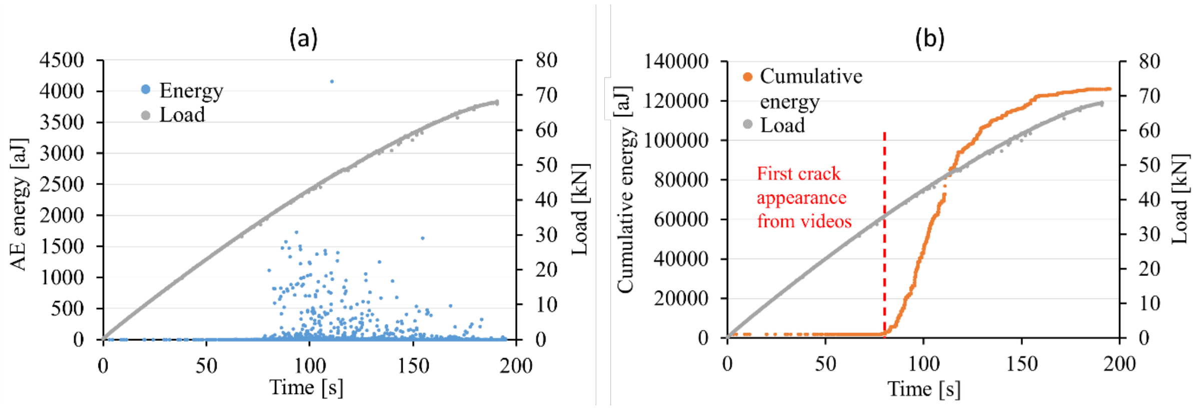

Figure 7.11. Typical AE results of a specimen fitted with the optimal sensor configuration: (a) acoustic emission energy and (b) cumulative energy in function of the applied uniaxial tensile load.

The onset of fragmentation in the sensing carbon layer is accompanied by a significant rise in the cumulative energy, as shown in Figure 7.11 (b). This corresponds to the AE energy diagram where fragmentation initiates at the same time as the rise of cumulative energy. The appearance of the striped pattern and the obtained AE signals show similarities with the work carried out by Fotouhi *et al.* [303] who correlated the number of AE events in a UD carbon/S-glass hybrid laminate with direct observations of fragmentation during the loading of the specimens.

According to Figure 7.11 (b), the onset of fragmentation from the AE starting at t = 84.69 s matches the appearance of the first crack in the carbon sensing layer observed and extracted from the recorded videos (t = 84.81 s).

7.5.5.6. Comparison of adhesives for retrofitted specimens

A brief study was carried out to determine the complexity and quality of the different bonding methods. It was concluded that the Araldite two-part epoxy adhesive, the MBond AE15 high elongation strain gauge epoxy adhesive and the Hexcel 913 resin film provided sufficient bonding when attaching sensors to the composite substrates. For these adhesives, all the sensors exhibited the expected striped pattern without any premature debonding. Overall, it can be stated that the Araldite epoxy system was the easiest and most cost efficient to apply, however the more expensive high strain MBond epoxy adhesive exhibited the best surface finish due to its translucent nature and low viscosity. The cyanoacrylate adhesive did not provide sufficient bonding between the sensor and the substrate material as the sensor delaminated during uniaxial tensile testing.

7.6. Application case study

In order to demonstrate the overload sensor concept, single ply XN80/epoxy short and long hybrid composite sensors were integrated on a commercially available carbon fibre reinforced polymer (CFRP) bike handlebar. The 3T Flat 720 Team Stealth mountain bike (MTB) mount flat handlebar was retrofitted with both long and short type sensors and a three-point bending test was carried out on the structure. The same test in a similar set-up was repeated for a handlebar without any sensors attached to it.

Due to the tubular shape of the component, the sensors had to be pre-curved in the appropriate direction (longitudinally or transversely to the fibres in the sensor) according to the loading conditions of the application. The sensor laminates were laid up onto an aluminium tube that was surface treated by a release agent (Loctite Freekote 700 NC). An envelope bagging process was applied on a hollow aluminium tool before autoclave curing.

The same diameter tooling was chosen, matching the curvature of the bike handlebars. For the retrofitting of these curved sensors, an Araldite 2014/1 type epoxy system has been utilised in a similar way to applying strain gauges for composite materials [304]. Additionally, to ensure a good surface quality and void free bonding, vacuum assisted envelope bagging was used when curing the adhesive in an atmospheric oven at 80 °C for 2 hrs.

The force-displacement curves of the tested mountain bike (MTB) handlebars can be seen in Figure 7.12. The graph highlights the point at which the long sensors activated as well as marking the load (1000 N) that generally applies for the testing of Racing Bicycle handlebars according to the European Standard (EN14781) [305].

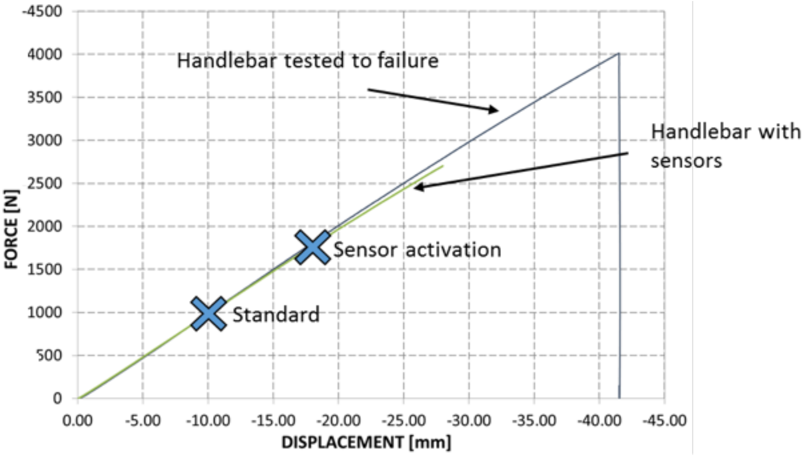

Figure 7.12. Force-displacement curves of the tested CFRP bike handlebars

Whilst the shorter sensors did not trigger for the applied load of 2700N, the first carbon layer fracture of the long sensors - visualizing the overload of the bar - was observed at 1750 N. It is worth noting that there was no stiffness increase observed on the force-displacement graphs indicating that the attached sensors did not make a significant difference to the loading of the tested handlebar.

The illustration of the handlebar with various sensors integrated to it can be seen in Figure 7.13. Overall, it can be said that the long sensors applied to the bike handlebar performed well in demonstrating the sensor concept and providing a warning to the user that an overload event had occurred.

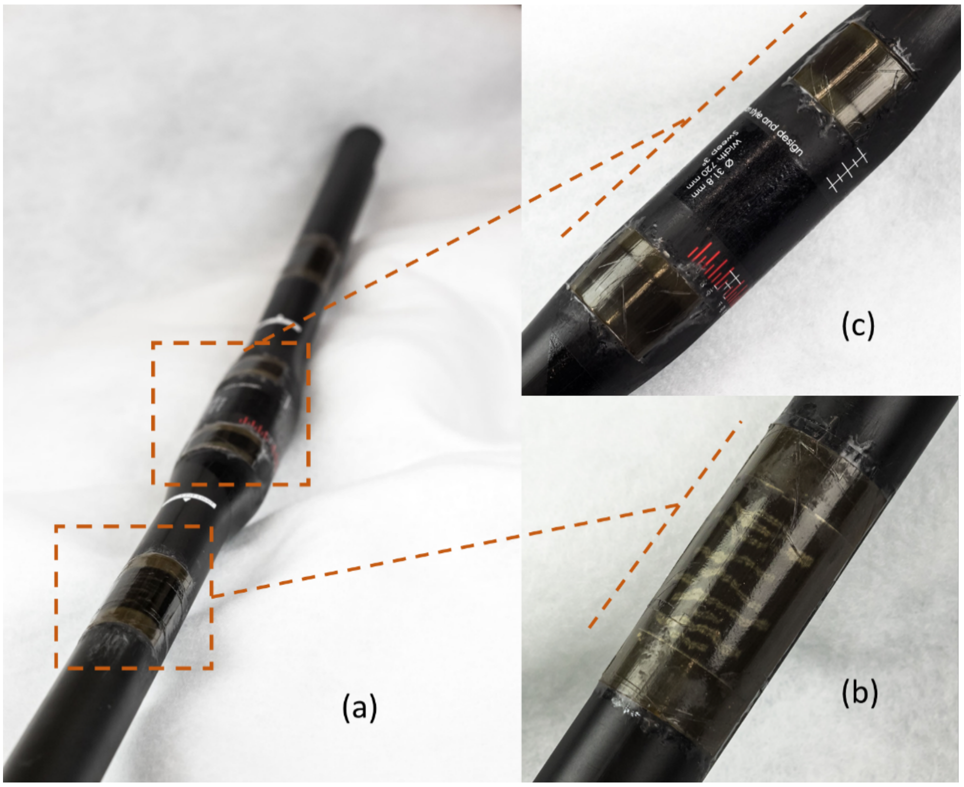

Figure 7.13. Bike handlebar fitted with hybrid composite overload sensors: (a) MTB Racing flat handlebar, retrofitted with (b) long single layer (c) short single layer sensors

7.7. Conclusion and future work

A novel Structural Health Monitoring (SHM) concept has been proposed that visually indicates the strain overload of a structure. The unidirectional (UD) hybrid composite sensors clearly exhibit a change in appearance when loaded over a predefined strain value. These purpose-designed composite sensors are lightweight, robust and completely wireless, hence it is a very promising technology in advanced safety-critical applications especially in the fields of sporting goods, civil engineering or pressure vessels.

They are highly tailorable as (i) they can be embedded or locally integrated to the structure, (ii) they can be designed for the desired application both in terms of the magnitude and direction of overload strain (applicable strain range: 0.3%-2%) and (iii) they can be designed for different substrate materials (including metals and composites).

The most important influencing parameters of such sensors are the ineffective length and the stiffness of the sensor relative to that of the substrate material. The sensor has to be designed for the substrate material/component for optimum performance.

An overall increase in the trigger strain was found for the shorter length sensors rendering them less accurate for overload strain indication. This is because a significant part of the short sensing layer was inactive. Therefore, it is recommended to use a sensor layer length of at least 5 times the critical length. An optimal configuration was found incorporating long single plies of XN80/epoxy and S-glass/epoxy material (30 mm for the sensing- and 50 mm for the translucent layer). The proof of concept of the presented hybrid composite sensors has been successfully demonstrated through mechanical characterisation on a coupon level and the integration of such sensors to a real-life application demonstrator: a CFRP bicycle handlebar.

Building up on the work presented here, a case study by Varkonyi B. [300] investigated methods to lower the trigger strain of the hybrid composite overload sensors and increase the applicability of the technology for high performance structural applications where allowable strains are rather low. The approaches were either using a different, lower failure strain and higher modulus carbon fibre sensing layer – YS-90 carbon/epoxy – or pre-weakening the sensing element in the hybrid sensors. By using a different material, a significant 18.5% decrease in the trigger strain was found when compared to the XN80 fibre type. Pre-weakening the sensing element reduced the trigger strain below 0.3%, expanding the strain range of the technology. Additionally, a new method was proposed to further understand the maximum strain experienced by the substrate material based on the failure pattern of the hybrid composite sensors.

Chapter 8

Conclusions and Future work

In the previous chapters various ways were presented showing how the failure of thin-ply carbon/epoxy composites can be controlled. The foundation to such laminate design was the basic characterisation of the material. Three concepts were presented with different multi-axial stress states imposed on the UD material through smart laminate design: the scissoring of angle-plies inducing transverse compression (Chapter 4) or transverse tension (Chapter 6), and thermal residual stresses generating transverse tension (Chapter 5). Additionally, a hybrid composite overload sensor concept was investigated that is based on the controlled failure of the incorporated thin-ply carbon/epoxy material. Overall, it can be said that the main aims and objectives of this thesis have been achieved. Firstly, novel specimen designs were created to investigate the effect of different stress components on the fibre direction failure strain/strength of the material. Secondly, thin-ply materials were successfully utilized to delay or suppress unwanted damage mechanisms such as micro-cracking and free edge delamination. By the combination of using thin-ply composites and designing for controlled failure (eg. by purpose designing the stress states within the material), reliable methods are developed that can help determine the failure properties rather accurately. In this chapter, the key findings are discussed in the context of failure prediction for composite materials and some directions for future work are also identified.

8.1. Conclusions

A framework was created using thin-ply materials that enables the development of novel laminate designs and tests to be carried out and acquire results that have not been previously possible.

The novelty of the PhD lies in generating in-plane multi-axial stress states in the UD material without having to apply additional external loads to the specimens. This way, such multi-axial loading scenarios can be imposed by using the simplest testing method in the mechanical characterisation of composites: a static tensile test. Additionally, the key limitation of such tensile tests – stress concentrations at the gripping areas – is also addressed by incorporating additional glass/epoxy layers to the laminate structure hence eliminating grip failures and providing an accurate representation of the material properties. The hybrid specimen testing method to eliminate stress concentrations was previously demonstrated only for UD composites, but in this thesis, it was successfully demonstrated for a range of multi-directional composite laminates and tests as well. Consequently, gauge section failures were achieved for different load cases both in tension and compression, under multi-axial loadings. These gauge section failures achieved are especially important as it was obtained whilst eg. having a very high in-plane transverse compression imposed on the UD layers.

The utilization of thin-ply composites allows for largely suppressing micro-cracking and edge delamination until reaching ultimate fibre failure which is usually catastrophic. Even if not all damage is suppressed, local damage does not necessarily cause significant reduction in the mechanical properties (see Chapter 5), yet it makes it possible to extend the ‘straining window’ of composite structures. The capability of the examined thin-ply carbon/epoxy has been proven through various characterisation tests as well as through controlled failure tests using smart laminate design.

Overall, when examining the tension side of the failure locus, the three stress components that can affect tensile failure are tension, compression and shear. In this thesis, it was demonstrated that (even very high) in-plane transverse compressive stresses do not significantly affect the tensile failure strain.

For shear, it was concluded previously by Jalalvand *et al.* [134] that in-plane shear stress does not have a significant influence on the tensile failure strain of TC35 carbon/epoxy composites as highlighted in the concluding remarks of Chapter 4.

With regard to in-plane transverse tension, it was shown that the generated stresses were sufficient to induce cracks in the 90° layers adjacent to the central 0° block in the cross-ply configurations. Transverse cracks could be expected to impose a larger effect on failure (due to the arising stress concentrations) than the stresses generated prior the initiation of micro-cracking. Matrix cracking was found to be a parameter influencing the tensile strength properties, but its overall effect is considered small. Consequently, one can postulate that the generated transverse tensile stresses are unlikely to significantly affect tensile failure either. Concluding for the tension quadrant, it can be inferred that other stress components do not have a significant influence on the tensile failure properties. To look at the impact of such results, it has to be noted that a lot of industries use the Maximum Stress or Maximum Strain (limit) criteria (not taking the interaction of other stress components into account) as the basis of their designs. Hence, the results presented (using maximum strain as failure allowable) for tension are consistent with what is often done in industry, provided that the strain is reasonably conservatively taken.

Compression in general seems to be more sensitive to transverse stresses than tension, hence the conclusions on tensile failure criteria do not apply in this case. It was shown, that transverse cracks due to transverse tensile stresses can result in a reduction in the longitudinal compressive strength of the material.

The interaction of compression and shear was also investigated for example by Jelf and Fleck [306] who showed a decrease in compressive strength with increasing shear stresses for composite tubes under combined compression and torsion. Industrial design for compression failure is highly influenced by impact damage considerations. Hence standard failure criteria and laminate analysis alone may not be sufficient to design composite structures against compressive loadings.

An additional impact is that by the findings of this PhD and the reliable experimental data generated, a more comprehensive understanding of the failure and damage mechanisms of these thin prepregs was achieved that provides added value to the existing literature on composite materials and makes it possible to compare with existing failure theories and models.

Finally, the presented UD hybrid composite sensors offer a reliable solution to indicate the overload of structures and components, especially since composite materials fail catastrophically, usually without warning of any kind. These sensors can be used in industry for Structural Health Monitoring (SHM) and if overload is indicated with enough accuracy and in time, smaller safety margins could be implemented.

8.2. Future work

The work presented in this thesis covered various aspects of thin-ply, multidirectional laminates and in this section, some key areas will be covered where further investigation is recommended by the author with regard to the specific chapters presented.

Overall, the author recommends looking at the interaction of longitudinal compression and transverse compression as future work to complete the investigation with regard to the compression loading quadrant. Furthermore, it is recommended that the developed laminate designs and generated multi-axial stress states should be applied to different types of carbon composite materials.

Chapter 3

As can be seen in Chapter 4, the angle-ply/UD specimens exhibited a highly non-linear behaviour under combined loading of longitudinal tension and transverse compression. To further investigate this non-linearity, better understand the material behaviour in the transverse direction and estimate the shear stresses in the angle-ply laminates more accurately, the transverse compressive stress-strain response of the material needs to be characterised for TC33/K51. Hence, it is suggested to use thicker specimens or design a better fixture so that transverse compression tests can be carried out to determine the material strength and feed it back to design and analysis.

Chapter 4

In the experimental campaign the longitudinal and transverse strains are measured for the different configurations with varying amount of transverse compression generated in the UD plies. From the measured strains, linear assumptions were used to estimate the stresses generated in the laminates taking account for the Poisson effect and the thermal residual stresses. Since non-linearity plays an important role in the mechanical response of such thin-ply carbon epoxy, a non-linear approach could be used for estimation of the stresses. The applied strains remain high in relation to the load bearing capacity of the fibres. A suggestion for better representation of stresses is to utilize a progressive failure model such as the OPFM used in Chapter 6 and compare the results with the linear estimations.

Chapter 5

It is recommended to use alternative approaches such as auxetic laminate design [181] (exhibiting a negative major Poisson's ratio) to design laminates exhibiting a multi-axial stress state of longitudinal tension and transverse tension in the material. Often in such designs, other stresses such as shear could be present in the laminates. However, when investigating the coupled behaviour with shear present in the laminate - knowing that shear does not affect the tensile failure – conclusions could be drawn on the interaction of longitudinal tension and transverse tension as well as on the combination of all three stress components present at the same time. With regard to the presented results, it can be stated that the reduction of strength due to the presence of free-edge and transverse cracks is small and has been qualitatively explained. However, to gain more understanding of the magnitude of stress concentrations imposed by the edge cracking on the UD strength, a 3D analysis with a fine mesh through the thickness and interface elements between the plies is recommended to be carried out.

Chapter 6

The damage state of the specimens needs further examination in order to be able to verify the presence or absence of transverse cracks in the Type I and Type II laminates. Acquiring such data would enable more definite conclusions on ply thickness effects and the strength reduction trends observed. Potentially, in-situ X-CT examination of interrupted specimens, and/or optical microscopy observations could provide such information about the fabricated coupons.

Chapter 7

For the development of the sensor technology presented, the key parameters identified in the chapter (ineffective length and the stiffness of the sensor relative to that of the substrate material) as well as the underlying failure mechanism need to be further studied. For the design of such sensors, new material combinations exhibiting similar failure patterns can be exploited. It is also suggested to look at the potential of surface sensing (incorporating a full sensing layer) for detecting overload over the full surface of a structure/component.

Chapter 9

Bibliography

[1] Adrian P. Mouritz, *Introduction to aerospace materials*. Woodhead Publishing, 2012.

[2] A. Quilter, “Composites in Aerospace Applications,” *Inf. Handl. Serv. Inc.*, pp. 1–5, 2004.

[3] T. Ishikawa *et al.*, “Overview of automotive structural composites technology developments in Japan,” *Compos. Sci. Technol.*, vol. 155, pp. 221–246, 2018.

[4] G. Martínez-Barrera, O. Gencel, and J. M. L. Reis, “Civil Engineering Applications of Polymer Composites,” *International Journal of Polymer Science*, vol. 2016, pp. 1–2, 2016.

[5] A. C. Long, *Design and Manufacture of Textile Composites*. Woodhead Publishing, 2006.

[6] W. D. Callister and D. G. Rethwisch, *Materials Science and Engineering: An Introduction*. 2010.

[7] P. Beaumont, “50 Years of Carbon Fibre,” *Appl. Compos. Mater.*, vol. 24, no. 2, pp. 271–275, 2017.

[8] R. Matulka, “Top 9 Things You Didn’t Know about Carbon Fiber - US. Department of Energy,” 2013. [Online]. Available: https://www.energy.gov/articles/top-9-things-you-didn-t-know-about-carbon-fiber.

[9] N. M. Chowdhury, W. K. Chiu, J. Wang, and P. Chang, “Experimental and finite element studies of bolted, bonded and hybrid step lap joints of thick carbon fibre/epoxy panels used in aircraft structures,” *Compos. Part B Eng.*, vol. 100, pp. 68–77, 2016.

[10] N. Guermazi, A. Ben Tarjem, I. Ksouri, and H. F. Ayedi, “On the durability of FRP composites for aircraft structures in hygrothermal conditioning,” *Compos. Part B Eng.*, vol. 85, pp. 294–304, 2013.

[11] Dr Roland Thévenin, “Airbus A380 Composite applications.” [Online]. Available: https://www.niar.wichita.edu/niarworkshops/Portals/0/Wednesday_945_Thevenin.pdf.

[12] G. Czél, M. Jalalvand, and M. R. Wisnom, “Demonstration of pseudo-ductility in unidirectional hybrid composites made of discontinuous carbon/epoxy and

continuous glass/epoxy plies," *Compos. Part A Appl. Sci. Manuf.*, vol. 72, pp. 75–84, May 2015.

[13] Q. Yangyang, C. Bisagni, and Y. Bai, "Experimental investigation and numerical simulation of unidirectional carbon fiber composite under multi-axial loadings," *Compos. Part B Eng.*, vol. 124, pp. 190–206, Sep. 2017.

[14] A. Kaddour and M. Hinton, "Maturity of 3D failure criteria for fibre-reinforced composites: Comparison between theories and experiments: Part B of WWFE-II," *J. Compos. Mater.*, vol. 47, no. 6–7, pp. 925–966, 2013.

[15] A. Kaddour, M. Hinton, and P. Smith, "The background to the third world-wide failure exercise," *J. Compos. Mater.*, vol. 47, no. 20–21, pp. 2417–2426, 2013.

[16] A. Kaddour, M. Hinton, P. Smith, and S. Li, "A comparison between the predictive capability of matrix cracking, damage and failure criteria for fibre reinforced composite laminates: Part A of the third world-wide failure exercise," *J. Compos. Mater.*, vol. 47, no. 20–21, pp. 2749–2779, 2013.

[17] M. J. Hinton, P. D. Soden, and A. S. Kaddour, "A Comparison of the Predictive Capabilities of Current Failure Theories for Composite Laminates, judged against experimental evidence," *Compos. Sci. Technol.*, vol. 62, pp. 1725–1797, 2002.

[18] R. M. Christensen, "Why progress on the failure of fiber composite materials has been so retarded," *J. Reinf. Plast. Compos.*, vol. 0, no. 0, pp. 1–3, 2017.

[19] J. S. Welsh and J. S. Mayes, "Recent biaxial test results of laminated composites and analytical MCT predictions," *49th International SAMPE Symposium and Exhibition: Materials and Processing Technology - 60 Years of SAMPE Progress, SAMPE 2004*. pp. 679–693, 2004.

[20] G. Czél, M. Jalalvand, and M. R. Wisnom, "Hybrid specimens eliminating stress concentrations in tensile and compressive testing of unidirectional composites," *Compos. Part A Appl. Sci. Manuf.*, vol. 91, pp. 436–447, 2016.

[21] M. R. Wisnom, "The Challenge of Predicting Failure in Composites," *19th Int. Conf. Compos. Mater.*, pp. 12–13, 2013.

[22] T. L. Anderson, *Fracture Mechanics: Fundamentals and Applications*. Boca Raton: CRC Press, 2005.

[23] P. K. Mallick, *Compsites Engineering Handbook*. Marcel Dekker, 1997.

[24] C. T. Herakovich, *Mechanics of Fibrous Composites*. New York: John Wiley & Sons, Inc., 1998.

[25] A. S. D. Wang, "Fracture analysis of matrix cracking in laminated composites.," in *Aircraft and Crew Systems Technology Directorate, Naval Air Development Center, Report no. NADC-85118-60*, 1985.

[26] M. R. Wisnom, "The role of delamination in failure of fibre-reinforced composites," *Philos. Trans. R. Soc. A Math. Phys. Eng. Sci.*, vol. 370, no. 1965, pp. 1850–1870,

2012.

[27] J. C. Brewer and P. A. Lagace, "Quadratic Stress Criterion for Initiation of Delamination," *J. Compos. Mater.*, vol. 22, no. 12, pp. 1141–1155, 1988.

[28] Y. W. Kwon and C. T. Liu, "Study of damage evolution in composites using damage mechanics and micromechanics," *Compos. Struct.*, vol. 38, no. 1–4, pp. 133–139, 1997.

[29] L. Tong, "An Assessment of Failure Criteria to Predict the Strength of Adhesively Bonded Composite Double Lap Joints," *Jounral Reinf. Plast. Compos.*, vol. 16, no. 8, pp. 698–713, 1997.

[30] A. C. Orifici, I. Herszberg, and R. S. Thomson, "Review of methodologies for composite material modelling incorporating failure," *Compos. Struct.*, vol. 86, no. 1–3, pp. 194–210, 2008.

[31] M. Rajanish, N. V Nanjundaradhya, and R. S. Sharma, "A review of failure of composite materials," *Int. J. Eng. Res. Appl.*, vol. 3, no. 2, pp. 122–124, 2013.

[32] M. J. Hinton and P. D. Soden, "Predicting failure in composite laminates: the background to the exercise," *Compos. Sci. Technol.*, vol. 58, no. 7, pp. 1001–1010, Jul. 1998.

[33] M. J. Hinton, A. S. Kaddour, and P. D. Soden, "Predicting Failure in Fibre Composites : Lessons Learned From the World-Wide Failure Exercise," in *ICCM 13 - 13th International Conference on Composite Materials*, 2000, no. November, pp. 1–13.

[34] C. T. Sun, B. J. Quinn, and J. Tao, "Comparative Evaluation of Failure Analysis Methods for Composite Laminates.," in *U.S. Department of Transportation, Report no. DOT/FAA/AR-95/109*, 1996, no. May.

[35] M. N. Nahas, "Survey of Failure and Post-Failure Theories of Laminated Fiber-Renforced Composites," *J. Compos. Technol. Res.*, vol. 8, no. 4, pp. 138–153, 1986.

[36] A. De Luca and F. Caputo, "A review on analytical failure criteria for composite materials," *AIMS Mater. Sci.*, vol. 4, no. 5, pp. 1165–1185, 2017.

[37] I. M. Daniel, "Failure of composite materials," *Strain*, vol. 43, no. 1, pp. 4–12, 2007.

[38] S. W. Tsai, "Strength characteristics of composite materials," in *Report no. NASA CR-224*, 1965.

[39] B. R. Producers and N. Bureau, "A theory of the yielding and plastic flow of anisotropic metals," *Proc. R. Soc. London. Ser. A. Math. Phys. Sci.*, vol. 193, no. 1033, pp. 281–297, 1948.

[40] S. W. Tsai and E. M. Wu, "A General Theory of Strength for Anisotropic Materials," *J. Compos. Mater.*, vol. 5, no. 1, pp. 58–80, 1971.

[41] O. Hoffman, "The Brittle Strength of Orthotropic Materials," *J. Compos. Mater.*,

vol. 1, no. 1967, pp. 200–206, 1967.

[42] Hashin Z., “Failure Criteria for Unidirectional Fiber Composites,” *ASME. J. Appllied Mech.*, vol. 47, no. 2, pp. 329–334, 1980.

[43] A. Puck and H. Schu, “Failure Analysis of Frp Laminates By Means of Physically Based Phenomenological Models1,” *Compos. Sci. Technol.*, vol. 58, no. 7, pp. 1045–1067, 1998.

[44] L. J. Hart-Smith, “Predictions of the original and truncated maximum-strain failure models for certain fibrous composite laminates,” *Compos. Sci. Technol.*, vol. 58, no. 1998, pp. 1151–1178, 1998.

[45] J. H. Gosse and S. Christensen, “Strain invariant failure criteria for polymers in composite materials,” in *19th AIAA Applied Aerodynamics Conference*, 2001.

[46] P. A. Zinoviev, S. V. Grigoriev, O. V. Lebedeva, and L. P. Tairova, “The strength of multilayered composites under a plane-stress state,” *Compos. Sci. Technol.*, vol. 58, pp. 1209–1223, 1998.

[47] L. Kroll and W. Hufenbach, “Physically Based Failure Criterion for Dimensioning of Thick-Walled Laminates,” *Appl. Compos. Mater.*, vol. 4, no. 5, pp. 321–332, 1997.

[48] S. E. Yamada and C. T. Sun, “Analysis of Laminate Strength and Its Distribution,” *J. Compos. Mater.*, vol. 12, no. 3, pp. 275–284, 1978.

[49] R. G. Cuntze, “The predictive capability of failure mode concept-based strength criteria for multi-directional laminates-Part B,” *Compos. Sci. Technol.*, vol. 64, pp. 343–377, 2004.

[50] H. G. Franklin, “Classic Theories of Failure of Anisotropic Materials,” *Fibre Sci. Technol.*, pp. 137–150, 1968.

[51] Z. Hashin and A. Rotem, “A Fatigue Failure Criterion for Fiber Reinforced Materials,” in *Air Force Office of Scientific research, MED Report no. 39, Scientific report no.3.*, 1973, no. March.

[52] C. G. Dávila, P. P. Camanho, and C. A. Rose, “Failure criteria for FRP laminates,” *J. Compos. Mater.*, vol. 39, no. 4, pp. 323–345, 2005.

[53] A. Puck and H. Schürmann, “Failure analysis of FRP laminates by means of physically based phenomenological models,” *Compos. Sci. Technol.*, vol. 58, pp. 1045–1067, 1998.

[54] R. M. Christensen, “Tensor Transformations and Failure Criteria for the Analysis of Fiber Composite Materials Part II: Necessary and Sufficient Conditions for Laminate Failure,” *J. Compos. Mater.*, vol. 22, pp. 874–897, 1990.

[55] R. S. Sandhu, “Ultimate strength analysis of symmetric laminates,” *Air Force Flight Dyn. Lab. Wright-Patterson Air Force Base, Ohio*, 1974.

[56] P. S. Theocaris, “Weighing Failure Tensor Polynomial Criteria for Composites,”

Int. J. Damage Mech., vol. 1, no. 1, pp. 4–46, 1992.

[57] C. H. Kim and H. Y. Yeh, "Development of a new yielding criterion: The Yeh-Stratton criterion," *Eng. Fract. Mech.*, vol. 47, no. 4, pp. 569–582, 1994.

[58] J. Echaabi and F. Trochu, "Failure Mode Dependent Strength Criteria for Composite Laminates," *J. Reinf. Plast. Compos.*, vol. 16, no. 10, pp. 926–945, 1997.

[59] P. F. Liu and J. Y. Zheng, "Recent developments on damage modeling and finite element analysis for composite laminates: A review," *Mater. Des.*, vol. 31, no. 8, pp. 3825–3834, Sep. 2010.

[60] K. Hayakawa, S. Murakami, and Y. Liu, "An irreversible thermodynamics theory for elastic-plastic-damage materials," *Eur. J. Mech. A/Solids*, vol. 17, no. 1, pp. 13–32, 1998.

[61] S. Murakami and K. Kamiya, "Constitutive and damage evolution equations of elastic-brittle materials based on irreversible thermodynamics," *Science (80-.).*, vol. 39, no. 4, pp. 473–486, 1997.

[62] R. A. Schapery, "A theory of mechanical behavior of elastic media with growing damage and other changes in structure," *J. Mech. Phys. Solids*, vol. 38, no. 2, pp. 215–253, 1990.

[63] M. Olsson and M. Ristinmaa, "Damage Damage Evolution in Elasto-plastic Materials - Material Response Due to Different Concepts," *Int. J. Damage Mech.*, vol. 12, no. April 2003, pp. 115–139, 2003.

[64] P. Maimí, P. P. Camanho, J. A. Mayugo, and C. G. Dávila, "A continuum damage model for composite laminates: Part II - Computational implementation and validation," *Mech. Mater.*, vol. 39, no. 10, pp. 909–919, 2007.

[65] A. Matzenmiller, J. Lubliner, and R. L. Taylor, "A constitutive model for anisotropic damage in fiber-composites," *Mech. Mater.*, vol. 20, pp. 125–152, 1995.

[66] R. Maa and J. Cheng, "A CDM-based failure model for predicting strength of notched composite laminates," *Compos. Part B Eng.*, vol. 33, pp. 479–489, 2002.

[67] P. P. Camanho, P. Maimí, and C. G. Dávila, "Prediction of size effects in notched laminates using continuum damage mechanics," *Compos. Sci. Technol.*, vol. 67, no. 13, pp. 2715–2727, 2007.

[68] J. H. A. Schipperen, "An anistropic damage model for the description of transversematrix cracking in a graphite-epoxy laminate," *Compos. Struct.*, vol. 53, no. 3, pp. 295–299, 2001.

[69] M. V. Donadon, S. F. M. de Almeida, M. A. Arbelo, and A. R. de Faria, "A Three-Dimensional Ply Failure Model for Composite Structures," *Int. J. Aerosp. Eng.*, vol. 2009, pp. 1–22, 2009.

[70] R. Talreja, *Damage Mechanics of Composite Materials*. Elsevier Science, 1994.

[71] F. P. Van Der Meer and L. J. Sluys, "Continuum models for the analysis of progressive failure in composite laminates," *J. Compos. Mater.*, vol. 43, no. 20, pp. 2131–2156, 2009.

[72] N. Germain, J. Besson, and F. Feyel, "Composite layered materials: Anisotropic nonlocal damage models," *Comput. Methods Appl. Mech. Eng.*, vol. 196, no. 41–44, pp. 4272–4282, 2007.

[73] I. Lapczyk and J. A. Hurtado, "Progressive damage modeling in fiber-reinforced materials," *Compos. Part A Appl. Sci. Manuf.*, vol. 38, no. 11, pp. 2333–2341, 2007.

[74] P. Maimí, P. P. Camanho, J. A. Mayugo, and C. G. Dávila, "A continuum damage model for composite laminates: Part II - Computational implementation and validation," *Mech. Mater.*, vol. 39, no. 10, pp. 909–919, 2007.

[75] S. T. Pinho, L. Iannucci, and P. Robinson, "Physically based failure models and criteria for laminated fibre-reinforced composites with emphasis on fibre kinking. Part II: FE implementation," *Compos. Part A Appl. Sci. Manuf.*, vol. 37, no. 5, pp. 766–777, 2006.

[76] V. Laš and R. Zemčík, "Progressive damage of unidirectional composite panels," *J. Compos. Mater.*, vol. 42, no. 1, pp. 25–44, 2008.

[77] P. Ladeveze, "A damage computational approach for composites: Basic aspects and micromechanical relations," *Comput. Mech.*, vol. 17, no. 1–2, pp. 142–150, 1995.

[78] B. El Said, F. Daghia, D. Ivanov, and S. R. Hallett, "An iterative multiscale modelling approach for nonlinear analysis of 3D composites," *Int. J. Solids Struct.*, vol. 132–133, pp. 42–58, 2018.

[79] T. E. Tay, G. Liu, V. B. C. Tan, X. S. Sun, and D. C. Pham, "Progressive failure analysis of composites," *J. Compos. Mater.*, vol. 42, no. 18, pp. 1921–1966, 2008.

[80] J. Llorca *et al.*, "Multiscale modeling of composite materials: A roadmap towards virtual testing," *Adv. Mater.*, vol. 23, no. 44, pp. 5130–5147, 2011.

[81] P. Kanouté, D. P. Boso, J. L. Chaboche, and B. A. Schrefler, "Multiscale methods for composites: A review," *Arch. Comput. Methods Eng.*, vol. 16, no. 1, pp. 31–75, 2009.

[82] A. A. Griffith, "The phenomena of rapture and flow in soilds," *Philosophical Transactions of the Royal Society of London*, vol. 221. pp. 163–198, 1920.

[83] L. Banks-Sills, "Application of the Finite Element Method to Linear Elastic Fracture Mechanics," *Appl. Mech. Rev.*, vol. 44, no. 10, pp. 447–461, Oct. 1991.

[84] J. Awerbuch and M. S. Madhukar, "Notched Strength of Composite Laminates: Predictions and Experiments--A Review," *J. Reinf. Plast. Compos.*, vol. 4, no. 1, pp. 3–159, 1985.

[85] M. F. Kanninen, E. F. Rybicki, and H. F. Brinson, “A critical look at current applications of fracture mechanics to the failure of fibre-reinforced composites,” *Composites*, vol. 8, no. 1, pp. 17–22, 1977.

[86] R. Krueger, “Computational Fracture Mechanics for Composites - State of the Art and Challenges,” in *NTRS NASA Report*, 2004.

[87] D. Van Hemelrijck, A. Makris, C. Ramault, E. Lamkanfi, W. Van Paepegem, and D. Lecompte, “Biaxial testing of fibre-reinforced composite laminates,” *Proc. Inst. Mech. Eng. Part L J. Mater. Des. Appl.*, vol. 222, no. 4, pp. 231–239, 2008.

[88] A. Smits *et al.*, “A Review of Biaxial Test Methods for Composites,” *Exp. Anal. Nano Eng. Mater. Struct.*, no. i, pp. 933–934, 2007.

[89] F. Pierron and A. Vautrin, “The 10° off-axis tensile test: A critical approach,” *Compos. Sci. Technol.*, vol. 56, no. 4, pp. 483–488, 1996.

[90] C. C. Chamis and J. H. Sinclair, “10° off-axis test for shear properties in fiber composites,” *NASA Tech. Memo. No. 73550*, 1971.

[91] P. W. Beaver, “A review of multiaxial fatigue and fracture of fibre reinforced composites,” *Dep. Defence, Def. Sci. Technol. Organ. Aeronaut. Res. Lab.*, 1937.

[92] A. S. Chen and F. L. Matthews, “A review of multiaxial/biaxial loading tests for composite materials,” *Composites*, vol. 24, no. 5, pp. 395–406, 1993.

[93] H. Thom, “A review of the biaxial strength of fibre-reinforced plastics,” *Compos. Part A Appl. Sci. Manuf.*, vol. 29, no. 8, pp. 869–886, 1998.

[94] R. Olsson, “A survey of test methods for multiaxial and out-of-plane strength of composite laminates,” *Compos. Sci. Technol.*, vol. 71, no. 6, pp. 773–783, 2011.

[95] S. R. Swanson, A. P. Christoforou, and G. E. Colvin, “Biaxial testing of fiber composites using tubular specimens,” *Exp. Mech.*, vol. 28, no. 3, pp. 238–243, 1988.

[96] S. R. Swanson, “Strength design criteria for carbon/epoxy pressure vessels,” *J. Spacecr. Rockets*, vol. 27, no. 5, pp. 522–526, Sep. 1990.

[97] S. R. Swanson, M. J. Messick, and Z. Tian, “Failure of Carbon/Epoxy Lamina Under Combined Stress,” *J. Compos. Mater.*, vol. 21, no. 7, pp. 619–630, 1987.

[98] D. Cohen, “Multi-Axial Composite Tube Test Method,” in *Composite Materials: Testing and Design and Acceptance Criteria, ASTM STP 1416*, 2002.

[99] J. S. Welsh, J. S. Mayes, and A. C. Biskner, “2-D biaxial testing and failure predictions of IM7/977-2 carbon/epoxy quasi-isotropic laminates,” *Compos. Struct.*, vol. 75, no. 1–4, pp. 60–66, 2006.

[100] J. S. Welsh and D. F. Adams, “An experimental investigation of the biaxial strength of IM6/3501-6 carbon/epoxy cross-ply laminates using cruciform specimens,” *Compos. - Part A Appl. Sci. Manuf.*, vol. 33, no. 6, pp. 829–839, 2002.

[101] A. Smits, D. Van Hemelrijck, T. P. Philippidis, and A. Cardon, “Design of a cruciform specimen for biaxial testing of fibre reinforced composite laminates,” *Compos. Sci. Technol.*, vol. 66, no. 7–8, pp. 964–975, 2006.

[102] M. Arcan, Z. Hashin, and A. Voloshin, “A method to produce uniform plane-stress states with applications to fiber-reinforced materials - A specially designed specimen yields material properties under pure shear or uniform plane-stress conditions,” *Exp. Mech.*, vol. 18, no. 4, pp. 141–146, 1978.

[103] S. T. Taher, O. T. Thomsen, J. M. Dulieu-Barton, and S. Zhang, “Determination of mechanical properties of PVC foam using a modified Arcan fixture,” *Compos. Part A Appl. Sci. Manuf.*, vol. 43, no. 10, pp. 1698–1708, 2012.

[104] J. L. Y. Tan, V. S. Deshpande, and N. A. Fleck, “Failure mechanisms of a notched CFRP laminate under multi-axial loading,” *Compos. Part A Appl. Sci. Manuf.*, vol. 77, pp. 56–66, 2015.

[105] A. Voloshin and M. Arcan, “Failure of unidirectional fiber-reinforced materials—New methodology and results,” *Exp. Mech.*, vol. 20, no. 8, pp. 280–284, 2006.

[106] K. W. Gan, T. Laux, S. T. Taher, J. M. Dulieu-Barton, and O. T. Thomsen, “A novel fixture for determining the tension/compression-shear failure envelope of multidirectional composite laminates,” *Compos. Struct.*, vol. 184, no. October 2017, pp. 662–673, 2018.

[107] T. Laux, K. W. Gan, J. M. Dulieu-Barton, and O. T. Thomsen, “A simple nonlinear constitutive model based on non-associative plasticity for UD composites: Development and calibration using a Modified Arcan Fixture,” *Int. J. Solids Struct.*, vol. 162, pp. 135–147, 2019.

[108] B. Vanden Broucke and M. C. D. E. Verdiere, “Failure and Impact Modelling of Textile composites: ITOOL PROJECT,” no. June 2014, pp. 227–232, 2007.

[109] T. Laux, K. W. Gan, J. M. Dulieu-Barton, and O. T. Thomsen, “Ply thickness and fibre orientation effects in multidirectional composite laminates subjected to combined tension/compression and shear,” *Compos. Part A Appl. Sci. Manuf.*, vol. 133, no. November 2019, p. 105864, 2020.

[110] Y. Swolfs, I. Verpoest, and L. Gorbatikh, “Recent advances in fibre-hybrid composites : materials selection , opportunities and applications,” *Int. Mater. Rev.*, pp. 1–35, 2018.

[111] K. R. Berg, “Typical properties for advanced composites,” in *Handbook of Composites*, 1998, p. Appendix A.

[112] “Skyflex prepreg - Material selection guide.” [Online]. Available: https://www.skchemicals.com/page/business/bs_skyflex.do.

[113] MIL-HDBK-17-1F, *Composite Materials Handbook - Polymer Matrix Composites Guidelines for Characterisation of Structural Materials*, vol. 1, no. June. U.S. Department of Defense, 2002.

[114] ASTM, “ASTM D3529M - Standard Test Methods for Constituent Content of Composite Prepreg,” *Annu. B. ASTM Stand.*, vol. 10.

[115] ASTM, “ASTM D3039/D3039M - Tensile Properties of Polymer Matrix Composite Materials,” *Annu. B. ASTM Stand.*, vol. 12, pp. 1–13.

[116] ASTM, “ASTM D3518/D3518M - Standard Test Method for In-Plane Shear Response of Polymer Matrix Composite Materials by Tensile Test of a 45 ° Laminate,” *Annu. B. ASTM Stand.*, vol. 94, pp. 1–7.

[117] J. Fuller, “PhD Thesis - Pseudo-ductility of thin ply angle-ply laminates,” University of Bristol, 2015.

[118] “Imetrum video gauge system.” [Online]. Available: www.imetrum.com.

[119] F. Laurin, N. Carrère, and J. F. Maire, “A multiscale progressive failure approach for composite laminates based on thermodynamical viscoelastic and damage models,” *Compos. Part A Appl. Sci. Manuf.*, vol. 38, no. 1, pp. 198–209, 2007.

[120] L. P. Kollár and G. S. Springer, “Mechanics of Composite Structures.” Cambridge Univeristy Press (2013).

[121] J. G. Häberle and F. L. Matthews, “An improved technique for compression testing of unidirectional fibre-reinforced plastics; development and results,” *Composites*, vol. 25, no. 5, pp. 358–371, 1994.

[122] L. J. Hart-Smith, “A Strain-Based Maximum-Shear-Stress Failure Criterion For Fibrous Composites,” in *AIAA Structures, Structural Dynamics and Materials Conference*, 1990.

[123] M. R. Wisnom, “The effect of transverse compressive stresses on tensile failure of glass fibre-epoxy,” *Compos. Struct.*, vol. 32, no. 1–4, pp. 621–626, 1995.

[124] S. R. Swanson and Y. Qian, “Multiaxial characterization of T800/3900-2 carbon/epoxy composites,” *Compos. Sci. Technol.*, vol. 43, no. 2, pp. 197–203, 1992.

[125] G. Catalanotti, P. P. Camanho, and A. T. Marques, “Three-dimensional failure criteria for fiber-reinforced laminates,” *Compos. Struct.*, vol. 95, pp. 63–79, 2013.

[126] S. Sihn, R. Y. Kim, K. Kawabe, and S. W. Tsai, “Experimental studies of thin-ply laminated composites,” *Compos. Sci. Technol.*, vol. 67, no. 6, pp. 996–1008, 2007.

[127] X. Xu and M. R. Wisnom, “An experimental and numerical investigation of the interaction between splits and edge delaminations in [+20m /-20m]ns carbon / epoxy laminates,” in *European Conference on Composite Materials - ECCM-15*, 2012, no. June, pp. 24–28.

[128] J. D. Fuller and M. R. Wisnom, “Pseudo-ductility and damage suppression in thin ply CFRP angle-ply laminates,” *Compos. Part A Appl. Sci. Manuf.*, vol. 69, pp. 64–71, Feb. 2015.

[129] J. Cugnoni *et al.*, “Towards aerospace grade thin-ply composites: Effect of ply

thickness, fibre, matrix and interlayer toughening on strength and damage tolerance," *Compos. Sci. Technol.*, vol. 168, no. August, pp. 467–477, 2018.

[130] J. Galos, "Thin-ply composite laminates: a review," *Compos. Struct.*, vol. 236, no. January, 2020.

[131] A. Arteiro, C. Furtado, G. Catalanotti, P. Linde, and P. P. Camanho, "Thin-ply polymer composite materials: a review," *Compos. Part A Appl. Sci. Manuf.*, p. 105777, 2020.

[132] T. Rev, G. Czél, and M. R. Wisnom, "A novel test method to induce bi-axial stress states in thin-ply carbon composites under combined longitudinal tension and transverse compression," in *ASC 33rd Annual Technical Conference on Composite Materials*, 2018.

[133] M. R. Wisnom, G. Czél, Y. Swolfs, M. Jalalvand, L. Gorbatikh, and I. Verpoest, "Hybrid effects in thin ply carbon/glass unidirectional laminates: Accurate experimental determination and prediction," *Compos. Part A Appl. Sci. Manuf.*, vol. 88, pp. 131–139, 2016.

[134] M. Jalalvand, M. Fotouhi, M. C. Leong, and M. R. Wisnom, "A Novel Tecnique to Aaccurately Measure The Fibre Failure Strain in Composite Laminates Under a Combined In-Plane Tension and Shear Stress State," in *21st International Conference on Composite Materials, ICCM21*, 2017, no. August.

[135] L. N. McCartney and A. Blazquez, "Delamination model for cross-ply laminates subject to biaxial loading and thermal stresses," *Int. Conf. Compos. Mater. ICCM*, 2009.

[136] H. Lahtinen, "Calculation of residual stresses of cross-ply laminates," *J. Compos. Mater.*, vol. 37, no. 11, pp. 945–966, 2003.

[137] I. G. García, V. Mantič, A. Blázquez, and F. París, "Transverse crack onset and growth in cross-ply [0/90]s laminates under tension. Application of a coupled stress and energy criterion," *Int. J. Solids Struct.*, vol. 51, no. 23–24, pp. 3844–3856, 2014.

[138] M. Jalalvand, M. R. Wisnom, H. Hosseini-Toudeshky, and B. Mohammadi, "Experimental and numerical study of oblique transverse cracking in cross-ply laminates under tension," *Compos. Part A Appl. Sci. Manuf.*, vol. 67, pp. 140–148, 2014.

[139] J. L. Rebière, "Matrix cracking and delamination evolution in composite cross-ply laminates," *Cogent Eng.*, vol. 1, no. 1, pp. 1–9, 2014.

[140] S. D. Wang and L. Palo, "Initiation and Growth of Transverse Cracks and Edge Delamination in Composite Laminates Part 1. An Energy Method," *J. Compos. Mater. Suppl.*, vol. 14, no. 1, pp. 71–87, 1980.

[141] A. S. D. Wang and F. W. Crossman, "Initiation and Growth of Transverse Cracks and Edge Delamination in Composite Laminates Part 2. An Experimental Correlation," *J. Compos. Mater.*, vol. 14, no. 1, pp. 88–108, 1980.

[142] R. Jamison, K. Schulte, K. Reifsnider, and W. Stinchcomb, “Characterization and Analysis of Damage Mechanisms in Tension-Tension Fatigue of Graphite/Epoxy Laminates,” *Eff. Defects Compos. Mater.*, pp. 21-21–35, 2008.

[143] T. A. Sebaey, J. Costa, P. Maimí, Y. Batista, N. Blanco, and J. A. Mayugo, “Measurement of the in situ transverse tensile strength of composite plies by means of the real time monitoring of microcracking,” *Compos. Part B Eng.*, vol. 65, pp. 40–46, 2014.

[144] J. M. Berthelot, “Transverse cracking and delamination in cross-ply glass-fiber and carbon-fiber reinforced plastic laminates: Static and fatigue loading,” *Appl. Mech. Rev.*, vol. 56, no. 1, pp. 111–147, 2003.

[145] J. A. Nairn, “Matrix Microcracking in Composites,” *Compr. Compos. Mater.*, vol. 2, pp. 403–432, 2000.

[146] C. T. Herakovich, J. Aboudi, S. W. Lee, and E. A. Strauss, “Damage in composite laminates: Effects of transverse cracks,” *Mech. Mater.*, vol. 7, no. 2, pp. 91–107, 1988.

[147] S. Abrate, “Matrix cracking in laminated composites: A review,” *Compos. Eng.*, vol. 1, no. 6, pp. 337–353, 1991.

[148] P. Cornetti, N. Pugno, A. Carpinteri, and D. Taylor, “Finite fracture mechanics: A coupled stress and energy failure criterion,” *Eng. Fract. Mech.*, vol. 73, no. 14, pp. 2021–2033, 2006.

[149] D. Leguillon, “Strength or toughness? A criterion for crack onset at a notch,” *Eur. J. Mech. A/Solids*, vol. 21, no. 1, pp. 61–72, 2002.

[150] A. Parvizi, K. W. Garrett, and J. E. Bailey, “Constrained cracking in glass fibre epoxy cross-ply laminates,” *J. Mater. Sci.*, vol. 13, pp. 195–201, 1978.

[151] K. W. Garrett and J. E. Bailey, “Multiple transverse fracture in 90° cross-ply laminates of a glass fibre-reinforced polyester,” *J. Mater. Sci.*, vol. 12, no. 1, pp. 157–168, 1977.

[152] J. E. Bailey and A. Parvizi, “On fibre debonding effects and the mechanism of transverse-ply failure in cross-ply laminates of glass fibre/thermoset composites,” *J. Mater. Sci.*, vol. 16, no. 3, pp. 649–659, 1981.

[153] J. E. Bailey, P. T. Curtis, and A. Parvizi, “On the Transverse Cracking and Longitudinal Splitting Behaviour of Glass and Carbon Fibre Reinforced Epoxy Cross Ply Laminates and the Effect of Poisson and Thermally Generated Strain.,” *Proc. R. Soc. London Ser A*, vol. 366, pp. 599–623, 1979.

[154] J. Aveston and A. Kelly, “Theory of multiple fracture of fibrous composites,” *J. Mater. Sci.*, vol. 8, no. 3, pp. 352–362, 1973.

[155] S. Kohler, J. Cugnoni, R. Amacher, and J. Botsis, “Transverse cracking in the bulk and at the free edge of thin-ply composites: Experiments and multiscale modelling,” *Compos. Part A Appl. Sci. Manuf.*, vol. 124, no. May, 2019.

[156] F. Crossman and A. Wang, “The Dependence of Transverse Cracking and Delamination on Ply Thickness in Graphite/Epoxy Laminates,” *Damage Compos. Mater. ASTM STP 775, K.L. Reifsnider, Ed., Am. Soc. Test. Mater.*, pp. 118–139, 1982.

[157] A. S. D. Wang, “Fracture Mechanics of Sublaminate Cracks in Composite Materials.,” *Compos. Technol. Rev.*, vol. 6, no. 2, pp. 45–62, 1984.

[158] A. S. D. Wang, P. C. Chou, and S. C. Lei, “A Stochastic Model for the Growth of Matrix Cracks in Composite Laminates,” *J. Compos. Mater.*, vol. 18, no. 3, pp. 239–254, 1984.

[159] A. S. D. Wang and F. W. Crossman, “Initiation and Growth of Transverse Cracks and Edge Delamination in Composite Laminates Part 1. An Energy Method,” *J. Compos. Mater.*, vol. 14, no. 1, pp. 71–87, 1980.

[160] M. M. Fikry, V. Vinogradov, and S. Ogihara, “Effect of Matrix Cracking on Mechanical Properties in FRP Angle-Ply Laminates,” *Mech. Adv. Mater. Mod. Process.*, 2018.

[161] S. G. Lim and C. S. Hong, “Prediction of Transverse Cracking and Stiffness Reduction in Cross-Ply Laminated Composites,” *J. Compos. Mater.*, vol. 23, no. 7, pp. 695–713, 1989.

[162] J. Tong, F. J. Guild, S. L. Ogin, and P. A. Smith, “On matrix crack growth in quasi-isotropic laminates - I. Experimental investigation,” *Compos. Sci. Technol.*, vol. 57, no. 11, pp. 1527–1535, 1997.

[163] J. A. Nairn and S. Hu, “Matrix Microcracking,” *Damage Mech. Compos. Mater.*, vol. 1, pp. 1–46, 1994.

[164] A. Highsmith and K. Reifsnider, “Stiffness-Reduction Mechanisms in Composite Laminates,” *Damage Compos. Mater. ASTM STP 775, K.L. Reifsnider, Ed., Am. Soc. Test. Mater.*, pp. 103–117, 1982.

[165] A. S. D. Wang, N. N. Kishore, and C. A. Li, “Crack development in graphite-epoxy cross-ply laminates under uniaxial tension,” *Compos. Sci. Technol.*, vol. 24, no. 1, pp. 1–31, 1985.

[166] M. Caslini, C. Zanotti, and T. K. O’Brien, “Study of Matrix Cracking and Delamination in Glass/Epoxy Laminates.,” *J. Compos. Technol. Res.*, vol. 9, no. 4, pp. 121–130, 1987.

[167] K. E. Evans and M. A. Nkansah, “Molecular network design,” *Nature*, vol. 353, no. September, p. 124, 1991.

[168] Z. Wang, A. Zulifqar, and H. Hu, “Auxetic composites in aerospace engineering,” *Adv. Compos. Mater. Aerosp. Eng.*, no. September 2017, pp. 213–240, 2016.

[169] R. Lakes, “Foam Structures with a Negative Poisson ’ s Ratio,” *Science (80-.).*, vol. 235, pp. 1038–1040, 1986.

[170] B. D. Caddock and K. E. Evans, “Microporous materials with negative Poisson’s ratios. I. Microstructure and mechanical properties,” *J. Phys. D. Appl. Phys.*, vol. 22, no. 12, pp. 1877–1882, 1989.

[171] K. L. Alderson and K. E. Evans, “The fabrication of microporous polyethylene having a negative Poisson’s ratio,” *Polymer (Guildf).*, vol. 33, no. 20, pp. 4435–4438, 1992.

[172] D. J. Gunton and G. A. Saunders, “The Young’s modulus and Poisson’s ratio of arsenic, antimony and bismuth,” *J. Mater. Sci.*, vol. 7, no. 9, pp. 1061–1068, 1972.

[173] R. H. Baughman, J. M. Shacklette, A. A. Zakhidov, and S. Stafstro, “Negative Poisson’s ratios as a common feature of cubic metals,” *Nature*, vol. 392, pp. 362–365, 1998.

[174] J. L. Williams and J. L. Lewis, “Properties and an anisotropic model of cancellous bone from the proximal tibial epiphysis,” *J. Biomech. Eng.*, vol. 104, no. 1, pp. 50–56, 1982.

[175] L. M. Frolich, M. LaBarbera, and W. P. Stevens, “Poisson’s ratio of a crossed fibre sheath: the skin of aquatic salamanders,” *J. Zool.*, vol. 232, no. 2, pp. 231–252, 1994.

[176] Q. Liu, “Literature review: materials with negative poisson’s ratios and potential applications to Aerospace and Defence,” *Aust. Gov. Dep. Def.*, pp. 1–47, 2006.

[177] A. Alderson and K. L. Alderson, “Auxetic materials,” *Proc. Inst. Mech. Eng. Part G J. Aerosp. Eng.*, vol. 221, no. 4, pp. 565–575, 2007.

[178] J. F. Clarke, R. A. Duckett, P. J. Hine, I. J. Hutchinson, and I. M. Ward, “Negative Poisson’s ratios in angle-ply laminates: theory and experiment,” *Composites*, vol. 25, no. 9, pp. 863–868, Oct. 1994.

[179] K. L. Alderson, V. R. Simkins, V. L. Coenen, P. J. Davies, A. Alderson, and K. E. Evans, “How to make auxetic fibre reinforced composites,” *Phys. Status Solidi Basic Res.*, vol. 242, no. 3, pp. 509–518, 2005.

[180] K. E. Evans, M. A. Nkansah, and I. J. Hutchinson, “Modelling negaitve Poisson ratio effects in network embedded composites,” *Acta Metall. Mater.*, vol. 40, no. 9, pp. 2463–2469, 1992.

[181] K. E. Evans, J. . Donoghue, and K. . Alderson, “The design, matching and manufacture of auxetic carbon fibre laminates,” *J. Compos. Mater.*, vol. 38, no. 2, pp. 95–106, 2004.

[182] K. L. Alderson and V. L. Coenen, “The low velocity impact response of auxetic carbon fibre laminates,” *Phys. Status Solidi Basic Res.*, vol. 245, no. 3, pp. 489–496, 2008.

[183] A. Bezazi, W. Boukharouba, and F. Scarpa, “Mechanical properties of auxetic carbon/epoxy composites: Static and cyclic fatigue behaviour,” *Phys. Status Solidi Basic Res.*, vol. 246, no. 9, pp. 2102–2110, 2009.

[184] J. P. Donoghue, K. L. Alderson, and K. E. Evans, “The fracture toughness of composite laminates with a negative Poisson’s ratio,” *Phys. Status Solidi Basic Res.*, vol. 246, no. 9, pp. 2011–2017, 2009.

[185] V. L. Coenen and K. L. Alderson, “Mechanisms of failure in the static indentation resistance of auxetic carbon fibre laminates,” *Phys. Status Solidi Basic Res.*, vol. 248, no. 1, pp. 66–72, 2011.

[186] ASTM, “ASTM D3039/D3039M - Standard Test Method for Tensile Properties of Polymer Matrix Composite Materials,” *Annu. B. ASTM Stand.*, pp. 1–13.

[187] D. S. Ivanov, F. Baudry, B. Van Den Broucke, S. V. Lomov, H. Xie, and I. Verpoest, “Failure analysis of triaxial braided composite,” *Spec. Issue 12th Eur. Conf. Compos. Mater. ECCM 2006*, vol. 69, no. 9, pp. 1372–1380, 2009.

[188] N. V. De Carvalho, S. T. Pinho, and P. Robinson, “An experimental study of failure initiation and propagation in 2D woven composites under compression,” *Compos. Sci. Technol.*, vol. 71, no. 10, pp. 1316–1325, 2011.

[189] J. Montesano, H. Bougherara, and Z. Fawaz, “Application of infrared thermography for the characterization of damage in braided carbon fiber reinforced polymer matrix composites,” *Compos. Part B Eng.*, vol. 60, pp. 137–143, 2014.

[190] F. Aymerich and S. Meili, “Ultrasonic evaluation of matrix damage in impacted composite laminates,” *Compos. Part B Eng.*, vol. 31, no. 1, pp. 1–6, 2000.

[191] K. Ogi, M. Takahashi, and S. Yashiro, “Empirical Models for Matrix Cracking in a CFRP Cross-Ply Laminate Under Static- and Cyclic-Fatigue Loadings,” *Polym. Compos.*, vol. 37, no. 1, pp. 915–924, 2016.

[192] L. Farge, J. Varna, and Z. Ayadi, “Damage characterization of a cross-ply carbon fiber/epoxy laminate by an optical measurement of the displacement field,” *Compos. Sci. Technol.*, vol. 70, no. 1, pp. 94–101, 2010.

[193] L. Farge, Z. Ayadi, and J. Varna, “Optically measured full-field displacements on the edge of a cracked composite laminate,” *Compos. Part A Appl. Sci. Manuf.*, vol. 39, no. 8, pp. 1245–1252, 2008.

[194] Y. J. Yan and L. H. Yam, “Online detection of crack damage in composite plates using embedded piezoelectric actuators/sensors and wavelet analysis,” *Compos. Struct.*, vol. 58, no. 1, pp. 29–38, 2002.

[195] D. L. Flaggs and M. H. Kural, “Experimental Determination of the In Situ Transverse Lamina Strength in Graphite/Epoxy Laminates,” *J. Compos. Mater.*, vol. 16, no. 2, pp. 103–116, 1982.

[196] W. Hufenbach *et al.*, “A test device for damage characterisation of composites based on in situ computed tomography,” *Compos. Sci. Technol.*, vol. 72, no. 12, pp. 1361–1367, 2012.

[197] E. Bayraktar, S. D. Antolovich, and C. Bathias, “New developments in non-destructive controls of the composite materials and applications in manufacturing

engineering," *J. Mater. Process. Technol.*, vol. 206, no. 1–3, pp. 30–44, 2008.

[198] D. J. Bull, L. Helfen, I. Sinclair, S. M. Spearing, and T. Baumbach, "A comparison of multi-scale 3D X-ray tomographic inspection techniques for assessing carbon fibre composite impact damage," *Compos. Sci. Technol.*, vol. 75, pp. 55–61, 2013.

[199] D. J. Bull, S. M. Spearing, I. Sinclair, and L. Helfen, "Three-dimensional assessment of low velocity impact damage in particle toughened composite laminates using micro-focus X-ray computed tomography and synchrotron radiation laminography," *Compos. Part A Appl. Sci. Manuf.*, vol. 52, pp. 62–69, 2013.

[200] R. Böhm *et al.*, "A quantitative comparison of the capabilities of in situ computed tomography and conventional computed tomography for damage analysis of composites," *Compos. Sci. Technol.*, vol. 110, pp. 62–68, 2015.

[201] C. Chateau *et al.*, "In situ X-ray microtomography characterization of damage in SiCf/SiC minicomposites," *Compos. Sci. Technol.*, vol. 71, no. 6, pp. 916–924, 2011.

[202] A. J. Moffat *et al.*, "In situ synchrotron computed laminography of damage in carbon fibre-epoxy [90/0]s laminates," *Scr. Mater.*, vol. 62, no. 2, pp. 97–100, 2010.

[203] K. E. Matheson, "Private communication." NASA Langley Research Center, 2019.

[204] X. Xu, M. R. Wisnom, K. Chang, and S. R. Hallett, "Unification of strength scaling between unidirectional, quasi-isotropic, and notched carbon/epoxy laminates," *Compos. Part A Appl. Sci. Manuf.*, vol. 90, pp. 296–305, 2016.

[205] A. Melnikov, Y. Swolfs, S. V. Lomov, and L. Gorbatikh, "Do transverse cracks affect the in-situ strength and fibre breaks accumulation in longitudinal plies of cross-ply laminates?," *18th Eur. Conf. Compos. Mater. - ECCM 2018*, no. June, 2020.

[206] F. Laurin, P. Paulmier, and F. X. Irisarri, "Determination of the longitudinal compressive strength of a CFRP ply through a tensile test on a laminate," *Compos. Part A Appl. Sci. Manuf.*, vol. 113, no. July, pp. 209–219, 2018.

[207] Y. Swolfs, I. Verpoest, and L. Gorbatikh, "Recent advances in fibre-hybrid composites: materials selection, opportunities and applications," *Int. Mater. Rev.*, vol. 64, no. 4, pp. 181–215, 2019.

[208] M. R. Wisnom, "Effect of shear stresses in indirect compression tests of unidirectional carbon fiber/epoxy," *AIAA J.*, vol. 29, no. 10, pp. 1692–1697, 1991.

[209] M. R. Wisnom, "The effect of fibre misalignment on the compressive strength of unidirectional carbon fibre/epoxy," *Composites*, vol. 21, no. 5, pp. 403–407, 1990.

[210] B. Budiansky and N. A. Fleck, "Compressive kinking of fiber composites: A topical review," *Appl. Mech. Rev.*, vol. 47, no. 6, pp. s246–s250, 1994.

[211] M. R. Wisnom, “Nonlinear analysis of misaligned unidirectional carbon fibre-epoxy compression specimens,” *Compos. Eng.*, vol. 3, no. 6, pp. 547–556, 1993.

[212] I. Chung and Y. Weitsman, “A mechanics model for the compressive response of fiber reinforced composites,” *Int. J. Solids Struct.*, vol. 31, no. 18, pp. 2519–2536, 1994.

[213] P. Berbinau, C. Soutis, and I. A. Guz, “Compressive failure of 0° unidirectional carbon-fibre-reinforced plastic (CFRP) laminates by fibre microbuckling,” *Compos. Sci. Technol.*, vol. 59, no. 9, pp. 1451–1455, 1999.

[214] O. Montagnier and C. Hochard, “Compression characterization of high-modulus carbon fibers,” *J. Compos. Mater.*, vol. 39, no. 1, pp. 35–49, 2005.

[215] T. Yokozeki, T. Ogasawara, and T. Ishikawa, “Nonlinear behavior and compressive strength of unidirectional and multidirectional carbon fiber composite laminates,” *Compos. Part A Appl. Sci. Manuf.*, vol. 37, no. 11, pp. 2069–2079, 2006.

[216] T. Yokozeki, T. Ogasawara, and T. Ishikawa, “Effects of fiber nonlinear properties on the compressive strength prediction of unidirectional carbon-fiber composites,” *Compos. Sci. Technol.*, vol. 65, no. 14, pp. 2140–2147, 2005.

[217] A. Jumahat, C. Soutis, F. R. Jones, and A. Hodzic, “Fracture mechanisms and failure analysis of carbon fibre/toughened epoxy composites subjected to compressive loading,” *Compos. Struct.*, vol. 92, no. 2, pp. 295–305, 2010.

[218] Y. Zhou and Z. M. Huang, “Failure of fiber-reinforced composite laminates under longitudinal compression,” *J. Compos. Mater.*, vol. 53, no. 24, pp. 3395–3411, 2019.

[219] R. Gutkin, S. T. Pinho, P. Robinson, and P. T. Curtis, “Micro-mechanical modelling of shear-driven fibre compressive failure and of fibre kinking for failure envelope generation in CFRP laminates,” *Compos. Sci. Technol.*, vol. 70, no. 8, pp. 1214–1222, 2010.

[220] M. J. Shuart, “Short-wavelength buckling and shear failures for compression-loaded composite laminates,” in *NASA Technical memorandum No. 87640*, 1985, no. November 1985.

[221] S. T. Pinho, L. Iannucci, and P. Robinson, “Physically-based failure models and criteria for laminated fibre-reinforced composites with emphasis on fibre kinking: Part I: Development,” *Compos. Part A Appl. Sci. Manuf.*, vol. 37, no. 1, pp. 63–73, 2006.

[222] S. Pimenta, R. Gutkin, S. T. Pinho, and P. Robinson, “A micromechanical model for kink-band formation: Part II-Analytical modelling,” *Compos. Sci. Technol.*, vol. 69, no. 7–8, pp. 956–964, 2009.

[223] N. Feld, O. Allix, E. Baranger, and J. M. Guimard, “A micromechanics-based mesomodel for unidirectional laminates in compression up to failure,” *J. Compos. Mater.*, vol. 46, no. 23, pp. 2893–2909, 2012.

[224] S. Drapier, J. C. Grandidier, and M. Potier-Ferry, “Towards a numerical model of the compressive strength for long fibre composites,” *Eur. J. Mech. A/Solids*, vol. 18, no. 1, pp. 69–92, 1999.

[225] E. T. Camponeschi, “Compression of composite materials: A review. US Navy Report AD-A189 272,” 1987.

[226] C. Soutis, “Measurement of the static compressive strength of carbon-fibre/epoxy laminates,” *Compos. Sci. Technol.*, vol. 42, no. 4, pp. 373–392, 1991.

[227] R. A. Chaudhuri, “Prediction of the Compressive Strength of Thick-Section Advanced Composite Laminates,” *J. Compos. Mater.*, vol. 25, no. 10, pp. 1244–1276, 1991.

[228] E. C. J. Wung and S. N. Chatterjee, “On the Failure Mechanisms in Laminate Compression Specimens and the Measurement of Strengths,” *J. Compos. Mater.*, vol. 26, no. 13, pp. 1885–1914, 1992.

[229] S. R. Frost, “Compressive Behaviour of Long-Fibre Unidirectional Composites,” *J. Compos. Mater.*, vol. 26, no. 8, pp. 1151–1172, 1992.

[230] B. Budiansky and N. A. Fleck, “Compressive failure of fibre composites,” *J. Mech. Phys. Solids*, vol. 41, no. 1, pp. 183–211, 1993.

[231] P. M. Jelf and N. A. Fleck, “Compression Failure Mechanisms in Unidirectional Composites,” *J. Compos. Mater.*, vol. 26, no. 18, pp. 2706–2726, 1992.

[232] C. Leopold *et al.*, “Compression fracture of CFRP laminates containing stress intensifications,” *Materials (Basel).*, vol. 10, no. 9, pp. 1–18, 2017.

[233] N. A. Fleck, P. M. Jelf, and P. T. Curtis, “Compressive failure of laminated and woven composites,” *J. Compos. Technol. Res.*, vol. 17, no. 3, pp. 212–220, 1995.

[234] P. M. Moran, X. H. Liu, and C. F. Shih, “Kink band formation and band broadening in fiber composites under compressive loading,” *Acta Metall. Mater.*, vol. 43, no. 8, pp. 2943–2958, 1995.

[235] B. Wang, N. Uda, K. Ono, and H. Nagai, “Effect of micro in-plane fiber waviness on compressive properties of unidirectional fabric composites,” *J. Compos. Mater.*, vol. 52, no. 15, pp. 2065–2074, 2018.

[236]M. R. Wisnom, “Analysis of shear instability in compression due to fibre waviness,” *J. Reinf. Plast. Compos.*, vol. 12, no. 11, pp. 1171–1189, 1993.

[237] M. R. Wisnom and J. W. Atkinson, “Compressive failure due to shear instability: experimental investigation of waviness and correlation with analysis,” *J. Reinf. Plast. Compos.*, vol. 15, no. 4, pp. 420–439, 1996.

[238] B. W. Rosen, “Mechanics of Composite Strengthening: Fibre Composite Materials,” in *Chapter 3*, American Society of Metals, 1965.

[239] K. E. Hofer and P. N. Rao, “A New Static Compression Fixture for Advanced Composite Materials,” *Jounral Test. Eval.*, vol. 5, no. 4, pp. 278–283, 1977.

[240] ASTM, “ASTM D3410M - Standard Test Method for Compressive Properties of Polymer Matrix Composite Materials with Unsupported Gage Section by Shear Loading,” *Annu. B. ASTM Stand.*, vol. 15.03, pp. 1–16, 2003.

[241] C. Soutis, J. Lee, and C. Kong, “Size effect on compressive strength of T300/924C carbon fibre-epoxy laminates,” *Plast. Rubber Compos.*, vol. 31, no. 8, pp. 364–370, 2002.

[242] ASTM, “Standard Test Method for Compressive Properties of Rigid Plastics,” *Annu. B. ASTM Stand.*, vol. i, pp. 1–8, 2008.

[243] ASTM, “Standard Test Method for Compressive Properties of Polymer Matrix Composite Materials Using a Combined Loading Compression (CLC) Test Fixture,” *Annu. B. ASTM Stand.*, pp. 1–11, 2012.

[244] J. Lee and C. Soutis, “Thickness effect on the compressive strength of T800/924C carbon fibre-epoxy laminates,” *Compos. Part A Appl. Sci. Manuf.*, vol. 36, no. 2 SPEC. ISS., pp. 213–227, 2005.

[245] J. Lee and C. Soutis, “A study on the compressive strength of thick carbon fibre-epoxy laminates,” *Compos. Sci. Technol.*, vol. 67, no. 10, pp. 2015–2026, 2007.

[246] M. R. Wisnom, “Size effects in the testing of fibre-composite materials,” *Compos. Sci. Technol.*, vol. 59, pp. 1937–1957, 1999.

[247] N. Carbajal and F. Mujika, “Determination of compressive strength of unidirectional composites by three-point bending tests,” *Polym. Test.*, vol. 28, no. 2, pp. 150–156, 2009.

[248] N. Carbajal and F. Mujika, “Determination of longitudinal compressive strength of long fiber composites by three-point bending of [0m/90n/0p] cross-ply laminated strips,” *Polym. Test.*, vol. 28, no. 6, pp. 618–626, 2009.

[249] P. J. Callus, “The Effects of Hole-size and Environment on the Mechanical Behaviour of a Quasi-isotropic AS4 / 3501-6 Laminate in Tension , Compression and Bending,” *Air Veh. Div. Def. Sci. Technol. Organ.*, pp. 1–82, 2007.

[250] M. R. Wisnom and J. W. Atkinson, “Constrained buckling tests show increasing compressive strain to failure with increasing strain gradient,” *Compos. Part A Appl. Sci. Manuf.*, vol. 28, no. 11, pp. 959–964, 1997.

[251] M. R. Wisnom, “On the high compressive strains achieved in bending tests on unidirectional carbon-fibre/epoxy,” *Compos. Sci. Technol.*, vol. 43, no. 3, pp. 229–235, 1992.

[252] F. Laurin, C. Julien, and P. Paulmier, “Damage and strength analysis of open-hole laminated plates under tensile, compressive and bending loadings,” in *Proceeding of the 17th European Conference on Composite Materials - ECCM 2016*, 2016.

[253] M. R. Wisnom, J. W. Atkinson, and M. I. Jones, “Reduction in compressive strain to failure with increasing specimen size in pin-ended buckling tests,” *Compos. Sci. Technol.*, vol. 57, no. 9–10, pp. 1303–1308, 1997.

[254] G. Eyer, O. Montagnier, C. Hochard, and J. P. Charles, “Effect of matrix damage on compressive strength in the fiber direction for laminated composites,” *Compos. Part A Appl. Sci. Manuf.*, vol. 94, pp. 86–92, 2017.

[255] F. Laurin, N. Carrere, C. Huchette, and J. F. Maire, “A multiscale hybrid approach for damage and final failure predictions of composite structures,” *J. Compos. Mater.*, vol. 47, no. 20–21, pp. 2713–2747, 2013.

[256]C. G. Davila, P. P. Camanho, and C. A. Rose, “Failure Criteria for FRP Laminates,” *J. Compos. Mater.*, vol. 39, no. 4, pp. 323–345, 2005.

[257] A. S. D. Wang, “Fracture Mechanics of Sublaminate Cracks in Composite Materials.,” *Compos. Technol. Rev.*, vol. 6, no. 2, pp. 45–62, 1984.

[258] P. P. Camanho, C. G. Dávila, S. T. Pinho, L. Iannucci, and P. Robinson, “Prediction of in situ strengths and matrix cracking in composites under transverse tension and in-plane shear,” *Compos. Part A Appl. Sci. Manuf.*, vol. 37, no. 2, pp. 165–176, 2006.

[259] A. K. Ditcher, J. P. H. Webber, and F. E. Rhodes, “Non-linear stress-strain behaviour of carbon fibre reinforced plastic laminates,” *J. Strain Anal. Eng. Des.*, vol. 16, no. 1, pp. 43–51, 1981.

[260] F. Laurin, “Private communication.” ONERA - The French Aerospace Lab, 2018.

[261] H. Hütter, U; Schelling, H; Krauss, “An experimental study to determine failure envelope of composite materials with tubular specimen under combined loads and comparison between several classical criteria.,” in *Failure modes of composite materials with organic matrices and other consequences on design, NATO, AGARD, no.163*, 1974, pp. 3-1-3–11.

[262] S. W. Tsai and T. H. Hahn, *Introduction to Composite Materials*. Technomic Publishing, 1980.

[263] X. Wu, “Private communication.” University of Bristol, 2020.

[264] S. Drapier, J. C. Grandidier, and M. Potier-Ferry, “A structural approach of plastic microbuckling in long fibre composites: Comparison with theoretical and experimental results,” *Int. J. Solids Struct.*, vol. 38, no. 22–23, pp. 3877–3904, 2001.

[265] “High Performance Ductile Composite Technology (HiPerDuCT) Programme Grant.” [Online]. Available: https://gow.epsrc.ukri.org/NGBOViewGrant.aspx?GrantRef=EP/I02946X/1.

[266] Y. Swolfs, L. Gorbatikh, and I. Verpoest, “Fibre hybridisation in polymer composites: A review,” *Compos. Part A Appl. Sci. Manuf.*, vol. 67, 2014.

[267] G. Czél and M. R. Wisnom, “Demonstration of pseudo-ductility in high performance glass/epoxy composites by hybridisation with thin-ply carbon prepreg,” *Compos. Part A Appl. Sci. Manuf.*, vol. 52, pp. 23–30, Sep. 2013.

[268] G. Czél, M. Jalalvand, and M. R. Wisnom, “Design and characterisation of advanced pseudo-ductile unidirectional thin-ply carbon/epoxy– glass/epoxy hybrid composites,” *Compos. Struct.*, vol. 143, pp. 362–370, Feb. 2016.

[269] M. Jalalvand, G. Czél, and M. R. Wisnom, “Parametric study of failure mechanisms and optimal configurations of pseudo-ductile thin-ply UD hybrid composites,” *Compos. Part A Appl. Sci. Manuf.*, vol. 74, pp. 123–131, Jul. 2015.

[270] M. Jalalvand, G. Czél, and M. R. Wisnom, “Numerical modelling of the damage modes in UD thin carbon/glass hybrid laminates,” *Compos. Sci. Technol.*, vol. 94, pp. 39–47, Apr. 2014.

[271] M. Jalalvand, G. Czél, and M. R. Wisnom, “Damage analysis of pseudo-ductile thin-ply UD hybrid composites - A new analytical method,” *Compos. Part A Appl. Sci. Manuf.*, vol. 69, pp. 83–93, 2015.

[272] M. R. Wisnom, “Mechanisms to create high performance pseudo-ductile composites,” *IOP Conf. Ser. Mater. Sci. Eng.*, vol. 139, no. 1, 2016.

[273] H. Yu, K. D. Potter, and M. R. Wisnom, “A novel manufacturing method for aligned discontinuous fibre composites (High Performance-Discontinuous Fibre method),” *Compos. Part A Appl. Sci. Manuf.*, vol. 65, pp. 175–185, 2014.

[274] H. Yu, M. L. Longana, M. Jalalvand, M. R. Wisnom, and K. D. Potter, “Pseudo-ductility in intermingled carbon/glass hybrid composites with highly aligned discontinuous fibres,” *Compos. Part A Appl. Sci. Manuf.*, vol. 73, pp. 35–44, 2015.

[275] M. L. Longana, H. N. Yu, M. Jalavand, M. R. Wisnom, and K. D. Potter, “Aligned discontinuous intermingled reclaimed/virgin carbon fibre composites for high performance and pseudo-ductile behaviour in interlaminated carbon-glass hybrids,” *Compos. Sci. Technol.*, vol. 143, pp. 13–21, 2017.

[276] J. D. Fuller, M. Jalalvand, and M. R. Wisnom, “Combining fibre rotation and fragmentation to achieve pseudo-ductile CFRP laminates,” *Compos. Struct.*, vol. 142, pp. 155–166, 2016.

[277] J. D. Fuller and M. R. Wisnom, “Exploration of the potential for pseudo-ductility in thin ply CFRP angle-ply laminates via an analytical method,” *Compos. Sci. Technol.*, vol. 112, pp. 8–15, 2015.

[278] G. Czél and M. R. Wisnom, “Demonstration of pseudo-ductility in high performance glass/epoxy composites by hybridisation with thin-ply carbon prepreg,” *Compos. Part A Appl. Sci. Manuf.*, vol. 52, pp. 23–30, 2013.

[279] C. Zweben, “Advanced composites for aerospace applications - A review of current status and future prospects,” *Composites*, vol. 12, no. October, pp. 235–240, 1981.

[280] E. Selman, A. Ghiami, and N. Alver, “Study of fracture evolution in FRP-strengthened reinforced concrete beam under cyclic load by acoustic emission technique: An integrated mechanical-acoustic energy approach,” *Constr. Build. Mater.*, vol. 95, pp. 832–841, 2015.

[281] D. Gay, S. V. Hoa, and S. W. Tsai, *Composite materials: Design and Applications*. London: CRC Press, 2003.

[282] M. Jalalvand, G. Czél, and M. R. Wisnom, "Parametric study of failure mechanisms and optimal configurations of pseudo-ductile thin-ply UD hybrid composites," *Compos. Part A Appl. Sci. Manuf.*, vol. 74, pp. 123–131, 2015.

[283] D. M. Amafabia, D. Montalvão, O. David-West, and G. Haritos, "A Review of Structural Health Monitoring Techniques as Applied to Composite Structures," *Struct. Durab. Heal. Monit.*, vol. 11, no. 2, pp. 91–147, 2017.

[284] S. Rana, S. P, R. Fangueiro, and A. Gomes Correia, "A review on smart self-sensing composite materials for civil engineering applications," *AIMS Mater. Sci.*, vol. 3, no. 2, pp. 357–379, 2016.

[285] C. C. Ciang, J.-R. Lee, and H.-J. Bang, "Structural health monitoring for a wind turbine system: a review of damage detection methods," *Meas. Sci. Technol.*, vol. 19, no. 12, 2008.

[286] D. Kinet, P. Mégret, K. W. Goossen, L. Qiu, D. Heider, and C. Caucheteur, "Fiber Bragg grating sensors toward structural health monitoring in composite materials: challenges and solutions," *Sensors*, vol. 14, no. 4, pp. 7394–7419, 2014.

[287] X. W. Ye, Y. H. Su, and J. P. Han, "Structural Health Monitoring of Civil Infrastructure Using Optical Fiber Sensing Technology: A Comprehensive Review.," *Sci. World J.*, vol. 2014, p. 652329, 2014.

[288] N. D. Alexopoulos, C. Bartholome, P. Poulin, and Z. Marioli-Riga, "Structural health monitoring of glass fiber reinforced composites using embedded carbon nanotube (CNT) fibers," *Compos. Sci. Technol.*, vol. 70, no. 2, pp. 260–271, 2010.

[289] A. Todoroki, M. Tanaka, and Y. Shimamura, "Electrical resistance change method for monitoring delaminations of CFRP laminates: Effect of spacing between electrodes," *Compos. Sci. Technol.*, vol. 65, no. 1, pp. 37–46, 2005.

[290] A. Todoroki, K. Omagari, Y. Shimamura, and H. Kobayashi, "Matrix crack detection of CFRP using electrical resistance change with integrated surface probes," *Compos. Sci. Technol.*, vol. 66, no. 11–12, pp. 1539–1545, 2006.

[291] J. Abry, "In situ detection of damage in CFRP laminates by electrical resistance measurements," *Compos. Sci. Technol.*, vol. 59, no. 6, pp. 925–935, 1999.

[292] D. Y. Song, N. Takeda, and A. Kitano, "Correlation between mechanical damage behavior and electrical resistance change in CFRP composites as a health monitoring sensor," *Mater. Sci. Eng. A*, vol. 456, no. 1–2, pp. 286–291, 2007.

[293] P. Pissis *et al.*, "Strain and Damage Sensing in Polymer Composites and Nanocomposites with Conducting Fillers," *Procedia Eng.*, vol. 114, pp. 590–597, 2015.

[294] D. J. Kwon, Z. J. Wang, J. Y. Choi, P. S. Shin, K. L. Devries, and J. M. Park, "Damage sensing and fracture detection of CNT paste using electrical resistance

measurements," *Compos. Part B Eng.*, vol. 90, pp. 386–391, 2016.

[295] W. Obitayo and T. Liu, "A review: Carbon nanotube-based piezoresistive strain sensors," *J. Sensors*, vol. 2012, 2012.

[296] J.-M. Park, D.-J. Kwon, Z.-J. Wang, and K. L. DeVries, "Review of self-sensing of damage and interfacial evaluation using electrical resistance measurements in nano/micro carbon materials-reinforced composites," *Adv. Compos. Mater.*, vol. 24, no. 3, pp. 197–219, 2015.

[297] C. E. Bakis, A. Nanni, J. A. Terosky, and S. W. Koehler, "Self-monitoring, pseudo-ductile, hybrid FRP reinforcement rods for concrete applications," *Compos. Sci. Technol.*, vol. 61, no. 6, pp. 815–823, 2001.

[298] F. Nanni, G. Ruscito, G. Forte, and G. Gusmano, "Design, manufacture and testing of self-sensing carbon fibre–glass fibre reinforced polymer rods," *Smart Mater. Struct.*, vol. 16, no. 6, pp. 2368–2374, 2007.

[299] M. R. Wisnom, K. Potter, G. Czel, and M. Jalalvand, "GB2544792-B - Granted Patent of Strain Overload Sensor."

[300] B. Varkonyi, "Report on Unidirectional hybrid composite overload sensors - methods to lower trigger strain utilising ultra high modulus YS-90 fibres," Bristol, UK, 2017.

[301] M. R. Wisnom and M. I. Jones, "Size effects in interlaminar tensile and shear strength of unidirectional glass fibre/epoxy," *J. Reinf. Plast. Compos.*, vol. 15, no. 1, pp. 2–15, 1996.

[302] T. Rev, G. Czél, M. Jalalvand, and M. R. Wisnom, "Unidirectional hybrid composite overload sensors – robust tools for visual overload indication," in *International Conference on Composite Materials - ICCM21*, 2017, vol. 1, no. August.

[303] M. Fotouhi, P. Suwarta, M. Jalalvand, G. Czel, and M. R. Wisnom, "Detection of fibre fracture and ply fragmentation in thin-ply UD carbon/glass hybrid laminates using acoustic emission," *Compos. Part A Appl. Sci. Manuf.*, vol. 86, pp. 66–76, 2016.

[304] Vishay Micro-measurements Application Note VMM-19, "Surface Preparation of Composites," no. Document no. 11183.

[305] CEN, "Racing bicycles - Safety requirements and test methods (EN 14781)," p. 80, 2005.

[306] P. M. Jelf and N. A. Fleck, "The failure of composite tubes due to combined compression and torsion," *J. Mater. Sci.*, vol. 29, no. 11, pp. 3080–3084, 1994.

Appendix A – Chapter 5

Figure A.1 X-CT image taken of a Type 1 specimen interrupted at 84.5 % of the peak failure load with maximum highlight showcasing dye penetrated areas typically connected to the surface of the specimen. There is no damage found in the presented specimen.

Appendix B – Chapter 6

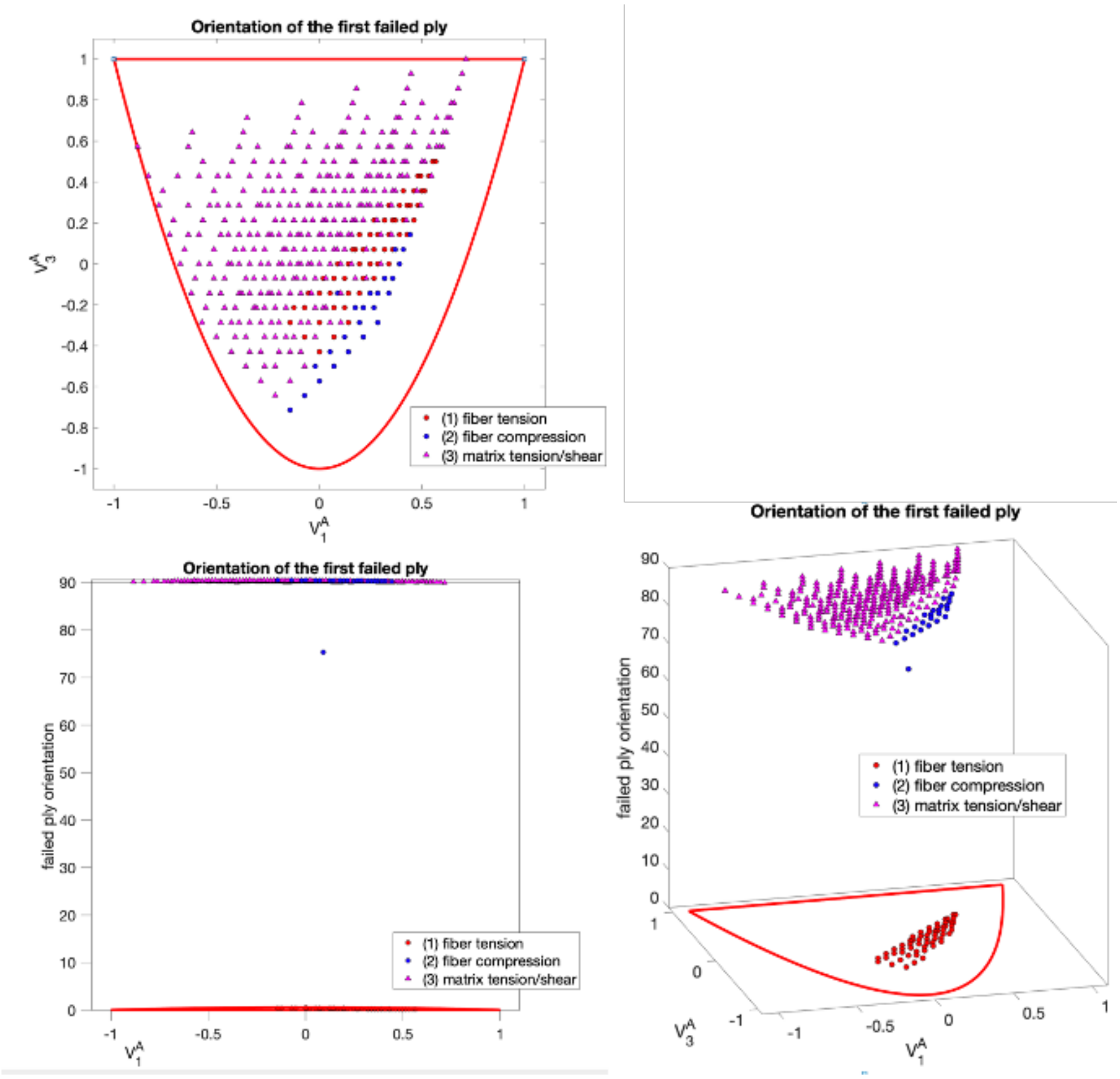

Figure B.1. Generated laminates defined by the DOE and categorised by the orientation of the first failed ply

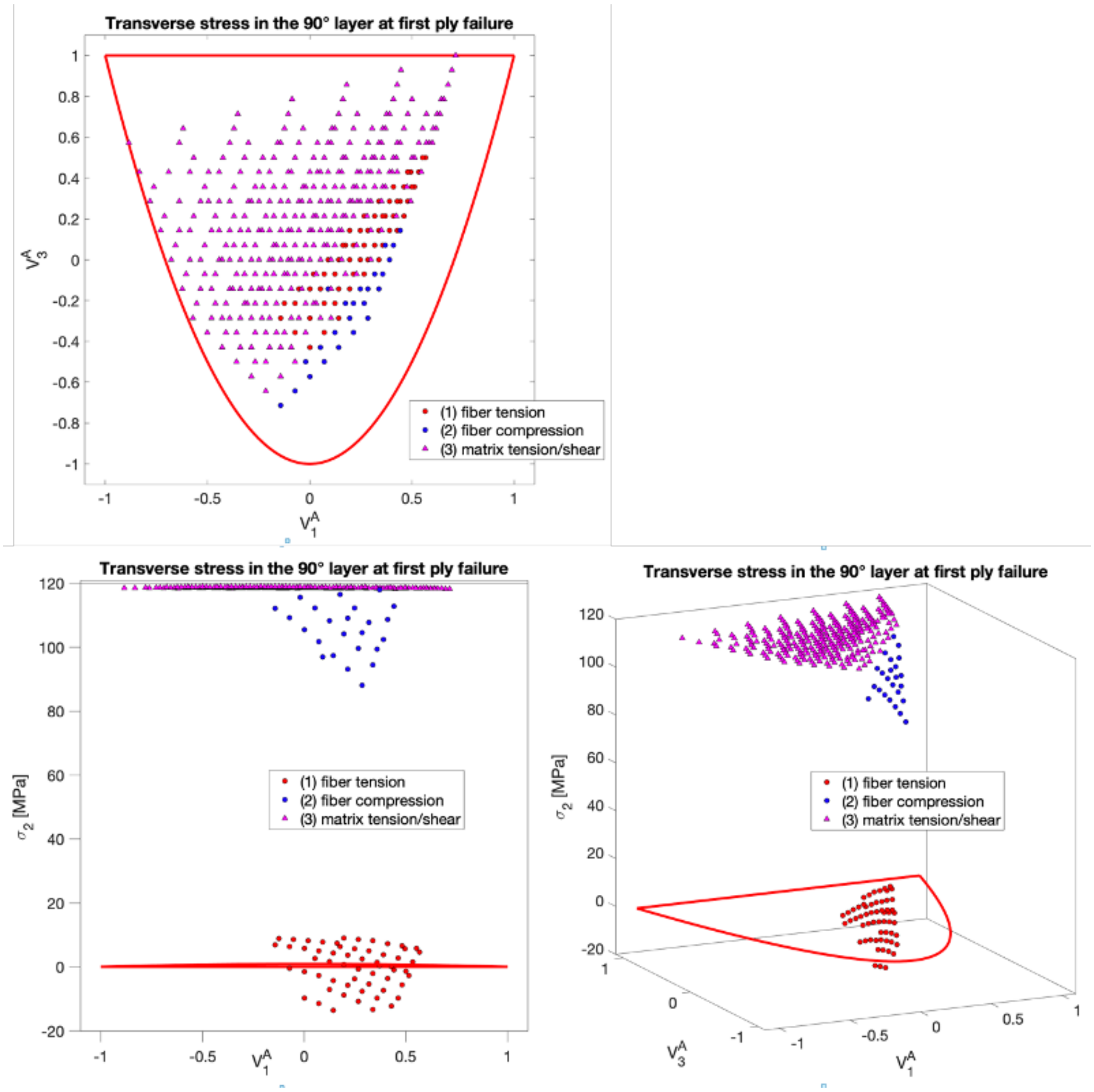

Figure B.2. Generated laminates defined by the DOE and categorised by the predicted transverse stress in the 90° layer at first ply failure

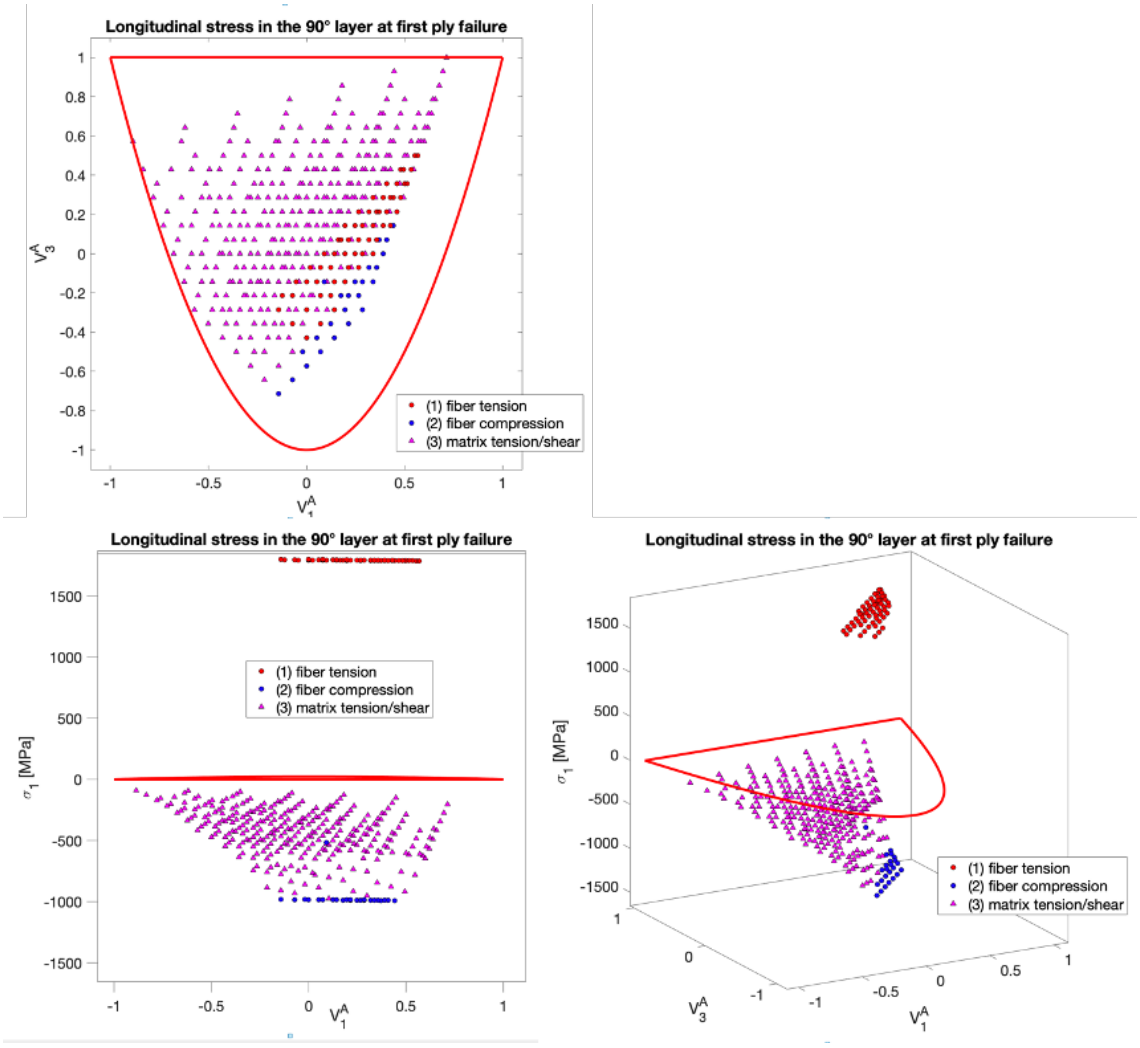

Figure B.3. Generated laminates defined by the DOE and categorised by the predicted longitudinal stress in the 90° layer at first ply failure

Figure B.4. Higher resolution SEM image example of a Type IV specimen with 25x magnification

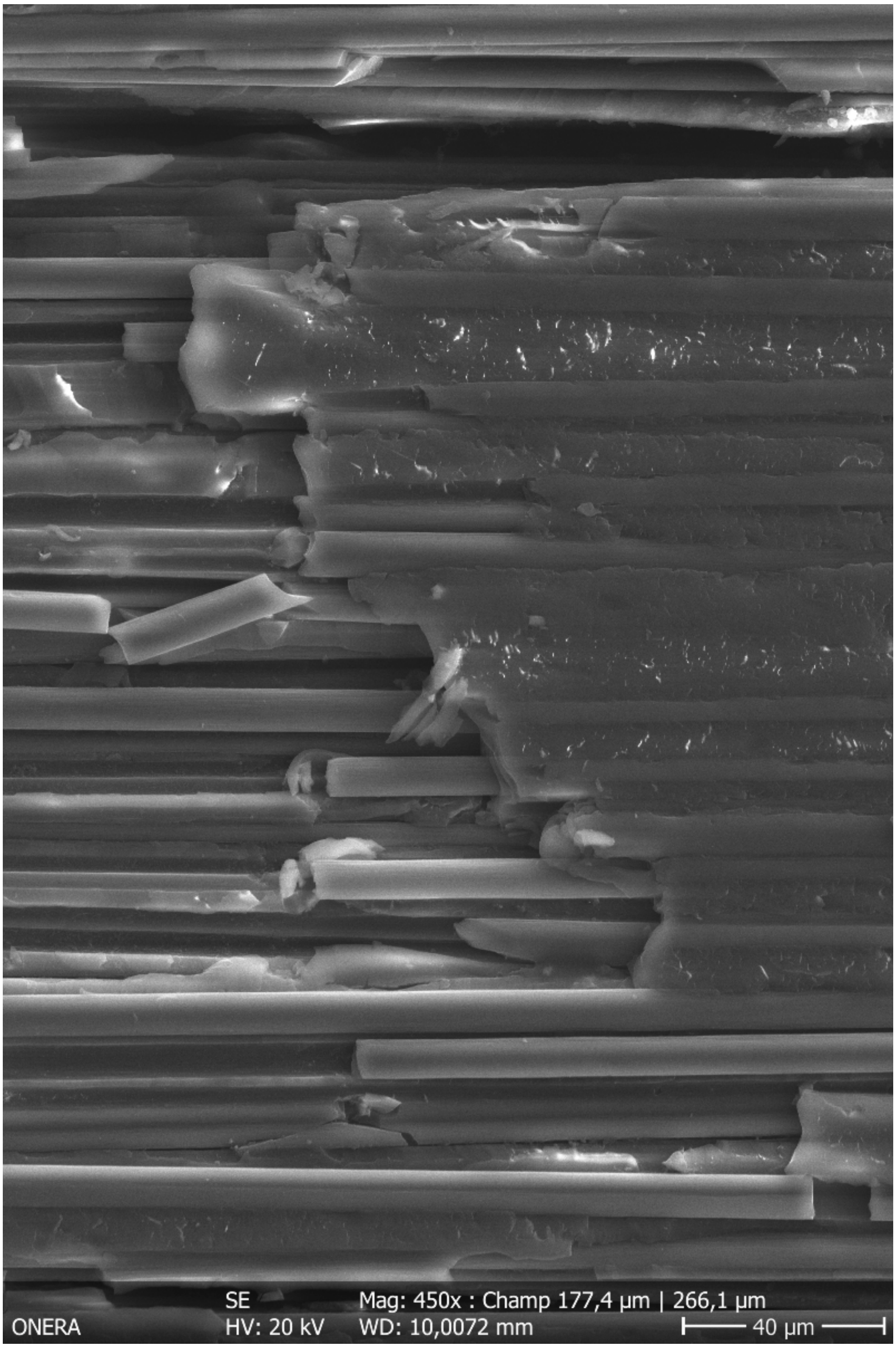

Figure B.5. Higher resolution SEM image example of a Type IV specimen with 450x magnification

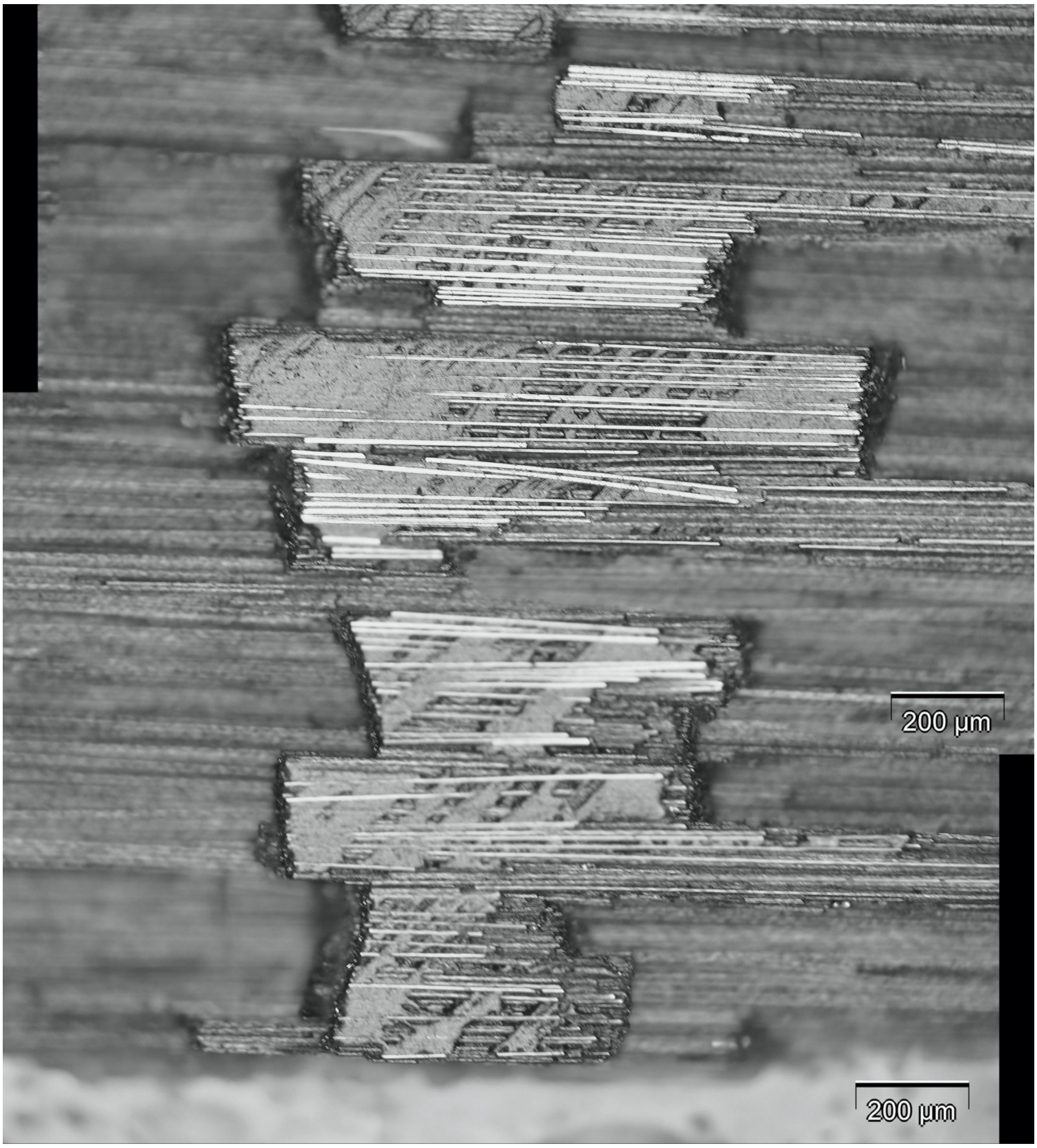

Figure B.6. Higher resolution stitched images taken by optical microscopy of the investigated Type IV coupon

Figure B.6. Higher resolution stitched images taken by optical microscopy of the investigated Type IV coupon